Design and Modification of Polyazine-Bridged Ru(II),Rh(III) Bimetallic and Trimetallic Supramolecular Complexes Applicable in Solar Energy Harvesting for the Photocatalytic Reduction of Water to Hydrogen

Travis Azor White

Dissertation submitted to the faculty of the Virginia Polytechnic Institute and State University in partial fulfillment of the requirements for the degree of

Doctor of Philosophy

In

Chemistry

Karen J. Brewer (Chair)

Harry C. Dorn

Brian E. Hanson

Brian M. Tissue

September 17th, 2012

Blacksburg, VA

Keywords: supramolecular complexes; electrochemistry; photophysics; photochemistry; photocatalysis; polyazine; ruthenium; rhodium; solar energy; water splitting; hydrogen production

Design and Modification of Polyazine-Bridged Ru(II),Rh(III) Bimetallic and Trimetallic Supramolecular Complexes Applicable in Solar Energy Harvesting for the Photocatalytic Reduction of Water to Hydrogen

Travis Azor White

Abstract

The goal of this research was to develop a series of mixed-metal supramolecular complexes through systematic component variation to better understand the role of structural modification on basic chemical and photochemical properties including photocatalysis of H_2O to H_2. Varying bidentate polypyridyl terminal ligands (TL), non-chromophoric halides (X), or number of Ru(II) light absorbers (LA) tunes the electrochemical, spectroscopic, photophysical, and photochemical properties within the supramolecular architecture. Ru(II),Rh(III),Ru(II) trimetallics of the design $[\{(TL)_2Ru(dpp)\}_2RhX_2](PF_6)_5$ (TL = phen = 1,10-phenanthroline or Ph_2phen = 4,7-diphenyl-1,10-phenanthroline; dpp = 2,3-bis(2-pyridyl)pyrazine; X = Cl^- or Br^-) covalently couple two Ru(II) LAs to a central Rh(III) electron collector (EC) through dpp polyazine bridging ligands (BL). Ru(II),Rh(III) bimetallics of the design $[(TL)_2Ru(dpp)RhCl_2(TL')](PF_6)_3$ (TL = Ph_2phen or bpy = 2,2′-bipyridine; TL′ = Ph_2phen or $^tBu_2bpy$ = 4,4′-Di-*tert*-butyl-2,2′-bipyridine) couple only one Ru(II) LA to a Rh(III) metal center through the dpp BL.

The Ru(II),Rh(III),Ru(II) trimetallic and Ru(II),Rh(III) bimetallic complexes are synthesized using a building block approach, permitting facile modification of the supramolecular architecture throughout molecular assembly. Electrochemical analysis of both architectures displays a Ru-based HOMO tuned by TL identity ($Ru^{II/III}$ = +1.62 V and +1.58 V vs. Ag/AgCl for TL = phen and Ph_2phen, respectively) and a Rh-based LUMO tuned by X identity ($Rh^{III/II/I}$ = −0.35 V and −0.32 V vs. Ag/AgCl for X = Cl^- and Br^-, respectively). Modification of TL′ at Rh(III) within the bimetallics provided varying LUMO identity. The trimetallics and bimetallics are efficient light absorbers throughout the UV and visible with $\pi\rightarrow\pi^*$ intraligand (IL) transitions in the UV and Ru(dπ)→ligand(π*) metal-to-ligand charge transfer (MLCT) transitions in the visible. While X identity does not vary the light absorbing properties within Ru(II),Rh(III),Ru(II) trimetallics, TL identity and the number of Ru(II) LAs strongly impacts spectral coverage and the extinction coefficient. Photoexcitation of the Ru(dπ)→dpp(π*) ^{1}MLCT results in near unity population of the weakly emissive, short-lived

Ru(dπ)→dpp(π*) ^{3}MLCT excited state, which is efficiently quenched by intramolecular electron transfer to populate a non-emissive Ru(dπ)→Rh(dσ*) metal-to-metal charge transfer (^{3}MMCT) excited state. Photolysis of the complexes in the presence of the sacrificial electron donor *N,N*-dimethylaniline (DMA) results in multi-electron collection at Rh, thereby converting Rh(III) to Rh(II) to Rh(I) accompanied by halide loss at each step. This establishes the Ru(II),Rh(III),Ru(II) and Ru(II),Rh(III) complexes as photochemical molecule devices (PMD) for photoinitiated electron collection (PEC).

The ability of these systems to undergo multiple redox cycles, absorb light efficiently, populate photoreactive excited states, and collect electrons at a reactive Rh metal center fulfills the requirements for H_2O reduction photocatalysts. Photolysis of trimetallic or bimetallic complexes at 470 nm in the presence of DMA and H_2O substrate yields photocatalytic H_2 production. Within $[\{(TL)_2Ru(dpp)\}_2RhX_2]^{5+}$ trimetallics (TL = phen or Ph_2phen; X = Cl^- or Br^-), varying the TL from phen to Ph_2phen and X from Cl^- to Br^- yielded the most active and robust photocatalyst with $[\{(Ph_2phen)_2Ru(dpp)\}_2RhBr_2]^{5+}$ producing 44 ± 6 mL H_2, 610 ± 90 mol H_2/mol Rh catalyst, and 7.3% maximum quantum efficiency (max. Φ_{H_2}) in a DMF solvent system after 20 h photolysis.

The proposed mechanism of PEC suggests bimetallic systems might be prepared that are active photocatalysts. Ru(II),Rh(III) bimetallics are synthetically more challenging and the energetic proximity of dpp(π*) and Rh(dσ*) orbitals make electronic tuning with steric protection of the photogenerated Rh(I) difficult. Within $[(TL)_2Ru(dpp)RhCl_2(TL')]^{3+}$ bimetallics (TL = Ph_2phen or bpy; TL′ = Ph_2phen or ^{t}Bu$_2$bpy), a careful balance of steric and electronic effects was required to produce active photocatalysts. The bimetallic $[(Ph_2phen)_2Ru(dpp)RhCl_2(Ph_2phen)]^{3+}$ produces 1.1 ± 0.07 mL H_2, 81 ± 5 TON, and 0.88% max. Φ_{H_2} in a DMF solvent system after 20 h photolysis. This establishes the $[(Ph_2phen)_2Ru(dpp)RhCl_2(Ph_2phen)]^{3+}$ complex as the first Ru(II),Rh(III) bimetallic to function as a homogeneous single-component H_2O reduction photocatalyst.

This dissertation reports the detailed analysis of the electrochemical, spectroscopic, photophysical, and photocatalytic properties of $[\{(TL)_2Ru(dpp)\}_2RhX_2]^{5+}$ trimetallic (TL = phen or Ph_2phen; X = Cl or Br) and $[(TL)_2Ru(dpp)RhCl_2(TL')]^{3+}$ bimetallic (TL = Ph_2phen or bpy; TL′ = Ph_2phen or ^{t}Bu$_2$bpy) supramolecular complexes. The design of the molecular architecture and the intrinsic properties of each component contribute to the overall function and efficiency of these systems. The careful design, meticulous synthesis and purification, detailed characterizations, and methodical experimentation have led to an in-depth understanding of the properties and factors needed for more efficient photocatalytic reduction of H_2O to H_2.

Acknowledgements

I wish to start by thanking the most important and influential person in the world to me; my mother, Brenda. Without her constant love and support, I would not be one tenth of the man I am today. My father Thomas and my sister Charlene have supported my decisions throughout life and continue to do so. My entire family has been a crutch for me to lean on when times get tough as I know that there are always people in this world who love me regardless. I wish to thank my two best friends, Christopher Finley and Joseph Decker, who can only be described as the two brothers I never had. I thank my instructors at UNC-Charlotte who introduced me to the wonderful world of chemistry and who were able to keep my interests. I thank Ms. Kathleen Nunnally from the University Center for Academic Excellence at UNC-Charlotte for her guidance and moral support throughout my undergraduate career. My co-workers at National Gypsum Company, Rick Atkisson and Joseph Bailey, exposed me to chemistry in the "real world" and gave me an appreciation for my work on a different level. I would like to thank my committee members, Prof. Harry C. Dorn, Prof. Brian E. Hanson, and Prof. Brian M. Tissue, for constantly challenging me to do better and to think at a higher level. I would like to thank Mr. William Bebout of Analytical Services at Virginia Tech for his assistance with mass spectral analyses. I would like to acknowledge those at UNC-Chapel Hill for allowing me to visit and perform transient absorption spectroscopy experiments using their instrumentation; Dr. M. Kyle Brennaman, Prof. Thomas J. Meyer, Dr. Erik Grumstrup, Mr. Ryan Vary, and Prof. John M. Papanikolas. I owe an immense debt of gratitude to members of the Brewer research group, past and present. I would like to specifically mention Dr. Krishnan Rangan, Dr. Shamindri M. Arachchige, Dr. Gerald F. Manbeck, Dr. David F. Zigler, Dr. Samantha L. H. Higgins, Dr. Avijita Jain, Mr. Jared R. Brown, Mr. Rongwei Zhou, Ms. Joan M. Zapiter, Mrs. Jing Wang, Ms. Hannah E. Mallalieu, Ms. Brittany N. Whitaker, and Ms. Jessica D. Knoll for their help and assistance throughout my graduate school career. Without the family-like environment and support I encountered within the Brewer group, I would not have been able to accomplish this. And finally, I have to give enormous thanks and acknowledgement to my graduate research advisor, Prof. Karen J. Brewer. Her guidance, support, and belief in me throughout my graduate career can never be repaid.

Table of Contents

List of Figures

List of Tables

List of Abbreviations

^{1}ES = Singlet excited state
^{1}GS = Singlet ground state
^{1}IL = Singlet intraligand
^{1}LF = Singlet ligand field
^{1}MLCT = Singlet metal-to-ligand charge transfer
^{3}ES = Triplet excited state
^{3}IL = Triplet intraligand
^{3}LF = Triplet ligand field
^{3}MLCT = Triplet metal-to-ligand charge transfer
^{3}MMCT = Triplet metal-to-metal charge transfer
BL = Bridging ligand
bpm = 2,2′-bipyrimidine
bpy = 2,2′-bipyridine
cm = Centimeter
CPE = Controlled potential electrolysis
CT = Charge transfer
CTTS = Charge transfer-to-solvent
CV = Cyclic voltammogram
d-d = Ligand field state
dmgBF$_2$ = (difluoroboryl)dimethylglyoximate
dpb = 2,3-bis(2-pyridyl)benzoquinoxaline
dpp = 2,3-bis(2-pyridyl)pyrazine
dpq = 2,3-bis(2-pyridyl)quinoxaline
DMA = *N*,*N*-dimethylaniline
EA = Electron acceptor
EC = Electron collector
ED = Electron donor
ER = Electron relay
ES = Excited state
et = Electron transfer
eV = Electron volt
GS = Ground state
H°_{comb} = Enthalpy of combustion
h = Hour
HOMO = Highest occupied molecular orbital
ic = Internal conversion
IL = Intraligand
IPCT = Ion pair charge transfer
irr = Irradiation

isc = Intersystem crossing
IVCT = Intervalence charge transfer
J = Joule
k = Rate constant
L-pyr = (4-pyridine)oxazolo[4,5-*f*]phenanthroline
LA = Light absorber
LC = Ligand centered
LF = Ligand field
LMCT = Ligand-to-metal charge transfer
LUMO = Lowest unoccupied molecular orbital
m = Meter
m/z = Mass-to-charge ratio
Mebpy-$(CH_2)_2$-Mebpy = 1,2-bis[4-(4′-methyl-2,2′-bipyridyl)]ethane.
Me_2bpy = 4,4′-dimethyl-2,2′-bipyridine
Me_2phen = 4,7-dimethyl-1,10-phenanthroline
min = Minutes
mL = Milliliter
MLCT = Metal-to-ligand charge transfer
MMCT = Metal-to-metal charge transfer
mM = Millimolar
NHE = Normal hydrogen electrode
nm = Nanometer
nr = Non-radiative deactivation
pbn = 2-(2-pyridyl)benzo[*b*]-1,5-naphthyridine
PEC = Photoinitiated electron collection/collector
Ph_2phen = 4,7-diphenyl-1,10-phenanthroline
phen = 1,10-phenanthroline
PMD = Photochemical molecular device
ppy = 2-phenylpyridine
r = Radiative deactivation
RM = Reactive metal
rxn = Reaction
SWV = Square wave voltammogram
$^{t}Bu_2$bpy = 4,4′-Di-*tert*-butyl-2,2′-bipyridine
tatpp = 9,11,20,22-tetraazatetrapyrido[3,2-*a*:2′,3′-*c*:3″,2″-*1*:2‴,3‴-*n*]pentacene
tatpq = 9,11,20,22-tetraazatetrapyrido[3,2-*a*:2′,3′-*c*:3″,2″-*1*:2‴,3‴-*n*]pentacene-10,21-quinone
TEA = Triethylamine
TEOA = Triethanolamine
TL,TL′ = Terminal ligand
tpphz = tetrapyrido[3,2-a:2′,3′-c:3″,2″-h:2‴,3‴-j]phenazine

TON = Turnover number
vr = Vibrational relaxation
W = Watts

ΔOD = Change in optical density
$\hat{\mu}_e$ = Dipole moment operator
τ = Excited state lifetime
Ψ_{ES} = Excited state wavefunction
ε = Extinction coefficient
Ψ_{GS} = Ground state wavefunction
μL = Microliter
μM = Micromolar
μmol = Micromole
f = Oscillator strength
hν = Photoexcitation
π = Pi-type interaction
Φ_{H_2} = Quantum efficiency of H_2 formation
Φ^{em} = Quantum yield of emission
Φ^{pop} = Quantum yield of population
σ = Sigma-type interaction
λ = Wavelength
ν = Scan rate

Thesis Statement

The goal of this research is to study the electrochemical, photophysical, and photochemical properties of polyazine-bridged Ru(II),Rh(III) supramolecular complexes and how tuning these properties through component modification influences basic chemical properties and the ability to photocatalytically reduce H_2O to H_2.

List of Publications

White, T. A.; Manbeck, G.; Whitaker, B.; Quinn, K.; Zhou, R.; Dent, E.; Knoll, J.; Wang, J.; Higgins, S.; Arachchige, S.; Brewer, K. J. "Supramolecular complexes as photochemical molecular devices for solar energy conversion via water reduction to produce hydrogen." *From Preprints of Symposia – American Chemical Society, Division of Fuel Chemistry* **2012**, *57*, 581-582.

White, T. A.; Knoll, J. D.; Arachchige, S. M.; Brewer, K. J. "A series of supramolecular complexes for solar energy conversion via water reduction to produce hydrogen: an excited state kinetic analysis of Ru(II),Rh(III),Ru(II) photoinitiated electron collectors." *Materials* **2012**, *5,* 27-46.

White, T. A.; Higgins, S. L. H.; Arachchige, S. M.; Brewer, K. J. "Efficient photocatalytic hydrogen production in a single-component system using Ru,Rh,Ru supramolecules containing 4,7-diphenyl-1,10-phenanthroline." *Angewandte Chemie: International Edition* **2011**, *50,* 12209-12213.

White, T. A.; Whitaker, B. N.; Brewer, K. J. "Discovering the balance of sterics and electronics needed to provide a new structural motif for photocatalytic hydrogen production from water." *Journal of the American Chemical Society* **2011**, *133*, 15332-15334.

Arachchige, S. M.; Shaw, R.; White, T. A.; Shenoy, V.; Tsui, H.-M.; Brewer, K. J. "High turnover in a photocatalytic system for water reduction to produce hydrogen using a Ru,Rh,Ru photoinitiated electron collector." *ChemSusChem* **2011**, *4,* 514-518.

Wang, J.; White, T. A.; Arachchige, S. M.; Brewer, K. J. "A new structural motif for photoinitiated electron collection: Ru,Rh bimetallics providing insight into H_2 production *via* photocatalysis of water reduction by Ru,Rh,Ru supramolecules." *Chemical Communications* **2011**, *47,* 4451-4453.

Higgins, S. L. H.; White, T. A.; Winkel, B. S. J.; Brewer, K. J. "Redox, spectroscopic, and photophysical properties of Ru-Pt mixed-metal complexes incorporating 4,7-diphenyl-1,10-phenanthroline as efficient DNA binding and photocleaving agents." *Inorganic Chemistry* **2011**, *50*, 463-470.

White, T. A.; Arachchige, S. M.; Sedai, B.; Brewer, K. J. "Emission spectroscopy as a probe into photoinduced intramolecular electron transfer in polyazine bridged Ru(II),Rh(III) supramolecular complexes." *Materials* **2010**, *3*, 4328-4354.

White, T. A.; Rangan, K.; Brewer, K. J. "Synthesis, characterization, and study of the photophysics and photocatalytic properties of the photoinitiated electron collector $[\{(phen)_2Ru(dpp)\}_2RhBr_2](PF_6)_5$." *Journal of Photochemistry and Photobiology A: Chemistry* **2010**, *209*, 203-209.

1. Introduction

Fuel consumption and availability are topics commonly discussed and debated in the presence of one another as modern society relies on energy from various sources to thrive.[1] As the human population on earth increases and the energy consumption of formerly impoverished people increases so does the consumption of fuels needed for daily functioning. The majority of energy used in today's world is derived from carbon-based, non-renewable sources such as oil, natural gas, and coal. Interestingly, these energy sources are generated from solar energy via biosynthesis. The inevitable depletion of these resources, coupled with environmental degradation due to large accumulations of combustion by-products over time, forces mankind to act immediately and search for a solution to the energy issue in order to sustain a suitable means of life.

The earth contains a multitude of energy sources at mankind's disposal to harness and transform into a beneficial product without causing long-term damage.[1] Solar, wind, water, and geothermal energies are capable of being converted into electricity with minimal to zero use of fossil fuels as energy storage and carrier units. Technological advances permit the development of materials that transduce solar energy (photovoltaic cell) and wind or water energy (turbine engine) into electrical energy. Of particular interest is the development and exploitation of materials that store energy in the form of chemical bonds producing high energy density transportable fuels. Solar energy-to-chemical energy conversion schemes provide a promising avenue to developing energy-rich fuels.[2,3]

1.1. Solar-to-Chemical Energy Conversion

1.1.1. Solar Energy

Solar energy is an immensely abundant, naturally occurring, inexhaustible resource provided by the sun. Earth receives more solar energy in one hour (4.3×10^{20} J) than the total energy consumed on the planet in one year (4.1×10^{20} J).[4] The sun emits polychromatic light and the majority of what reaches the earth's surface is between 280 nm (4.4 eV) and 2,500 nm (0.50 eV). The most intense solar wavelengths that reach the earth's surface occur in the visible region (400-700 nm) and deliver a maximum of 1.6 $W \cdot m^{-2} \cdot nm^{-1}$ (**Figure 1.1**).[5] Taking advantage of this abundant energy source to potentially drive thermodynamically uphill reactions such as H_2O

splitting or CO_2 reduction is paramount in the development of alternative fuel sources derived from the sun.

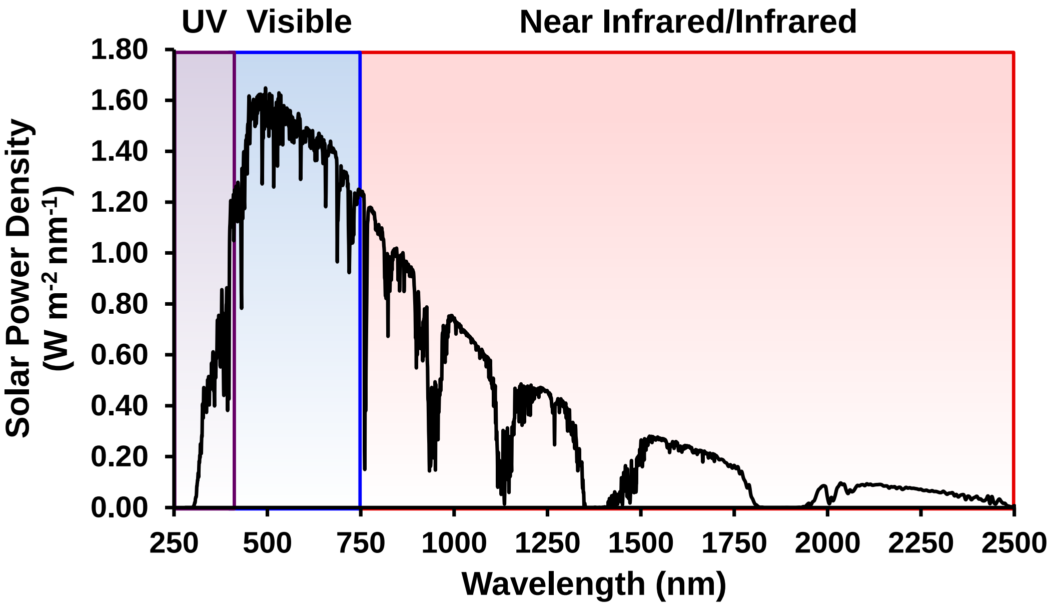

Figure 1.1: Solar irradiance spectrum depicting solar power density reaching the earth's surface as a function of wavelength.[5] Solar power density units correspond to the intensity of light at each wavelength (nm) absorbed by a surface with an area of 1 m^2.

1.1.2. Thermodynamics of H_2O Splitting

Splitting H_2O into its molecular components of H_2 and O_2 has been proposed to help fill the void in terms of producing a carbon-neutral, renewable fuel source as H_2O is an abundant resource.[6,7] Splitting H_2O into H_2 and O_2 is a thermodynamically uphill reaction that requires 1.23 V/e^- via a multi-electron process.[8] Both H_2O oxidation and reduction are pH and temperature dependent with **equations 1.1-1.3** displaying the overall and pertinent half reactions at pH = 7 and 25°C (potentials vs. NHE).[8,9] Potentials of reactions are related to free energy via $\Delta G° = -nFE°$ where $\Delta G°$ is the standard change in Gibbs free energy, n is the number of electrons, F is Faraday's constant (96,485 C/mol), and E° is the standard reduction potential.

Overall Reaction

$2\ H_2O_{(l)} \rightarrow 2\ H_{2(g)} + O_{2(g)}$ $E = -1.23\ V$ eq. 1.1

Hydrogen Production

$4\ e^- + 4\ H^+_{(aq)} \rightarrow 2\ H_{2(g)}$ $E = -0.41\ V$ eq. 1.2

Oxygen Production

$2\ H_2O_{(l)} \rightarrow 4\ e^- + 4\ H^+_{(aq)} + O_{2(g)}$ $E = -0.82\ V$ eq. 1.3

Producing H_2 as a fuel source is an attractive alternative to carbon-based energy sources. Hydrogen combustion is an energy rich, exothermic chemical reaction ($H^{\circ}_{comb} = -143$ kJ/g) containing the highest power density per gram of non-nuclear based fuels.[10] The products of combustion are H_2O and heat which eliminates the emission of CO_2. The gaseous nature of this fuel presents storage challenges but research is developing a multitude of materials such as porous polymer membranes and metal-organic frameworks for solid phase storage.[11] Solar energy storage in the form of H_2 via solar water splitting is an attractive and feasible approach to solar-to-chemical energy conversion.

The challenging task of reducing H_2O to H_2 fuel via solar energy has several requirements: (1) light must be absorbed efficiently by the medium to induce a highly energetic state, (2) charges need to be separated to generate a potential at the molecular level, (3) multiple reducing equivalents must be accumulated to provide for energetically feasible reactions, and (4) chemical bonds must be broken and formed.[12-15] As shown by **equation 1.2**, aqueous protons are reduced to H_2 at an applied potential of −0.41 V vs. NHE. While the sun provides sufficient energy to drive thermodynamically uphill water splitting, H_2O does not absorb most sunlight that reaches the earth's surface and does not cleave upon light exposure.[8] This multi-electron reaction requires an accumulation of negative charges to be delivered to the protons or water substrate. Incorporating molecular photocatalysts to the system that function as photosensitizers to efficiently absorb light, electron relays to shuttle electrons, and catalytically active sites to deliver electrons to the substrate is an attractive approach.

The initial process in any solar energy conversion scheme is the efficient absorption of photons throughout the UV and visible regions to generate high energy oxidizing and reducing species. The prototypical inorganic light absorber (LA) $[Ru(bpy)_3]^{2+}$ (bpy = 2,2′-bipyridine) and related metal-based chromophores have been utilized in solar energy harnessing and conversion applications due to their favorable electrochemical, light absorbing, excited state, and photochemical properties.[16-18] $[Ru(bpy)_3]^{2+}$ possesses large molar absorptivity (ε) values throughout the UV ($\varepsilon > 80{,}000\ M^{-1}cm^{-1}$) and visible ($\varepsilon > 10{,}000\ M^{-1}cm^{-1}$) that lead to near unity population of low-energy ($\lambda^{em} = 603$ nm), long-lived ($\tau = 850$ ns), highly-emissive ($\Phi^{em} = 0.070$), photoreactive metal-to-ligand charge transfer (MLCT) excited states that are stronger oxidizing and reducing agents than the ground state species.[19-21] The rich, stable redox-active properties and photoreactive excited states of such metal-based chromophores have led many research groups to exploit these complexes as photosensitizers in electron and energy transfer schemes within solar energy conversion.

1.1.3. Photochemical Production of H_2

Since the discovery of the Honda-Fujishima effect[22] whereby photocatalysis ($\lambda^{irr} < 415$ nm) of H_2O to H_2 and O_2 in the presence of a titanium-oxide electrode (anode) and a platinum electrode (cathode) is achieved, efforts have been undertaken to better understand each half reaction at the molecular level. Molecular photocatalysts for the photochemical production of H_2 from H_2O are well established throughout the literature with a plethora of systems that allow for structural and component modification to study the factors influencing H_2 production.[20,23-36] Early studies of multi-component systems utilized $[Ru(bpy)_3]^{2+}$ LA as the photosensitizing unit, $[Rh(bpy)_3]^{3+}$ electron relays (ER) to shuttle electrons, Pt colloid reactive metal (RM) catalysts formed *in situ* from K_2PtCl_4, and triethanolamine (TEOA) sacrificial electron donors (ED) to regenerate the oxidized light absorber.[25,26,28] After 45 h photolysis of the aqueous solution at $\lambda^{irr} = 450 \pm 20$ nm, 22.4 mL of H_2 were produced which established this as a functioning molecular photocatalytic system for H_2O reduction to H_2. This photosystem functions through successive excited state (ES) and ground state (GS) electron transfer events mediated by diffusional factors (**Figure 1.2**). Inherent downsides to such multi-component systems are the often efficient back electron transfer reactions prior to cage escape and the possibility of unwanted side reactions. Reduction of the $[Rh^{III}(bpy)_3]^{3+}$ ER to $[Rh^{II}(bpy)_3]^{2+}$ leads to disproportionation to form

$[Rh^I(bpy)_2]^+$ and $[Rh^{III}(bpy)_3]^{3+}$. Dimerization of the $[Rh^I(bpy)_2]^+$ species through Rh(I)-Rh(I) bond formation to generate $[Rh^I(bpy)_2]_2^{2+}$ or $[Rh^I(bpy)_2]_2H^{3+}$ is expected to inhibit photocatalysis throughout the catalytic cycle.[24] While multi-component systems may not be as beneficial in studying the complex processes involved in H_2 formation from H_2O, they provide the back drop for developing covalently coupled large assemblies capable of performing specific light-driven tasks at the molecular level.

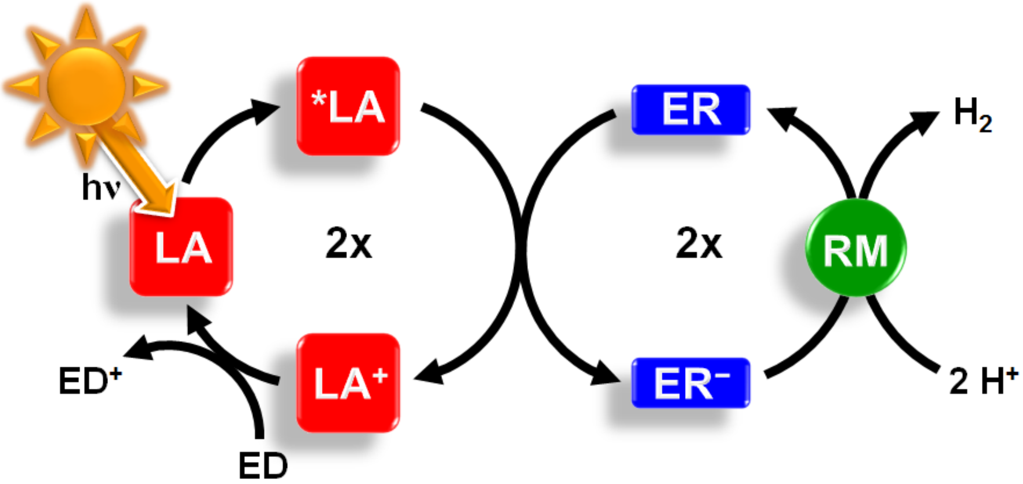

Figure 1.2: Photocatalytic cycle for the reduction of H_2O to H_2 using a multi-component system. The 2x indicates each cycle must occur twice per H_2 molecule formation. LA = light absorber; ER = electron relay; RM = reactive metal; ED = electron donor; hν = photoexcitation.

1.2. Supramolecular Chemistry

Advances in chemical education and research have driven chemists to progress from the study of small, simple molecules to the understanding of large molecular assemblies. The field of supramolecular chemistry encompasses a wide array of molecules that are governed at the molecular level from weak interactions (hydrogen bonding, intermolecular forces) to strong interactions (covalent bonding).[37-40] This area of chemistry focuses on systems, labeled supramolecular complexes, comprised of multiple components that combine and contribute to the functioning and identity of the large molecular assembly connected by coordinate covalent bonds. Nature's development and evolution of natural photosynthesis through the complex structures of Photosystem I and II have fascinated scientists for centuries. Only recently has science begun to emulate nature by attempting to mimic natural photosynthesis through the development of artificial photosynthetic assemblies. The vast number of components within Photosystem I and II play specific roles within the supramolecular assembly and can be studied to obtain more insight for designing efficient supramolecular complexes toward artificial photosynthesis.

1.2.1. Supramolecular Complexes Defined

With respect to this dissertation, supramolecular complexes are defined as molecular machines comprised of molecular components coupled via coordination bonds whose individual acts and properties contribute to the overall functioning of the newly formed supramolecule as first proposed by Balzani.[41,42] The capabilities of the newly generated supramolecular complex are determined by the molecular components chosen and the molecular architecture design. In the realm of supramolecular photochemistry, supramolecular complexes must be able to absorb photons and subsequently undergo photophysical and/or photochemical reactions to perform task-specific, complex functions.

1.2.2. Photochemical Molecular Devices for Photoinitiated Electron Collection

Supramolecular complexes that perform a specific light-induced function are labeled photochemical molecular devices (PMDs).[41-44] These systems are of particular interest as they take advantage of sunlight as the thermodynamic driving force behind propelling a particular reaction. Judicious design and assembly of the molecular components within PMDs provide supramolecular complexes capable of performing complex tasks at the molecular level. Systems engineered to populate high energy excited states upon photoexcitation, followed by charge migration and/or accumulation between suitable electron donor (ED) and electron acceptor (EA) sites, **Figure 1.3**, are of considerable interest in the realm of artificial photosynthesis, molecular photovoltaics, and solar energy conversion.

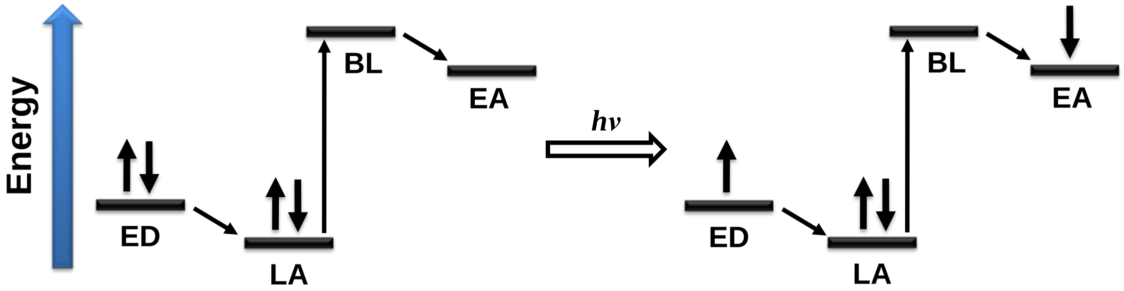

Figure 1.3: Orbital energy diagram depicting orbital energetics required for a molecular photovoltaic whereby photoexcitation induces charge separation to generate a potential. LA = light absorber; BL = bridging ligand; ED = electron donor; EA = electron acceptor; hν = photoexcitation.

Collection of multiple reducing equivalents at a central site via photoinitiated processes is beneficial to drive multi-electron photocatalysts. Photoinitiated electron collectors (PECs) are a type of PMD typically comprised of metal-based LAs covalently coupled to an electron collecting (EC) site through polyazine bridging ligands (BL).[42] **Figure 1.4** shows the assembly proposed for a PEC whereby photoexcitation of the peripheral LAs affords collection of two electrons at the centralized EC site through the bound BL connector units in the presence of a sacrificial electron donor (ED).

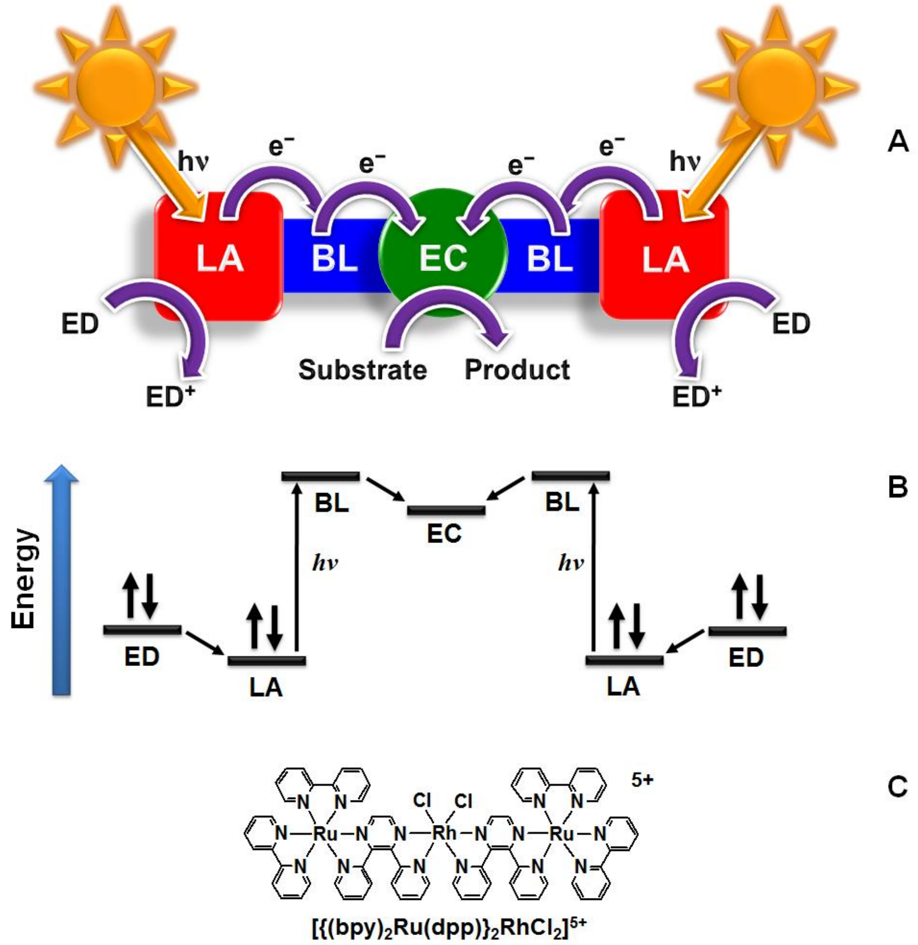

Figure 1.4: (A) Proposed photochemical molecular device for photoinitiated electron collection; (B) Orbital energy diagram depicting orbital energetics required for photoinitiated electron collection at a localized site; (C) Structure of $[\{(bpy)_2Ru(dpp)\}_2RhCl_2]^{5+}$, a reported PMD for PEC. LA = light absorber; BL = bridging ligand; EC = electron collector; ED = electron donor; hν = photoexcitation; e^- = electron; bpy = 2,2′-bipyridine; dpp = 2,3-bis(2-pyridyl)pyrazine.

1.2.3. Molecular Components

Designing PMDs for PEC requires an in-depth understanding of the molecular components that make up the molecular assembly, the role each subunit plays in the functioning of the supramolecular complex, and the perturbation of subunit properties upon assembly.[45] Generating a knowledge base for such systems allows for coarse and fine tuning of the supramolecular assembly properties through component variation to predict how a system will function. The ultimate goal for designing PMDs for PEC requires photoexcitation of light absorbing species to populate high energy excited states which undergo intramolecular electron transfer through the connecting unit to the electron collecting species. Factors that affect the properties of these systems are the nature of the polyazine BL, the polypyridyl ligand set identity of the Ru(II) LA, and the coordination environment of the EC subunit. An issue that arises with electron collection at a central site is the coulombic barrier encountered due to electron-electron repulsion resulting in high energy, non-stable intermediates. Molecular components of interest include polyazine BLs, Ru(II)-polypyridyl LAs, and metal- or ligand-based ECs.[20,41,46-49]

Polyazine BLs are crucial to the expansion of molecular architectures with polyazine MLCT chromophores that incorporate multiple components.[41,47,48] **Figure 1.5** displays examples of bis-bidentate polyazine BLs that serve to connect the Ru(II) LA to the EC unit. The coordinate covalent bond formed between the polyazine BL and metal centers perturbs the properties of both subunits with a stabilization of the BL π* acceptor orbitals through σ-donation to the electropositive metal center. The BL mediates intercomponent electronic communication between the LA and EC from strong to negligible depending on the nature of the BL, metals, and ligand set of each metal. Supramolecular complexes containing aliphatic linkers display properties that are additive of the molecular components due to negligible electronic communication between subunits, whereas aromatic linkers perturb the properties of each molecular component involved resulting in properties unique to the supramolecular assembly.

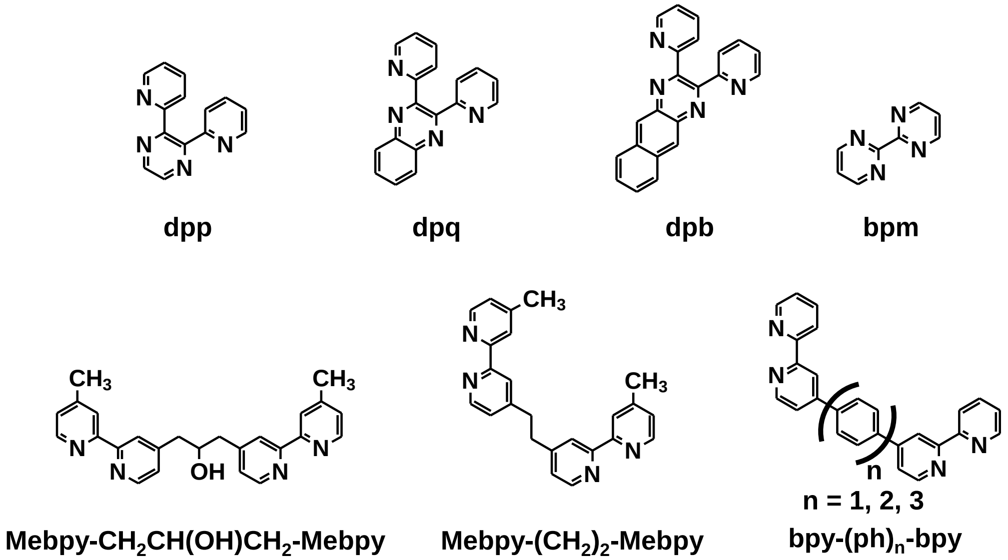

dpp dpq dpb bpm

$n = 1, 2, 3$

Mebpy-$CH_2CH(OH)CH_2$-Mebpy Mebpy-$(CH_2)_2$-Mebpy bpy-$(ph)_n$-bpy

Figure 1.5: Examples of bis-bidentate polyazine bridging ligands (BL). dpp = 2,3-bis(2-pyridyl)pyrazine; dpq = 2,3-bis(2-pyridyl)quinoxaline; dpb = 2,3-bis(2-pyridyl)benzoquinoxaline; bpm = 2,2′-bipyrimidine; Mebpy-$(CH_2)_2$-Mebpy = 1,2-bis[4-(4′-methyl-2,2′-bipyridyl)]ethane.

Ru(II)-polypyridyl complexes, such as $[Ru(bpy)_3]^{2+}$, are efficient LAs that serve to harness solar energy throughout the UV and visible region of the electromagnetic spectrum.[20,41,49,50] Polypyridyl terminal ligands (TL) tune the redox, light absorbing, and excited state properties of the complex due to the electron-withdrawing or -donating character of the ligand-based π* orbitals, as well as the overlap between the Ru(dπ) and ligand-based π* orbitals.[51] **Figure 1.6** displays examples of bidentate TLs with varying substituents. Photoexcitation of the Ru(II) LA throughout the UV and visible populate π→π* intraligand (IL) and Ru(dπ)→TL(π*) metal-to-ligand charge transfer (MLCT) excited states, respectively, which undergo intersystem crossing to populate low-lying emissive ^{3}MLCT excited states with unit efficiency. Substituting one or more of the polypyridyl TLs for polyazine BLs allows for the supramolecular architecture to expand and include multiple metal centers through coordination to the remote sites of the BL. Their light absorbing capabilities are important as well as their emissive properties, which are a probe into excited state reactions and long-lived ^{3}MLCT states. Ligand substitution shifts electron density within the complex as BLs are typically more electron-deficient than TLs and possess lower-lying unoccupied π* molecular orbitals, establishing the LUMO as BL(π*)-based. Photoexcitation results in efficient population of the lowest-lying excited state that is a

$Ru(d\pi) \rightarrow BL(\pi^*)$ ^{3}MLCT. The identity of the TL and/or BL coordinated to the Ru(II) LA tunes the energy of the formally $Ru(d\pi)$ donor orbitals thus allowing Ru to serve as an electron donor (ED) in the supramolecular complexes.

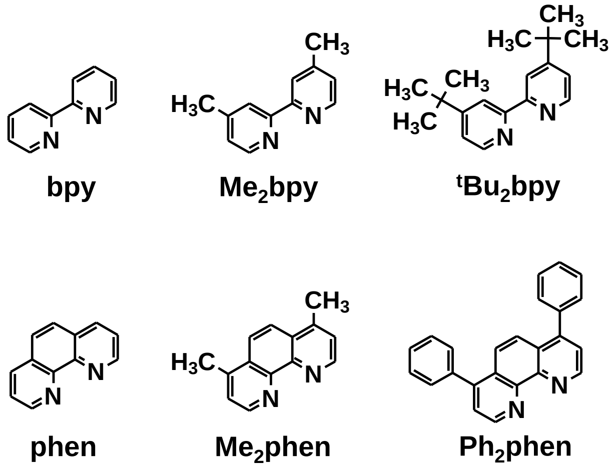

Figure 1.6: Examples of bidentate polypyridyl terminal ligands (TL). bpy = 2,2′-bipyridine; Me_2bpy = 4,4′-dimethyl-2,2′-bipyridine; ^{t}Bu_2bpy = 4,4′-Di-*tert*-butyl-2,2′-bipyridine; phen = 1,10-phenanthroline; Me_2phen = 4,7-dimethyl-1,10-phenanthroline; Ph_2phen = 4,7-diphenyl-1,10-phenanthroline.

Supramolecular complexes designed for PEC require the directional flow of charge to a localized site to afford collection of multiple reducing equivalents.[46,47] A coulombic barrier exists to collecting electrons, as simple $[(TL)_2Ru(BL)Ru(TL)_2]^{4+}$ motifs do not collect multiple electrons as reduction by one electron destabilizes this orbital and shortens excited state lifetimes, prohibiting electron collection. This barrier is overcome by having a separate spectroscopic and electron collecting orbital. Multi-electron reduction of molecular components that possess low-lying unoccupied molecular orbitals permit the accumulation of electrons with the potential for delivery to an appropriate substrate. Optical excitation of bound Ru(II) LAs allows for electron transfer through the polyazine BL to a single orbital or set of orbitals on the electron collector (EC) within a supramolecular complex to afford PEC. Unoccupied π^* and $d\sigma^*$ molecular orbitals within polyazine ligands and metal centers, respectively, can fulfill this requirement.

1.3. Properties of Ru(II)-Polypyridyl Complexes

The observed electrochemical and spectroscopic properties of Ru(II)-polypyridyl complexes can be described in terms of a localized molecular orbital approach, by which mixing of metal- and ligand-based linear combinations of atomic orbitals (LCAOs) results in MOs specific to the octahedral coordination complex.[52] **Figure 1.7** depicts a simplified block molecular orbital diagram of a d^6 octahedral complex containing π-backbonding ligands where MOs are represented as blocks. MOs of the same symmetry are able to overlap and this is shown as lines in the figure. This approach allows formal assignment of molecular orbitals as displaying predominately metal- or ligand-based character even though significant mixing occurs.

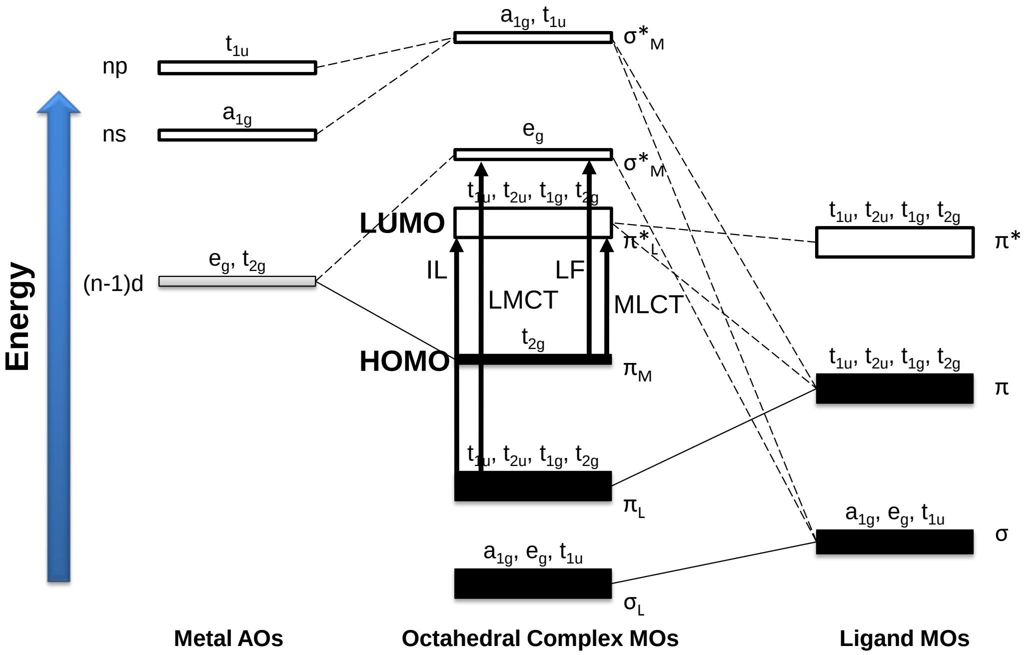

Figure 1.7: Simplified block molecular orbital diagram for a d^6 octahedral complex containing π-backbonding ligands. Black blocks represent filled orbitals, white blocks represent unfilled orbitals, and gray blocks represent partially filled orbitals. AO = atomic orbitals, MO = molecular orbitals, HOMO = highest occupied molecular orbital, LUMO = lowest unoccupied molecular orbital; IL = intraligand transition; LF = ligand field transition; LMCT = ligand-to-metal charge transfer transition; MLCT = metal-to-ligand charge transfer transition. Constructed using information from reference [52].

1.3.1. Electrochemical Properties

Electrochemistry provides insight into the energetics of frontier molecular orbitals within redox-active species and the stability of oxidized or reduced forms of a molecule.[53,54] Generally, anodic scans show reversible $Ru^{II/III}$ oxidation redox couples. The energy of the Ru(dπ) orbital set is modulated by the ligands attached, with electron-donating or -withdrawing groups destabilizing or stabilizing the Ru(dπ) orbitals, respectively.[17] Cathodic scans typically display reversible ligand-based redox couples indicative of electron placement within the ligand π* orbital. The electron-donating or -withdrawing properties of the ligand depend on the inductive (σ-type interaction) or resonance (π-type interaction) properties specific to the ligand design.

The $[Ru(bpy)_3]^{2+}$ LA contains three equivalent bidentate bpy TLs bound to the Ru(II) metal center through coordinate covalent bonds. This interaction results in rich electrochemical activity with anodic scans displaying a reversible $Ru^{II/III}$ oxidation (+1.31 V vs. Ag/AgCl) and cathodic scans displaying successive, reversible $bpy^{0/-}$ reductions (−1.30 V, −1.49 V, and −1.74 V vs. Ag/AgCl) for each bpy TL.[16,19] This establishes the HOMO and LUMO within this system as being Ru(dπ)- and bpy(π*)-based, respectively. **Table 1.1** contains electrochemical data for $[Ru(LL)_3]^{2+}$ homoleptic monometallic complexes (LL = bidentate polypyridyl TL or bis-bidentate polyazine BL). Structural modification of the bpy TL skeletal backbone to form 1,10-phenanthroline (phen) or 4,7-diphenyl-1,10-phenanthroline (Ph_2phen) does not alter the Ru(dπ) HOMO and ligand(π*) LUMO energetics significantly, suggesting bpy, phen, and Ph_2phen TLs possess similar electronic properties. Replacing TLs with electron-withdrawing BLs such as 2,3-bis(2-pyridyl)pyrazine (dpp) stabilize the Ru(dπ) orbitals ($Ru^{II/III}$ = +1.72 V vs. Ag/AgCl) and ligand(π*) orbitals ($dpp^{0/-}$ = −0.91 V vs.Ag/AgCl) due to the weaker Lewis basicity of dpp vs. bpy ($pK_{a(1)}$ = 2.90 ($dppH^+$) and 4.45 ($bpyH^+$)), **Figure 1.8**.[17]

Table 1.1: Electrochemical Properties of $[Ru(LL)_3]^{2+}$ Homoleptic Monometallic Complexes [a]

Complex	$Ru^{II/III}$	$LL^{0/-}$	$LL^{0/-}$	ΔE_{redox} [b]	Ref.
$[Ru(bpy)_3]^{2+}$	+1.31	−1.30	−1.49	2.61	[19]
$[Ru(phen)_3]^{2+}$	+1.31	−1.31	−1.42	2.62	[19]
$[Ru(Ph_2phen)_3]^{2+}$	+1.29	−1.27	[c]	2.56	[55]
$[Ru(dpp)_3]^{2+}$	+1.72	−0.91	−1.08	2.63	[56]

[a] LL = bidentate polypyridyl TL or bis-bidentate polyazine BL. Potentials reported in CH_3CN at RT and converted to V vs. Ag/AgCl. bpy = 2,2′-bipyridine; phen = 1,10-phenanthroline; Ph_2phen = 4,7-diphenyl-1,10-phenanthroline; dpp = 2,3-bis(2-pyridyl)pyrazine.

[b] $\Delta E_{redox} = E_{½}^{ox} - E_{½}^{red}$ or the energy gap (V) between $Ru^{II/III}$ oxidation and first reduction.

[c] Values not reported.

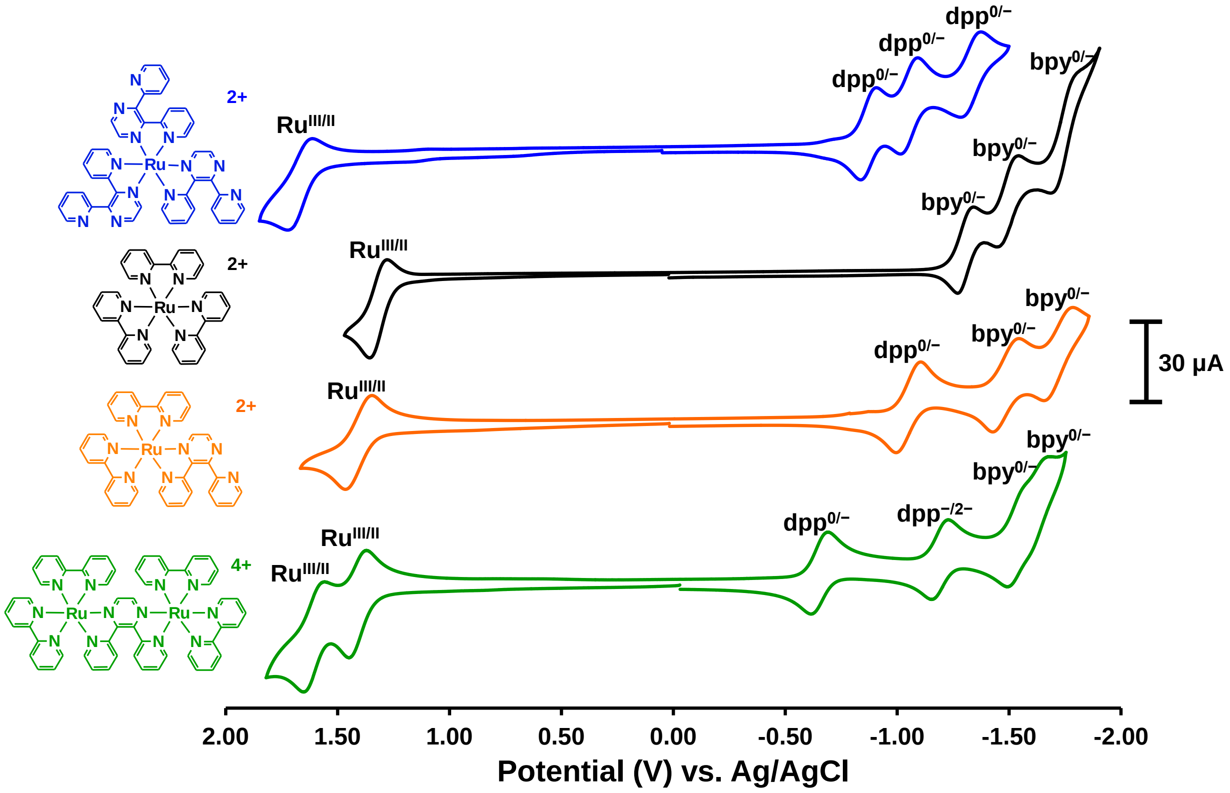

Figure 1.8: Cyclic voltammograms (CV) of $[Ru(dpp)_3]^{2+}$ (—),[57] $[Ru(bpy)_3]^{2+}$ (—),[58] $[(bpy)_2Ru(dpp)]^{2+}$ (—),[59] and $[\{(bpy)_2Ru\}_2(dpp)]^{4+}$ (—)[59] measured using a Pt disk working electrode, Pt wire auxiliary electrode, and Ag wire pseudo-reference electrode (converted to Ag/AgCl using ferrocene as an internal standard; $Fe(C_5H_5)_2^{0/+}$ = 0.46 V vs. Ag/AgCl). Measurements were made at RT in CH_3CN using 0.1 M Bu_4NPF_6 supporting electrolyte at a scan rate of 100 mV/s under an inert Ar atmosphere. bpy = 2,2′-bipyridine; dpp = 2,3-bis(2-pyridyl)pyrazine. Cyclic voltammograms produced are in agreement with literature references.

Substitution of a bidentate TL in $[Ru(TL)_3]^{2+}$ complexes for an electron-deficient BL to form $[(TL)_2Ru(BL)]^{2+}$ shifts the first reduction to more positive potential, resulting in stabilization of the ligand-based LUMO.[59] As shown in **Table 1.2** and **Figure 1.8**, the $[(bpy)_2Ru(dpp)]^{2+}$ heteroleptic monometallic complex undergoes reduction of the dpp BL at −1.01 V vs. Ag/AgCl, prior to the bpy TL reduction at −1.46 V vs. Ag/AgCl. This establishes the LUMO within this system as localized on the dpp BL, thus shifting electron density away from the bpy TL. The $Ru^{II/III}$ redox couple also shifts to a more positive potential (+1.31 V to +1.38 V) indicative of Ru(dπ) orbital stabilization from the electron-withdrawing character of the coordinated dpp BL. The energy gap between the $Ru^{II/III}$ oxidation and the first reduction, ΔE_{redox}, decreases upon substitution of a TL for a BL. Modifying the TL from bpy to phen or Ph_2phen does not strongly impact the Ru(dπ) orbitals but instead shifts the $dpp^{0/-}$ reduction to more negative potential.

Table 1.2: Electrochemical Properties of $[(TL)_2Ru(BL)]^{2+}$ Heteroleptic Monometallic and $[\{(TL)_2Ru\}_2(BL)]^{4+}$ Homobimetallic Complexes [a]

Complex	$Ru^{II/III}$	$Ru^{II/III}$	$BL^{0/-}$	$BL^{-/2-}$	$TL^{0/-}$	ΔE_{redox} [b]	Ref.
$[(bpy)_2Ru(dpp)]^{2+}$	+1.38	-	−1.01	-	−1.46	2.39	60
$[(phen)_2Ru(dpp)]^{2+}$	+1.39	-	−1.07	-	−1.35	2.46	56,61
$[(Ph_2phen)_2Ru(dpp)]^{2+}$	+1.39	-	−1.04	-	−1.38	2.43	55
$[\{(bpy)_2Ru\}_2(dpp)]^{4+}$	+1.43	+1.61	−0.61	−1.09	[c]	2.04	60
$[\{(phen)_2Ru\}_2(dpp)]^{4+}$	+1.44	+1.65	−0.64	−1.13	−1.38	2.08	56,61

[a] TL = bidentate polypyridyl terminal ligand; BL = bis-bidentate polyazine bridging ligand. Potentials recorded in CH_3CN at RT and converted to V vs. Ag/AgCl. bpy = 2,2′-bipyridine; phen = 1,10-phenanthroline; Ph_2phen = 4,7-diphenyl-1,10-phenanthroline; dpp = 2,3-bis(2-pyridyl)pyrazine.

[b] ΔE_{redox} = energy gap (V) between $Ru^{II/III}$ oxidation and first reduction

[c] Values not reported.

Expansion of the $[(TL)_2Ru(BL)]^{2+}$ molecular architecture is achieved through coordination of a second electropositive Ru(II) metal center to the BL's uncoordinated site to form $[\{(TL)_2Ru\}_2(BL)]^{4+}$ homobimetallic complexes.[59,62] This further stabilizes the BL π* orbitals through σ-donation to the electropositive metal with the second Ru(II) metal center serving as an electron-withdrawing moiety. The $BL^{0/-}$ reduction is shifted to a more positive potential from $[(bpy)_2Ru(dpp)]^{2+}$ to $[\{(bpy)_2Ru\}_2(dpp)]^{4+}$ (−1.01 V to −0.61 V vs. Ag/AgCl), as well as a concurrent stabilization of the Ru(dπ) orbitals as observed by the $Ru^{II/III}$ oxidation shifting from +1.38 V to +1.43 V, **Figure 1.8**. Of interest is the presence of a second $Ru^{II/III}$ oxidation at +1.61 V, indicating electronic communication between the two Ru(II) metal centers. The HOMO-LUMO energy gap between $Ru^{II/III}$ and $dpp^{0/-}$ decreases for the $[\{(bpy)_2Ru\}_2(dpp)]^{4+}$ homobimetallic (ΔE_{redox} = 2.04 V) as compared to $[(bpy)_2Ru(dpp)]^{2+}$ monometallic (ΔE_{redox} = 2.39 V). The same trend is observed for TL variation from bpy to phen, whereby coordination of a second Ru(II) further stabilizes the Ru(dπ) and BL(π*) orbitals. These structural modifications alter the molecular orbital energetics and allow for appropriate tuning of the redox-active properties within supramolecular complexes.

1.3.2. Light Absorbing Properties

Electronic absorption spectroscopy provides insight into the light absorbing capabilities of chromophores and photoactive species.[16,17,63,64] In order for any photophysical or photochemical process to take place, absorption of a photon must occur. Photon absorption transitions the GS species to a higher energy ES species by movement of an electron from an occupied to an unoccupied molecular orbital. The corresponding energies and intensities of such transitions in an electronic absorption spectrum provide insight into accessible electronic ES. For an electronic transition to occur, the electronic ground state (Ψ_{GS}) and excited state (Ψ_{ES}) wavefunctions must overlap and the transition obey the symmetry and spin selection rules. As shown in **equation 1.4**, the dipole moment operator ($\hat{\mu}_e$), which corresponds to the interaction between the photoexcitation electric vector and the electrons within the GS species, dictates the intensity of the transition moment for an electronic transition from the GS to the ES, $<\Psi_{GS}|\hat{\mu}_e|\Psi_{ES}>$.[16,17,63,64]

$$< \Psi_{GS}|\hat{\mu}_e|\Psi_{ES} > = \int \Psi_{GS}\,\hat{\mu}_e\Psi_{ES}d\nu \qquad \text{eq. 1.4}$$

The probability for transition GS→ES to occur is proportional to the square of the transition moment ($<\Psi_{GS}|\hat{\mu}_e|\Psi_{ES}>^2$) and is directly proportional to the oscillator strength (f) for such a transition. The oscillator strength is a dimensionless unit that describes the strength of a transition with values ranging from 0 (no transition) to 1 (strong transition) and is given by **equation 1.5**

$$f = 4.32\ x\ 10^{-9} \int_{-\nu}^{\nu} \varepsilon(\nu) d\nu \qquad \text{eq. 1.5}$$

where ε(ν) is the extinction coefficient value at a specific energy. The intensity of *f* relates to the extinction coefficient (ε) from the Beer-Lambert law, **equation 1.6**

$$A_\lambda = \varepsilon_\lambda cb \qquad \text{eq. 1.6}$$

where A_λ is absorbance at wavelength λ, ε_λ is the extinction coefficient in units of $M^{-1}cm^{-1}$ at wavelength λ, c is the species concentration in M, and b is the cell path length in cm. The Beer-Lambert law displays the degree of allowedness or forbiddenness through the value of ε for a transition at a specific energy. Spin selection rules for electronic transitions state that the spin multiplicity must not change from GS to ES. However, deviation from this selection rule is observed due to spin-orbit coupling resulting from the electromagnetic interaction of an electron's spin coupling with its orbital motion. For an allowed transition, the extinction coefficient (ε) ranges from 10^2-10^5 $M^{-1}cm^{-1}$. Conversely, ε for a formally forbidden transition ranges from 1-10^2 $M^{-1}cm^{-1}$.

Transitions observed in d^6 octahedral complexes (**Figure 1.7**) include intraligand (IL)/ligand centered (LC) π→π*, ligand field (LF)/metal centered (MC) dπ→dσ*, and charge transfer (CT) transitions. Ligand or metal centered transitions involve molecular orbitals which are primarily ligand or metal based in character, respectively. Charge transfer transitions involve movement of charge from a molecular orbital that is primarily one type of character to a molecular orbital that is primarily another type of character and can be separated into intramolecular and intermolecular type transitions. Intramolecular CT transitions, ligand-to-metal (LMCT), metal-to-ligand (MLCT), metal-to-metal (MMCT), and intervalence (IVCT), occur within the same molecule, while intermolecular CT transitions, charge transfer-to-solvent (CTTS) and ion pair (IPCT), involve multiple molecules. The transition's orbital origin and destination determine the potential reactivity of the excited state species.[65] LF transitions are influenced by the degree of metal d-orbital splitting (dπ and dσ*) which is determined by the strength of the field generated by the ligands, the oxidation state of the metal ion, and the size of the metal. Population of LF states can induce ligand photodissociation by increasing the electron density within the dσ* anti-bonding orbital set, thus weakening the metal-ligand bond. IL transitions are influenced by the extent of delocalization and rigidity within the π system and ligand skeletal backbone. IL states are typically non-reactive and deactivate through lower energy excited states, but are capable of energy transfer within extended aromatic systems. Factors which influence MLCT and LMCT transitions can be viewed as a combination of factors which impact LF and IL transitions (i.e. metal ion oxidation state, molecular orbital occupation and distribution, ligand coordination set, ligand delocalization and rigidity). MLCT and LMCT excited states are better reducing and oxidizing agents in comparison to the electronic GS due to a shift in electron density between molecular orbital basis sets. These states can react photochemically to afford electron transfer, photoisomerization, ligand photodissociation, and ligand photosubstitution products.

As shown by electrochemical analyses, the identity of the TL and/or BL set strongly impacts molecular orbital energetics within $[Ru(LL)_3]^{2+}$ homoleptic monometallic, $[(TL)_2Ru(BL)]^{2+}$ heteroleptic monometallic, and $[\{(TL)_2Ru\}_2(BL)]^{4+}$ homobimetallic complexes. **Tables 1.3** and **1.4** summarize the dominant transitions observed for these complexes. The $[Ru(bpy)_3]^{2+}$ LA possesses bpy IL $\pi \rightarrow \pi^*$ transitions in the UV (λ_{max} = 286 nm; $\varepsilon = 8.7 \times 10^4$ $M^{-1}cm^{-1}$) and Ru(dπ)→bpy(π^*) MLCT transitions in the visible (λ_{max} = 449 nm; $\varepsilon = 1.5 \times 10^4$ $M^{-1}cm^{-1}$). The large ε values ($\varepsilon \geq 10^3$ $M^{-1}cm^{-1}$) indicate the allowed character for these transitions. TL variation from bpy to phen displays small shifts to higher energy for the TL $\pi \rightarrow \pi^*$ (286 to 262 nm) and Ru(dπ)→TL(π^*) ^{1}MLCT (449 to 443 nm) transitions, with a concurrent increase in the extinction coefficient value. For TL = Ph_2phen, the Ru(dπ)→TL(π^*) ^{1}CT transitions shifts to 460 nm with a concurrent increase of the observed ε value (30,000 $M^{-1}cm^{-1}$). Use of BLs in place of TLs for the tris-homoleptic $[Ru(dpp)_3]^{2+}$ monometallic shifts the lowest energy ^{1}MLCT transition to lower energy (457 nm) compared to $[Ru(bpy)_3]^{2+}$ (449 nm) and $[Ru(phen)_3]^{2+}$ (443 nm), but similar in energy to $[Ru(Ph_2phen)_3]^{2+}$ (460 nm).

Table 1.3: Light Absorbing Properties of $[Ru(LL)_3]^{2+}$ Homoleptic Monometallic Complexes [a]

	LL π→π*		Ru(dπ)→LL(π*)		
Complex	λ (nm)	ε (10^4 $M^{-1}cm^{-1}$)	λ (nm)	ε (10^4 $M^{-1}cm^{-1}$)	Ref.
$[Ru(bpy)_3]^{2+}$	286	8.7	449	1.5	19
$[Ru(phen)_3]^{2+}$	262	10.2	443	1.7	19
$[Ru(Ph_2phen)_3]^{2+}$ [b]	[c]	[c]	460	3.0	66
$[Ru(dpp)_3]^{2+}$	294	4.4	457	1.4	67

[a] LL = bidentate polypyridyl TL or bis-bidentate polyazine BL. Values reported in CH_3CN at RT. bpy = 2,2′-bipyridine; phen = 1,10-phenanthroline; Ph_2phen = 4,7-diphenyl-1,10-phenanthroline; dpp = 2,3-bis(2-pyridyl)pyrazine.

[b] Value reported in H_2O.

[c] Values not reported.

Incorporation of a bis-bidentate BL to form $[(bpy)_2Ru(BL)]^{2+}$ (BL = dpp) decreases the energy of the lowest observed ^{1}MLCT transition with dpp (464 nm) (**Figure 1.9**), following the same trend observed electrochemically due to the electron-withdrawing character and increased BL π* stabilization. This establishes the lowest energy transition and excited state as being Ru(dπ)→BL(π*) MLCT in nature, therefore shifting charge density away from the TL and toward the BL. Substituting the bpy TL for phen to form $[(phen)_2Ru(dpp)]^{2+}$ does not substantially impact the visible region with Ru(dπ)→TL(π*) and Ru(dπ)→BL(π*) occurring at similar energies and with similar light absorbing capabilities for the two monometallics. The increased molar absorptivity observed for $[Ru(Ph_2phen)_3]^{2+}$ is shown with the $[(Ph_2phen)_2Ru(dpp)]^{2+}$ heteroleptic monometallic as well, suggesting inclusion of phenyl substituents strongly impacts light absorbing properties. Coordinating a second Ru(II) LA subunit to the BL shifts the Ru(dπ)→BL(π*) ^{1}MLCT transition to even lower energy due to stabilization of the BL π* orbitals. Homobimetallic complexes $[\{(bpy)_2Ru\}_2(dpp)]^{4+}$ and $[\{(phen)_2Ru\}_2(dpp)]^{4+}$ possess similar light absorbing characteristics with Ru(dπ)→TL(π*) ^{1}CT centered at 426 and 423 nm, respectively, and the Ru(dπ)→dpp(π*) ^{1}CT centered at 523 and 525 nm, respectively.

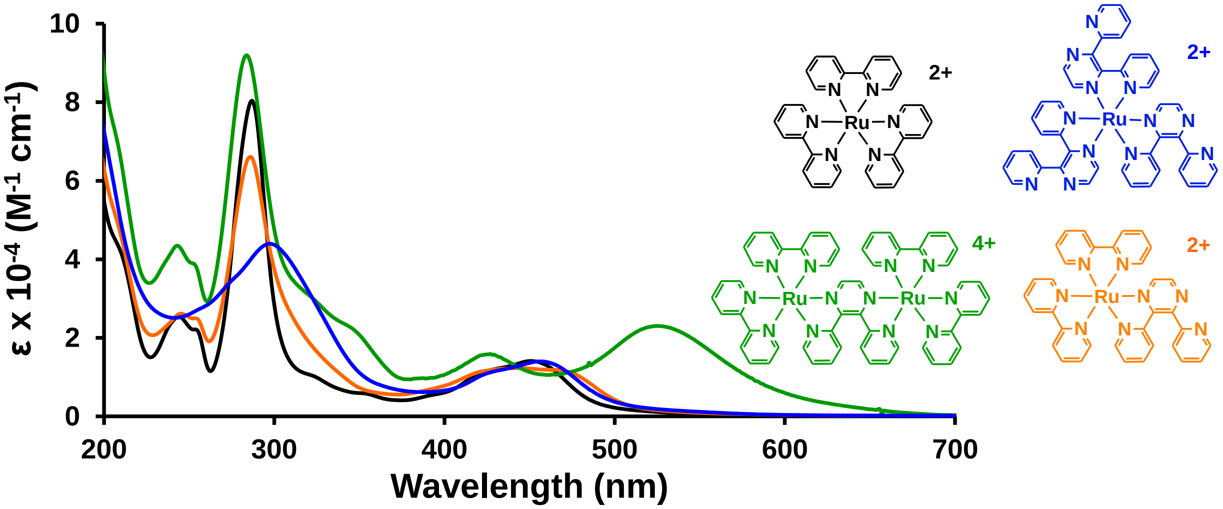

Figure 1.9: Electronic absorption spectra of [Ru(bpy)$_3$]$^{2+}$ (—),[18] [Ru(dpp)$_3$]$^{2+}$ (—),[57] [(bpy)$_2$Ru(dpp)]$^{2+}$ (—),[59] and [{(bpy)$_2$Ru}$_2$(dpp)]$^{4+}$ (—)[59] measured at RT in CH$_3$CN solvent using a 1 cm quartz cuvette. bpy = 2,2′-bipyridine; dpp = 2,3-bis(2-pyridyl)pyrazine. Electronic absorption spectra produced are in agreement with literature references.

Table 1.4: Light Absorbing Properties of [(TL)$_2$Ru(BL)]$^{2+}$ Heteroleptic Monometallic and [{(TL)$_2$Ru}$_2$(BL)]$^{4+}$ Homobimetallic Complexes [a]

	Ru(dπ)→TL(π*)		Ru(dπ)→BL(π*)		
Complex	λ (nm)	ε (10^4 M^{-1}cm^{-1})	λ (nm)	ε (10^4 M^{-1}cm^{-1})	Ref.
[(bpy)$_2$Ru(dpp)]$^{2+}$	441	1.2	464	1.2	61
[(phen)$_2$Ru(dpp)]$^{2+}$	434	1.4	465	1.1	61
[(Ph$_2$phen)$_2$Ru(dpp)]$^{2+}$	424	1.8	474	1.5	68
[{(bpy)$_2$Ru}$_2$(dpp)]$^{4+}$	426	2.0	523	2.3	61
[{(phen)$_2$Ru}$_2$(dpp)]$^{4+}$	423	2.1	525	2.3	61

[a] LL = bidentate polypyridyl TL or bis-bidentate polyazine BL. Values reported in CH$_3$CN at RT. bpy = 2,2′-bipyridine; phen = 1,10-phenanthroline; Ph$_2$phen = 4,7-diphenyl-1,10-phenanthroline; dpp = 2,3-bis(2-pyridyl)pyrazine; dpq = 2,3-bis(2-pyridyl)quinoxaline.

1.3.3. Excited State Properties

The observed photophysical and/or photochemical processes of Ru(II)-polypyridyl complexes provide information regarding the excited state dynamics and reactivity of these species.[16,17,63,64] **Figure 1.10** shows Morse potential energy surfaces and simplified state diagram representation of interstate conversion following excitation.

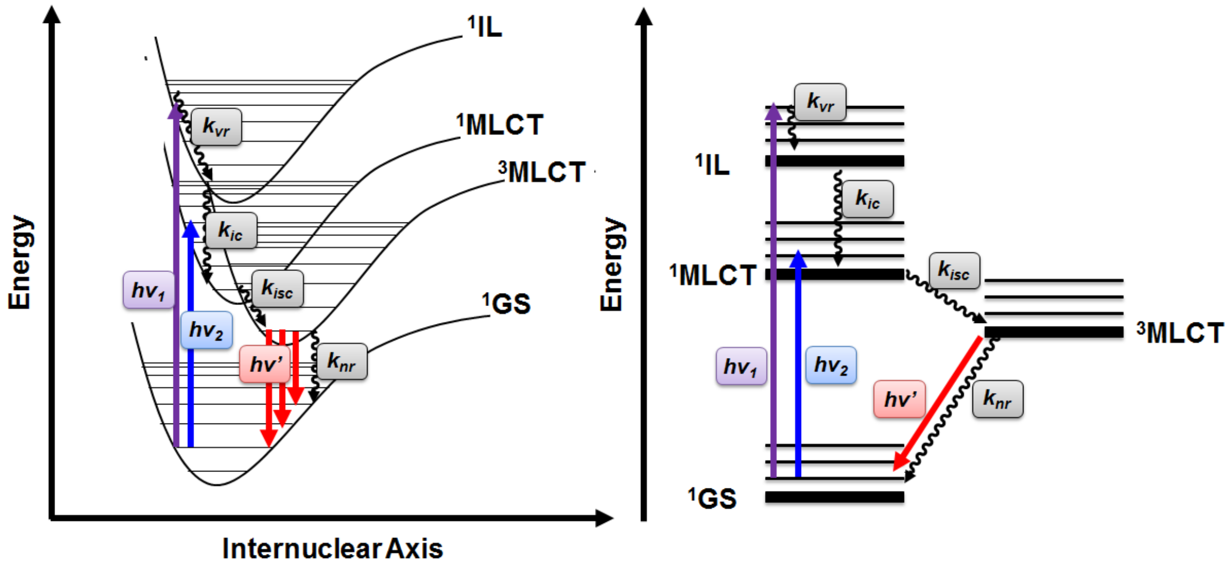

Figure 1.10: Morse potential energy diagram (left) and simplified state diagram (right) showing excited state processes within vibrational and electronic states for a Ru(II)-polypyridyl complex. Wavy lines depict non-radiative processes and straight lines depict radiative processes. $h\nu_n$ = photoexcitation; hν′ = radiative relaxation (photon emission); k_{vr} = vibrational relaxation rate constant; k_{ic} internal conversion rate constant; k_{isc} = intersystem crossing rate constant; k_{nr} = non-radiative decay rate constant.

Photoexcitation from the ^{1}GS throughout the UV and visible results in population of high energy π→π* IL or Ru(dπ)→ligand(π*) MLCT singlet excited states (^{1}ES). Internal conversion (k_{ic}) to populate lower energy ^{1}MLCT states occurs followed by intersystem crossing (k_{isc}) with near unit efficiency to populate Ru(dπ)→ligand(π*) ^{3}MLCT states. Deactivation from this ^{3}MLCT excited state can occur in the form of radiative (k_r) relaxation, non-radiative (k_{nr}) relaxation, or a photochemical reaction (k_{rxn}). The specific case of radiative relaxation that results in a change in spin is termed phosphorescence (k_p) and provides a measureable parameter of excited state dynamics and reactions for Ru(II)-polypyridyl complexes. The excited state lifetime (τ) of a particular state is inversely related to the sum of rates of the deactivating processes from that state (**equation 1.7**).

$$\tau = \frac{1}{(k_r + k_{nr} + k_{rxn})} \qquad \text{eq. 1.7}$$

Quantum yield (Φ) is a ratio between the moles of any process of interest and the moles of photons absorbed, **equation 1.8**.

$$\Phi = \frac{moles\ of\ process\ of\ interest}{moles\ of\ photons\ absorbed} \qquad \text{eq. 1.8}$$

The quantum yield of population (Φ^{pop}) or emission (Φ^{em}, **equation 1.9**) for the ^{3}MLCT excited state is the efficiency with which photon absorption results in formation of the ^{3}MLCT or emission of a photon from the ^{3}MLCT, respectively, in the absence of any photochemical reaction.

$$\Phi^{em}_{3MLCT} = \Phi^{pop}_{3MLCT} \frac{k_r}{(k_r + k_{nr})} \qquad \text{eq. 1.9}$$

For Ru(II)-polypyridyl complexes including $[Ru(bpy)_3]^{2+}$, Φ^{pop} is typically unity for the ^{3}MLCT excited state, therefore τ and Φ^{em} for the Ru(dπ)→bpy(π*) ^{3}MLCT excited state can be described using **equation 1.10**:

$$\Phi^{em}_{3MLCT} = k_r\tau \qquad \text{eq. 1.10}$$

$[Ru(bpy)_3]^{2+}$ is a strong red-emitter, **Figure 1.12**, with photoexcitation throughout the UV and visible resulting in emission from the ^{3}MLCT excited state (λ^{em} = 603 nm, $\Phi^{em}_{3_{MLCT}} = 0.070$, and $\tau_{3_{MLCT}}$ = 850 ns at 298 K in deoxygenated CH_3CN).[19,61] **Figure 1.11** shows the simplified Jablonski state diagram for $[Ru(bpy)_3]^{2+}$. Deactivation of the ^{3}MLCT excited state can occur through non-radiative or radiative decay to the ^{1}GS, interaction with another species to induce a photochemical reaction, or thermal population of energetically close ^{3}LF states ($k_{d\text{-}d}$).

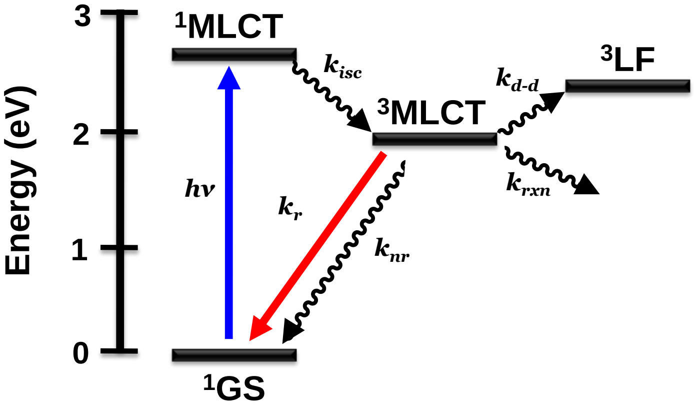

Figure 1.11: Jablonski state diagram for $[\mathrm{Ru(bpy)_3}]^{2+}$. Wavy lines depict non-radiative processes and straight lines depict radiative processes. hν = photoexcitation; k_{isc} = intersystem crossing rate constant; k_{nr} = non-radiative rate constant; k_{r} = radiative rate constant; $k_{\mathrm{d\text{-}d}}$ = ligand field state population rate constant; k_{rxn} = photochemical reaction rate constant.

Probing the excited state at 77 K in an EtOH:MeOH rigid glass matrix inhibits thermal population of the ^{3}LF state and non-radiative decay, providing an estimate to the $E^{0\text{-}0}$ transition which is the energy gap between the lowest vibrational state in the lowest excited state ($\nu' = 0$) and the lowest vibrational state in the ground state ($\nu = 0$).[50,69,70] $[\mathrm{Ru(bpy)_3}]^{2+}$ displays a vibrational progression of ~1300 $\mathrm{cm^{-1}}$ at 77 K (λ^{em} = 580 nm)[19] indicating the dominant excited state deactivation mode is from a series of medium frequency ligand-based stretching acceptor modes.[71-73] Modification of the bpy TL skeletal backbone to phen displays large variations to the observed excited state dynamics. The emission maximum shifts to higher energy (λ^{em} = 585 nm) while $\Phi^{\mathrm{em}}_{^3\mathrm{MLCT}}$ (0.020) and $\tau_{^3\mathrm{MLCT}}$ (400 ns) decrease when measured in $\mathrm{CH_3CN}$ at 298 K.[19] Ru(II)-polypyridyl complexes that emit at higher energies are usually more emissive than their low energy counterparts, in accordance with the energy gap law which states that the rate constant for non-radiative decay (k_{nr}) increases as the energy gap between the emitting excited state and ground state (ΔE) decreases.[74-76] For $[\mathrm{Ru(phen)_3}]^{2+}$, this observed decrease in quantum yield and excited state lifetime can be ascribed to more efficient thermal population of the higher-lying ^{3}LF state through internal conversion from the ^{3}MLCT state than for $[\mathrm{Ru(bpy)_3}]^{2+}$ in $\mathrm{CH_3CN}$ solvent.[21] Phenyl substitution greatly enhances $\Phi^{\mathrm{em}}_{^3\mathrm{MLCT}}$ and $\tau_{^3\mathrm{MLCT}}$ (0.366 and 6400 ns, respectively) for $[\mathrm{Ru(Ph_2phen)_3}]^{2+}$ in 4:1 EtOH:MeOH at 20 °C while also displaying a lower energy λ^{em} (618 nm) when compared to analogous measurements made for $[\mathrm{Ru(phen)_3}]^{2+}$ ($\Phi^{\mathrm{em}}_{^3\mathrm{MLCT}}$ = 0.019; $\tau_{^3\mathrm{MLCT}}$ = 450 ns; λ^{em} = 595 nm).[77] Emission from the Ru(dπ)→BL(π*) ^{3}MLCT excited state for $[Ru(dpp)_3]^{2+}$ is shifted to lower energy (λ^{em} = 623, **Figure 1.12**) and the lifetime decreased (τ = 183), indicative of enhanced stabilization of the ^{3}MLCT excited state and subsequent increased overlap with the ^{1}GS potential energy surface increasing k_{nr}.[61]

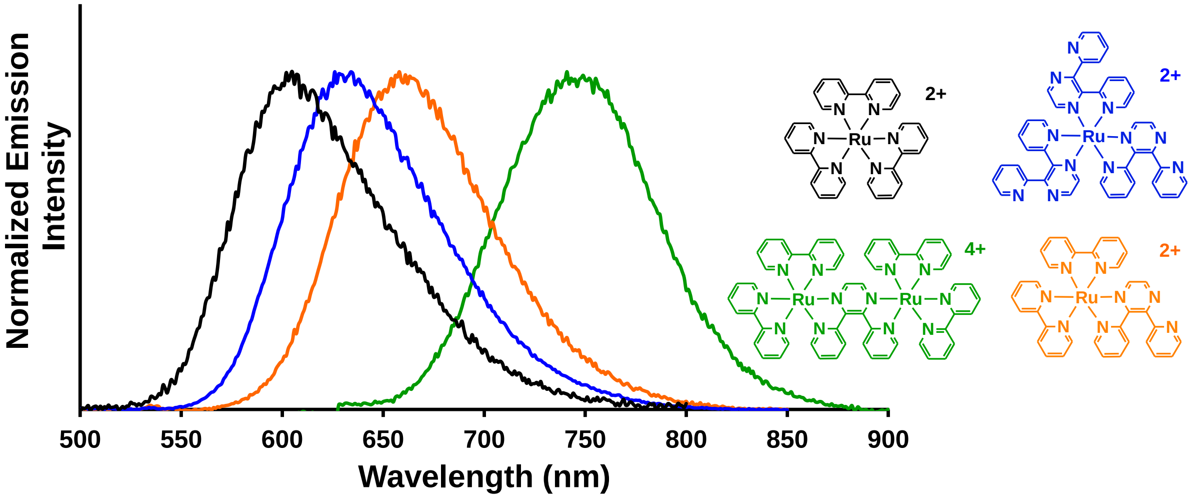

Figure 1.12: Normalized steady-state emission spectra of $[Ru(bpy)_3]^{2+}$ (—),[18] $[Ru(dpp)_3]^{2+}$ (—),[57] $[(bpy)_2Ru(dpp)]^{2+}$ (—),[59] and $[\{(bpy)_2Ru\}_2(dpp)]^{4+}$ (—)[59] measured at RT in deoxygenated CH_3CN solvent using a 1 cm quartz cuvette. bpy = 2,2′-bipyridine; dpp = 2,3-bis(2-pyridyl)pyrazine. Emission profiles are in agreement with literature references.

Heteroleptic monometallic complexes, $[(bpy)_2Ru(dpp)]^{2+}$, $[(phen)_2Ru(dpp)]^{2+}$ and $[(Ph_2phen)_2Ru(dpp)]^{2+}$, display emission from the lowest energy Ru(dπ)→BL(π*) ^{3}MLCT excited state. Electrochemical analyses indicated the LUMO within these systems as BL(π*) in nature and the lowest energy absorption as Ru(dπ)→BL(π*) ^{1}MLCT-based. The energy of emission, excited state lifetime, and emission quantum yield for $[(bpy)_2Ru(dpp)]^{2+}$ (λ^{em} = 691 nm; τ = 240 ns; $\Phi^{em}_{^3MLCT}$ = 0.023),[43] $[(phen)_2Ru(dpp)]^{2+}$ (λ^{em} = 652 nm; τ = 252 ns),[61] and $[(Ph_2phen)_2Ru(dpp)]^{2+}$ (λ^{em} = 664 nm; τ = 820 ns; $\Phi^{em}_{^3MLCT}$ = 0.035)[68] are all decreased compared to their homoleptic analogues. This indicates charge density is directed towards the dpp BL and away from the bpy, phen, or Ph_2phen TL, an important aspect for designing supramolecular complexes capable of spatially separating charges. TL identity influences the formally Ru(dπ)→dpp(π*) ^{3}MLCT excited state, suggesting the contribution to the Ru(dπ) orbital set from the TL are significant.

Coupling a second Ru(II) metal further stabilizes the Ru(dπ)→BL(π*) ^{3}MLCT excited state, red shifting the emission and decreasing the ES lifetime for $[\{(bpy)_2Ru\}_2(dpp)]^{4+}$ (λ^{em} = 752 nm; τ = 140 ns; $\Phi^{em}_{^3MLCT}$= 1.1 x 10^{-3}) and $[\{(phen)_2Ru\}_2(dpp)]^{4+}$ (λ^{em} = 746 nm; τ = 153 ns).[61,67]

1.4. Properties of Rh(III)-Polypyridyl Complexes

1.4.1. Electrochemical Properties

Redox chemistry of *cis*-$[Rh(LL)_2X_2]^+$ complexes (LL = bidentate polypyridyl ligand; X = halide) displays rich cathodic electrochemistry with the ligand set identity strongly influencing redox properties and orbital energetics. Scanning cathodically at 200 mV/s presents irreversible, overlapping reductions of *cis*-$[Rh^{III}(bpy)_2Cl_2]^+$ at −0.89 V vs. Ag/AgCl resulting in the generation of $[Rh^{I}(bpy)_2]^+$ and free Cl^- in solution, **Figure 1.13**.[78,79] The electrochemical mechanism displays $Rh^{III/II}$ reduction followed by halide loss is quasi-reversible at fast scan rates (≥ 46 V/s), indicating the quasi-stable nature of the generated Rh(II) species. Therefore, the process is actually two-overlapping, one-electron reductions of $Rh^{III/II}$ and $Rh^{II/I}$ with continued cathodic scanning displaying reduction of the bpy ligands at −1.32 V and −1.62 V vs. Ag/AgCl. The LUMO for $[Rh(LL)_2X_2]^+$ systems is Rh(dσ*) in character. Increasing electron density surrounding Rh by inclusion of σ-donating *tert*-butyl substituents on bpy shifts the irreversible $Rh^{III/II/I}$ couples to −0.96 V vs. Ag/AgCl.[79] The reversible, one-electron $^tBu_2bpy^{0/-}$ couples appear at −1.37 V and −1.65 V vs. Ag/AgCl. Further modifying the coordination environment surrounding Rh by varying X to produce $[Rh(bpy)_2Br_2]^+$ stabilizes the Rh(dσ*) orbitals with the $Rh^{III/II/I}$ irreversible couples appearing at −0.79 V vs. Ag/AgCl and free Br^- in solution.[80] The weaker σ-donating character of Br^- vs. Cl^- stabilizes the Rh(dσ*) orbitals. Further stabilization of the Rh(dσ*) orbitals is achieved through substitution of bidentate TLs for bis-bidentate BLs to generate $[Rh(dpp)_2Br_2]^+$.[80] The electron-withdrawing character of dpp BLs shifts the $Rh^{III/II/I}$ couples to more positive potential (−0.60 V vs. Ag/AgCl) with sequential $dpp^{0/-}$ reductions occurring at −1.05 V and −1.19 V vs. Ag/AgCl. The ability of Rh to undergo two irreversible, one-electron reductions whose orbital energetics can be controlled by ligand set identity is crucial in generating an electron acceptor (EA) of appropriate energy for electron collection (EC) and photocatalysis.

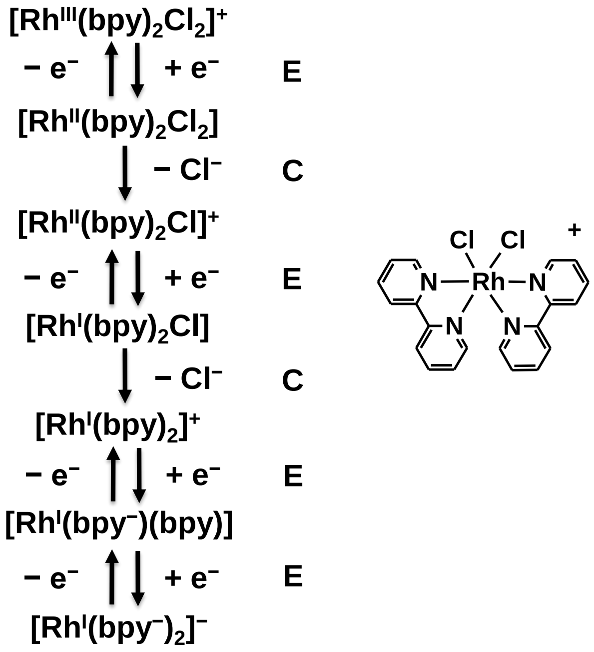

Figure 1.13: Electrochemical mechanism for the reduction of $[Rh^{III}(bpy)_2Cl_2]^+$ in CH_3CN as proposed DeArmond.[78] E = electron transfer, C = chemical step, bpy = 2,2′-bipyridine.

1.4.2. Light Absorbing Properties

Bis-polypyridyl Rh(III) complexes, $[Rh(LL)_2X_2]^+$, display intense absorption throughout the UV and near-UV regions due to ligand-based π→π* IL transitions.[17] Weak absorption into the visible region is attributed to metal-centered d→d transitions. The lack of MLCT-based transitions within the visible region indicates these transitions occur at higher energy and are probably masked by the intense IL transitions. The *cis*-dihalide complexes $[Rh(bpy)_2Cl_2]^+$ (302 nm and 310 nm) and $[Rh(bpy)_2Br_2]^+$ (302 nm and 311 nm) display similar IL transition energies suggesting the halide identity does not greatly perturb the ligand-based transitions. Modifying the ligand set from bpy to dpp, $[Rh(dpp)_2Br_2]^+$, shows a change in energy of the observed transitions (280 nm and 328 nm), further emphasizing the absorbance influence from the ligand character.[80]

1.4.3. Excited State Properties

The excited state properties of $[Rh(LL)_2X_2]^+$ complexes are indicative of population of a ^{3}LF state.[17,46,80-82] Photoexcitation throughout the UV and visible results in population of ^{1}IL and ^{1}LF states that undergo rapid intersystem crossing with near unit efficiency to populate ^{3}LF states.

The low energy, broad, structureless emission is only observed at low temperatures and is influenced by ligand set identity.[17,46,80-82] Comparing the excited state properties of $[Rh(bpy)_2Br_2]^+$ and $[Rh(dpp)_2Br_2]^+$ at 77 K in 4:1 EtOH/MeOH frozen glass matrix shows that substituting the bpy TL for the electron-withdrawing dpp BL shifts the emission maximum from 660 nm to 707 nm.[80] This shift to lower energy for the weaker σ-donating dpp BL is expected as the degree of d-orbital splitting (Δ_o) is smaller in comparison to the stronger σ-donating bpy TL.

1.5. Properties of Polyazine-Bridged Ru(II),Rh(III) Complexes

Coordination of a Rh(III) metal center to the Ru(II) polypyridyl LA through a polyazine BL extends the molecular architecture while also introducing metal-based acceptors via low-lying unoccupied Rh(dσ*) molecular orbitals.[46,82-89] These complexes can be described as electron donor/bridging ligand/electron acceptor (ED/BL/EA) systems with Ru(II) serving as an ED upon photoexcitation and Rh(III) serving as the EA, **Figure 1.14**.[45,90] The observed electrochemical, light absorbing, and excited state properties are greatly dictated by the orbital energetics and electronic coupling between the two subunits. The choice of a polyazine BL that contains aliphatic linkers (methylene groups),[87,89] aromatic linkers (phenylene groups),[84] or a pyrazine unit[82,83] strongly influences the degree of electronic communication between the Ru(II) and Rh(III) subunits within the supramolecular assembly. **Figure 1.15** displays structures of Ru(II),Rh(III) bimetallic complexes bridged by methylene-, phenylene-, and pyrazine-linker BLs.

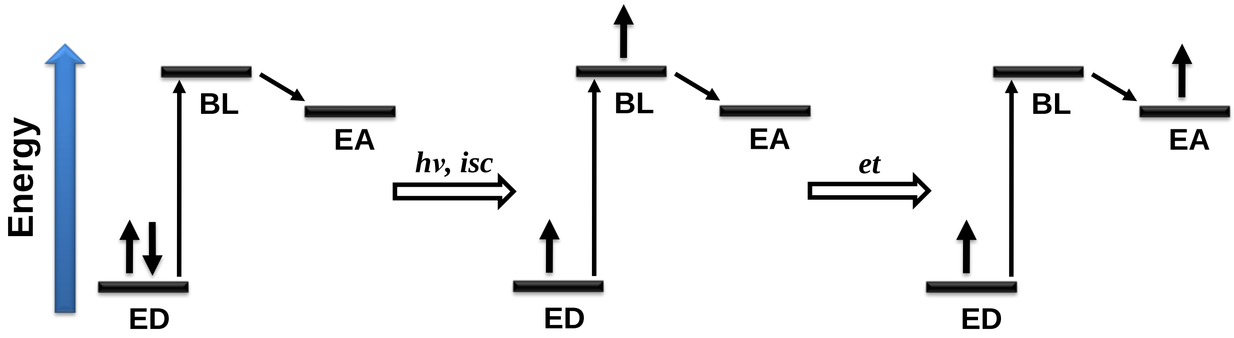

Figure 1.14: Simplified molecular orbital diagrams of ED-BL-EA system following photoexcitation (hν), intersystem crossing (isc), and intramolecular electron transfer (et). ED = electron donor; BL = bridging ligand; EA = electron acceptor.

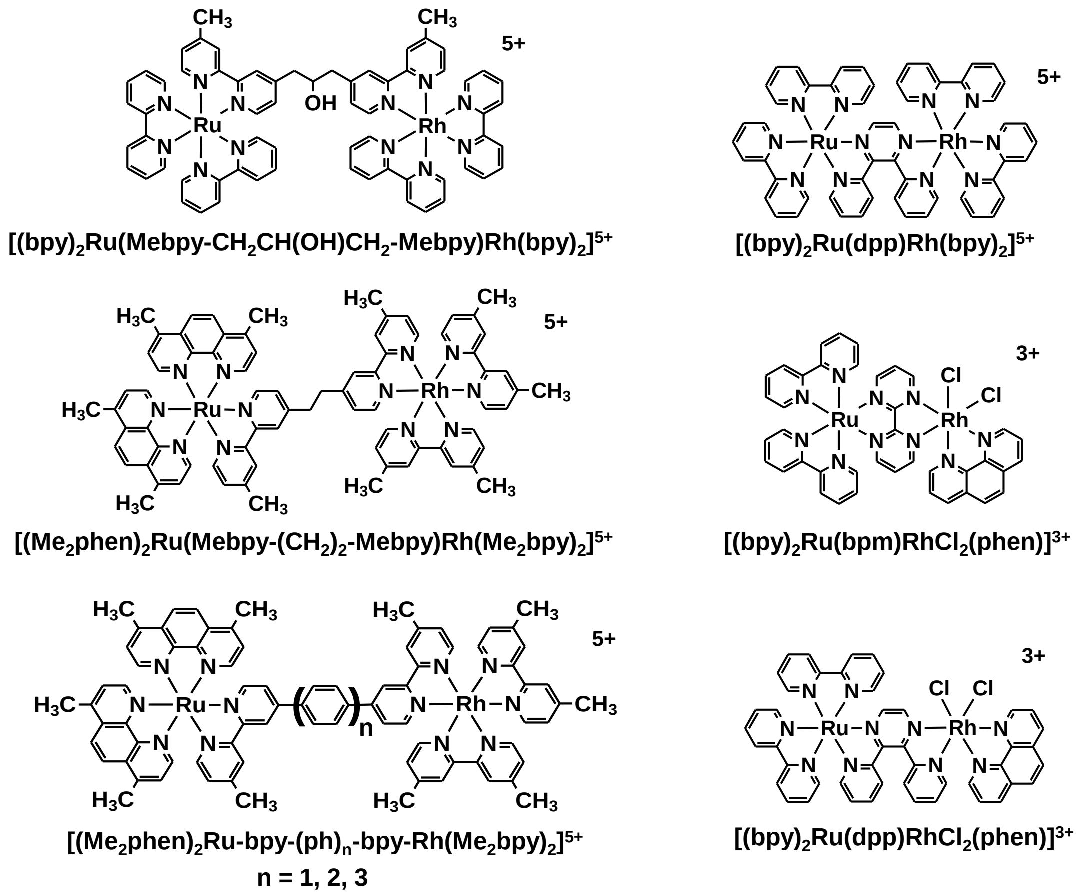

$[(bpy)_2Ru(Mebpy\text{-}CH_2CH(OH)CH_2\text{-}Mebpy)Rh(bpy)_2]^{5+}$

$[(bpy)_2Ru(dpp)Rh(bpy)_2]^{5+}$

$[(Me_2phen)_2Ru(Mebpy\text{-}(CH_2)_2\text{-}Mebpy)Rh(Me_2bpy)_2]^{5+}$

$[(bpy)_2Ru(bpm)RhCl_2(phen)]^{3+}$

$[(Me_2phen)_2Ru\text{-}bpy\text{-}(ph)_n\text{-}bpy\text{-}Rh(Me_2bpy)_2]^{5+}$
$n = 1, 2, 3$

$[(bpy)_2Ru(dpp)RhCl_2(phen)]^{3+}$

Figure 1.15: Structures of polyazine-bridged Ru(II),Rh(III) bimetallic complexes. bpy = 2,2′-bipyridine; Me_2phen = 4,7-dimethyl-1,10-phenanthroline; Me_2bpy = 4,4′-dimethyl-2,2′-bipyridine; phen = 1,10-phenanthroline; Mebpy-$(CH_2)_2$-Mebpy = 1,2-bis[4-(4′-methyl-2,2′-bipyridyl)]ethane; dpp = 2,3-bis(2-pyridyl)pyrazine; bpm = 2,2′-bipyrimidine.

1.5.1. Electrochemical Properties

The observed electrochemical properties of Ru(II),Rh(III) bimetallic complexes depend greatly on the nature of the linking BL subunit. Heterobimetallic complexes bridged by methylene- or phenylene-containing BLs display electrochemical properties that are a summation of the respective Ru(II) and Rh(III) monometallic precursors.[84,87,89] The complexes $[(bpy)_2Ru(Mebpy\text{-}CH_2CH(OH)CH_2\text{-}Mebpy)Rh(TL)_2]^{5+}$ (TL = bpy or phen), $[(Me_2phen)_2Ru(Mebpy\text{-}(CH_2)_2\text{-}Mebpy)Rh(Me_2bpy)_2]^{5+}$, and $[(Me_2phen)_2Ru(bpy\text{-}(ph)_n\text{-}bpy)Rh(Me_2bpy)_2]^{5+}$ (n = 1, 2, 3) possess a reversible one-electron $Ru^{II/III}$ oxidation at +1.31 V, +1.17 V, and +1.22 V vs. Ag/AgCl, respectively, at potentials similar to the Ru(II) monometallic precursor.[84,87,89] As shown for the Ru(II) monometallic complexes, inclusion of methyl substituents destabilizes the Ru(dπ) HOMO set and shifts the $Ru^{II/III}$ oxidation potential less positive. Reductively, an irreversible $Rh^{III/II}$ reduction (−0.66 V, −0.88 V, and −0.80 V, respectively) occurs prior to the $BL^{0/-}$ reduction in all three complexes. The same trend is observed for electron-donating methyl substituents coordinated to Rh(III) on the $[(Me_2phen)_2Ru(Mebpy\text{-}CH_2CH_2\text{-}Mebpy)Rh(Me_2bpy)_2]^{5+}$ and $[(Me_2phen)_2Ru(bpy\text{-}(ph)_n\text{-}bpy)Rh(Me_2bpy)_2]^{5+}$ bimetallics, whereby the Rh(dσ*) orbital set is destabilized and shifts the first reduction potential more negative relative to the $Rh^{III}(bpy)_2$ or $Rh^{III}(phen)_2$ containing bimetallic. This establishes the LUMO in all three complexes as Rh-based but also indicates the lack of significant electronic coupling between the Ru(II) and Rh(III) metal centers as the electrochemical properties of the bimetallics were not perturbed relative to the respective monometallic subunits. The tris-bidentate coordination of the Rh center also provides for no net photochemistry in these motifs.

Coupling the Ru(II) LA and Rh(III) metal center through a pyrazine-containing BL greatly perturbs the electrochemical properties of the newly formed bimetallic relative to the Ru(II) and Rh(III) monometallic units. The bimetallic complexes $[(bpy)_2Ru(dpp)Rh(bpy)_2]^{5+}$, $[(bpy)_2Ru(dpp)RhCl_2(phen)]^{3+}$, and $[(bpy)_2Ru(bpm)RhCl_2(phen)]^{3+}$ electronically couple the Ru(II) and Rh(III) metal centers through the pyrazine-type bridge, resulting in stabilization of the Ru-based oxidation, as well as the Rh- and BL-based reductions.[82,83] Of significant interest is the complexity involved with assigning the reduction processes due to the close energetic proximity of the perturbed Rh(dσ*) and BL(π*) orbitals. For the $[(bpy)_2Ru(dpp)Rh(bpy)_2]^{5+}$ bimetallic, the first reduction is an irreversible couple occurring at −0.61 V vs. Ag/AgCl and is noted that the $Rh^{III/II}$ and $dpp^{0/-}$ are expected to occur at similar potentials.[82] For the $[(bpy)_2Ru(dpp)RhCl_2(phen)]^{3+}$ and $[(bpy)_2Ru(bpm)RhCl_2(phen)]^{3+}$ bimetallics, the first reduction is labeled as $Rh^{III/II}$ (−0.39 V vs. Ag/AgCl) and $bpm^{0/-}$ (−0.14 V vs. Ag/AgCl), respectively, indicating the LUMO as being primarily Rh-based for the prior and bpm BL-based for the latter.[83]

1.5.2. Light Absorbing Properties

Similar to the electrochemical analyses, light absorption of Ru(II),Rh(III) bimetallic complexes is dictated by the degree of electronic coupling between the two metal centers but dominated by the ligands in the UV and Ru in the visible. For methylene- and phenylene-linked bimetallics, the electronic absorption spectrum is an overlay of the absorption characteristics of the Ru(II) and Rh(III) monometallic subunits due to weak coupling between the two metal centers.[84,87,89] The complexes $[(bpy)_2Ru(Mebpy\text{-}CH_2CH(OH)CH_2\text{-}Mebpy)Rh(TL)_2]^{5+}$ (TL = bpy or phen), $[(Me_2phen)_2Ru(Mebpy\text{-}(CH_2)_2\text{-}Mebpy)Rh(Me_2bpy)_2]^{5+}$, and $[(Me_2phen)_2Ru(bpy\text{-}(ph)_n\text{-}bpy)Rh(Me_2bpy)_2]^{5+}$ (n = 1, 2, 3) are unique in that both the Ru(II) and Rh(III) components are strong light absorbers that contribute to the observed electronic absorption spectrum. The UV contains $\pi \rightarrow \pi^*$ IL transitions from the ligands coordinated to Ru(II) and Rh(III). The visible is dominated by $Ru(d\pi) \rightarrow ligand(\pi^*)$ ^1MLCT transitions that are nearly identical in energy and extinction coefficient with the respective Ru(II) monometallic precursor.

The electronic absorption spectra of pyrazine-bridged Ru(II),Rh(III) bimetallics $[(bpy)_2Ru(dpp)Rh(bpy)_2]^{5+}$, $[(bpy)_2Ru(dpp)RhCl_2(phen)]^{3+}$, and $[(bpy)_2Ru(bpm)RhCl_2(phen)]^{3+}$ indicate dpp BL π^* stabilization.[82,83] Similar to $[\{(TL)_2Ru\}_2(BL)]^{4+}$ homobimetallic complexes, coordination of the Rh(III) metal center to the uncoordinated BL site shifts the BL-based transitions to lower energy. The dpp-bridged complexes display low energy absorption of the $Ru(d\pi) \rightarrow dpp(\pi^*)$ ^1MLCT transition at $\lambda^{abs} = 514$ nm ($\varepsilon = 14{,}400\ M^{-1}cm^{-1}$) for $[(bpy)_2Ru(dpp)Rh(bpy)_2]^{5+}$ and $\lambda^{abs} = 509$ nm ($\varepsilon = 14{,}700\ M^{-1}cm^{-1}$) for $[(bpy)_2Ru(dpp)RhCl_2(phen)]^{3+}$ in CH_3CN at RT.[82,83] The $Ru(d\pi) \rightarrow dpp(\pi^*)$ ^1MLCT transition of the monometallic $[(bpy)_2Ru(dpp)]^{2+}$ precursor occurs at higher energy ($\lambda^{abs} = 464$ nm; $\varepsilon = 12{,}000\ M^{-1}cm^{-1}$).[61] The same trend is observed for $[(bpy)_2Ru(bpm)RhCl_2(phen)]^{3+}$, whereby coordination of the Rh(III) metal center to bpm shifts the $Ru(d\pi) \rightarrow bpm(\pi^*)$ ^1MLCT transition from 422 nm ($\varepsilon = 9{,}100\ M^{-1}cm^{-1}$) for $[(bpy)_2Ru(bpm)]^{2+}$ to 594 nm ($\varepsilon = 9{,}900\ M^{-1}cm^{-1}$) for $[(bpy)_2Ru(bpm)RhCl_2(phen)]^{3+}$.[83,91] Enhanced absorptivity at lower energies due to stabilization of the $Ru(d\pi) \rightarrow dpp(\pi^*)$ ^1MLCT transition is important when designing solar photocatalysts, as much of the energy that reaches the Earth's surface from the sun occurs within the visible and near-infrared regions of the spectrum, **Figure 1.1**.

1.5.3. Excited State Properties

Photoexcitation of Ru(II),Rh(III) bimetallic complexes results in population of emissive $Ru(d\pi) \rightarrow BL(\pi^*)$ MLCT excited states and potential population of non-emissive $Ru(d\pi) \rightarrow Rh(d\sigma^*)$ MMCT excited states. Bimetallic complexes $[(bpy)_2Ru(Mebpy\text{-}CH_2CH(OH)CH_2\text{-}Mebpy)Rh(TL)_2]^{5+}$ (TL = bpy or phen) display weak emission from the

Ru(dπ)→BL(π*) ^{3}MLCT excited state (λ^{em} = 610 nm in H_2O) that is quenched 88% (TL = bpy) and 83% (TL = phen) relative to the $[(bpy)_2Ru(Me_2bpy)]^{2+}$ monometallic model.[89] This is ascribed to intramolecular electron transfer to populate Ru(dπ)→Rh(dσ*) ^{3}MMCT excited states with k_{et} = 1.4 and 1.1 x 10^7 s^{-1} for TL = bpy and phen, respectively. Modeling a Ru,Rh bimetallic from monometallic species may not provide the best interpretation as the Ru,Ru bimetallic may have enhanced k_{nr} due to the extended linker. The methylene-linked bimetallic $[(Me_2phen)_2Ru(Mebpy\text{-}(CH_2)_2\text{-}Mebpy)Rh(Me_2bpy)_2]^{5+}$ displays ~99% emission quenching (λ^{em} = 610 nm; Φ^{em}_{3MLCT} = 7.6 x 10^{-4}; τ = 6 ns) at RT in CH_3CN compared to the monometallic $[(Me_2phen)_2Ru(Mebpy\text{-}(CH_2)_2\text{-}Mebpy)]^{2+}$ model (λ^{em} = 610 nm; $\Phi^{em}_{^3MLCT}$ = 0.11; τ = 1.8 μs) with a value of 1.7 x 10^8 s^{-1} for k_{et}.[87] The increase in k_{et} by an order of magnitude for the BL = Mebpy-$(CH_2)_2$-Mebpy complex compared to BL = Mebpy-$CH_2CH(OH)CH_2$-Mebpy was attributed to the smaller number of carbon-linkers (two vs. three), thereby decreasing the distance between the Ru(II) ED and Rh(III) EA.

The phenylene-linked bimetallics $[(Me_2phen)_2Ru(bpy\text{-}(ph)_n\text{-}bpy)Rh(Me_2bpy)_2]^{5+}$ (n = 1, 2, 3) display weak coupling between the Ru(II) and Rh(III) subunits as the energy of the Ru(dπ)→BL(π*) ^{3}MLCT excited state (λ^{em} = 640-652 nm) is similar to the Ru(II) monometallic synthons (λ^{em} = 642-652 nm) at RT.[84] Interestingly, the value of τ for the ^{3}MLCT excited state increases (τ = 0.36, 2.3, and 94 ns for n = 1, 2, or 3, respectively) as the number of phenylene-linkers and distance between Ru(II) and Rh(III) increases. This results in *ca.* an order of magnitude decrease of k_{et} for each additional phenylene-linker within the BL (k_{et} = 3.0 x 10^9, 4.3 x 10^8, and 1.0 x 10^7 s^{-1} for n = 1, 2, and 3, respectively). When compared to the analogous methylene-linked bimetallic $[(Me_2phen)_2Ru(Mebpy\text{-}(CH_2)_2\text{-}Mebpy)Rh(Me_2bpy)_2]^{5+}$ with a value of k_{et} ~ 10^7 s^{-1} and similar distance between Ru(II) LA and Rh(III) EA, the intrinsic nature of the phenylene-linked BL for $[(Me_2phen)_2Ru(bpy\text{-}(ph)_1\text{-}bpy)Rh(Me_2bpy)_2]^{5+}$ accounts for the nearly two-order magnitude increase of k_{et}. Comparison to Ru,Ru bimetallics might provide enhanced information about intramolecular electron transfer in these Ru,Rh bimetallic systems.

The pyrazine-linked Ru(II),Rh(III) bimetallic complexes display stabilization of dpp BL π* orbital set in comparison to the Ru monometallic analogue. Emission from the Ru(dπ)→dpp(π*) ^{3}MLCT excited state for $[(bpy)_2Ru(dpp)Rh(bpy)_2]^{5+}$ (λ^{em} = 778 nm; τ = 37 ns) and $[(bpy)_2Ru(dpp)RhCl_2(phen)]^{3+}$ (λ^{em} = 786 nm; τ = 30 ns; Φ^{em} = 2.3 x 10^{-4}) is greatly red-shifted when compared with the $[(bpy)_2Ru(dpp)]^{2+}$ monometallic precursor (λ^{em} = 660 nm), providing further support of dpp π* stabilization.[82,83] The $[\{(bpy)_2Ru\}_2(dpp)]^{4+}$ bimetallic is used as a model for excited state studies due to the similar nature and energy of the emissive Ru(dπ)→μ-dpp(π*) ^{3}MLCT state (λ^{em} = 758 nm; τ = 124 ns; $\Phi^{em} = 1.4 \times 10^{-3}$). This model is substantiated by similar band shapes, energies, and excited lifetimes at 77 K for Ru,Ru and Ru,Rh bimetallics where intramolecular electron transfer is prohibited due to the large structural reorganization needed but is prohibited in a rigid matrix. Values of $k_{et} \sim 2 \times 10^7$ s^{-1} are lower than would be initially expected given the close proximity of the Ru(II) and Rh(III) subunits, however the nature of the dpp BL and lack of conformational flexibility may account for these observed k_{et} values. Conversely, it is also possible that methylene- and phenylene-linked studies over estimate k_{et} by choice of the monometallic model. No RT emission was observed for the $[(bpy)_2Ru(bpm)RhCl_2(phen)]^{3+}$ bimetallic complex due to the expected weak and more red-shifted emission for bpm-bridged Ru(II) complexes (λ^{em} = 790 nm; $\tau \leq 20$ ns; $\Phi^{em} \leq 4.2 \times 10^{-4}$ for $[\{(bpy)_2Ru\}_2(bpm)]^{4+}$ in CH_3CN at RT).[67]

1.6. Photoinitiated Electron Collectors

Photoinitiated electron collectors (PECs) can be viewed as two, three-component systems of the design LA-BL-EC that are fused through the central EC subunit to generate a LA-BL-EC-BL-LA type architecture, **Figure 1.4**.[42] Functional PECs are governed by the ability of the system to initiate electron transfer from the metal-based LA to the EC subunit, which is mediated by the intrinsic properties of the BL. Incorporation of a sacrificial ED prevents unwanted back electron transfer from the EC to the LA, thereby collecting electrons on a central site.

1.6.1. Ligand-Centered Electron Collection

Ligand-based photoinitiated electron collectors (PECs) are capable of storing multiple reducing equivalents within a π* aromatic system of a ligand, **Figure 1.16**. Collecting electrons on a molecule is complicated by a coulombic barrier, with most $[(TL)_2Ru(BL)Ru(TL)_2]^{4+}$ motifs not providing electron collection as one e^- reduction prevents further photoreduction. The first reported PMD for PEC, $[\{(bpy)_2Ru(dpb)\}_2IrCl_2](PF_6)_5$ (dpb = 2,3-bis(2-pyridyl)benzoquinoxaline), covalently couples two $(bpy)_2Ru^{II}$ chromophores to a central $(dpb)Ir^{III}Cl_2(dpb)$ electron collecting subunit.[92,93] Photoexcitation of this Ru(II),Ir(III),Ru(II) trimetallic complex in the presence of DMA affords two sequential one-electron transfer events to generate the doubly reduced $[\{(bpy)_2Ru(dpb^-)\}_2IrCl_2]^{3+}$ species. The high energy Ir(dσ*) orbitals prevent electron transfer to the Ir center, instead localizing an electron within each dpb π* orbital. It has been previously shown that electrons localized on two separate ligands can be provided to a single substrate in the electrocatalytic reduction of CO_2 using $[Rh(bpy)_2Cl_2]^+$.[79] The homobimetallic complexes $[(phen)_2Ru(BL)Ru(phen)](PF_6)_4$ (BL = tatpp = 9,11,20,22-tetraazatetrapyrido[3,2-*a*:2′,3′-*c*:3″,2″-*1*:2‴,3‴-*n*]pentacene or tatpq = 9,11,20,22-tetraazatetrapyrido[3,2-*a*:2′,3′-*c*:3″,2″-*1*:2‴,3‴-*n*]pentacene-10,21-quinone) reversibly collect two (tatpp) and four (tatpq) reducing equivalents on the extended π* aromatic system of the bridging ligands.[94,95] Photoexcitation of the Ru(II) LA in the presence of TEA (triethylamine) using visible light affords multi-electron collection and is confirmed using spectroelectrochemical techniques to produce electronic absorption spectra similar to photochemical and electrochemical reduction. A separate spectroscopic and electron collection orbital on the extended π aromatic BL provides for PEC. The monometallic complex $[(bpy)_2Ru(pbn)](PF_6)_2$ (pbn = 2-(2-pyridyl)benzo[*b*]-1,5-naphthyridine) undergoes two proton-coupled electron transfers (PCET) to afford electron collection on the extended pbn π* aromatic system. Photoexcitation in the presence of TEA in CH_3CN generates the doubly reduced, doubly protonated $[(bpy)_2Ru(pbnHH)]^{2+}$ species in an effort to mimic the NAD^+/NADH-type redox-active system observed in many biological systems to avoid high energy intermediates.[96,97]

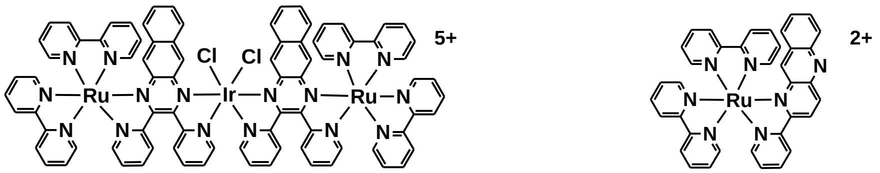

$[\{(bpy)_2Ru(dpb)\}_2IrCl_2]^{5+}$ $[(bpy)_2Ru(pbn)]^{2+}$

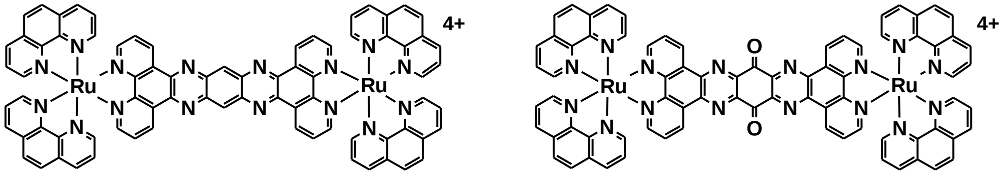

$[(phen)_2Ru(tatpp)Ru(phen)_2]^{4+}$ $[(phen)_2Ru(tatpq)Ru(phen)_2]^{4+}$

Figure 1.16: Structures of ligand-based photochemical molecular devices for photoinitiated electron collection. bpy = 2,2′-bipyridine; dpb = 2,3-bis(2-pyridyl)benzoquinoxaline; phen = 1,10-phenanthroline; tatpp = 9,11,20,22-tetraazatetrapyrido[3,2-*a*:2′,3′-*c*:3″,2″-*1*:2‴,3‴-*n*]pentacene; tatpq = 9,11,20,22-tetraazatetrapyrido[3,2-*a*:2′,3′-*c*:3″,2″-*1*:2‴,3‴-*n*]pentacene-10,21-quinone; pbn = 2-(2-pyridyl)benzo[*b*]-1,5-naphthyridine.

1.6.2. Metal-Centered Electron Collection

Metal-based photoinitiated electron collectors are designed to store multiple reducing equivalents on metal centers, **Figure 1.17**. The first reported metal-based PMD for PEC to stay intact after PEC was $[\{(bpy)_2Ru(dpp)\}_2RhCl_2](PF_6)_5$ which couples two peripheral $(bpy)_2Ru^{II}$ LA subunits to a *cis*-$Rh^{III}Cl_2$ EC metal center through dpp BLs.[98] Electrochemical analysis shows two overlapping, one-electron reversible $Ru^{II/III}$ oxidations at +1.63 V vs. Ag/AgCl with $\Delta E_p \approx$ 130 mV, indicating the two Ru LA centers are weakly coupled electronically and establishes Ru(dπ) as the HOMO. Cathodic scans display irreversible overlapping one-electron reductions at $E_p^c = -0.37$ V vs. Ag/AgCl corresponding to the $Rh^{III/II/I}$ reduction, followed by sequential reversible $dpp^{0/-}$ reductions at $E_{½} = -0.76$ V and −1.00 V vs. Ag/AgCl, establishing Rh(dσ*) as the LUMO within this Ru(II),Rh(III),Ru(II) trimetallic supramolecular complex. Visible light photoexcitation results in population of the Ru(dπ)⟶dpp(π*) ^{3}MLCT ES that is reductively quenched in the presence of DMA with subsequent electron collection at the Rh metal center. Modification of the trimetallic architecture through halide (Cl^- to Br^-) and TL (bpy to phen) variation displays similar electrochemical and photophysical properties with electron collection at the Rh metal center observed in the presence of light and DMA.[99,100]

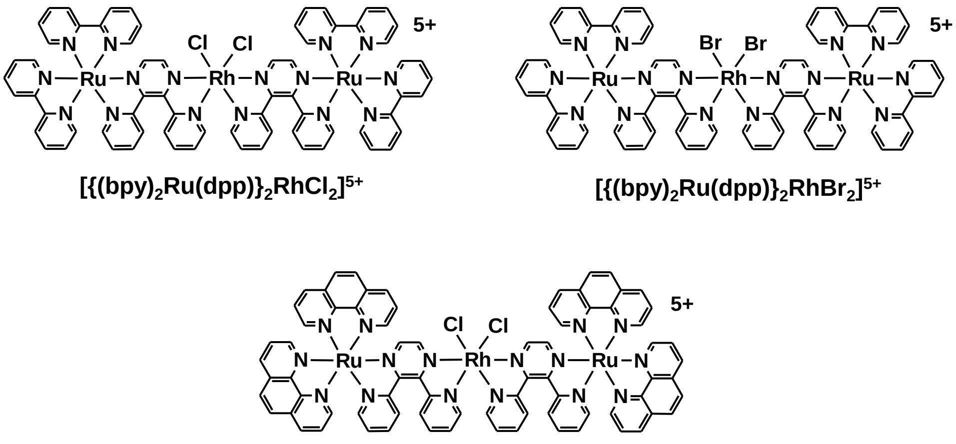
$[\{(bpy)_2Ru(dpp)\}_2RhCl_2]^{5+}$

$[\{(bpy)_2Ru(dpp)\}_2RhBr_2]^{5+}$

$[\{(phen)_2Ru(dpp)\}_2RhCl_2]^{5+}$

Figure 1.17: Structures of metal-based photochemical molecular devices for photoinitiated electron collection. bpy = 2,2′-bipyridine; phen = 1,10-phenanthroline; dpp = 2,3-bis(2-pyridyl)pyrazine.

1.7. Photocatalytic H_2 *Production by Supramolecular Complexes*

The appropriate choice of molecular components and architecture provide for active photocatalysts in the reduction of H_2O to H_2 which covalently couple the metal-based LA to the catalytically active RM center through BL subunits. Supramolecular architectures have been reported that utilize one, two, or three LA subunits bridged to the RM site and function as H_2O reduction photocatalysts.[101-104] **Figure 1.18** displays bimetallic, trimetallic, and tetrametallic structures of reported supramolecular complexes that reduce H_2O to H_2.

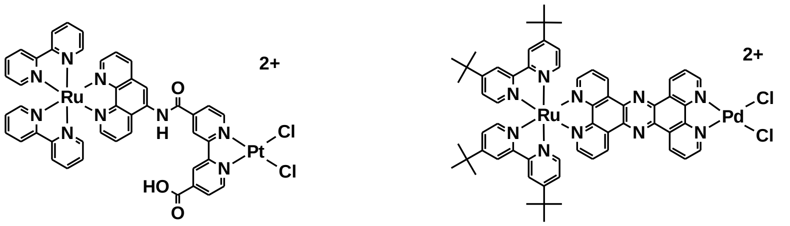

$[(bpy)_2Ru(phen\text{-}NHCO(COOHbpy))PtCl_2]^{2+}$ $[(^tBu_2bpy)_2Ru(tpphz)PdCl_2]^{2+}$

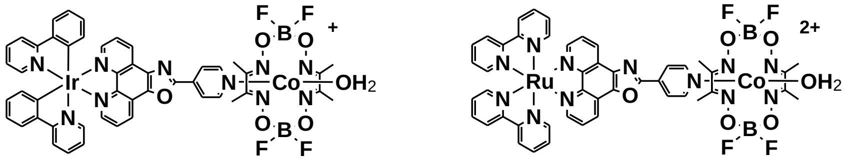

$[(ppy)_2Ir(L\text{-}pyr)Co(dmgBF_2)_2(OH_2)]^+$ $[(bpy)_2Ru(L\text{-}pyr)Co(dmgBF_2)_2(OH_2)]^{2+}$

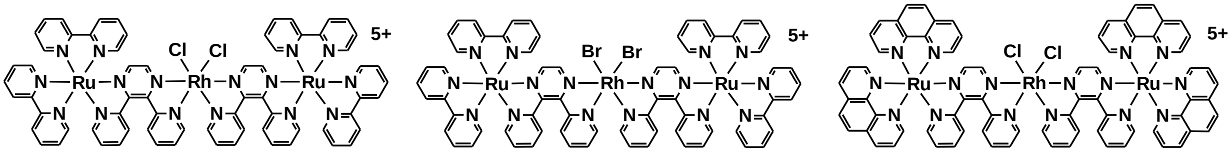

$[\{(bpy)_2Ru(dpp)\}_2RhCl_2]^{5+}$ $[\{(bpy)_2Ru(dpp)\}_2RhBr_2]^{5+}$ $[\{(phen)_2Ru(dpp)\}_2RhCl_2]^{5+}$

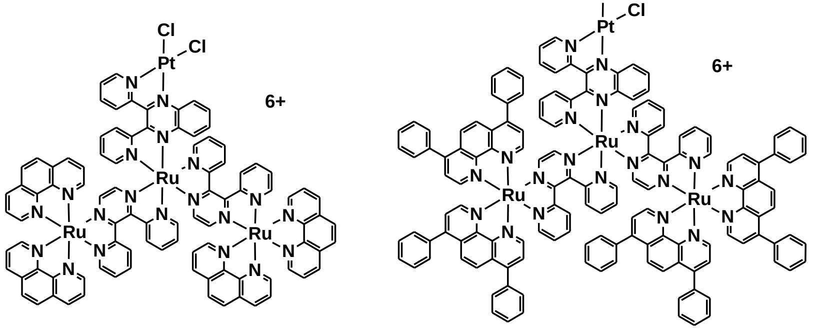

$[\{(phen)_2Ru(dpp)\}_2Ru(dpq)PtCl_2]^{6+}$ $[\{(Ph_2phen)_2Ru(dpp)\}_2Ru(dpq)PtCl_2]^{6+}$

Figure 1.18: Structures of supramolecular complexes that function as photocatalysts for the reduction of H_2O to H_2. bpy = 2,2′-bipyridine; phen = 1,10-phenanthroline; Ph_2phen = 4,7-diphenyl-1,10-phenanthroline; $^tBu_2$bpy = 4,4′-Di-*tert*-butyl-2,2′-bipyridine; ppy = 2-phenylpyridine; tpphz = tetrapyrido[3,2-a:2′,3′-c:3″,2″-h:2‴,3‴-j]phenazine; L-pyr = (4-pyridine)oxazolo[4,5-*f*]phenanthroline; $dmgBF_2$ = (difluoroboryl)dimethylglyoximate; dpp = 2,3-bis(2-pyridyl)pyrazine; dpq = 2,3-bis(2-pyridyl)quinoxaline.

Bimetallic supramolecular architectures directly couple one LA subunit to one RM catalytic site.[102] The Ru(II),Pt(II) bimetallic complex, $[(bpy)_2Ru(phen\text{-}NHCO(COOHbpy))PtCl_2]^{2+}$, couples a Ru(II) LA to a *cis*-$Pt^{II}Cl_2$ RM center through a polyazine-amide BL, affording 4.8 TONs and 2.4 μmol H_2 after 10 h photolysis using EDTA as the sacrificial ED (390 nm < λ^{irr} < 490 nm; Φ_{H_2} = 0.61%; pH = 5.0; 0.1 M acetate buffer solution).[105,106] The Ru(II),Pd(II) bimetallic complex, $[(^{t}Bu_2bpy)_2Ru(tpphz)PdCl_2]^{2+}$ ($^{t}Bu_2bpy$ = 4,4′-Di-*tert*-butyl-2,2′-bipyridine, tpphz = tetrapyrido[3,2-a:2′,3′-c:3″,2″-h:2‴,3‴-j]phenazine) bridges the Ru(II) LA and *cis*-$Pd^{II}Cl_2$ RM using an extended π-aromatic tpphz BL. After 30 h photolysis at λ^{irr} = 470 nm, H_2 was produced resulting in 56 TONs using TEA as the ED in a CH_3CN solvent system.[107] The structural integrity of the reported Ru(II),Pt(II) and Ru(II),Pd(II) bimetallic photocatalysts has come into question, suggesting the formation of colloidal Pt and Pd as the active catalyst.[108,109] Coupling a Ru(II) or Ir(III) LA to a cobaloxime-based RM center forms the bimetallic complexes $[(bpy)_2Ru(L\text{-}pyr)Co(dmgBF_2)_2(OH_2)]^{2+}$ and $[(ppy)_2Ir(L\text{-}pyr)Co(dmgBF_2)_2(OH_2)]^{+}$ (L-pyr = (4-pyridine)oxazolo[4,5-*f*]phenanthroline; $dmgBF_2$ = (difluoroboryl)dimethylglyoximate; ppy = 2-phenylpyridine). Irradiation of $[(bpy)_2Ru(L\text{-}pyr)Co(dmgBF_2)_2(OH_2)]^{2+}$ in acetone at λ^{irr} < 380 nm affords 103 TON after 15 h photolysis in the presence of TEA/$TEAH^+$ as the sacrificial ED and proton source.[110] Photolyzing $[(ppy)_2Ir(L\text{-}pyr)Co(dmgBF_2)_2(OH_2)]^{+}$ in acetone at λ^{irr} > 380 nm results in 210 TON after 15 photolysis, suggesting the identity of the LA subunit strongly impacts photocatalytic functioning within the cobaloxime-based systems.[111]

Trimetallic complexes of the molecular architecture $[\{(TL)_2Ru(dpp)\}_2RhX_2]^{5+}$ (TL = bpy or phen; X = Cl^- or Br^-) covalently couple two peripheral Ru(II) LAs to a central Rh(III) EC center through dpp BLs. Photolysis of $[\{(bpy)_2Ru(dpp)\}_2RhCl_2]^{5+}$ at λ^{irr} = 470 nm in a CH_3CN solvent system using 65 μM trimetallic complex, 1.5 M DMA, 0.62 M H_2O, and 0.11 mM $[CF_3SO_3^-][DMAH^+]$ results in 6.0 ± 0.7 μmol H_2 (21 TON) after 2 h photolysis.[112] Varying the halide coordinated to Rh(III) from Cl^- to Br^-, $[\{(bpy)_2Ru(dpp)\}_2RhBr_2]^{5+}$, results in a small increase in H_2 production yielding 7.2 ± 0.8 μmol (25 TON) after 2 h.[100] This difference in photocatalytic activity was attributed to the weaker σ-donating ability of Br^- vs. Cl^- and the subsequent stabilization of the Ru(dπ)→Rh(dσ*) ^{3}MMCT excited state. Photolysis in the presence of DMA, followed by halide loss, should result in the same $[\{(bpy)_2Ru(dpp)\}_2Rh^{I}]^{5+}$ complex; however, the identity of the halide could influence the rate of formation of this state. Modification of the TL within the Ru(II),Rh(III),Ru(II) trimetallic architecture from bpy to phen produces the complex $[\{(phen)_2Ru(dpp)\}_2RhCl_2]^{5+}$. This trimetallic displays similar photocatalytic activity (5.4 ± 0.5 μmol H_2; 19 TON) when compared with the TL = bpy analogue.[99]

Expanding the supramolecular architecture from two Ru(II) LA subunits to three and changing the RM to Pt(II) yields the tetrametallic complex $[\{(phen)_2Ru(dpp)\}_2Ru(dpq)PtCl_2]^{6+}$.[113,114] Visible light excitation (λ^{irr} = 470 nm) in the presence of 50 μM tetrametallic complex, 1.5 M DMA, 0.62 M H_2O, and 0.11 mM $[CF_3SO_3^{-}][DMAH^{+}]$ produces 15 ± 1 μmol H_2 (66 ± 4 TON) after 10 h photolysis. This unique structural motif functions by photoexcitation throughout the UV and visible to populate a $Ru(d\pi)\rightarrow dpq(\pi^*)$ ^3CS (charge separated) excited state where the hole is located at the terminal Ru and the electron is located at the dpq BL next to the Pt(II) RM center. Variation of the TL from phen to Ph_2phen, $[\{(Ph_2phen)_2Ru(dpp)\}_2Ru(dpq)PtCl_2]^{6+}$ (Ph_2phen = 4,7-diphenyl-1,10-phenanthroline), increases photocatalytic functioning to 21 ± 1 μmol H_2 (94 ± 6 TON). The enhanced spectral coverage for the TL = Ph_2phen tetrametallic complex compared to the TL = phen complex may attribute to the observed differences in H_2 production.

1.8. Project Description

The goal of this research is to obtain an in-depth, fundamental understanding of how component variation within Ru(II),Rh(III) supramolecular complexes influences the observed electrochemical, photophysical, and photochemical properties, and how structural design affects the visible light-induced photocatalysis of H_2O to H_2. Systematic component variation within the previously established Ru(II),Rh(III),Ru(II) trimetallic supramolecular architecture, $[\{(TL)_2Ru(dpp)\}_2RhX_2]^{5+}$ (TL = bidentate terminal ligand; X = halide; dpp = 2,3-bis(2-pyridyl)pyrazine), provides insight into how tuning the electrochemical, light absorbing, photophysical, and photochemical properties impacts photocatalysis. In an effort to assay structural influences on photocatalysis, the Ru(II),Rh(III) bimetallic supramolecular architecture, $[(TL)_2Ru(dpp)RhCl_2(TL')]^{3+}$ (TL,TL′ = bidentate terminal ligand; dpp = 2,3-bis(2-pyridyl)pyrazine), was employed as well.

The trimetallic complexes $[\{(bpy)_2Ru(dpp)\}_2RhCl_2]^{5+}$, $[\{(bpy)_2Ru(dpp)\}_2RhBr_2]^{5+}$, and $[\{(phen)_2Ru(dpp)\}_2RhCl_2]^{5+}$ are previously reported H_2O reduction photocatalysts with component variation impacting photocatalysis. The Br^{-} analogue, $[\{(phen)_2Ru(dpp)\}_2RhBr_2]^{5+}$, was synthesized and studied to confirm the halide variation trend (Cl^{-} vs. Br^{-}) observed with TL = bpy trimetallics. The TL was varied from phen to Ph_2phen, generating the trimetallic complexes $[\{(Ph_2phen)_2Ru(dpp)\}_2RhCl_2]^{5+}$ and $[\{(Ph_2phen)_2Ru(dpp)\}_2RhBr_2]^{5+}$. Enhanced spectral coverage by the Ph_2phen TLs allows for more efficient light absorption to generate photoactive excited state species and the increased size of the Ph_2phen TLs provides steric bulk to protect the photogenerated Rh(I) catalytically active site. The supramolecular architecture was varied from the Ru(II),Rh(III),Ru(II) trimetallic to Ru(II),Rh(III) bimetallic, $[\{(Ph_2phen)_2Ru(dpp)\}_2RhCl_2]^{5+}$ to $[(Ph_2phen)_2Ru(dpp)RhCl_2(Ph_2phen)]^{3+}$, to investigate the impact one Ru(II) LA coupled to the Rh(III) RM center has on properties and photocatalysis. The TL coordinated to Rh(III) was varied from Ph_2phen to ${}^tBu_2$bpy, $[(Ph_2phen)_2Ru(dpp)RhCl_2({}^tBu_2bpy)]^{3+}$, as well as the TL′ coordinated to Ru(II) was varied from Ph_2phen to bpy, $[(bpy)_2Ru(dpp)RhCl_2({}^tBu_2bpy)]^{3+}$, to study the impact steric and electronic factors have on characterizations and photocatalysis. **Figure 1.19** depicts the generalized variations to the molecular architecture.

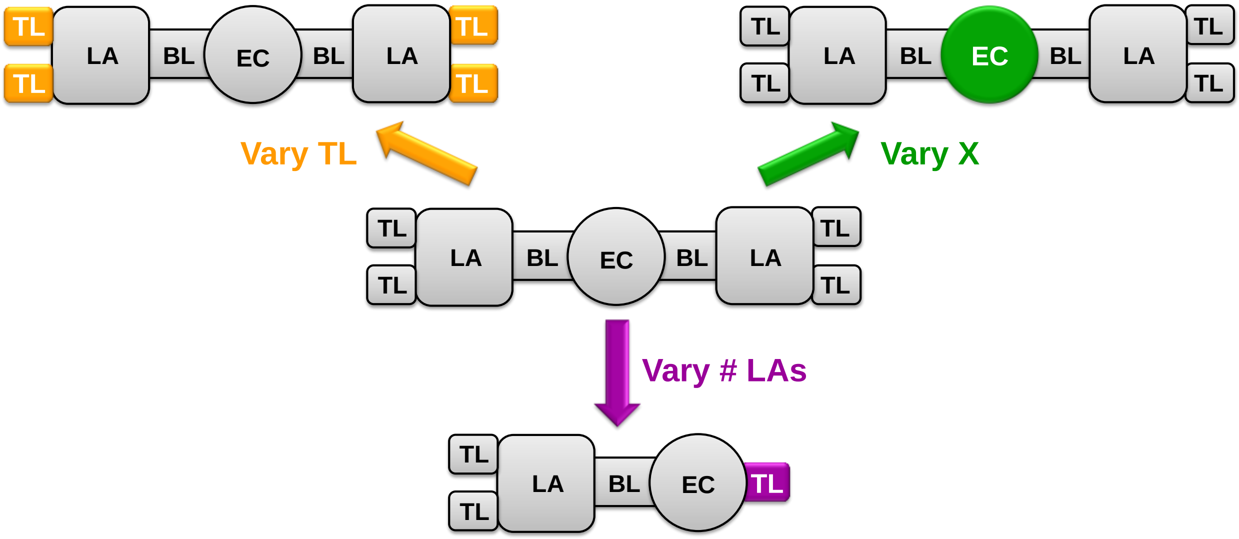

Figure 1.19: Structural variations to the Ru(II),Rh(III),Ru(II) trimetallic architecture. TL = bidentate bridging ligand; LA = light absorber; BL = bis-bidentate bridging ligand; EC = electron collector; X = halide.

2. Experimental

2.1. Materials and Synthesis

2.1.1. Materials

All materials for syntheses, purifications, characterizations, and photolysis experiments were used as received unless otherwise stated. Ruthenium trichloride trihydrate ($RuCl_3 \cdot 3H_2O$), rhodium trichloride trihydrate ($RhCl_3 \cdot 3H_2O$), rhodium tribromide trihydrate ($RhBr_3 \cdot 3H_2O$), lithium chloride (LiCl), silver trifluoromethanesulfonate ($AgOSO_2CF_3$), trifluoromethanesulfonic acid (CF_3SO_3H), and 4,7-diphenyl-1,10-phenanthroline (Ph_2phen) were purchased from Alfa Aesar. Sephadex® LH-20, 1,10-phenanthroline (phen), 4,4′-Di-*tert*-butyl-2,2′-bipyridine ($^tBu_2$bpy), 2,3-bis(2-pyridyl)pyrazine (dpp) and *N*,*N*-dimethylaniline (DMA) were purchased from Aldrich Chemical Company. Tetra-n-butylammonium hexafluorophosphate (Bu_4NPF_6) was purchased from Fluka. Ammonium hexafluorophosphate (NH_4PF_6) and *cis*-dichlorobis(2,2′-bipyridine)ruthenium(II) [$(bpy)_2RuCl_2$] were purchased from Strem Chemicals, Inc. Ethanol (EtOH) was purchased from Decon Labs. Spectral grade acetonitrile (CH_3CN) and *N*,*N*-dimethylformamide (DMF) were purchased from Burdick and Jackson. Acetone, acetonitrile (CH_3CN), chloroform ($CHCl_3$), dichloromethane (CH_2Cl_2), diethyl ether, methanol (MeOH), *N*,*N*-dimethylformamide (DMF), toluene, and 80-200 mesh alumina were purchased from Fisher Scientific. Deactivated alumina was prepared by adding MeOH to activated alumina and allowing the MeOH to evaporate overnight.

2.1.2. Synthesis and Purification

2.1.2.1. [$(phen)_2RuCl_2$]

The Ru(II) monometallic precursor [$(phen)_2RuCl_2$] was synthesized by modification of a previously reported method.[115] The Ru(III) starting material $RuCl_3 \cdot 3H_2O$ (1.6 g, 6.2 mmol), phen TL (2.0 g, 11 mmol), and LiCl (3.9 g, 92 mmol) were heated at reflux in 80 mL of DMF for 6 h. The reaction changed from a brown solution to a dark purple solution within 1 h of heating at reflux. The reaction was allowed to cool to room temperature, added to 100 mL of acetone, and placed in the refrigerator overnight. The dark purple solution was added to 200 mL saturated LiCl (aq), allowed to stir for 30 min, collected by vacuum filtration, washed with H_2O until filtrate was clear (~100 mL), and dried using 150 mL of diethyl ether. The dark purple crude product was purified using column chromatography (3.5 cm width x 12 cm height) with methanol deactivated adsorption alumina in a 4:1 CH_2Cl_2:acetone solvent system. Dissolution of the product required 15-20 mL of solvent and was syringe filtered prior to column loading. A faint yellow band which eluted first was discarded and the dark purple band containing the desired product was collected. The $[Ru(phen)_3]^{2+}$ impurity remained at the top of the column as a bright orange band and was discarded. The volume of the dark purple solution was reduced by rotary evaporation, redissolved in 20 mL of CH_2Cl_2, precipitated in 500 mL of diethyl ether, and collected by vacuum filtration to afford the desired product as a dark purple solid (1.2 g, 2.2 mmol, yield = 35%).

2.1.2.2. $[(Ph_2phen)_2RuCl_2]$

The Ru(II) monometallic precursor $[(Ph_2phen)_2RuCl_2]$ was synthesized by modification of a previously reported method.[116] The Ru(III) starting material $RuCl_3 \cdot 3H_2O$ (0.87 g, 3.3 mmol), Ph_2phen TL (2.0 g, 6.0 mmol) and LiCl (2.8 g, 67 mmol) were heated at reflux in 80 mL of DMF for 6 h. The reaction changed from a brown solution to a dark purple solution within 1 h of heating at reflux. The reaction was allowed to cool to room temperature, added to 100 mL of acetone, and placed in the refrigerator overnight. The dark purple solution was added to 200 mL saturated LiCl (aq), allowed to stir for 30 min, collected by vacuum filtration, washed with 100 mL of H_2O or until filtrate was clear, and dried using 150 mL of diethyl ether. The dark purple crude product was purified using column chromatography (3.5 cm width x 12 cm height) with methanol deactivated adsorption alumina in a 4:1 CH_2Cl_2:acetone solvent system. Dissolution of the product required 15-20 mL of solvent and was syringe filtered prior to column loading. A faint yellow band which eluted first was discarded and the dark purple band containing the desired product was collected. The $[Ru(Ph_2phen)_3]^{2+}$ impurity remained at the top of the column as a bright orange band and was discarded. The volume of the dark purple solution was reduced by rotary evaporation, redissolved in 20 mL of CH_2Cl_2, precipitated in 500 mL of diethyl ether, and collected by vacuum filtration to afford the desired product as a dark purple solid (1.1 g, 1.3 mmol, yield = 40%).

2.1.2.3. *[$RhCl_3$(^{t}Bu_2bpy)(CH_3OH)]*

Original syntheses of Rh(III) monometallic complexes required extensive use and heating of concentrated HCl to produce [Rh(TL)Cl_4]$^-$ species.[83,117] This technique proved unsuccessful in attempts to produce [Rh(^{t}Bu_2bpy)Cl_4]$^-$ and required a different, more facile synthetic method. The Rh(III) monometallic [$RhCl_3$(^{t}Bu_2bpy)(CH_3OH)] was synthesized by adaptation from the synthesis of [$RhCl_3$(bpy)(CH_3OH] and [$RhCl_3$(^{t}Bu_2bpy)(DMF)].[118,119] The Rh(III) starting material $RhCl_3$·3H_2O (0.10 g, 0.38 mmol) and ^{t}Bu_2bpy TL (0.10 g, 0.38 mmol) were dissolved separately in 30 mL CH_2Cl_2:MeOH (1:1). The ^{t}Bu_2bpy TL solution was then added drop-wise to the Rh(III) solution and heated at reflux for 2 h. The golden yellow solution was allowed to cool to room temperature, from which yellow precipitate formed. The resulting precipitate was collected by vacuum filtration and dissolved through the glass frit using 30-40 mL of MeOH. The filtrate was collected, volume reduced by rotary evaporation, and redissolved in 10 mL of MeOH. The yellow solution was reprecipitated by adding drop-wise into 200 mL of diethyl ether and the pale yellow solid was collected by vacuum filtration (0.052 g, 0.10 mmol, yield = 27%) (+)ESI-MS: [M+NH_4]$^+$, m/z = 526.07. Calculated and measured mass spectra for the molecular ion peak are shown in the Appendix, **Figures A-1**.

2.1.2.4. *[$RhCl_3$(Ph_2phen)(CH_3OH)]*

The Rh(III) starting material $RhCl_3$·3H_2O (0.10 g, 0.38 mmol) and Ph_2phen TL (0.11 g, 0.35 mmol) were dissolved separately in 30 mL CH_2Cl_2:MeOH (1:1). The Ph_2phen TL solution was then added drop-wise to the Rh(III) solution and heated at reflux for 2 h. The golden yellow solution was allowed to cool to room temperature, from which yellow precipitate formed. The resulting precipitate was collected by vacuum filtration and dissolved through the glass frit using 30-40 mL of MeOH. The filtrate was collected, volume reduced by rotary evaporation, and redissolved in 10 mL of MeOH. The yellow solution was reprecipitated by adding drop-wise into 200 mL of diethyl ether and the pale yellow solid was collected by vacuum filtration (0.067 g, 0.12 mmol, yield = 30%) (+)ESI-MS: [M−Cl+CH_3CN]$^+$, m/z = 578.03. Calculated and measured mass spectra for the molecular ion peak are shown in the Appendix, **Figures A-2**.

2.1.2.5. [(bpy)$_2$Ru(dpp)](PF$_6$)$_2$

The Ru(II) monometallic [(bpy)$_2$Ru(dpp)](PF$_6$)$_2$ was synthesized by modification of a previously reported method.[59] The monometallic precursor [(bpy)$_2$RuCl$_2$] (2.0 g, 3.8 mmol) and dpp BL (1.4 g, 5.8 mmol) were heated at reflux in 60 mL of a 2:1 EtOH:H$_2$O solvent mixture for 3 h. The small excess of dpp BL was used to minimize formation of the unwanted [{(bpy)$_2$Ru}$_2$(dpp)]$^{4+}$ product. The reaction changed from dark purple to dark orange-red after 30 minutes of heating and reflux. The dark orange-red solution was allowed to cool to room temperature, added drop-wise to 150 mL NH$_4$PF$_6$ (aq) (1.5 g) to induce precipitation, and allowed to stir for 30 min. The dark orange-red precipitate was collected by vacuum filtration, washed with 60 mL of H$_2$O, and dried using 150 mL of diethyl ether. The crude monometallic complex was purified using column chromatography (3.5 cm width x 8 cm height) with methanol deactivated adsorption alumina in a 2:3 CH$_3$CN:toluene solvent system. Dissolution of the product required 15-20 mL of solvent and was syringe filtered prior to column loading. Excess dpp BL eluted first as a pale yellow-orange band which was discarded, followed by the desired [(bpy)$_2$Ru(dpp)]$^{2+}$ product as a deep orange band which was collected and rotary evaporated to dryness. The small dark purple band at the top of the column was the unwanted [{(bpy)$_2$Ru}$_2$(dpp)]$^{4+}$ product and was discarded. The dark orange solid was precipitated using 15 mL of CH$_3$CN in 300 mL diethyl ether and collected by vacuum filtration to afford an orange solid that was dried under vacuum (1.9 g, 2.1 mmol, yield = 54%).

2.1.2.6. [(phen)$_2$Ru(dpp)](PF$_6$)$_2$

The Ru(II) monometallic [(phen)$_2$Ru(dpp)](PF$_6$)$_2$ was synthesized by modification of a previously reported method.[61] The monometallic precursor [(phen)$_2$RuCl$_2$] (2.0 g, 3.7 mmol) and dpp BL (1.8 g, 7.5 mmol) were heated at reflux in 60 mL of a 2:1 EtOH:H$_2$O solvent mixture for 3 h. The small excess of dpp BL was used to minimize formation of the unwanted [{(phen)$_2$Ru}$_2$(dpp)]$^{4+}$ product. The reaction changed from dark purple to dark orange-red after 30 minutes of heating and reflux. The dark orange-red solution was allowed to cool to room temperature, added drop-wise to 150 mL NH$_4$PF$_6$ (aq) (1.5 g) to induce precipitation, and allowed to stir for 30 min. The dark orange-red precipitate was collected by vacuum filtration, washed with 60 mL of H$_2$O, and dried using 150 mL of diethyl ether. The crude monometallic complex was purified using column chromatography (3.5 cm width x 8 cm height) with methanol deactivated adsorption alumina in a 2:3 CH_3CN:toluene solvent system. Dissolution of the product required 15-20 mL of solvent and was syringe filtered prior to column loading. Excess dpp BL eluted first as a pale yellow-orange band which was discarded, followed by the desired $[(phen)_2Ru(dpp)]^{2+}$ product as a deep orange band which was collected and rotary evaporated to dryness. The small dark purple band at the top of the column was the unwanted $[\{(phen)_2Ru\}_2(dpp)]^{4+}$ product and was discarded. The dark orange solid was precipitated using 15 mL of CH_3CN in 300 mL diethyl ether and collected by vacuum filtration to afford an orange solid that was dried under vacuum (1.4 g, 1.4 mmol, yield = 38%).

2.1.2.7. $[(Ph_2phen)_2Ru(dpp)](PF_6)_2$

The Ru(II) monometallic $[(Ph_2phen)_2Ru(dpp)](PF_6)_2$ was synthesized by modification of a previously reported method.[55] The monometallic precursor $[(Ph_2phen)_2RuCl_2]$ (0.77 g, 0.92 mmol) and dpp BL (0.43 g, 1.8 mmol) were heated at reflux in 30 mL of a 2:1 EtOH:H_2O solvent mixture for 3 h. The small excess of dpp BL was used to minimize formation of the unwanted $[\{(Ph_2phen)_2Ru\}_2(dpp)]^{4+}$ product. The reaction changed from dark purple to dark orange-red after 30 minutes of heating and reflux. The dark orange-red solution was allowed to cool to room temperature, added drop-wise to 150 mL NH_4PF_6 (aq) (1.5 g) to induce precipitation, and allowed to stir for 30 min. The dark orange-red precipitate was collected by vacuum filtration, washed with 60 mL of H_2O, and dried using 150 mL of diethyl ether. The crude monometallic complex was purified using column chromatography (3.5 cm width x 8 cm height) with methanol deactivated adsorption alumina in a 2:3 CH_3CN:toluene solvent system. Dissolution of the product required 15-20 mL of solvent and was syringe filtered prior to column loading. Excess dpp BL eluted first as a pale yellow-orange band which was discarded, followed by the desired $[(Ph_2phen)_2Ru(dpp)]^{2+}$ product as a deep orange band which was collected and rotary evaporated to dryness. The small dark purple band at the top of the column was the unwanted $[\{(Ph_2phen)_2Ru\}_2(dpp)]^{4+}$ product and was discarded. The dark orange solid was precipitated using 15 mL of CH_3CN in 300 mL diethyl ether and collected by vacuum filtration to afford an orange solid that was dried under vacuum (0.72 g, 0.056 mmol, yield = 61%).

2.1.2.8. *$[\{(Ph_2phen)_2Ru\}_2(dpp)](PF_6)_4$*

The Ru(II),Ru(II) bimetallic $[\{(Ph_2phen)_2Ru\}_2(dpp)](PF_6)_4$ was synthesized using a building block approach. The starting material $[(Ph_2phen)_2RuCl_2]$ (0.12 g, 0.14 mmol) and $AgSO_3CF_3$ (0.11 g, 0.42 mmol) were heated at reflux in 40 mL of EtOH for 24 h to substitute the Cl^- ligands for the more labile $CF_3SO_3^-$ ligands. The reaction was allowed to cool to room temperature, filtered to remove AgCl solid which formed, and the maroon filtrate collected. The dpp BL (0.016 g, 0.068 mmol) was added to the filtrate and the solution was heated at reflux for 3 d. The solution was allowed to cool to room temperature, added drop-wise to 150 mL saturated KPF_6 (aq) to induce precipitation, and allowed to stir for 30 minutes. The dark purple precipitate was collected by vacuum filtration, washed with 60 mL of H_2O, and dried using 150 mL of diethyl ether. The crude bimetallic complex was purified using column chromatography (3.5 cm width x 8 cm height) with methanol deactivated adsorption alumina in a 2:3 CH_3CN:toluene solvent system. Dissolution of the product required 15-20 mL of solvent and was syringe filtered prior to column loading. The $[(Ph_2phen)_2Ru(dpp)]^{2+}$ orange band that eluted first was discarded and the dark purple band was collected by increasing the polarity of the CH_3CN:toluene solvent system due to the desired product's strong interaction with the alumina column. The dark purple solution was rotary evaporated to reduce solvent volume, redissolved in 10-15 mL of CH_3CN and precipitated by adding drop-wise into 300 mL of diethyl ether to afford a dark purple solid that was dried under vacuum (0.030 g, 0.013 mmol, yield = 20%) (+)ESI-MS: $[M-2PF_6]^{2+}$, m/z = 1028.14. Calculated and measured mass spectra for the molecular ion peak are shown in the Appendix, **Figures A-3**.

2.1.2.9. *$[(bpy)_2Ru(dpp)RhCl_2(^tBu_2bpy)](PF_6)_3$*

The Ru(II),Rh(III) bimetallic $[(bpy)_2Ru(dpp)RhCl_2(^tBu_2bpy)](PF_6)_3$ was synthesized using a building block approach. The Ru(II) monometallic $[(bpy)_2Ru(dpp)](PF_6)_2$ (0.11 g, 0.11 mmol) and Rh(III) monometallic $[RhCl_3(^tBu_2bpy)(CH_3OH)]$ (0.070 g, 0.14 mmol) were dissolved separately in 10 mL of a 2:1 EtOH:H_2O solvent system. Following dissolution, the dark orange Ru(II) monometallic solution was added drop-wise to the stirring dark yellow Rh(III) monometallic solution and heated at reflux for 1 h. The dark purple reaction was allowed to cool to room temperature, added drop-wise to stirring 75 mL NH_4PF_6 (aq) (1.0 g) to induce precipitation, and allowed to stir for 30 min. The precipitate was collected by vacuum filtration, washed with 60 mL of H_2O, and dried with 150 mL of diethyl ether. The dark purple crude product was purified using size-exclusion chromatography with a Sephadex® LH-20 column (2.2 cm width x 100 cm height) in a 2:1 EtOH:CH_3CN solvent system. The product was dissolved in 10-15 mL of the solvent system and syringe filtered prior to column loading. The desired product eluted first as a dark purple band, followed by an orange band corresponding to unreacted $[(bpy)_2Ru(dpp)]^{2+}$ monometallic, and a faint yellow band corresponding to unreacted $[RhCl_3(^tBu_2bpy)(CH_3OH)]$ monometallic. The dark purple solution was rotary evaporated to reduce solvent volume, reprecipitated by dissolving in 10-15 mL of CH_3CN, and added to 300 mL of diethyl ether. The precipitate was vacuum filtered and dried with 50 mL of diethyl ether to yield a dark purple product (0.057 g, 0.037 mmol, yield = 34%) (+)ESI-MS: $[M-PF_6]^+$, m/z = 1379.10. Calculated and measured mass spectra for the molecular ion peak are shown in the Appendix, **Figures A-5**.

2.1.2.10. $[(Ph_2phen)_2Ru(dpp)RhCl_2(^tBu_2bpy)](PF_6)_3$

The Ru(II),Rh(III) bimetallic $[(Ph_2phen)_2Ru(dpp)RhCl_2(^tBu_2bpy)](PF_6)_3$ was synthesized using a building block approach. The Ru(II) monometallic $[(Ph_2phen)_2Ru(dpp)](PF_6)_2$ (0.20 g, 0.15 mmol) and Rh(III) monometallic $[RhCl_3(^tBu_2bpy)(CH_3OH)]$ (0.12 g, 0.23 mmol) were dissolved separately in 10 mL of a 2:1 EtOH:H_2O solvent system. Following dissolution, the dark orange Ru(II) monometallic solution was added drop-wise to the stirring dark yellow Rh(III) monometallic solution and heated at reflux for 1 h. The dark purple reaction was allowed to cool to room temperature, added drop-wise to stirring 75 mL NH_4PF_6 (aq) (1.0 g) to induce precipitation, and allowed to stir for 30 min. The precipitate was collected by vacuum filtration, washed with 60 mL of H_2O, and dried with 150 mL of diethyl ether. The dark purple crude product was purified using size-exclusion chromatography with a Sephadex® LH-20 column (2.2 cm width x 100 cm height) in a 2:1 EtOH:CH_3CN solvent system. The product was dissolved in 10-15 mL of the solvent system and syringe filtered prior to column loading. The desired product eluted first as a dark purple band, followed by an orange band corresponding to unreacted $[(Ph_2phen)_2Ru(dpp)]^{2+}$ monometallic, and a faint yellow band corresponding to unreacted $[RhCl_3(^tBu_2bpy)(CH_3OH)]$ monometallic. The dark purple solution was rotary evaporated to reduce solvent volume, reprecipitated by dissolving in 10-15 mL of CH_3CN, and added to 300 mL of diethyl ether. The precipitate was vacuum filtered and dried with 50 mL of diethyl ether to yield a dark purple product (0.075 g, 0.040 mmol, yield = 27%) (+)ESI-MS: $[M-PF_6]^+$, m/z = 1733.22. Calculated and measured mass spectra for the molecular ion peak are shown in the Appendix, **Figures A-4**.

2.1.2.11. *$[(Ph_2phen)_2Ru(dpp)RhCl_2(Ph_2phen)](PF_6)_3$*

The Ru(II),Rh(III) bimetallic $[(Ph_2phen)_2Ru(dpp)RhCl_2(Ph_2phen)](PF_6)_3$ was synthesized using a building block approach. The Ru(II) monometallic $[(Ph_2phen)_2Ru(dpp)](PF_6)_2$ (0.10 g, 0.078 mmol) and Rh(III) monometallic $[RhCl_3(Ph_2phen)(CH_3OH)]$ (0.050 g,0.087 mmol) were dissolved separately in 10 mL of a 2:1 EtOH:H_2O solvent system. Following dissolution, the dark orange Ru(II) monometallic solution was added drop-wise to the stirring dark yellow Rh(III) monometallic solution and heated at reflux for 1 h. The dark purple reaction was allowed to cool to room temperature, added drop-wise to stirring 75 mL NH_4PF_6 (aq) (1.0 g) to induce precipitation, and allowed to stir for 30 min. The precipitate was collected by vacuum filtration, washed with 60 mL of H_2O, and dried with 150 mL of diethyl ether. The dark purple crude product was purified using size-exclusion chromatography with a Sephadex® LH-20 column (2.2 cm width x 100 cm height) in a 2:1 EtOH:CH_3CN solvent system. The product was dissolved in 10-15 mL of the solvent system and syringe filtered prior to column loading. The desired product eluted first as a dark purple band, followed by an orange band corresponding to unreacted $[(Ph_2phen)_2Ru(dpp)]^{2+}$ monometallic, and a faint yellow band corresponding to unreacted $[RhCl_3(Ph_2phen)(CH_3OH)]$ monometallic. The dark purple solution was rotary evaporated to reduce solvent volume, reprecipitated by dissolving in 10-15 mL of CH_3CN, and added to 300 mL of diethyl ether. The precipitate was vacuum filtered and dried with 50 mL of diethyl ether to yield a dark purple product (0.030 g, 0.015 mmol, yield = 20%) (+)ESI-MS: $[M-PF_6]^+$, m/z = 1797.15. Calculated and measured mass spectra for the molecular ion peak are shown in the Appendix, **Figures A-6**.

2.1.2.12. *$[\{(phen)_2Ru(dpp)\}_2RhCl_2](PF_6)_5$*

The Ru(II),Rh(III),Ru(II) trimetallic $[\{(phen)_2Ru(dpp)\}_2RhCl_2](PF_6)_5$ was synthesized by modification of a previously reported method.[99] The Ru(II) monometallic $[(phen)_2Ru(dpp)](PF_6)_2$ (0.32 g, 0.32 mmol) and Rh(III) starting material $RhCl_3 \cdot 3H_2O$ (0.053 g, 0.20 mmol) were heated at reflux in 15 mL of a 2:1 EtOH:H_2O solvent mixture for 1 h. The dark purple reaction was allowed to cool to room temperature, added drop-wise to stirring 75 mL NH_4PF_6 (aq) (1 g) to induce precipitation, and allowed to stir for 30 min. The purple precipitate was collected by vacuum filtration, washed with 60 mL of H_2O, and dried with 150 mL of diethyl ether. Previous purification techniques used to remove $[(phen)_2Ru(dpp)]^{2+}$ monometallic impurity required hot ethanol reprecipitations which were time consuming and difficult to remove trace amounts of the emissive monometallic species. This purification issue was alleviated by washing the crude product with three 25 mL portions of CH_2Cl_2 to remove the unwanted $[(phen)_2Ru(dpp)]^{2+}$ monometallic impurity that dissolved in the glass frit and appeared as orange filtrate. The remaining dark purple product was dissolved using 10-15 mL of CH_3CN and reprecipitated by addition to 300 mL of diethyl ether. The purified product was vacuum filtered to yield the desired dark purple product (0.17 g, 0.074 mmol, yield = 37%).

2.1.2.13. $[\{(phen)_2Ru(dpp)\}_2RhBr_2](PF_6)_5$

The Ru(II),Rh(III),Ru(II) trimetallic $[\{(phen)_2Ru(dpp)\}_2RhBr_2](PF_6)_5$ was synthesized using a building block approach. The Ru(II) monometallic $[(phen)_2Ru(dpp)](PF_6)_2$ (0.25 g, 0.26 mmol) and Rh(III) starting material $RhBr_3{\cdot}3H_2O$ (0.064 g, 0.16 mmol) were heated at reflux in 15 mL of a 2:1 EtOH:H_2O solvent mixture for 1 h. The dark purple reaction was allowed to cool to room temperature, added drop-wise to stirring 75 mL NH_4PF_6 (aq) (1 g) to induce precipitation, and allowed to stir for 30 min. The purple precipitate was collected by vacuum filtration, washed with 60 mL of H_2O, and dried with 150 mL of diethyl ether. The crude product was purified by washing with three 25 mL portions of CH_2Cl_2 to remove the unwanted $[(phen)_2Ru(dpp)]^{2+}$ monometallic impurity that dissolved in the glass frit and appeared as orange filtrate. The remaining dark purple product was dissolved using 10-15 mL of CH_3CN and reprecipitated by addition to 300 mL of diethyl ether. The purified product was vacuum filtered to yield the desired dark purple product (0.18 g, 0.074 mmol, yield = 46%) (+)ESI-MS: $[M-PF_6]^+$, m/z = 2234.86. Calculated and measured mass spectra for the molecular ion peak are shown in the Appendix, **Figures A-7**.

2.1.2.14. $[\{(Ph_2phen)_2Ru(dpp)\}_2RhCl_2](PF_6)_5$

The Ru(II),Rh(III),Ru(II) trimetallic $[\{(Ph_2phen)_2Ru(dpp)\}_2RhCl_2](PF_6)_5$ was synthesized using a building block approach. The Ru(II) monometallic $[(Ph_2phen)_2Ru(dpp)](PF_6)_2$ (0.30 g, 0.23 mmol) and Rh(III) starting material $RhCl_3 \cdot 3H_2O$ (0.041 g, 0.016 mmol) were heated at reflux in 15 mL of a 2:1 $EtOH:H_2O$ solvent mixture for 2 h. The dark maroon reaction was allowed to cool to room temperature, added drop-wise to stirring 75 mL NH_4PF_6 (aq) (1 g) to induce precipitation, and allowed to stir for 30 min. The maroon precipitate was collected by vacuum filtration, washed with 60 mL of H_2O, and dried with 150 mL of diethyl ether. Unlike the TL = phen trimetallic species, purification by CH_2Cl_2 washing was not possible due to the high solubility of the TL = Ph_2phen trimetallic complexes. This purification issue was alleviated by exploitation of the desired product's insolubility in toluene and the $[(Ph_2phen)_2Ru(dpp)]^{2+}$ monometallic impurity's solubility in toluene at elevated temperatures. This was achieved by dissolving the crude product in ~5 mL of CH_3CN and adding drop-wise to 300 mL of stirring hot toluene. The stirring solution was continually heated for 30 min to allow for CH_3CN evaporation and slow precipitation of the desired product. The precipitate was vacuum filtered while warm and the process was performed three times to ensure removal of the highly emissive $[(Ph_2phen)_2Ru(dpp)]^{2+}$ monometallic impurity. The purified product was dissolved in 10 mL of CH_3CN, syringe filtered into 200 mL of diethyl ether to induce precipitation, and vacuum filtered to yield the desired dark maroon product (0.14 g, 0.048 mmol, yield = 31%) (+)ESI-MS: $[M-2PF_6]^{2+}$, m/z = 1305.12. Calculated and measured mass spectra for the molecular ion peak are shown in the Appendix, **Figures A-8**.

2.1.2.15. *$[\{(Ph_2phen)_2Ru(dpp)\}_2RhBr_2](PF_6)_5$*

The Ru(II),Rh(III),Ru(II) trimetallic $[\{(Ph_2phen)_2Ru(dpp)\}_2RhBr_2](PF_6)_5$ was synthesized using a building block approach. The Ru monometallic $[(Ph_2phen)_2Ru(dpp)](PF_6)_2$ (0.21 g, 0.16 mmol) and Rh starting material $RhBr_3 \cdot 3H_2O$ (0.043 g, 0.11 mmol) were heated at reflux in 15 mL of a 2:1 $EtOH:H_2O$ solvent mixture for 2 h. The dark maroon reaction was allowed to cool to room temperature, added drop-wise to stirring 75 mL NH_4PF_6 (aq) (1 g) to induce precipitation, and allowed to stir for 30 min. The maroon precipitate was collected by vacuum filtration, washed with 60 mL of H_2O, and dried with 150 mL of diethyl ether. Unlike the TL = phen trimetallic species, purification by CH_2Cl_2 washing was not possible due to the high solubility of the TL = Ph_2phen trimetallic complexes. This purification issue was alleviated by exploitation of the desired product's insolubility in toluene and the $[(Ph_2phen)_2Ru(dpp)]^{2+}$ monometallic impurity's solubility in toluene at elevated temperatures. This was achieved by dissolving the crude product in ~5 mL of CH_3CN and adding drop-wise to 300 mL of stirring hot toluene. The stirring solution was continually heated for 30 min to allow for CH_3CN evaporation and slow precipitation of the desired product. The precipitate was vacuum filtered while warm and the process was performed three times to ensure removal of the highly emissive $[(Ph_2phen)_2Ru(dpp)]^{2+}$ monometallic impurity. The purified product was dissolved in 10 mL of CH_3CN, syringe filtered into 200 mL of diethyl ether to induce precipitation, and vacuum filtered to yield the desired dark maroon product (0.16 g, 0.054 mmol, yield = 50%) (+)ESI-MS: $[M{-}2PF_6]^{2+}$, m/z = 1349.07. Calculated and measured mass spectra for the molecular ion peak are shown in the Appendix, **Figures A-9**.

2.1.2.16. Electrochemical and Spectroscopic Purity Determination

The building block approach permits purification at each synthetic step to remove electroactive and/or spectroscopic impurities that inhibit proper analyses of the basic chemical properties of the target supramolecular complexes. Sensitive electrochemical and spectroscopic techniques such as Osteryoung square wave voltammetry[120] and steady-state luminescence spectroscopy[121], respectively, are capable of detecting low concentrations of electroactive species (10^{-7} M) or emissive species (single molecule detection). Characterization of the title Ru(II),Ru(III),Ru(II) trimetallic and Ru(II),Rh(III) bimetallic complexes requires minimal electroactive and spectroscopic impurities which interfere with these characterizations and analyses of electrochemical or photochemical experiments. A typical impurity encountered is excess $[(TL)_2Ru(dpp)]^{2+}$ monometallic remaining after synthesis. **Figure 2.1** shows how Osteryoung square wave voltammetry is useful in the detection of low concentrations of Ru(II) monometallic species. Anodic electrochemical analysis of $[\{(phen)_2Ru(dpp)\}_2RhBr_2](PF_6)_5$ (1.2×10^{-3} M) in the presence of increasing $[(phen)_2Ru(dpp)](PF_6)_2$ concentration shows that at concentrations as low as 6.4×10^{-5} M, monometallic is detectable. The bold orange lines shows the two overlapping $Ru^{II/III}$ couples at 1.62 V vs. Ag/AgCl corresponding to $[\{(phen)_2Ru(dpp)\}_2RhBr_2](PF_6)_5$, whereas the thin orange lines correspond to increasing concentrations of $[(phen)_2Ru(dpp)](PF_6)_2$ (6.4×10^{-5} M to 2.6×10^{-4} M). The shoulder appearing at 1.45 V represents the $Ru^{II/III}$ couple of $[(phen)_2Ru(dpp)](PF_6)_2$, giving an indication to the relative concentration of monometallic present. The bold turquoise line shows the $Ru^{II/III}$ couple at 1.45 V vs. Ag/AgCl for $[(phen)_2Ru(dpp)](PF_6)_2$ (1.3×10^{-3} M) in the absence of any trimetallic.

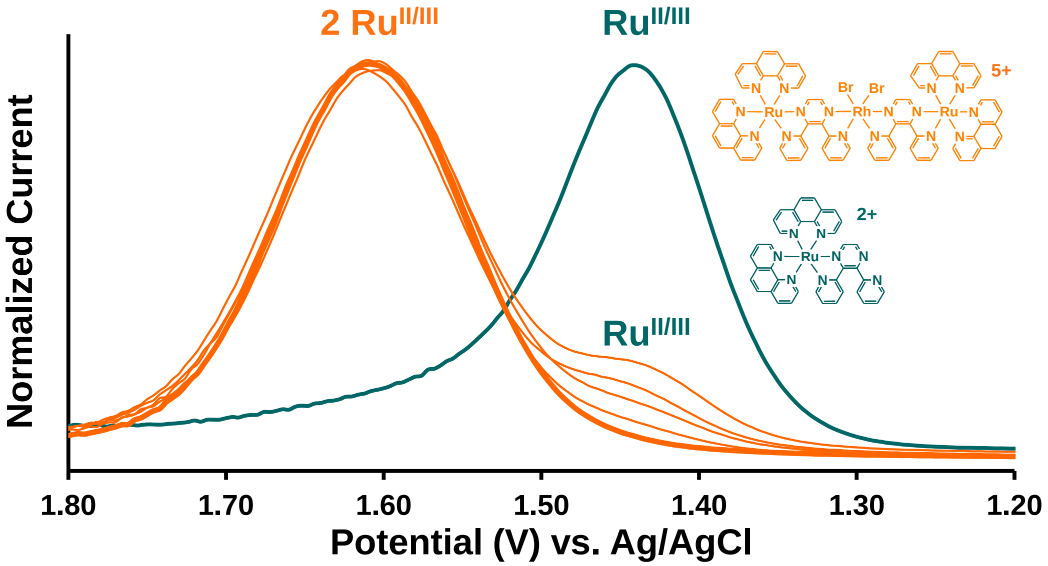

Figure 2.1: Osteryoung square wave voltammograms of $[\{(phen)_2Ru(dpp)\}_2RhBr_2](PF_6)_5$ (bold orange line) in the presence of increasing concentrations of $[(phen)_2Ru(dpp)](PF_6)_2$ (thin orange lines) measured using a Pt disk working electrode, Pt wire auxiliary electrode, and Ag wire pseudo-reference electrode (converted to Ag/AgCl using ferrocene as an internal standard; $Fe(C_5H_5)_2^{0/+}$ = 0.46 V vs. Ag/AgCl). Measurements were made at RT in CH_3CN using 0.1 M Bu_4NPF_6 supporting electrolyte at a scan rate of 100 mV/s under an inert Ar atmosphere. phen = 1,10-phenanthroline; dpp = 2,3-bis(2-pyridyl)pyrazine.

Spectroscopic analysis using luminescence spectroscopy allows for the detection of low concentrations of highly emissive impurities. The large discrepancy between the emission quantum yield of monometallic ($\Phi^{em}_{^3MLCT} \approx 10^{-2}$) compared to trimetallic ($\Phi^{em}_{^3MLCT} \approx 10^{-4}$) requires a high level of spectroscopic purity to allow for proper photophysical and photochemical analyses. **Figure 2.2** shows the emission profiles of $[(phen)_2Ru(dpp)](PF_6)_2$ (turquoise line) and $[\{(phen)_2Ru(dpp)\}_2RhBr_2](PF_6)_5$ (orange line) absorbance matched samples (0.18) excited at 460 nm. This was done to calculate the amount of emissive monometallic impurity in the weakly emissive trimetallic sample. Comparing the emission profile intensity at 670 nm of the $[(phen)_2Ru(dpp)](PF_6)_2$ sample to that of the $[\{(phen)_2Ru(dpp)\}_2RhBr_2](PF_6)_5$ sample indicated the presence of <0.5% (<6.3 x 10^{-8} M) monometallic impurity and therefore >99.5% spectroscopic purity for the desired trimetallic complex.

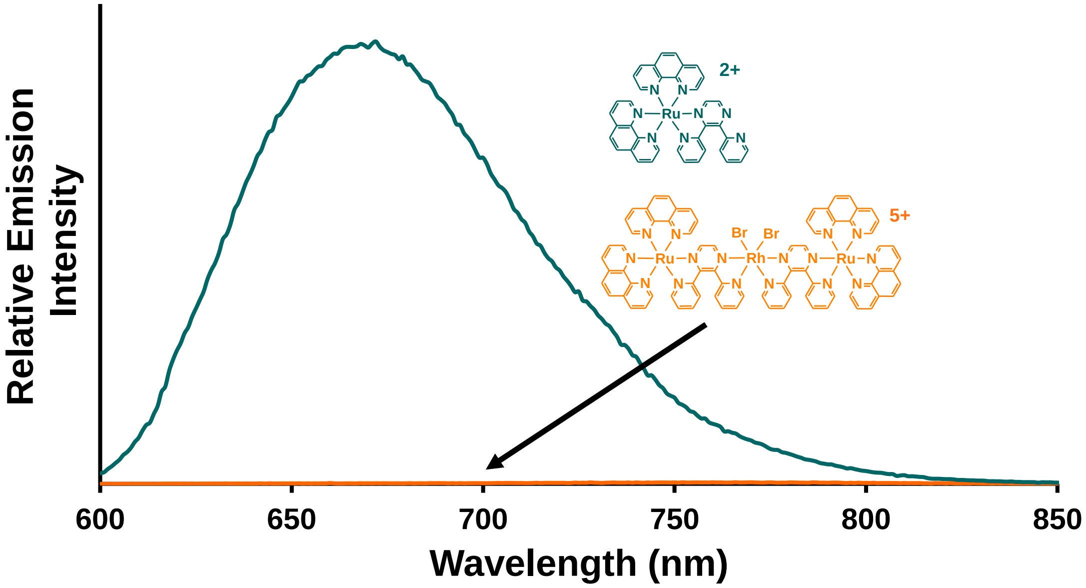

Figure 2.2: Steady-state emission profiles for [{(phen)$_2$Ru(dpp)}$_2$RhBr$_2$](PF$_6$)$_5$ (orange line) and [(phen)$_2$Ru(dpp)](PF$_6$)$_2$ (turquoise line) excited at 460 nm (absorbance = 0.18) and measured in deoxygenated CH$_3$CN at RT using a 1 cm quartz cuvette. Excitation and emission monochromator compartment entrance and exit slit widths set to 1.5 mm (corresponds to ± 6 nm). phen = 1,10-phenanthroline; dpp = 2,3-bis(2-pyridyl)pyrazine.

2.2. Instrumentation and Methods

2.2.1. Mass Spectrometry

Mass spectrometry was performed by William Bebout of the Virginia Tech Chemistry Department Analytical Service laboratory in Blacksburg, VA. Positive ion electrospray ionization mass spectra ((+)ESI-MS)[122] were collected using an Agilent Technologies 6220 Accurate-Mass time-of-flight (TOF) LC–MS with a dual ESI source. The sample was dissolved in HPLC grade acetonitrile and injected through a preloading capillary at 1.2 kV with a flow rate of 0.4 mL/min. N$_2$ gas was used as the inert nebulizing gas at a pressure of 60 psig. The charging voltage was set to 2000 V, the fragmentor voltage set to 125 V, and the skimmer voltage set to 65 V. The observed molecular ion peaks were confirmed using Sheffield Chemputer isotopic pattern calculator.[123]

2.2.2. Electrochemistry

Electrochemical methods were performed using a Bioanalytical System (BAS) Epsilon potentiostat with a single-cell, three-electrode configuration (**Figure 2.3**). The three-electrode system consisted of a Pt disk working electrode, Pt wire auxiliary electrode, and Ag wire pseudo-reference electrode which was calibrated using ferrocene and converted to Ag/AgCl ($Fe(C_5H_5)_2^{0/+}$ = 0.46 V vs. Ag/AgCl (3 M NaCl))[124] for each measurement. Electrochemical measurements were performed at room temperature under Ar with 0.1 M Bu_4NPF_6 supporting electrolyte in acetonitrile unless otherwise stated.

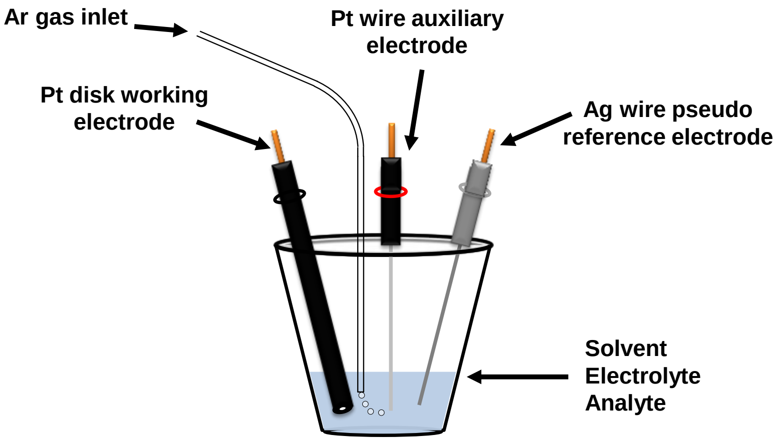

Figure 2.3: Schematic showing the single-compartment cell for electrochemical measurements containing Pt disk working electrode, Pt disk auxiliary electrode, Ag wire pseudo-reference electrode calibrated with ferrocene, and 0.1 M Bu_4NPF_6 supporting electrolyte in solvent under an Ar atmosphere.

Cyclic voltammetric analyses[54,125] were performed in a single-cell, three-electrode configuration (**Figure 2.3**) at room temperature under Ar with 0.1 M Bu_4NPF_6 in acetonitrile at a scan rate of 100 mV/s unless otherwise stated. **Figure 2.4** displays a typical triangular waveform applied where $E_{initial}$ is the initial potential, E_{SP1} is the first switching potential, E_{SP2} is the second switching potential, and E_{final} is the final potential. This method is beneficial as it provides information regarding the reversibility of a redox process as well as the $E_{½}$ for a reversible process.

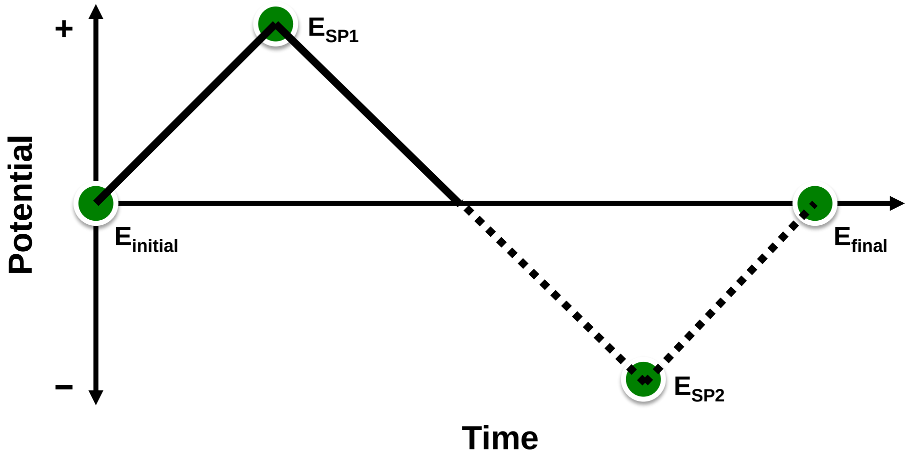

Figure 2.4: Diagram depicting a triangular waveform used for cyclic voltammetric analyses where $E_{initial}$ = initial potential, E_{SP1} = first switching potential, E_{SP2} = second switching potential, and E_{final} = final potential.

Osteryoung square wave voltammetric[54,120,125] analyses were performed in a single-cell, three-electrode configuration (**Figure 2.3**) at room temperature under Ar with 0.1 M Bu_4NPF_6 in acetonitrile. The pulse frequency (τ) was 15 Hz, the pulse time (t_p) was 7.5 Hz, the magnitude of the fixed pulse potential (ΔE_p) was 25 mV, and the potential step of the staircase (ΔE_s) was 4 mV. **Figure 2.5** displays the pulsed staircase waveform applied. This method provides enhanced signal to noise ratio for a higher level of detection (10^{-7} M) of electroactive impurities.

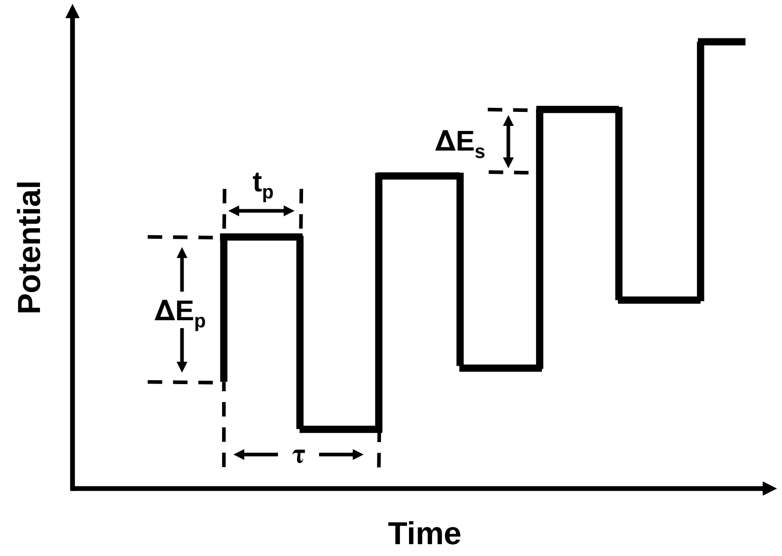

Figure 2.5: Diagram depicting a pulsed staircase waveform for square wave voltammetric analyses where ΔE_p = magnitude of the fixed pulse potential, ΔE_S = potential step of the staircase, t_p = pulse time, and τ = pulse frequency.

Constant potential coulometric methods[125] to electrolyze a bulk solution as well as cyclic and square wave voltammetric measurements of the electrolyzed solution were performed in the same cell. **Figure 2.6** shows the two-cell system separated by a porous vycor tip, five-electrode configuration that permits facile cyclic and square wave voltammetric measurements using 0.1 M Bu_4NPF_6 in CH_3CN as the supporting electrolyte. The bulk electrolysis measurements consisted of a Pt mesh working electrode, Pt wire enclosed in a glass tube with a vycor tip as an auxiliary electrode compartment, and Ag/AgCl reference electrode. The cyclic and square wave voltammetry measurements consisted of a Pt disk working electrode, Pt wire auxiliary electrode, and Ag/AgCl reference. After a constant-potential was applied to electrolyze the bulk solution, the electrode connectors were switched from the bulk electrolysis configuration to the cyclic and square wave voltammetry configuration. The number of electrons passed per redox event was calculated using **Equation 2.1**

$$Q = nFn_A \qquad \text{eq. 2.1}$$

where Q is the net charge passed in coulombs I, n is the number of electrons, F is Faraday's constant of 96,485 C/mol, and n_A is the number of moles of analyte.

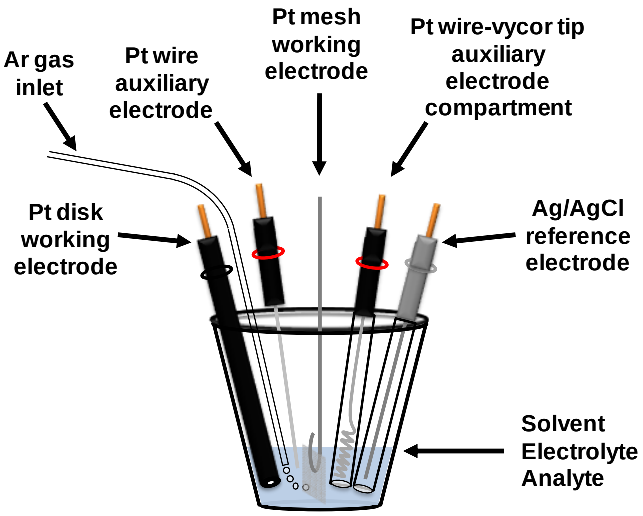

Figure 2.6: Schematic showing the two-compartment configuration for constant-potential coulometry and cyclic voltammetry measurements using a Pt mesh working electrode (bulk electrolysis), Pt wire enclosed in a glass tube with a vycor tip as an auxiliary electrode compartment (bulk electrolysis), Pt disk working electrode (cyclic voltammetry), Pt wire auxiliary electrode (cyclic voltammetry), and Ag/AgCl reference electrode (bulk electrolysis and cyclic voltammetry). The supporting electrolyte was 0.1 M Bu_4NPF_6 in CH_3CN.

2.2.3. Electronic Absorption Spectroscopy

Electronic absorption spectra were collected using either a Hewlett-Packard 8452A (2 nm resolution) or an Agilent 8453 (1 nm resolution) diode array spectrophotometer. Spectra were collected at room temperature in spectral grade acetonitrile using 0.2 cm path length glass cuvettes or 1 cm path length quartz cuvettes (Starna Cells, Inc.; Atascadero, CA, USA) unless otherwise stated. The molar extinction coefficient (ε) values for the complexes were obtained using a 1 cm path length quartz cuvette in spectral grade acetonitrile. Values are the average of triplicate measurements of different solutions prepared gravimetrically.

2.2.4. Spectroelectrochemistry

Spectroelectrochemical analyses were performed using a Bioanalytical System (BAS) Epsilon potentiostat and an Agilent 8453 diode array spectrophotometer (1 nm resolution). A two-compartment H-cell design was used to separate the carbon cloth auxiliary electrode from the Pt mesh working electrode, **Figure 2.7**.[126] The working compartment was a 1 cm quartz cuvette and contained the working electrode, Ag/AgCl (3 M $NaCl_{(aq)}$) reference electrode, Ar gas inlet, 0.1 M Bu_4NPF_6 supporting electrolyte in CH_3CN, and the analyte. A constant potential was applied to the cell with Ar bubbling for deoxygenation and stirring lifted out of solution to blanket when changes in the electronic absorption spectrum were recorded.

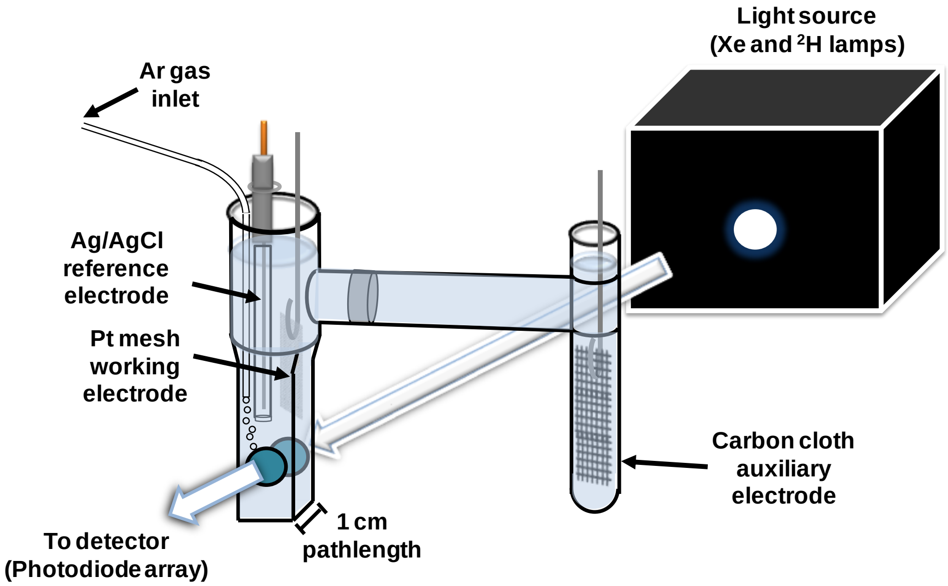

Figure 2.7: Schematic showing the two-compartment H-cell for spectroelectrochemical analysis using a carbon cloth auxiliary electrode, Pt mesh working electrode and Ag/AgCl (3 M $NaCl_{(aq)}$) reference electrode in 0.1 M Bu_4NPF_6 in CH_3CN under an Ar atmosphere.

2.2.5. Steady-State Luminescence Spectroscopy

Steady-state luminescence spectra were collected using a customized Quanta Master Model QM-200-45E fluorimeter from Photon Technologies International, Inc. The excitation source was a water-cooled 150 W Xenon arc lamp with the corresponding emission collected at a 90° angle using a thermoelectrically cooled Hamamatsu 1527 photomultiplier tube operating in photon counting mode with 0.25 nm resolution. The emission monochromator contained a Czerny-Turner style grating monochromator set to 1200 line/mm 750 nm blaze. The instrumental schematic is shown in **Figure 2.8**. The room temperature emission spectra were measured in deoxygenated solvents using a 1 cm path length quartz cuvette equipped with a screw top (Starna Cells, Inc.; Atascadero, CA, USA). The 77 K emission measurements were obtained using a 4:1 EtOH/MeOH solution in a glass tube submerged in a quartz finger dewar containing liquid N_2 to form a rigid glass matrix. **Figure 2.9** shows the emission profile correcting for PMT response.

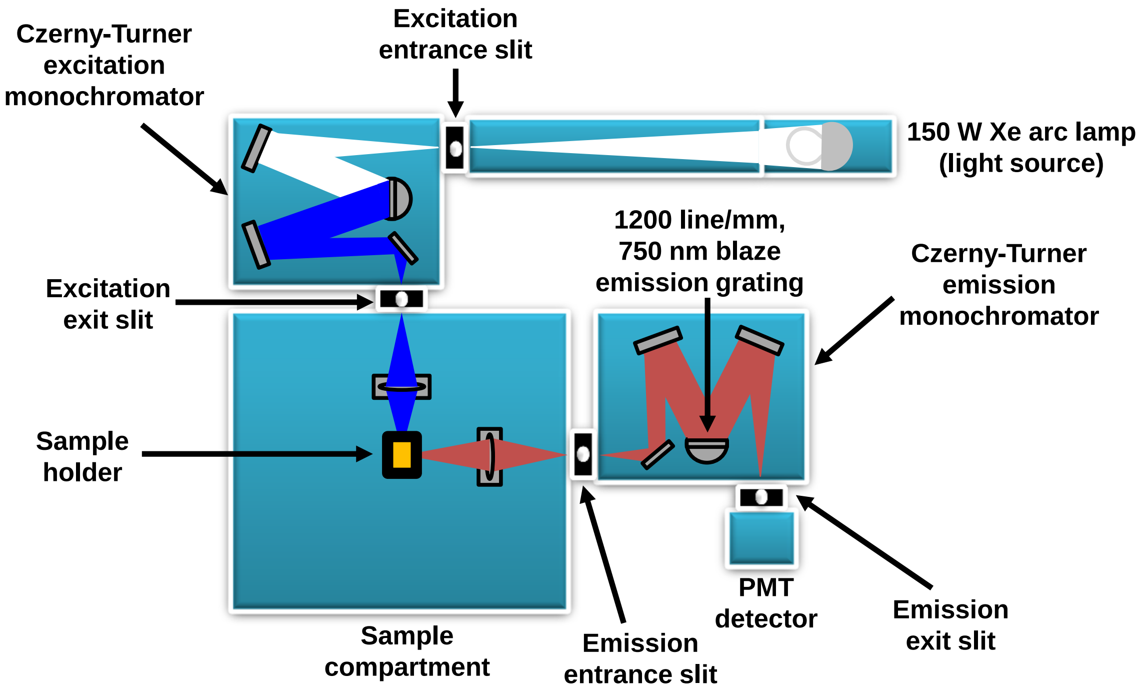

Figure 2.8: Schematic displaying the experimental set-up for steady-state luminescence spectroscopy. Example shown depicts excitation of a $[(TL)_2Ru(dpp)]^{2+}$ monometallic (TL = bpy, phen, or Ph_2phen) using blue light (470 nm) and emission of red light at 90° of the incident light. bpy = 2,2′-bipyridine; phen = 1,10-phenanthroline; Ph_2phen = 4,7-diphenyl-1,10-phenanthroline; dpp = 2,3-bis(2-pyridyl)pyrazine.

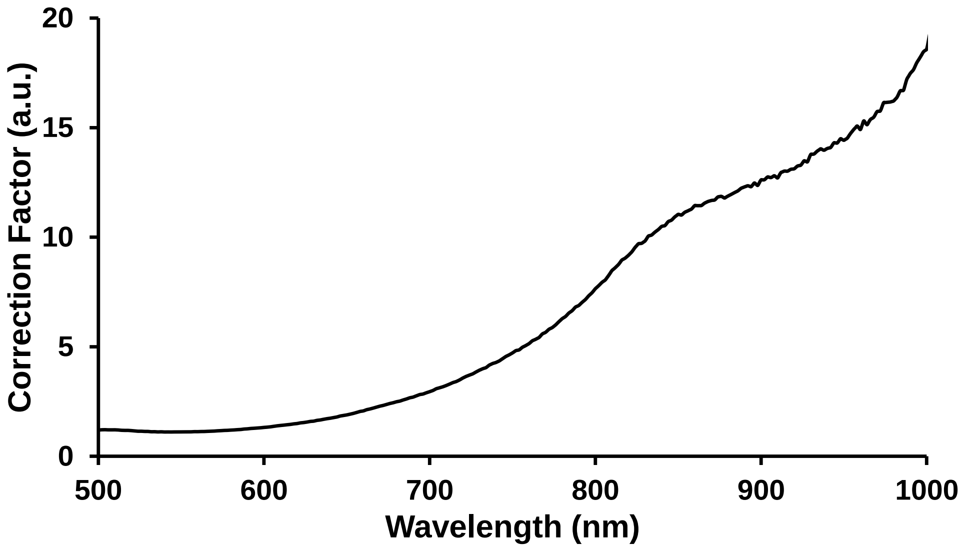

Figure 2.9: Graph containing the emission correction file for the Hamamatsu 1527 photomultiplier tube.

The quantum yield of emission (Φ^{em}) was measured using a customized Quanta Master Model QM-200-45E fluorimeter from Photon Technologies International, Inc. by absorbance matching the samples (absorbance = 0.30) with the reference compound $[Os(bpy)_3]^{2+}$ ($\Phi^{em} = 4.62 \times 10^{-3}$) at the wavelength of excitation.[75] **Equation 2.2** below was used to calculated Φ^{em}

$$\Phi_{samp}^{em} = \Phi_{ref}^{em} x \frac{Area_{samp}}{Area_{ref}} x \frac{Abs_{ref}}{Abs_{samp}} \qquad \text{eq. 2.2}$$

where Φ_{samp}^{em} is the quantum yield of emission for the sample, Φ_{ref}^{em} is the quantum yield of emission for the reference compound, $Area_{samp}$ is the area under the curve from the sample's emission profile, $Area_{ref}$ is the area under the curve from the reference compound's emission profile, Abs_{ref} is the absorbance of the reference compound at the wavelength of excitation obtained from the electronic absorption spectrum, and Abs_{samp} is the absorbance of the sample at the wavelength of excitation obtained from the electronic absorption spectrum. Reference and sample compounds were deoxygenated by bubbling Ar through the prepared solution in a 1 cm quartz cuvette for 15-20 min prior to analysis. **Figure 2.10** displays the emission profile for $[Os(bpy)_3](PF_6)_2$ excited at 540 nm, measured at room temperature in deoxygenated acetonitrile, and corrected for PMT response.

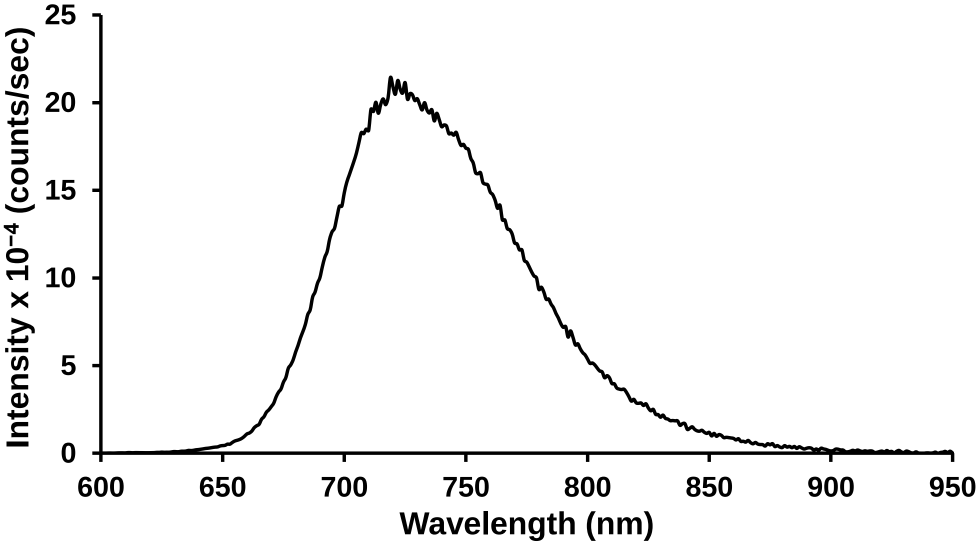

Figure 2.10: Emission profile for the reference compound $[Os(bpy)_3](PF_6)_2$ excited at 540 nm (absorbance = 0.30), measured at room temperature in CH_3CN using a 1 cm quartz cuvette, and corrected for PMT response. Excitation and emission monochromator compartment entrance and exit slit widths set to 1.5 mm (corresponds to ± 6 nm). bpy = 2,2′-bipyridine.

2.2.6. Time-Resolved Luminescence Spectroscopy

Time-resolved luminescence studies were performed using a Photon Technologies International, Inc. PL-2300 N_2 laser with an attached PL-201 tunable dye laser as the excitation source. The dye used was Coumarin 500 and the excitation monochromator was set to 470 nm for the monometallic complexes and 520 nm for the bimetallic and trimetallic complexes. Emission was detected at a 90° angle from the excitation source after passing through an emission monochromator set to the maximum wavelength obtained from the steady-state luminescence spectrum using a Hamamatsu R928 photomultiplier tube (PMT) operating in direct analog mode, which terminated into a resistor in the oscilloscope. The signal was recorded using a LeCroy 9361 oscilloscope which averaged the results of 300 sweeps. The 77 K excited state lifetime measurements were obtained using a 4:1 ethanol/methanol solution in a glass tube submerged in a finger dewar containing liquid N_2 to form a rigid glass matrix. **Figure 2.11** displays the experimental set-up for the time-resolved luminescence experiments.

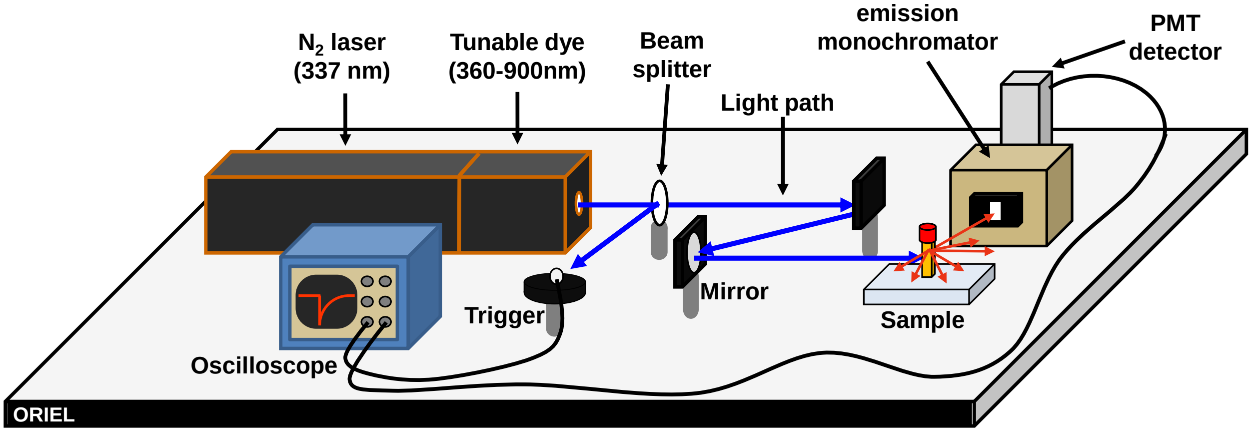

Figure 2.11: Schematic displaying the experimental set-up for time-resolved luminescence spectroscopy. Example shown depicts excitation of a $[(TL)_2Ru(dpp)]^{2+}$ monometallic (TL = bpy, phen, or Ph_2phen) using blue light (470 nm) and emission of red light at 90° of the incident light. bpy = 2,2′-bipyridine; phen = 1,10-phenanthroline; Ph_2phen = 4,7-diphenyl-1,10-phenanthroline; dpp = 2,3-bis(2-pyridyl)pyrazine.

The lifetime of the emissive excited state was measured using a PL-2300 N_2 laser with an attached PL-201 tunable dye compartment from Photon Technologies International, Inc. Samples with an absorbance between 0.10-0.30 were deoxygenated by bubbling Ar through the prepared solution in a 1 cm quartz cuvette for 15-20 min prior to analysis. The excited state decay of the complexes was fit to an exponential (**Equation 2.3**) decay curve

$$I(t) = \sum_i \alpha_i \, e^{\frac{-t}{\tau_i}} \qquad \text{eq. 2.3}$$

where $I(t)$ is the signal intensity at time *t* after the laser pulse, $\sum_i \alpha_i$ is the sum of fractions each decay component contributes to the overall observed decay curve, *i* is an integer number, and τ_i is the excited state lifetime of each component. The intensity, measured as a potential (V), is graphed as a function of time, whereby applying the ln function to **Equation 2.3** generates **Equation 2.4**. From this equation, the excited state lifetime of the compound (τ_i) is obtained from the slope of the line. **Figure 2.12** shows the I vs. t and ln(I) vs. t decay plots for $[\{(bpy)_2Ru\}_2(dpp)](PF_6)_4$ with $\tau_{^3MLCT}$ = 140 ns.[67] The slope of the line for the ln(I) vs. t decay plot was measured from t = 0 ns to t = 600 ns after the laser pulse.

$$\ln\big(I(t)\big) = -\frac{t}{\tau_i} + \ln(\alpha_i) \qquad \text{eq. 2.4}$$

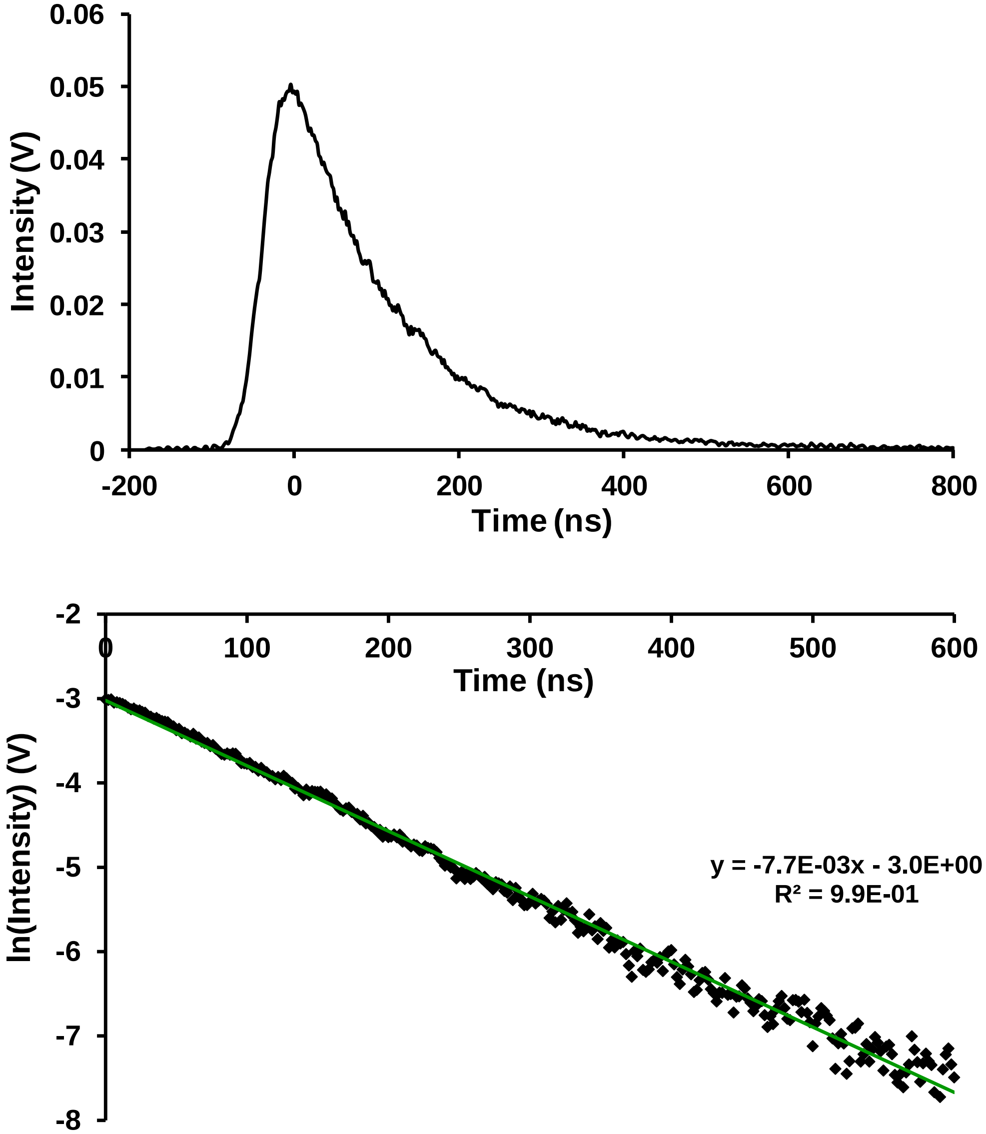

Figure 2.12: Time-resolved luminescence profiles depicting intensity vs. time (top) and ln(intensity) vs. time (bottom) for $[\{(bpy)_2Ru\}_2(dpp)](PF_6)_4$ excited at 540 nm and emission monitored at 750 nm in deoxygenated CH_3CN. Emission monochromator compartment entrance and exit slit widths set to 1.0 mm (corresponds to ± 4 nm). The slope of the decay curve provides a measured excited state lifetime of 140 ns, in good agreement with cited reference values.[67] bpy = 2,2′-bipyridine; dpp = 2,3-bis(2-pyridyl)pyrazine.

2.2.7. Excited State Reductive Quenching

Luminescence quenching from the emissive excited state was probed using a modified Quanta Master Model QM-200-45E fluorimeter from Photon Technologies International, Inc. Stock solutions of the complexes and the sacrificial electron donor DMA were prepared separately in spectral grade acetonitrile and deoxygenated. Sample solutions were composed of a fixed final concentration of complex (~30 μM) in a 1 cm quartz cuvette with increasing final concentrations of DMA (0-2.4 x 10^{-2} M) added to a new sample. DMA was injected into the sample in the dark using a syringe just prior to excitation from the 150 W Xe arc lamp light source. The steady-state emission spectrum for each sample was obtained and a Stern-Volmer plot of I_0/I vs. [DMA] was plotted (I_0 = emission intensity in the absence of DMA; I = emission intensity in the presence of DMA).[121] **Equations 2.5-2.7** depict this relationship

$$\frac{I_0}{I} = 1 + K_{SV}[DMA] \qquad \text{eq. 2.5}$$

$$K_{SV} = k_q \tau_0 \qquad \text{eq. 2.6}$$

$$\frac{I_0}{I} = 1 + \frac{(k_{q1} + k_2)}{(k_1 + k_{et})}[DMA] \qquad \text{eq. 2.7}$$

where K_{SV} is the Stern-Volmer quenching constant, k_q is the bimolecular quenching rate constant, τ_0 is the lifetime of the ^{3}MLCT ES in the absence of DMA, k_{q1} is the ES reductive quenching rate constant, k_2 is the bimolecular deactivation rate constant, k_1 is the summation of radiative (k_r) and non-radiative (k_{nr}) rate constants from the ^{3}MLCT excited state to the ^{1}GS, and k_{et} is the intramolecular electron transfer from ^{3}MLCT to ^{3}MMCT excited state rate constant.

2.2.8. Photochemical Reduction

Photochemical reduction of the trimetallic complexes in the presence of the sacrificial electron donor DMA was observed through spectral shifts in the electronic absorption spectra. Solutions containing CH_3CN, 30 μM complex, and 4.0 x 10^{-3} M DMA were deoxygenated using Ar gas and photolyzed using a 470 nm LED light source. The electronic absorption spectra were recorded using a Hewlett Packard 8452A diode array spectrophotometer (2 nm resolution) and were measured every few seconds to observe changes in the light absorbing properties of the photoreduced species. Small changes in the spectra were omitted with the resulting spectrum showing initial time = 0 seconds to final time = 120 seconds of photolysis.

2.2.9. LED Array

Photolysis studies were performed using two LED arrays constructed in our laboratory, **Figure 2.13**, for small scale and large scale photocatalytic studies.[127,128] The LEDs used were blue Luxeon® V Star LEDs with a spectral coverage of 470 ± 10 nm and a lambertian radiation pattern. For the small scale array, LED power was adjusted using a rheostat built into the array and set to 200 mW using a Scientech, Inc. (Boulder, CO) MC 2501 calorimeter and Mentor Model MA 10 indicator. The flux of each LED was measured using $K_3[Fe(C_2O_4)_3]$ chemical actinometer and the average value was $2.36 \pm 0.05 \times 10^{19}$ photons/min for the small scale LED array, consistent with power meter measurements.[129] For the large scale array, the LED power was not adjustable and the total flux of four LEDs was measured using $K_3[Fe(C_2O_4)_3]$ chemical actinometer and the average value was $6.27 \pm 0.01 \times 10^{19}$ photons/min.[128,129]

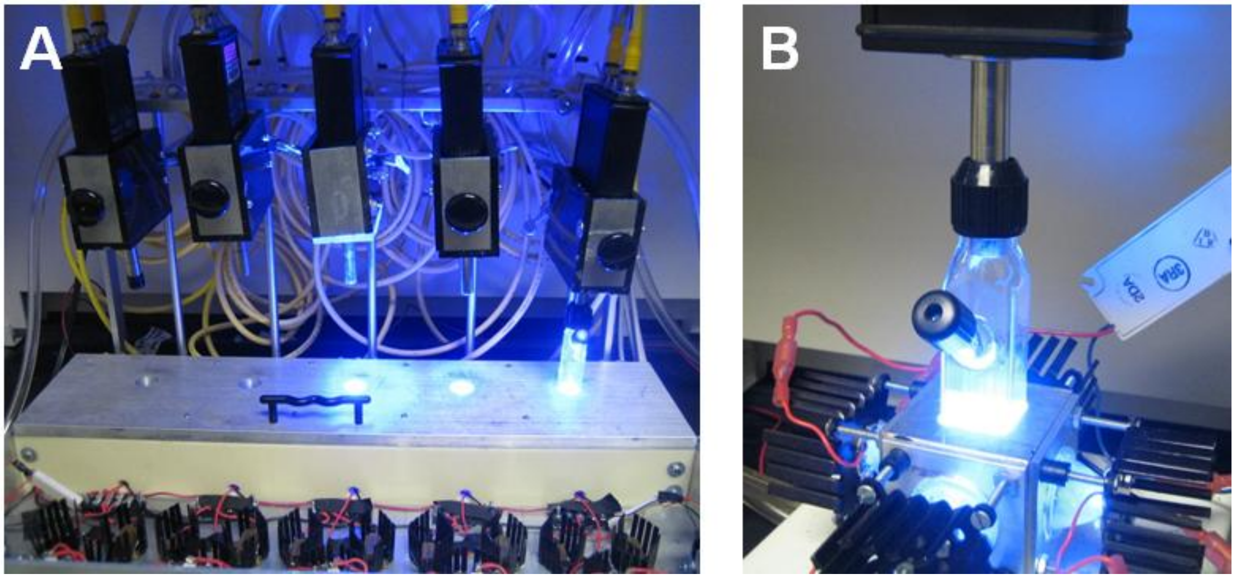

Figure 2.13: (A) Picture of the small scaled LED array used for photocatalytic H_2 production experiments with five $\lambda_{exc} = 470 \pm 10$ nm blue LEDs. Five HY-OPTIMA™ H_2 sensors were used for to permit simultaneous, real-time analysis of multiple samples. (B) Picture of the large scaled LED array used for photocatalytic H_2 production experiments with four $\lambda_{exc} = 470 \pm 10$ nm blue LEDs surrounding one photolysis reaction cell.

2.2.10. H_2 Sensors

The quantity of H_2 produced was monitored in real-time using HY-OPTIMA^{TM} 700 Process Hydrogen Analyzer solid state sensors from H2scan (Valencia, CA, USA) connected to the photolysis reaction cells, **Figure 2.14**. The sensors contained factory calibrated H_2 values that were preset to a voltage or current analog output that was converted to a digital output for RS232 serial COM connector compatibility. Multiple sensors were used simultaneously by connection to a USB-8COMi-RM data communication serial port (Vision Systems; Norderstedt, Germany) to allow interface of multiple sensors to the computer. To ensure proper functioning of the sensors, calibration curves for H_2 sensitivity were generated by injecting known quantities of H_2 gas into the reaction cells connected to the sensors. The sensors are functional from 0.1% to 100% H_2 by volume at 1 atm with 2-3% relative error for each measurement.

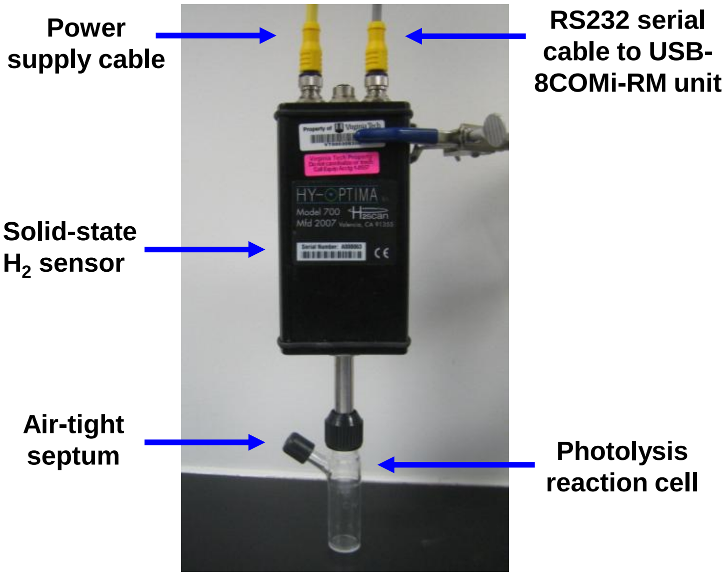

Figure 2.14: Picture of a HY-OPTIMA^{TM} 700 Process Hydrogen Analyzer connected to a photolysis reaction cell used for photocatalytic H_2 production experiments.

2.2.11. Gas Chromatography

A series 580 GOW-MAC gas chromatograph equipped with a rhenium-tungsten thermal conductivity detector and a 5 Å molecular sieves column using ultra-high purity argon as the carrier gas was used to qualitatively or quantitatively analyze the reaction cell headspace. A 100 μL sample from the reaction cell headspace was injected into the gas chromatograph using an air tight syringe. The gas chromatograph signal was amplified with a Vernier Software instrument amplifier and recorded using Logger Pro 3.4.5 software. The gas chromatograph was calibrated for H_2 signal sensitivity by injecting known amounts of H_2 gas and generating a calibration curve.

2.2.12. Photocatalytic H_2 Production Experiments

The photocatalytic H_2 production experiments were performed using modifications of previously reported conditions.[112,128] Photolysis reaction cells were connected to the solid-state H_2 sensors on the LED array and 10 mm air tight septa were attached. The cells were deoxygenated for 30 minutes using Ar gas prior to turning on the sensors. After the sensors were turned on and allowed to warm-up for 15 minutes, 5% of H_2 by reaction cell volume (1 mL for small scale reaction cell; 2.5 mL for large scale reaction cell) was injected into the reaction cells using an air tight syringe to initiate the solid-state H_2 sensors. The cells were then deoxygenated for 30 minutes to remove H_2, as determined by the sensor reading. Stock solutions of the sample complex in the appropriate solvent and H_2O acidified to pH 2 using CF_3SO_3H were injected into the photolysis cells. The cells were deoxygenated for 15 minutes while a vial containing the sacrificial electron donor was deoxygenated separately. The electron donor was injected into the reaction cells just prior to photolysis. The cells were covered with aluminum foil to prevent stray light from the laboratory. Small scale photocatalytic H_2 production experiments utilized photolysis reaction cells that were photolyzed from the bottom using one 470 nm LED as the light source with a light flux = $2.36 \pm 0.05 \times 10^{19}$ photons/min.[127,129] Large scale experiments utilized photolysis reactions cells that were photolyzed from the sides using four 470 nm LEDs as the light source with a light flux = $6.27 \pm 0.01 \times 10^{17}$ photons/min.[128] The resulting % H_2 in the head space was monitored in real-time using the MOXA Pcomm Lite terminal emulator software and converted to volume and moles of H_2 produced. The turnover number (TON) at time *t* corresponding to the amount of H_2 produced per Rh catalytic center, the quantum efficiency of H_2 formation (Φ_{H_2}) at time *t*, and the instantaneous quantum efficiency of H_2 formation (instantaneous Φ_{H_2}) at time *t* were calculated using **Equations 2.8-2.10**

$$TON(t) = \frac{moles\ of\ H_2\ produced}{moles\ of\ Rh\ catalytic\ centers} \qquad \text{eq. 2.8}$$

$$\Phi_{\mathrm{H_2}}(t) = \frac{moles\ of\ H_2\ produced}{moles\ of\ photons} \times 2 \qquad \text{eq. 2.9}$$

$$\text{Instantaneous } \Phi_{\mathrm{H_2}}(t_1) = \frac{moles\ of\ H_2\ produced(t_2 - t_1)}{moles\ of\ photons(t_2 - t_1)} \times 2 \qquad \text{eq. 2.10}$$

The values in **Equations 2.9** and **2.10** are multiplied by two as two photons are required per one mole of H_2 formed.

3. Results and Discussion

3.1. Design and Synthetic Approach

The mixed-metal supramolecular complexes were designed to contain a Ru(II)-polypyridyl light absorber that is covalently coupled to a *cis*-$Rh^{III}X_2$ electron collecting site through a polyazine bridging ligand.[83,92,93,98,130,131] The choice of molecular components throughout the building process dictates the observed properties of the final product. Systems designed were expected to possess Rh(dσ*) LUMOs capable of photoinitiated electron collection and catalysis of H_2O reduction to H_2. Synthesis of mixed-metal supramolecular complexes was achieved using a building block approach to couple individual molecular components, **Figure 3.1**.[59,62] Synthetic schemes for the synthesis of $[\{(Ph_2phen)_2Ru(dpp)\}_2RhCl_2](PF_6)_5$ and $[(Ph_2phen)_2Ru(dpp)RhCl_2(^tBu_2bpy)](PF_6)_3$ are shown in **Figures 3.3** and **3.4** (*vide infra*). This methodology permits purification at each synthetic step to prevent unwanted impurities in the target complex, as well as product characterization of each step in the reaction scheme to obtain a better understanding of the properties contributing to the overall supramolecular complex.

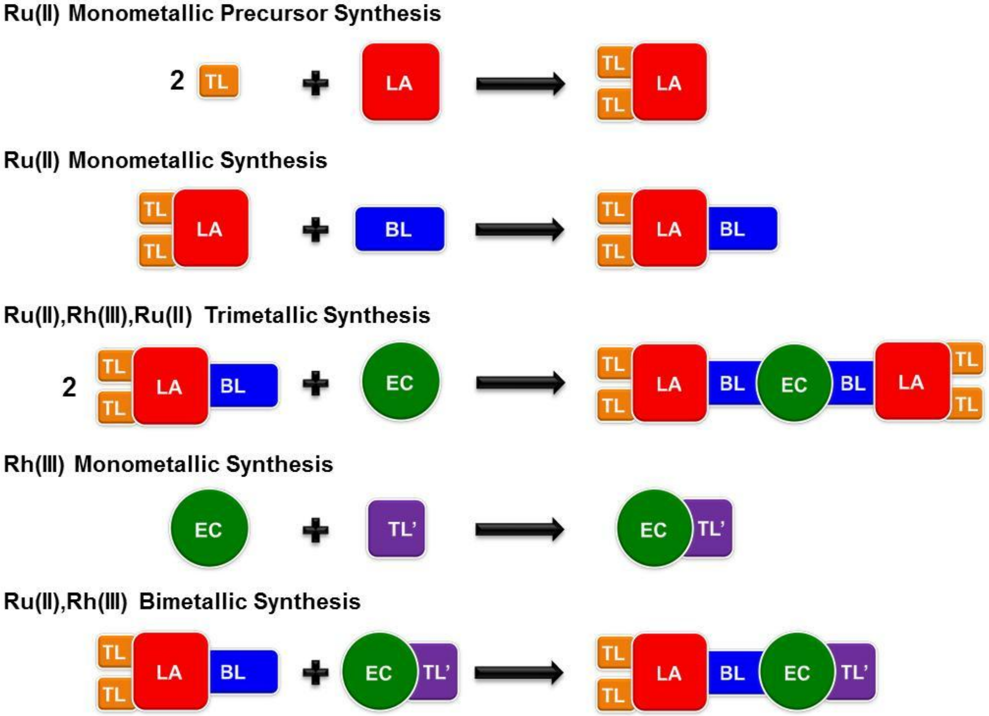

Figure 3.1: Generalized scheme depicting the building block approach for synthesis of Ru(II),Rh(III),Ru(II) trimetallic and Ru(II),Rh(III) bimetallic supramolecular complexes. TL/TL′ = terminal ligand; LA = light absorber; BL = bridging ligand; EC = electron collector.

Synthesis of a typical mixed-metal Ru(II),Rh(III) supramolecular complex begins with synthesis of the Ru(II)-based LA moiety, $[(TL)_2RuCl_2]$ (TL = bpy, phen, or Ph_2phen).[115,116] The identity of the TL affects the light absorbing capabilities of the final target complex and finely tunes the Ru(dπ) orbital energetics. The second step involves coordination of the dpp polyazine BL to produce Ru(II) monometallic complexes, $[(TL)_2Ru(dpp)]^{2+}$ (TL = bpy, phen, or Ph_2phen), that allow for extension of the supramolecular architecture to incorporate multiple metal centers.[55,59,61] The low-lying, unoccupied π* molecular orbitals located on dpp shifts the LUMO from TL to BL and establishes the lowest energy allowed electronic transition as Ru(dπ)→dpp(π*) ^{1}MLCT and lowest energy electronic ES as Ru(dπ)→dpp(π*) ^{3}MLCT. For synthesis of Ru(II),Rh(III),Ru(II) trimetallic complexes of the architecture $[\{(TL)_2Ru(dpp)\}_2RhX_2]^{5+}$ (TL = phen or Ph_2phen; X = Cl^- or Br^-), the final step couples two $[(TL)_2Ru(dpp)]^{2+}$ LAs to a *cis*-dihalide rhodium(III) electron collecting, reactive metal center.[98,131] This step introduces lowest-lying Rh(III)-based dσ* orbitals, establishing this as the site of electron collection within the supramolecular architecture. Synthesis of Ru(II),Rh(III) bimetallic complexes of the architecture $[(TL)_2Ru(dpp)RhCl_2(TL')]^{3+}$ (TL = bpy or Ph_2phen; TL′ = $^tBu_2$bpy or Ph_2phen) is more challenging due to the tendency of $RhX_3 \cdot nH_2O$ starting materials to produce *cis*-$[Rh(NN)_2X_2]^+$ (NN = diimine ligand) when diimine TLs are employed. Bimetallic formation requires synthesis of the Rh(III) monometallic subunit $[RhCl_3(TL')(CH_3OH)]$ by coordinating a single TL′ to the Rh(III) metal center.[118,132] Electron-donating or withdrawing properties of the TL′ energetically modulates the Rh(dσ*) orbital set. The final step for Ru(II),Rh(III) bimetallic synthesis is the coupling of the $[(TL)_2Ru(dpp)]^{2+}$ LA and $[RhCl_3(TL')(CH_3OH)]$ EC subunits.[83] **Figure 3.2** displays the systematic variation of molecular components within the supramolecular architecture to provide insight into individual component contributions to the overall properties of the complex.

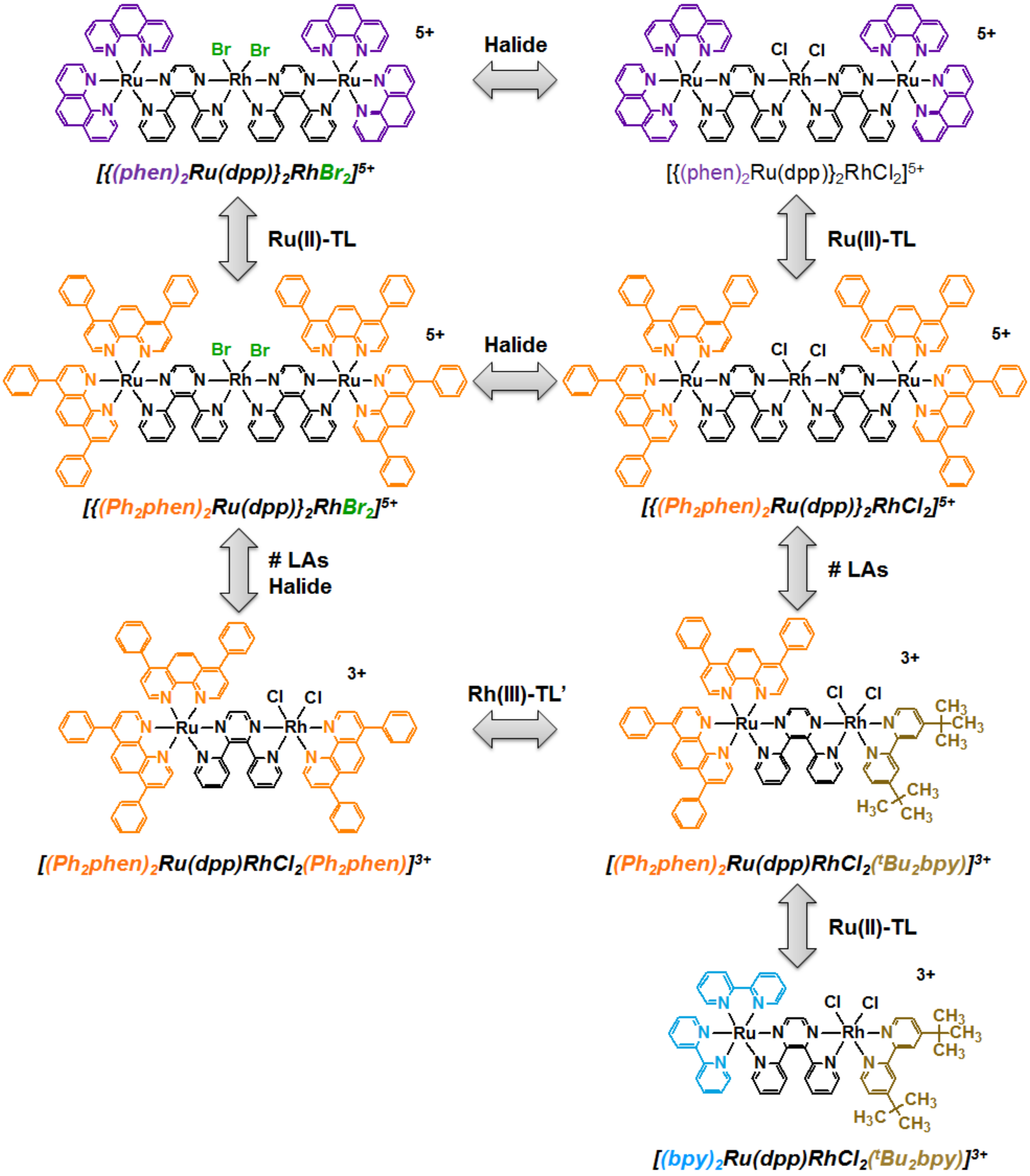

Figure 3.2: Systematic variation of molecular components within polyazine-bridged Ru(II),Rh(III) supramolecular complexes. TL/TL′ = terminal ligand; LA = light absorber; bpy = 2,2′-bipyridine; ^{t}Bu$_2$bpy = 4,4′-Di-*tert*-butyl-2,2′-bipyridine; phen = 1,10-phenanthroline; Ph$_2$phen = 4,7-diphenyl-1,10-phenanthroline; dpp = 2,3-bis(2-pyridyl)pyrazine. Newly synthesized complexes are designated by italicized, bold font.

3.1.1. Ru(II) Monometallics

Synthesis of the Ru(II) monometallic complexes, $[(bpy)_2Ru(dpp)](PF_6)_2$, $[(phen)_2Ru(dpp)](PF_6)_2$ and $[(Ph_2phen)_2Ru(dpp)](PF_6)_2$ (bpy = 2,2′-bipyridine; phen = 1,10-phenanthroline; Ph_2phen = 4,7-diphenyl-1,10-phenanthroline; dpp = 2,3-bis(2-pyridyl)pyrazine), require a two-step synthetic method with the Ru(II) monometallic precursors, $[(bpy)_2RuCl_2]$ (which was purchased), $[(phen)_2RuCl_2]$, or $[(Ph_2phen)_2RuCl_2]$, being synthesized prior to coordination of the bis-bidentate, polypyridyl BL dpp. The Ru(II) monometallic precursors were synthesized as previously reported, with minor modifications to the synthetic method, by heating at reflux $RuCl_3{\cdot}3H_2O$, TL and excess LiCl (1:2:15 molar ratio) in DMF for 6 h.[115,116] DMF was used as the solvent system due to its high boiling point and ability to serve as the reducing agent in the reduction of the Ru(III) starting material to the desired Ru(II) final product. Excess LiCl was used to minimize formation of $[Ru(TL)_3]Cl_2$. The reaction solution was cooled to RT and added to an equivalent volume of acetone and placed in the refrigerator overnight to induce precipitation. The dark purple sample was added to saturated LiCl (aq) to induce precipitation and assist in the removal of the DMF solvent and unwanted $[Ru(TL)_3]Cl_2$ impurity. Vacuum filtration followed by several washes with H_2O yields the crude product as a dark purple solid. Further purification to provide a high level of purity with respect to the highly emissive $[Ru(TL)_3]^{2+}$ is required to allow detection of the typical ca. 10^{-4} Φ^{em} of the final Ru(II),Rh(III) bimetallic and Ru(II),Rh(III),Ru(II) trimetallic products. The $[(TL)_2RuCl_2]$ crude product was purified by adsorption column chromatography using methanol-deactivated alumina as the stationary phase and CH_2Cl_2/acetone (4:1 volume ratio) as the mobile phase. The purple band containing the desired product eluted prior to the orange $[Ru(TL)_3]Cl_2$ impurity. The product was collected by dissolution in minimal CH_2Cl_2 and precipitation by addition to diethyl ether, followed by vacuum filtration to obtain a dark purple product. A typical yield for this reaction is 40% due to the necessity to remove even trace amounts of the highly emissive $[Ru(TL)_3]Cl_2$ impurity.

The target Ru(II) monometallic complexes, $[(bpy)_2Ru(dpp)](PF_6)_2$, $[(phen)_2Ru(dpp)](PF_6)_2$, and $[(Ph_2phen)_2Ru(dpp)](PF_6)_2$, were synthesized with minor modifications to previously reported methods.[55,59,61,68] The two reactants, $[(TL)_2RuCl_2]$ and dpp BL (1:2 molar ratio), were heated at reflux in a EtOH/H_2O (2:1 volume ratio) solvent system for 3 h. Excess dpp was used to minimize formation of the undesired Ru(II),Ru(II) homobimetallic complex, $[\{(TL)_2Ru\}_2(dpp)]^{4+}$. The dark orange reaction mixture was cooled to RT and added to NH_4PF_6 (aq) to induce precipitation as a PF_6^- salt. The orange solid was collected by vacuum filtration, washed with H_2O, and dried with diethyl ether. The Ru(II) monometallic complexes were purified by adsorption column chromatography using methanol-deactivated alumina in a CH_3CN/toluene (2:3 volume ratio) solvent system. Excess dpp BL eluted from the column as a pale yellow-orange band prior to the desired dark orange band containing $[(TL)_2Ru(dpp)]^{2+}$. The purple band containing unwanted $[\{(TL)_2Ru\}_2(dpp)]^{4+}$ remained at the top of the column and was discarded. The dark orange band was collected and the solvent volume reduced by rotary evaporation. The purified product was dissolved in minimal CH_3CN, precipitated into diethyl ether, and vacuum filtered to dryness to provide an orange solid. A typical yield for this reaction is 50% due to losses of desired product throughout the purification steps.

3.1.2. Rh(III) Monometallics

The newly synthesized Rh(III) monometallic complexes, $[RhCl_3(^tBu_2bpy)(CH_3OH)]$ and $[RhCl_3(Ph_2phen)(CH_3OH)]$, were synthesized following a procedure for $[RhCl_3(bpy)(CH_3OH)]$ which coordinates a single bidentate polypyridyl TL to a Rh(III) metal center.[118,132] The first step requires that $RhCl_3{\cdot}3H_2O$ and TL′ (1:1 molar ratio) be dissolved separately in a CH_2Cl_2/CH_3OH (1:1 volume ratio) solvent system. Both solutions were heated gently to ensure dissolution, followed by the TL′ solution being added drop-wise to the stirring, dark red $RhCl_3{\cdot}3H_2O$ solution to minimize formation of the $[Rh(TL')_2Cl_2]Cl$ unwanted impurity. The resultant mixture was then heated at reflux for 2 h. After cooling to RT, the reaction solution was filtered, washed with methanol, and the pale-yellow filtrate collected. The filtrate solvent volume was reduced by rotary evaporation. The product was reprecipitated by dissolving in minimal MeOH and adding drop-wise to stirring diethyl ether. To ensure removal of any unreacted $RhCl_3$ starting material, the product was washed with H_2O and dried using diethyl ether. A typical yield for this reaction is 30% due to the high propensity of diimine ligands to produce *cis*-$[Rh(NN)_2Cl_2]^+$ (NN = diimine ligand).

3.1.3. Ru(II),Rh(III),Ru(II) Trimetallics

The previously reported Ru(II),Rh(III),Ru(II) trimetallic $[\{(phen)_2Ru(dpp)\}_2RhCl_2](PF_6)_5$, as well as the newly reported trimetallics, $[\{(phen)_2Ru(dpp)\}_2RhBr_2](PF_6)_5$,

$[\{(Ph_2phen)_2Ru(dpp)\}_2RhCl_2](PF_6)_5$ and $[\{(Ph_2phen)_2Ru(dpp)\}_2RhBr_2](PF_6)_5$, were synthesized by modifications to previously reported synthetic methods.[93,99,100] **Figure 3.3** displays the synthetic scheme for preparation of $[\{(Ph_2phen)_2Ru(dpp)\}_2RhBr_2](PF_6)_5$. The trimetallics were synthesized by heating at reflux $RhX_3{\cdot}3H_2O$ and $[(TL)_2Ru(dpp)](PF_6)_2$ (1:1.6 molar ratio) in a EtOH/H_2O (2:1 volume ratio) solvent system for 1-2 h. Attempts to increase the molar ratio of the reactions to include 1 Rh to 2 LA proved to only generate more unreacted $[(TL)_2Ru(dpp)](PF_6)_2$. Elongating the reaction time also served to be unbeneficial as excess Ru(II) monometallic was still present. After 1-2 h, the reaction was allowed to cool to RT before added to NH_4PF_6 (aq) to induce precipitation as a PF_6^- salt. The dark purple or maroon precipitate was collected by vacuum filtration, washed with H_2O, and dried using diethyl ether.

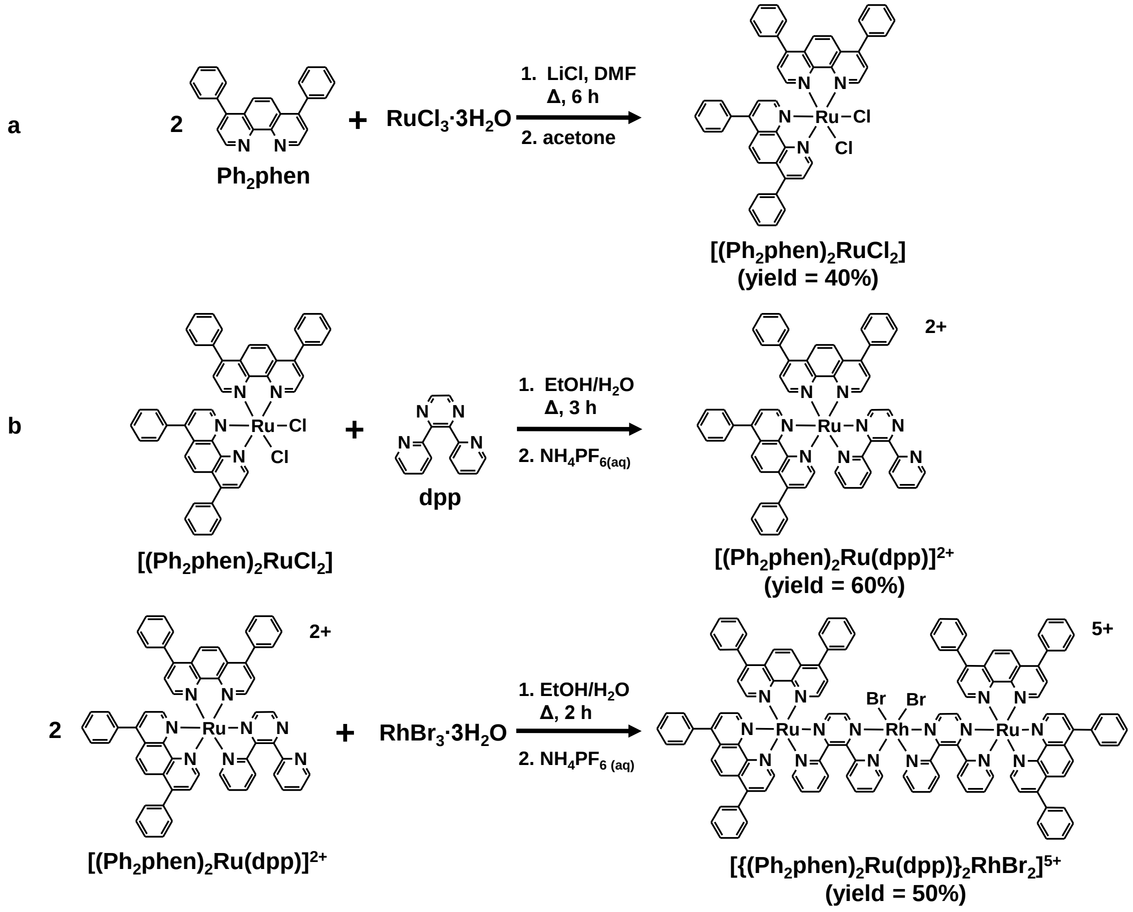

Figure 3.3: Synthetic scheme for the Ru(II),Rh(III),Ru(II) trimetallic supramolecular complex $[\{(Ph_2phen)_2Ru(dpp)\}_2RhBr_2](PF_6)_5$. [a] Reference [116]. [b] Reference [55]. Ph_2phen = 4,7-diphenyl-1,10-phenanthroline; dpp = 2,3-bis(2-pyridyl)pyrazine.

Purification methods used for the Ru(II),Rh(III),Ru(II) trimetallic complexes depended on the identity of the TL attached. For the trimetallic complexes $[\{(phen)_2Ru(dpp)\}_2RhCl_2](PF_6)_5$ and $[\{(phen)_2Ru(dpp)\}_2RhBr_2](PF_6)_5$, CH_2Cl_2 was added to the samples while still in the glass frits used for vacuum filtration. The unreacted $[(phen)_2Ru(dpp)](PF_6)_2$ monometallic impurity is highly soluble in CH_2Cl_2, while the target TL = phen trimetallic complexes are only sparingly soluble in CH_2Cl_2. Prior purification methods for these trimetallic complexes required several hot EtOH reprecipitations which proved to be time consuming (several hours each) and produce lower yields (< 25%), due to the slight solubility of trimetallics in EtOH, when aiming for spectroscopically pure Ru(II),Rh(III),Ru(II) trimetallic samples free of unreacted Ru(II) monometallic. This CH_2Cl_2 purification technique reduced the synthesis and purification time from requiring multiple days to requiring less than 5 h. Typical yield for this reaction is 40% due to the need for removal of trace $[(phen)_2Ru(dpp)](PF_6)_2$ ($\Phi^{em} \approx 10^{-2}$) to allow accurate emission analysis of the typical $\Phi^{em} \approx 10^{-4}$ of these products.

The $[\{(Ph_2phen)_2Ru(dpp)\}_2RhCl_2](PF_6)_5$ and $[\{(Ph_2phen)_2Ru(dpp)\}_2RhBr_2](PF_6)_5$ trimetallic complexes are easily dissolved into CH_2Cl_2, preventing this method for purification of TL = Ph_2phen trimetallics. As mentioned above, a common issue with the hot EtOH reprecipitations was the high propensity to generate a low yield of a spectroscopically pure product following purification steps. This warranted the use of a different hot solvent reprecipitation method. The TL = Ph_2phen trimetallics were dissolved in minimal CH_3CN and added to hot toluene while stirring. The $[(Ph_2phen)_2Ru(dpp)](PF_6)_2$ present in the product is more soluble in hot toluene than the target $[\{(Ph_2phen)_2Ru(dpp)\}_2RhCl_2](PF_6)_5$ and $[\{(Ph_2phen)_2Ru(dpp)\}_2RhBr_2](PF_6)_5$ trimetallic complexes. Continued heating removes the CH_3CN from the solvent mixture, forcing the TL = Ph_2phen trimetallics to precipitate out of solution and leave the unwanted $[(Ph_2phen)_2Ru(dpp)](PF_6)_2$ in the warm toluene. Filtration of the sample while warm prevents monometallic from precipitating out of solution, yielding the desired Ru(II),Rh(III),Ru(II) trimetallic product. The solid was collected and reprecipitated by dissolving in minimal CH_3CN and adding drop-wise to diethyl ether. The precipitate was vacuum filtered and rinsed with diethyl ether to yield a dark maroon solid. Typical yield for this reaction is 35% due to the need for removal of trace $[(Ph_2phen)_2Ru(dpp)](PF_6)_2$ ($\Phi^{em} \approx 10^{-2}$) to allow accurate emission analysis of the typical $\Phi^{em} \approx 10^{-4}$ of these products.

3.1.4. Ru(II),Rh(III) Bimetallics

The Ru(II),Rh(III) bimetallic complexes, $[(bpy)_2Ru(dpp)RhCl_2(^tBu_2bpy)](PF_6)_3$, $[(Ph_2phen)_2Ru(dpp)RhCl_2(^tBu_2bpy)](PF_6)_3$, and $[(Ph_2phen)_2Ru(dpp)RhCl_2(Ph_2phen)](PF_6)_3$, were synthesized (with assistance from Brittany N. Whitaker) by minor modifications to a previously reported synthetic method.[83] Synthesis of these complexes was more difficult as Rh(III) monometallics had to be synthesized prior to coordination to the Ru(II) monometallic unit. This synthetic step involves the covalent coupling of the synthesized Ru(II) monometallic component $[(TL)_2Ru(dpp)](PF_6)_2$ and Rh(III) monometallic component $[RhCl_3(TL')(CH_3OH)]$. **Figure 3.4** displays the synthetic scheme for preparation of $[(Ph_2phen)_2Ru(dpp)RhCl_2(^tBu_2bpy)](PF_6)_3$. The Ru(II) monometallic and Rh(III) monometallic (1:1.2 molar ratio) components were dissolved separately in a EtOH/H_2O solvent system (2:1 volume ratio) by gently warming. Upon dissolution of both components, the orange Ru(II) monometallic solution was added drop-wise to the stirring yellow Rh(III) monometallic solution and the temperature was increased to allow the reaction to heat at reflux for 1 h. After 10-15 min, the reaction color changed from orange to dark purple (TL = bpy) or dark maroon (TL = Ph_2phen). The reaction was cooled to RT and added drop-wise to an aqueous NH_4PF_6 solution to induce precipitation as a PF_6^- salt. The resulting precipitate was vacuum filtered, washed with H_2O, and dried with diethyl ether to yield a dark purple solid for $[(bpy)_2Ru(dpp)RhCl_2(^tBu_2bpy)](PF_6)_3$ or a dark maroon solid for $[(Ph_2phen)_2Ru(dpp)RhCl_2(^tBu_2bpy)](PF_6)_3$ and $[(Ph_2phen)_2Ru(dpp)RhCl_2(Ph_2phen)](PF_6)_3$ complexes.

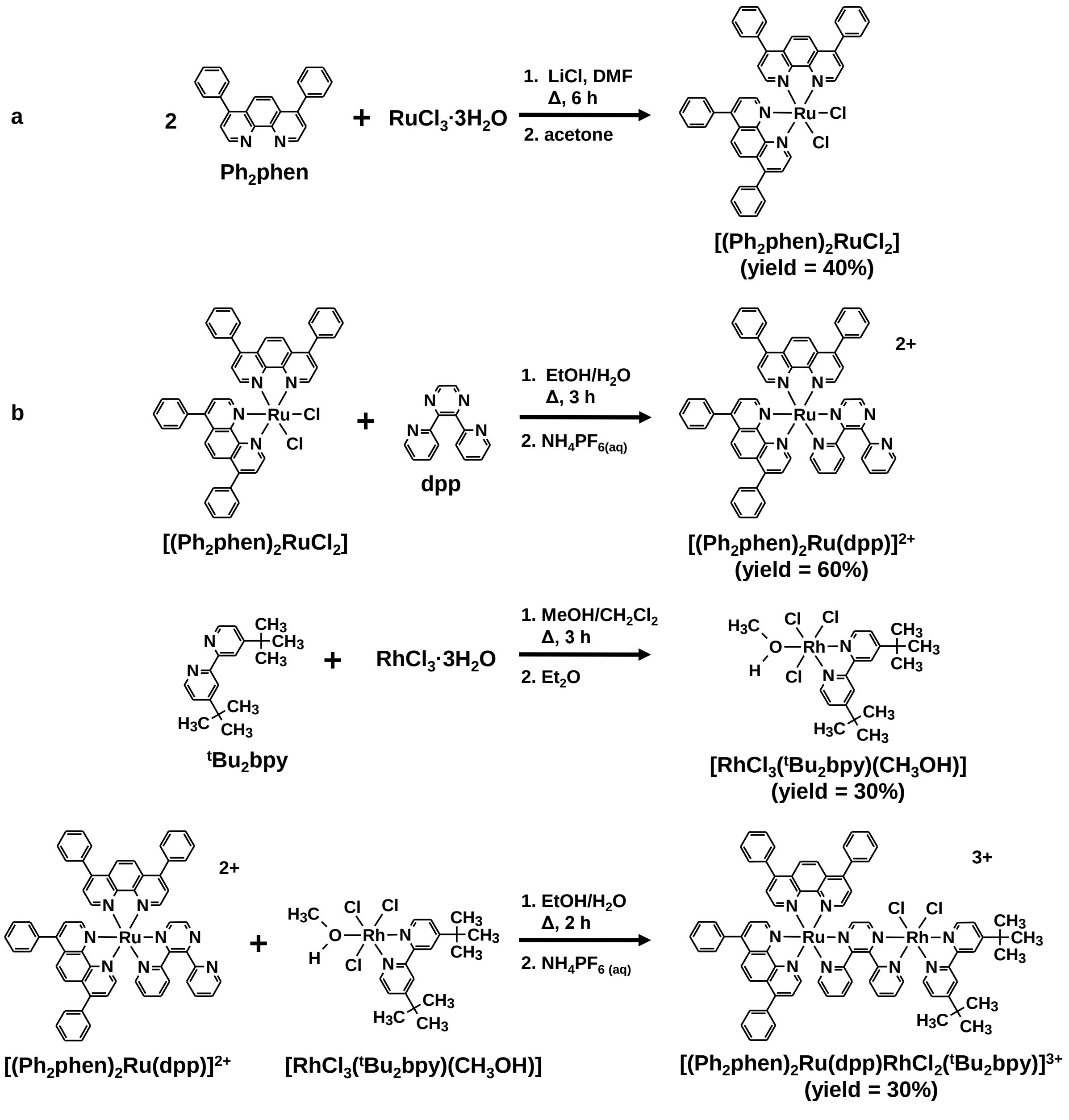

Figure 3.4: Synthetic scheme for the Ru(II),Rh(III) bimetallic supramolecular complex $[(Ph_2phen)_2Ru(dpp)RhCl_2(^tBu_2bpy)](PF_6)_3$. [a] Reference [116]. [b] Reference [55]. Ph_2phen = 4,7-diphenyl-1,10-phenanthroline; $^tBu_2$bpy = 4,4′-Di-*tert*-butyl-2,2′-bipyridine; dpp = 2,3-bis(2-pyridyl)pyrazine.

Purification of the Ru(II),Rh(III) bimetallics was achieved using size-exclusion column chromatography to separate the target bimetallic complexes from any unreacted Ru(II) or Rh(III) monometallic species. A glass column measuring 120 cm x 2 cm containing Sephadex® LH-20 as the stationary phase and EtOH/CH_3CN (2:1 volume ratio) solvent system as the mobile phase was used. The Sephadex® LH-20 in the solvent system was filled to 100 cm and allowed to settle prior to addition of the Ru(II),Rh(III) bimetallic sample. The dark purple or maroon band of the target species elutes prior to the orange band of the Ru(II) monometallic impurity. The solid sample was collected and precipitated by rotary evaporation to reduce solvent volume, dissolving the sample with minimal CH_3CN and adding drop-wise to diethyl ether. Vacuum filtration and diethyl ether rinses yield spectroscopically pure dark purple solid for $[(bpy)_2Ru(dpp)RhCl_2(^tBu_2bpy)](PF_6)_3$ or a dark maroon solid for $[(Ph_2phen)_2Ru(dpp)RhCl_2(^tBu_2bpy)](PF_6)_3$ and $[(Ph_2phen)_2Ru(dpp)RhCl_2(Ph_2phen)](PF_6)_3$ complexes. Typical yield for this reaction is 30% due to the need for removal of trace Ru(II) monometallic ($\Phi^{em} \approx 10^{-2}$) to allow accurate emission analysis of the typical $\Phi^{em} \approx 10^{-4}$ of these products.

3.2. Ru(II),Rh(III),Ru(II) Trimetallic Complexes

The design of the Ru(II),Rh(III),Ru(II) molecular architecture permits photoinitiated electron collection at a centralized Rh metal center due to the low-lying unoccupied Rh(dσ*) orbitals, with the ability to interact with an appropriate substrate.[45,98,131] The $[\{(TL)_2LA(BL)\}_2EC\text{-}X_2]^{5+}$ (TL = terminal ligand, LA = metal-based light absorber; BL = bridging ligand; EC = electron collector; X = halide) molecular architecture presents opportunity to vary the molecular components according to specific requirements. The work presented in this dissertation for Ru(II),Rh(III),Ru(II) trimetallic complexes analyzes how variation of the bidentate, polypyridyl TL attached to the Ru-based LA influences the light absorbing properties of the overall complexes, as well as how variation of X attached to the Rh-based EC influences the properties associated with the Rh site. Therefore, the general formula $[\{(\mathbf{TL})_2Ru(dpp)\}_2Rh\mathbf{X_2}]^{5+}$ (TL = phen or Ph_2phen, X = Cl^- or Br^-) can be used to describe the trimetallic complexes that were studied.

3.2.1. Electrochemical Properties

Electrochemical analysis provides insight into the redox processes and orbital energetics within the Ru(II),Rh(III),Ru(II) trimetallic architecture. These supramolecular complexes display rich electrochemistry with retention of the electrochemical properties specific to each molecular building block, while gaining properties unique to the newly formed species.[41] Scanning anodically displays two overlapping, one-electron reversible $Ru^{II/III}$ redox couples with large $\Delta E_p \approx 130$ mV, while scanning cathodically displays an irreversible $Rh^{III/II/I}$ reduction followed by two sequential, one-electron reversible $dpp^{0/-}$ redox couples. These observations establish Ru as the HOMO and Rh as the LUMO, suggesting the presence of a low-lying metal-to-metal charge transfer (MMCT) excited state upon photoexcitation. Bidentate polypyridyl TLs (phen or Ph_2phen) undergo one-electron reduction at more negative potentials than dpp. The weak Lewis basicity of dpp stabilizes the π* orbitals to a greater degree providing dpp with lower reduction potentials than TLs. This concept is important to designing PECs as photoexcitation is expected to initially generate an excited state where the formal oxidation of Ru(II) to Ru(III) and formal reduction of the dpp^0 to dpp^- places charge density within close proximity to the Rh EC subunit and not on the TL. With regards to the Rh EC subunit, unoccupied Rh(dσ*) orbitals that display an irreversible cathodic wave representing the $Rh^{III/II/I}$ couple at lower potential than the dpp π* orbitals fulfills the requirement for electron collection at a metal center.

Cyclic voltammetry (CV) (**Figure 3.5**) provides insight into the reversible character of a redox event and the number of electrons transferred.[53,54,125] Square wave voltammetry (SWV) (**Figure 3.6**) provides information on the number of electrons within a reversible redox event and greatly enhanced signal-to-noise with no information regarding reversibility.[53,54,120,125] The energy of the molecular orbital set involved can be gained from either electrochemical method although care must be taken when interpreting a redox couple that is not the first oxidation or reduction as a different redox state is present at this point. **Table 3.1** contains the tabulated redox potentials for Ru(II),Rh(III),Ru(II) trimetallics of the architecture $[\{(TL)_2Ru(dpp)\}_2RhX_2](PF_6)_5$ (TL = phen or Ph_2phen; X = Cl^- or Br^-).

Table 3.1: Electrochemical Properties of Ru(II) Monometallic, Ru(II),Ru(II) Homobimetallic, and Ru(II),Rh(III),Ru(II) Trimetallic Complexes

Complex [a]	$E_{1/2}$ (V)	Assignment
$[(phen)_2Ru(dpp)]^{2+}$ [c]	+1.45	$Ru^{II/III}$
	−1.02	$dpp^{0/-}$
	−1.42	$phen^{0/-}$
$[(Ph_2phen)_2Ru(dpp)]^{2+}$ [d]	+1.41	$Ru^{II/III}$
	−0.98	$dpp^{0/-}$
	−1.35	$Ph_2phen^{0/-}$

$[\{(phen)_2Ru\}_2(dpp)]^{4+}$ [c]	+1.69	Ru$^{II/III}$
	+1.50	Ru$^{II/III}$
	−0.62	dpp$^{0/-}$
	−1.12	dpp$^{-/2-}$
	−1.41	2 phen$^{0/-}$
$[\{(Ph_2phen)_2Ru\}_2(dpp)]^{4+}$	+1.64	Ru$^{II/III}$
	+1.45	Ru$^{II/III}$
	−0.61	dpp$^{0/-}$
	−1.11	dpp$^{-/2-}$
	−1.35	2 Ph$_2$phen$^{0/-}$
$[\{(phen)_2Ru(dpp)\}_2RhCl_2]^{5+}$ [e]	+1.61	2 Ru$^{II/III}$
	−0.35 [b]	Rh$^{III/II/I}$
	−0.75	dpp$^{0/-}$
	−1.02	dpp$^{0/-}$
$[\{(phen)_2Ru(dpp)\}_2RhBr_2]^{5+}$	+1.62	2 Ru$^{II/III}$
	−0.32 [b]	Rh$^{III/II/I}$
	−0.71	dpp$^{0/-}$
	−1.01	dpp$^{0/-}$
$[\{(Ph_2phen)_2Ru(dpp)\}_2RhCl_2]^{5+}$	+1.58	2 Ru$^{II/III}$
	−0.35 [b]	Rh$^{III/II/I}$
	−0.74	dpp$^{0/-}$
	−0.98	dpp$^{0/-}$
$[\{(Ph_2phen)_2Ru(dpp)\}_2RhBr_2]^{5+}$	+1.58	2 Ru$^{II/III}$
	−0.32 [b]	Rh$^{III/II/I}$
	−0.69	dpp$^{0/-}$
	−0.98	dpp$^{0/-}$

---

[a] All complexes were measured using Pt disk working electrode, Pt wire auxiliary electrode, and Ag wire pseudo-reference electrode (converted to Ag/AgCl using ferrocene as an internal standard; $Fe(C_5H_5)_2^{0/+}$ = 0.46 V vs. Ag/AgCl). Measurements were made at a scan rate of 100 mV/s using deoxygenated 0.1 M Bu_4NPF_6 in CH_3CN at RT. phen = 1,10-phenanthroline; Ph$_2$phen = 4,7-diphenyl-1,10-phenanthroline; dpp = 2,3-bis(2-pyridyl)pyrazine. Adapted from ref [133,134].

[b] Reported E_p^c of irreversible process.

[c] Values consistent with those in reference [61].

[d] Values consistent with those in reference [55,68].

[e] Values consistent with those in reference [99].

Anodic scans within CV or SWV typically display a reversible oxidation event associated with Ru$^{II/III}$. Incorporation of a Rh(III) metal center within the trimetallic molecular architecture between the two Ru(II) metal centers largely disrupts electronic communication between the two chromophores. As shown in **Figure 3.5** for the trimetallic complexes $[\{(phen)_2Ru(dpp)\}_2RhBr_2]^{5+}$, $[\{(Ph_2phen)_2Ru(dpp)\}_2RhBr_2]^{5+}$, and $[\{(Ph_2phen)_2Ru(dpp)\}_2RhCl_2]^{5+}$, scanning anodically displays two overlapping, one-electron reversible oxidations that are assigned as 2 $Ru^{II/III}$ redox events at $E_{½} = +1.62$ V for $[\{(phen)_2Ru(dpp)\}_2RhBr_2]^{5+}$ and $E_{½} = +1.58$ V for $[\{(Ph_2phen)_2Ru(dpp)\}_2RhBr_2]^{5+}$ and $[\{(Ph_2phen)_2Ru(dpp)\}_2RhCl_2]^{5+}$ with $\Delta E_p \approx 130$ mV. This establishes the HOMO within $[\{(TL)_2Ru(dpp)\}_2RhX_2]^{5+}$ trimetallic complexes as being Ru(dπ) in nature.

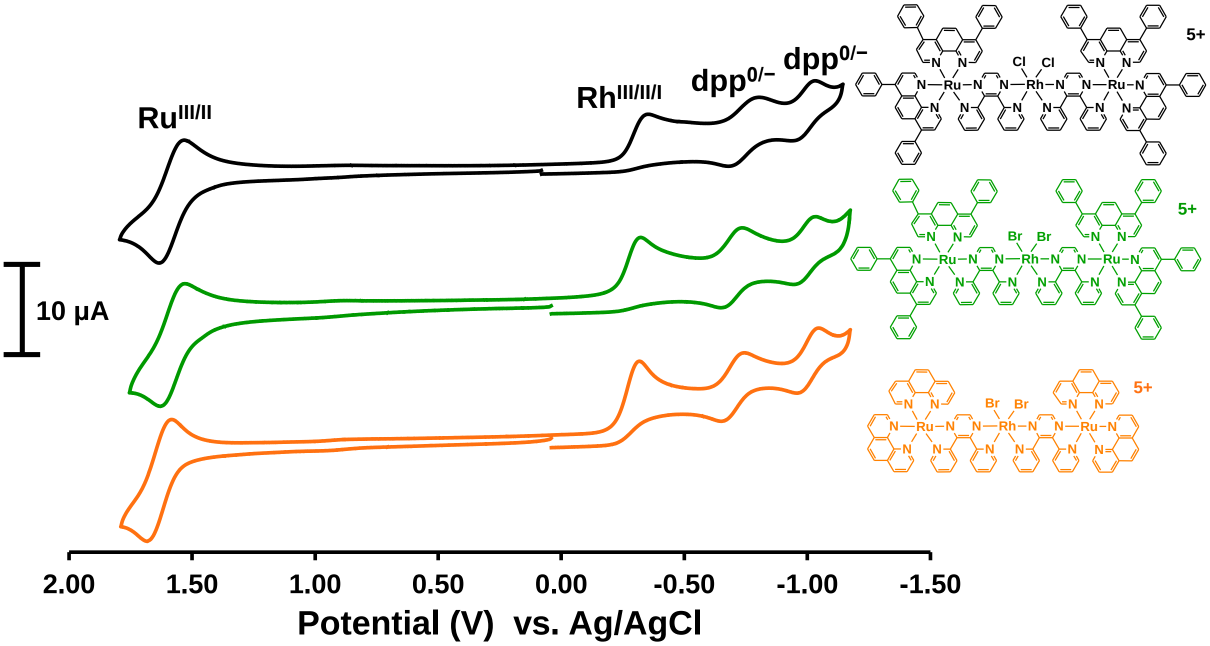

Figure 3.5: Cyclic voltammograms of $[\{(Ph_2phen)_2Ru(dpp)\}_2RhCl_2]^{5+}$ (— top), $[\{(Ph_2phen)_2Ru(dpp)\}_2RhBr_2]^{5+}$ (— middle), and $[\{(phen)_2Ru(dpp)\}_2RhBr_2]^{5+}$ (— bottom) measured using a Pt disk working electrode, Pt wire auxiliary electrode, and Ag wire pseudo-reference electrode (converted to Ag/AgCl using ferrocene as an internal standard; $Fe(C_5H_5)_2^{0/+} = 0.46$ V vs. Ag/AgCl). Measurements were made at RT in CH_3CN using 0.1 M Bu_4NPF_6 supporting electrolyte at a scan rate of 100 mV/s under an inert Ar atmosphere. phen = 1,10-phenanthroline; Ph_2phen = 4,7-diphenyl-1,10-phenanthroline; dpp = 2,3-bis(2-pyridyl)pyrazine.

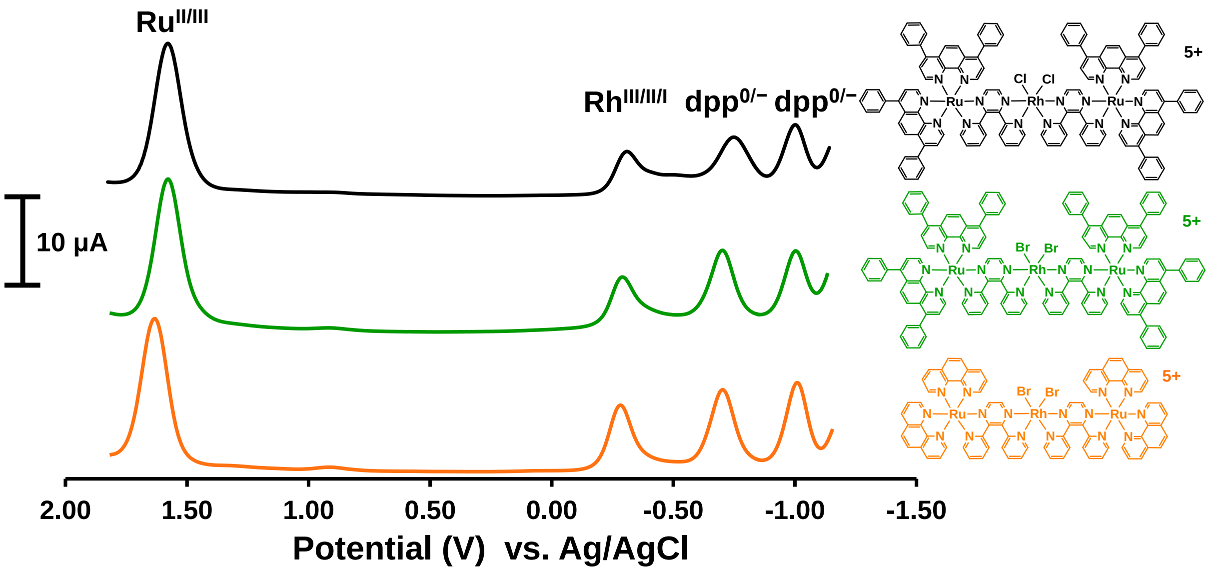

Figure 3.6: Square wave voltammograms of $[\{(Ph_2phen)_2Ru(dpp)\}_2RhCl_2]^{5+}$ (— top), $[\{(Ph_2phen)_2Ru(dpp)\}_2RhBr_2]^{5+}$ (— middle), and $[\{(phen)_2Ru(dpp)\}_2RhBr_2]^{5+}$ (— bottom) measured using a Pt disk working electrode, Pt wire auxiliary electrode, and Ag wire pseudo-reference electrode (converted to Ag/AgCl using ferrocene as an internal standard; $Fe(C_5H_5)_2^{0/+}$ = 0.46 V vs. Ag/AgCl). Measurements were made at RT in CH_3CN using 0.1 M Bu_4NPF_6 supporting electrolyte at a scan rate of 100 mV/s under an inert Ar atmosphere. phen = 1,10-phenanthroline; Ph$_2$phen = 4,7-diphenyl-1,10-phenanthroline; dpp = 2,3-bis(2-pyridyl)pyrazine.

Scanning cathodically typically displays reversible ligand-based reductions and irreversible metal-based reductions. The title $[\{(TL)_2Ru(dpp)\}_2RhX_2]^{5+}$ trimetallics incorporate a Rh(III) metal center which introduce low-lying, unoccupied Rh(dσ*) orbitals capable of accepting two electrons. An irreversible redox wave is observed prior to the reversible dpp$^{0/-}$ redox couples and is identified as the Rh$^{III/II/I}$ reduction process at $E_p^c = -0.35$ V for $[\{(Ph_2phen)_2Ru(dpp)\}_2RhCl_2]^{5+}$ and $E_p^c = -0.32$ V for $[\{(Ph_2phen)_2Ru(dpp)\}_2RhBr_2]^{5+}$ and $[\{(phen)_2Ru(dpp)\}_2RhBr_2]^{5+}$. Labeling of the irreversible Rh$^{III/II/I}$ redox couple is supported by previous experiments where rigorous electrochemical analyses of Rh(III) monometallics of the design $[Rh(NN)_2Cl_2]^+$ (NN = bidentate, polypyridyl terminal or bridging ligands) displayed an ECEC mechanism (E = electron transfer, C = chemical step).[78,80,135,136] **Figure 3.7** provides the electrochemical mechanism for $[\{(TL)_2Ru(dpp)\}_2RhX_2]^{5+}$ trimetallics which display a EEECECEE mechanism. This establishes the LUMO within $[\{(TL)_2Ru(dpp)\}_2RhX_2]^{5+}$

trimetallic complexes as being localized on Rh and suggests the presence of a low-lying Ru(dπ)→Rh(dσ*) metal-to-metal charge transfer (MMCT) excited state.

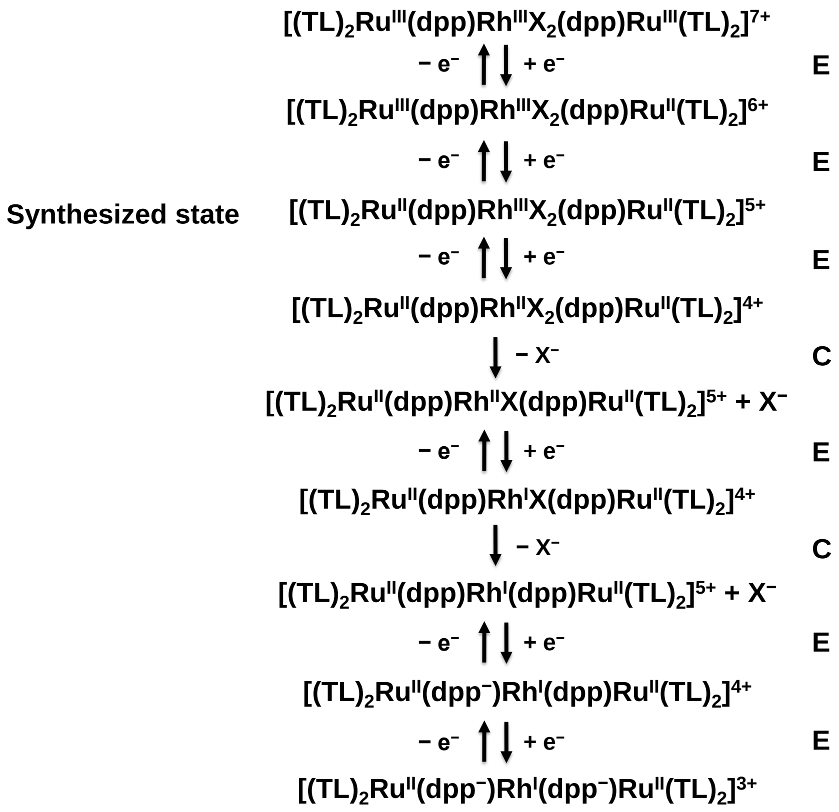

Figure 3.7: EEECECEE electrochemical mechanism for $[\{(TL)_2Ru(dpp)\}_2RhX_2]^{5+}$ (TL = phen or Ph_2phen; X = Cl^- or Br^-) trimetallic complexes. E = electron transfer; C = chemical step. phen = 1,10-phenanthroline; Ph_2phen = 4,7-diphenyl-1,10-phenanthroline; dpp = 2,3-bis(2-pyridyl)pyrazine.

Modification of the terminal ligand (TL) and halide (X) components within the trimetallic architecture influences the observed electrochemical properties. TL variation between phen and Ph_2phen to include phenyl substituents at the 4 and 7 positions slightly perturbs the formally Ru(dπ) orbital energetics. The Ph_2phen TL-containing trimetallics possess $Ru^{II/III}$ oxidations (+1.58 V vs. Ag/AgCl) that are less positive than the phen TL analogues (+1.62 V vs. Ag/AgCl), suggesting weak donating character of the phenyl substituents to destabilize the Ru(dπ) orbitals relative to TL = phen. Halide variation between Cl and Br perturbs the Rh(dσ*) orbital set with the stronger σ-donating Cl^- ligand increasing the ligand field strength, therefore increasing splitting for the Rh-based d-orbitals. This trend is consistently observed for all sets of X variation in **Table 3.1** with the $Rh^{III/II/I}$ reduction occurring at more negative potential for Cl (−0.35 V vs. Ag/AgCl) vs. Br (−0.32 V vs. Ag/AgCl).[99] While the irreversible nature of the $Rh^{III/II/I}$ reduction prevents knowledge of the $E_{1/2}$ for this redox event, it is very interesting to note that the following $dpp^{0/-}$ reduction appears to be influenced by the nature of X coordinated within the original trimetallic complex. This suggests that following $Rh^{III/II/I}$ reduction, halide is present within the outer coordination sphere of the trimetallic complexes, which is feasible given the large positive oxidation state (+5) of the trimetallics and the negative charge of the halides (−1). Further reduction of the trimetallic complexes reduces the second dpp BL ($dpp^{0/-}$) with no significant trend being observed between Cl^- vs. Br^- containing complexes. Varying the TL between phen and Ph_2phen, as well as varying X between Cl^- and Br^- within $[\{(TL)_2Ru(dpp)\}_2RhX_2]^{5+}$ trimetallic complexes modulates the electrochemical properties of these species, albeit through fine tuning. These variations maintain the Ru-based HOMO and Rh-based LUMO necessary for photoinitiated electron collection at the Rh-metal center.

3.2.2. Light Absorbing Properties

Electronic absorption spectroscopy provides a measure of the light absorbing capabilities of the Ru(II),Rh(III),Ru(II) trimetallic complexes. **Table 3.2** summarizes the dominant transitions within the trimetallic complexes, as well as the Ru(II) monometallic and Ru(II),Ru(II) bimetallic analogues.

Table 3.2: Light Absorbing Properties of Ru(II) Monometallic, Ru(II),Ru(II) Homobimetallic, and Ru(II),Rh(III),Ru(II) Trimetallic Complexes

Complex [a]	λ^{abs} (nm)	ε x 10^{-4} ($M^{-1}cm^{-1}$)	Assignment
$[(phen)_2Ru(dpp)]^{2+}$ [b]	262	9.7	phen $\pi \rightarrow \pi^*$
	290	3.7	dpp $\pi \rightarrow \pi^*$
	432	1.5	Ru(dπ) → phen(π^*) CT
	465	1.4	Ru(dπ) → dpp(π^*) CT
$[(Ph_2phen)_2Ru(dpp)]^{2+}$ [c]	278	10.2	Ph_2phen $\pi \rightarrow \pi^*$
	314	3.7	dpp $\pi \rightarrow \pi^*$
	438	2.1	Ru(dπ) → Ph_2phen(π^*) CT
	470	1.9	Ru(dπ) → dpp(π^*) CT

$[\{(\text{phen})_2\text{Ru}\}_2(\text{dpp})]^{4+}$[b]	262	13.6	phen $\pi\rightarrow\pi^*$
	364	2.3	dpp $\pi\rightarrow\pi^*$
	424	2.0	Ru(dπ) → phen(π^*) CT
	526	2.3	Ru(dπ) → dpp(π^*) CT
$[\{(\text{Ph}_2\text{phen})_2\text{Ru}\}_2(\text{dpp})]^{4+}$	278	18.4	Ph_2phen $\pi\rightarrow\pi^*$
	382	3.4	dpp $\pi\rightarrow\pi^*$
	436	3.8	Ru(dπ) → Ph_2phen(π^*) CT
	540	2.9	Ru(dπ) → dpp(π^*) CT
$[\{(\text{phen})_2\text{Ru}(\text{dpp})\}_2\text{RhCl}_2]^{5+}$[d]	262	13.0	phen $\pi\rightarrow\pi^*$
	346	4.0	dpp $\pi\rightarrow\pi^*$
	412	1.6	Ru(dπ) → phen(π^*) CT
	516	2.6	Ru(dπ) → dpp(π^*) CT
$[\{(\text{phen})_2\text{Ru}(\text{dpp})\}_2\text{RhBr}_2]^{5+}$	262	13.0	phen $\pi\rightarrow\pi^*$
	346	3.9	dpp $\pi\rightarrow\pi^*$
	412	1.7	Ru(dπ) → phen(π^*) CT
	516	2.6	Ru(dπ) → dpp(π^*) CT
$[\{(\text{Ph}_2\text{phen})_2\text{Ru}(\text{dpp})\}_2\text{RhCl}_2]^{5+}$	278	18.5	Ph_2phen $\pi\rightarrow\pi^*$
	366	4.8	dpp $\pi\rightarrow\pi^*$
	426	3.5	Ru(dπ) → Ph_2phen(π^*) CT
	516	3.2	Ru(dπ) → dpp(π^*) CT
$[\{(\text{Ph}_2\text{phen})_2\text{Ru}(\text{dpp})\}_2\text{RhBr}_2]^{5+}$	278	18.4	Ph_2phen $\pi\rightarrow\pi^*$
	366	4.6	dpp $\pi\rightarrow\pi^*$
	426	3.7	Ru(dπ) → Ph_2phen(π^*) CT
	516	3.1	Ru(dπ) → dpp(π^*) CT

[a] Measured in spectral grade CH_3CN at RT using a 1 cm quartz cuvette. phen = 1,10-phenanthroline; Ph_2phen = 4,7-diphenyl-1,10-phenanthroline; dpp = 2,3-bis(2-pyridyl)pyrazine. Adapted from ref [133,134].

[b] Values consistent with those in reference [61].

[c] Values consistent with those in reference [55,68].

[d] Values consistent with those in reference [99].

The $[\{(\text{TL})_2\text{Ru}(\text{dpp})\}_2\text{RhX}_2]^{5+}$ (TL = phen or Ph_2phen; X = Cl^- or Br^-) complexes are efficient light absorbers throughout the UV and visible with the UV displaying intense TL- and BL-based IL $\pi\rightarrow\pi^*$ transitions and the visible displaying Ru(dπ)→TL(π^*) and BL(π^*) MLCT transitions.[20,41,49] The phen and Ph_2phen IL $\pi\rightarrow\pi^*$ transitions are centered at 262 nm and 278 nm, respectively, for the trimetallic complexes as well as the precursor building blocks. The energy of the dpp BL $\pi\rightarrow\pi^*$ transition is sensitive to the number of electropositive metal centers attached, with multiple metal coordination shifting the dpp IL transition to lower energy. This is also observed electrochemically for the multimetallic systems where stabilization of the dpp π* orbitals resulted in a less negative reduction potential.[59,61,116]

The visible region is dominated by Ru(dπ)→TL(π*) and Ru(dπ)→dpp(π*) ^{1}CT transitions (TL = phen or Ph_2phen) with the Ru(dπ)→TL(π*) transitions occurring at higher energy. The μ-dpp systems absorb light into the lower energy visible with high ε relative to often employed $[Ru(bpy)_3]^{2+}$ and related chromophores, allowing for absorption of more of the solar spectrum. The number of metal centers does not strongly influence the energy of the Ru(dπ)→TL(π*) ^{1}MLCT transition; however, the identity of the TL does affect the light absorbing properties of this transition. The energy of the Ru(dπ)→dpp(π*) ^{1}MLCT transition is strongly influenced by the number of metal centers coordinated to the dpp BL. Incorporating the electron-accepting *cis*-$Rh^{III}X_2$ EC metal center to form $[\{(TL)_2Ru(dpp)\}_2RhX_2]^{5+}$ trimetallics results in low energy absorption of the Ru(dπ)→dpp(π*) transition at 520 nm for TL = phen or Ph_2phen trimetallics. This stabilization of the dpp π* orbital set upon a second electropositive metal coordination is observed in the electrochemistry of these complexes when compared with the analogous Ru(II) monometallics and Ru(II),Ru(II) bimetallics.

Modification of the TL attached to the Ru(II) LA strongly influences the observed light absorbing properties of $[\{(TL)_2Ru(dpp)\}_2RhX_2]^{5+}$ trimetallics (TL = phen or Ph_2phen; X = Cl^- or Br^-). Complexes containing TL = Ph_2phen display a substantially larger ε value for the TL π→π* and Ru(dπ)→TL(π*) ^{1}CT transitions when compared to analogous TL = phen complexes. **Figure 3.8** displays the disparity between the light absorbing properties for TL = Ph_2phen vs. TL = phen trimetallic complexes. The larger ε values for TL = Ph_2phen complexes indicate a stronger oscillator strength and therefore a larger transition dipole moment integral for transitions involving Ph_2phen (ε_{MLCT} = 3.0 and 1.7 x 10^4 $M^{-1}cm^{-1}$ for $[Ru(Ph_2phen)_3]^{2+}$ and $[Ru(phen)_3]^{2+}$, respectively). This intrinsic property of the Ph_2phen TL provides enhanced spectral coverage through minimal modifications to the ligand structure. Halide variation from Cl^- to Br^- does not show appreciable changes to the electronic absorption spectra for $[\{(TL)_2Ru(dpp)\}_2RhX_2]^{5+}$ trimetallics. **Figure 3.9** displays this relationship for $[\{(Ph_2phen)_2Ru(dpp)\}_2RhCl_2]^{5+}$ and $[\{(Ph_2phen)_2Ru(dpp)\}_2RhBr_2]^{5+}$ complexes. This indicates the identity of the halide attached to the *cis*-$Rh^{III}X_2$ site does not influence the light absorbing properties of the complexes. From these observations, the lowest energy transition populates an excited state that is Ru(dπ)→dpp(π*)

MLCT in character and allows for electron density to be localized in close proximity to the Rh(III) electron accepting site.

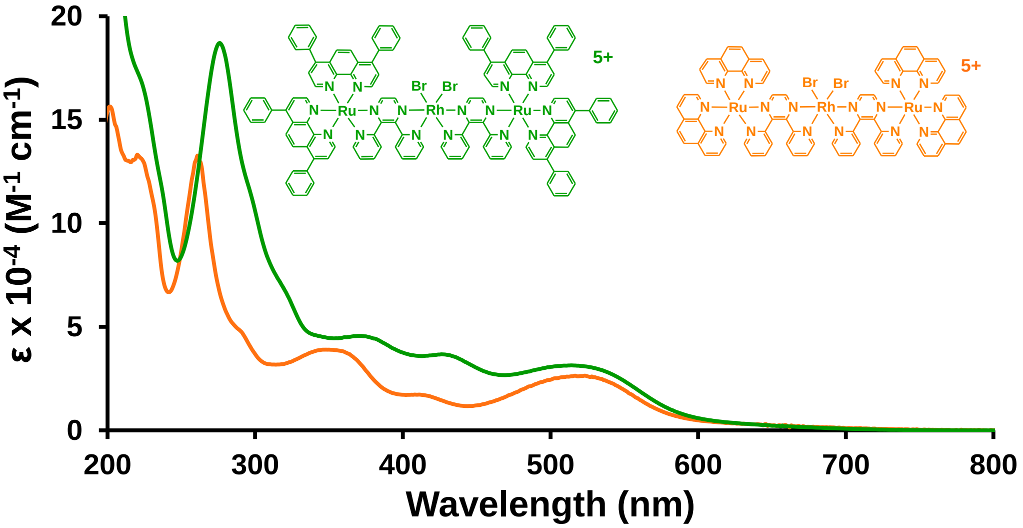

Figure 3.8: Electronic absorption spectra of $[\{(phen)_2Ru(dpp)\}_2RhBr_2](PF_6)_5$ (—) and $[\{(Ph_2phen)_2Ru(dpp)\}_2RhBr_2](PF_6)_5$ (—) measured at RT in spectral grade CH_3CN using a 1 cm quartz cuvette. phen = 1,10-phenanthroline; Ph_2phen = 4,7-diphenyl-1,10-phenanthroline; dpp = 2,3-bis(2-pyridyl)pyrazine.

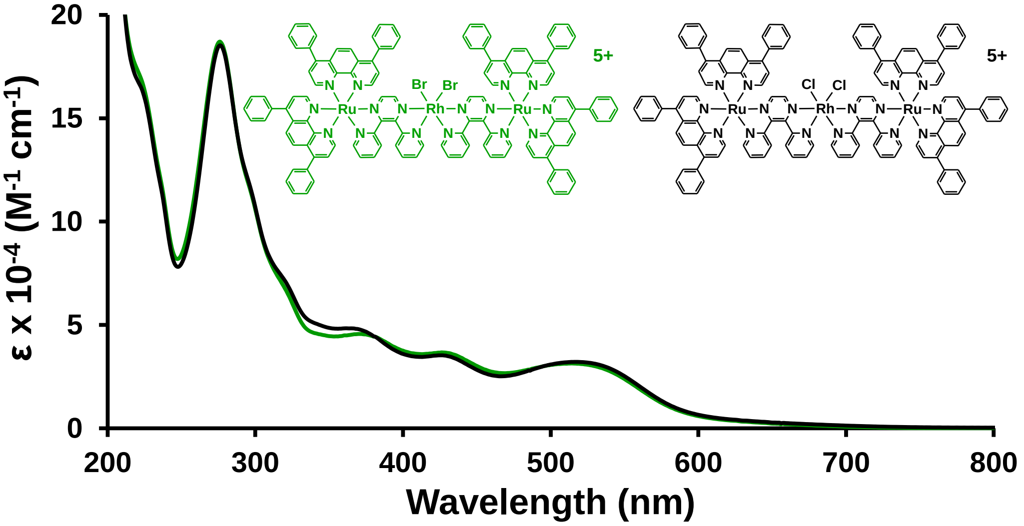

Figure 3.9: Electronic absorption spectra of $[\{(Ph_2phen)_2Ru(dpp)\}_2RhCl_2](PF_6)_5$ (—) and $[\{(Ph_2phen)_2Ru(dpp)\}_2RhBr_2](PF_6)_5$ (—) measured at RT in spectral grade CH_3CN using a 1 cm quartz cuvette. Ph_2phen = 4,7-diphenyl-1,10-phenanthroline; dpp = 2,3-bis(2-pyridyl)pyrazine.

3.2.3. *Excited State Properties*

Steady-state and time-resolved luminescence spectroscopy provide insight into the complex excited state dynamics of Ru(II),Rh(III),Ru(II) trimetallic complexes.[64,121] **Table 3.3** summarizes the excited state properties of $[\{(TL)_2Ru(dpp)\}_2RhX_2]^{5+}$ trimetallics (TL = phen or Ph_2phen; X = Cl^- or Br^-) and the model Ru(II),Ru(II) bimetallic complexes, $[\{(TL)_2Ru\}_2(dpp)]^{4+}$ (TL = phen or Ph_2phen). The Ru(II),Ru(II) bimetallics are used as models due to the similar energy and nature of the emissive Ru(dπ)→μ-dpp(π*) ^{3}MLCT excited state and 77K excited state lifetime. TL variation has been shown to modulate the non-radiative rate constant (k_{nr}) for excited state decay and the energetics of the Ru(dπ)→μ-dpp(π*) ^{3}MLCT excited state due to TL contribution to the formally Ru(dπ) donor orbitals, therefore TL = phen and Ph_2phen Ru(II),Ru(II) bimetallics were used as models for TL = phen and Ph_2phen trimetallics, respectively. $[(TL)_2Ru(dpp)]^{2+}$ monometallics are not appropriate models as the energy and nature of the monometallic emissive Ru(dπ)→dpp(π*) ^{3}MLCT excited state are not similar to the trimetallic emissive excited state. **Figure 3.10** displays the simplified Jablonski state diagram for $[\{(Ph_2phen)_2Ru(dpp)\}_2RhCl_2](PF_6)_5$ and $[\{(Ph_2phen)_2Ru\}_2(dpp)](PF_6)_4$.

Table 3.3: Excited State Properties of Ru(II),Rh(III),Ru(II) Trimetallic Complexes and Model Ru(II),Ru(II) Bimetallic Complexes

	RT [a]						77 K [b]	
Complex	λ^{em} (nm)[c]	Φ^{em} (x 10^4)[d]	τ (ns)[e]	k_r ($10^3\ s^{-1}$)	k_{nr} ($10^6\ s^{-1}$)	k_{et} ($10^7\ s^{-1}$)	λ^{em} (nm)[c]	τ (μs)[e]
$[\{(phen)_2Ru\}_2(dpp)]^{4+}$	750	16	170	9.4	5.9	-	695	2.0
$[\{(Ph_2phen)_2Ru\}_2(dpp)]^{4+}$	754	17	192	9.0	5.2	-	698	2.0
$[\{(phen)_2Ru(dpp)\}_2RhCl_2]^{5+}$	780	2.2	38	9.4	5.9	2.3	706	1.8
$[\{(phen)_2Ru(dpp)\}_2RhBr_2]^{5+}$	780	1.7	34	9.4	5.9	2.8	706	1.9
$[\{(Ph_2phen)_2Ru(dpp)\}_2RhCl_2]^{5+}$	770	2.4	52	9.0	5.2	1.4	696	1.8
$[\{(Ph_2phen)_2Ru(dpp)\}_2RhBr_2]^{5+}$	770	2.0	40	9.0	5.2	2.0	696	1.9

[a] Measured in deoxygenated CH_3CN at RT using a 1 cm quartz cuvette. phen = 1,10-phenanthroline; Ph_2phen = 4,7-diphenyl-1,10-phenanthroline; dpp = 2,3-bis(2-pyridyl)pyrazine. Adapted from ref [133,134,137].

[b] Measured in 4:1 EtOH:MeOH at 77 K in a quartz finger dewar.

[c] Emission corrected for PMT response using manufacturer-provided correction file.

[d] Error associated with quantum yield measurements ± 5%.

[e] Error associated with lifetime measurements ± 5%.

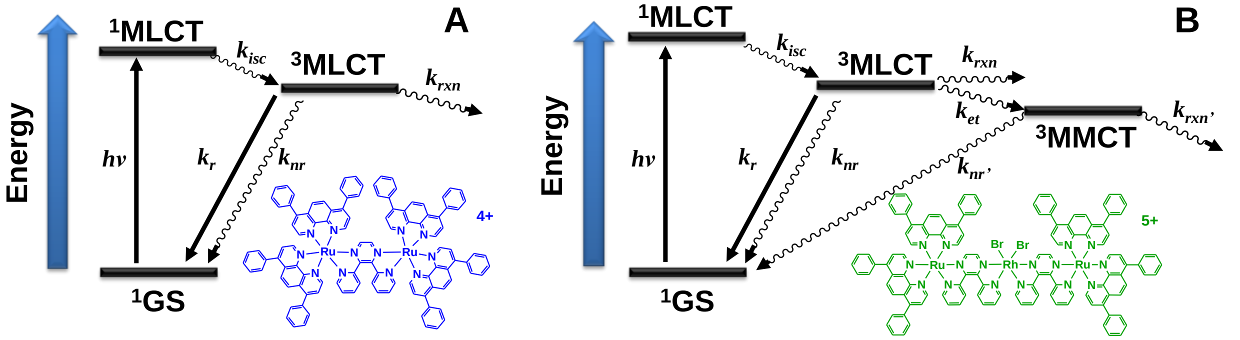

Figure 3.10: State diagrams for the Ru(II),Ru(II) bimetallic model complex $[\{(Ph_2phen)_2Ru\}_2(dpp)]^{4+}$ (A) and the Ru(II),Rh(III),Ru(II) trimetallic complex $[\{(Ph_2phen)_2Ru(dpp)\}_2RhBr_2]^{5+}$ (B). hν = photoexcitation, k_{isc} = intersystem crossing rate constant, k_r = radiative deactivation rate constant, k_{nr} or $k_{nr'}$ = non-radiative deactivation rate constant, k_{et} = intramolecular electron transfer rate constant, k_{rxn} or $k_{rxn'}$ = photochemical reaction rate constant. Ph_2phen = 4,7-diphenyl-1,10-phenanthroline; dpp = 2,3-bis(2-pyridyl)pyrazine.

Photoexcitation of the trimetallic complexes throughout the UV or visible populates ^{1}IL and ^{1}MLCT excited state that undergo a series of internal conversion and intersystem crossing processes to populate the Ru(dπ)→dpp(π*) ^{3}MLCT excited state with near unit efficiency.[138] The excited state dynamics of the complexes are probed through this emissive ^{3}MLCT state. A weak emission ($\Phi^{em} = 1.7 \pm 0.09 \times 10^{-4}$ to $2.4 \pm 0.1 \times 10^{-4}$) and shortened lifetime ($\tau = 34 \pm 1$ ns to 52 ± 1 ns) of the Ru(dπ)→dpp(π*) ^{3}MLCT excited state is observed when compared with the analogous TL model bimetallic systems ($\Phi^{em} = 16 \pm 1 \times 10^{-4}$ to $17 \pm 1 \times 10^{-4}$; τ = 170-192 ns), which possess the same Ru(dπ)→μ-dpp(π*) ^{3}MLCT emissive state but lack a Rh(III)-based metal center. The RT emission of the trimetallic complexes is quenched ~85-90% relative to the Ru(II),Ru(II) bimetallics and this relationship is displayed in **Figure 3.11** with the emission of $[\{(Ph_2phen)_2Ru(dpp)\}_2RhBr_2]^{5+}$ quenched 88% of $[\{(Ph_2phen)_2Ru\}_2(dpp)]^{4+}$.

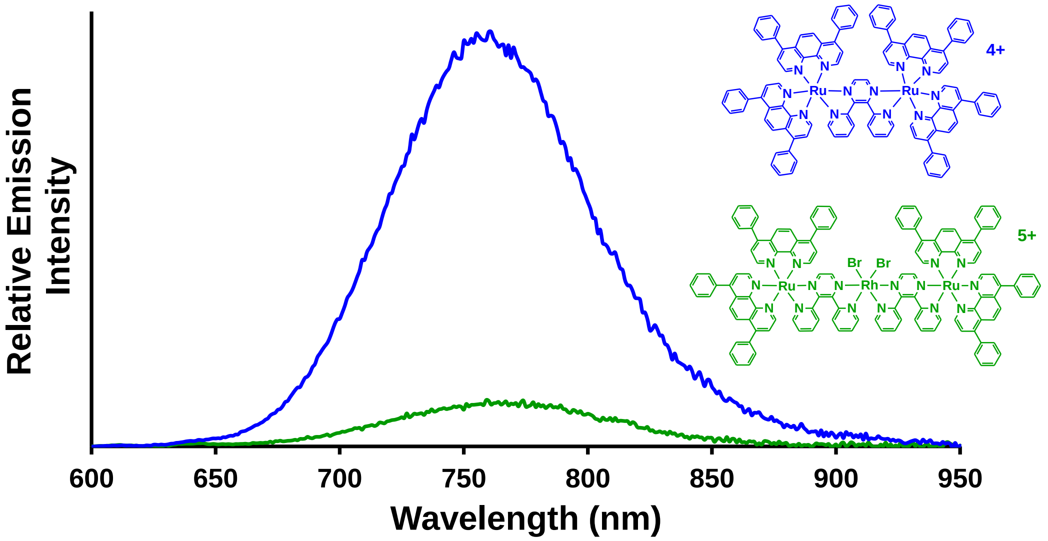

Figure 3.11: Emission spectra of $[\{(Ph_2phen)_2Ru(dpp)\}_2RhBr_2]^{5+}$ (—) and $[\{(Ph_2phen)_2Ru\}_2(dpp)]^{4+}$ (—) excited at 540 nm (absorbance = 0.30), measured in deoxygenated CH_3CN at RT using a 1 cm quartz cuvette, and emission profile corrected for PMT response. Excitation and emission monochromator compartment entrance and exit slit widths set to 1.5 mm (corresponds to ± 6 nm). Ph_2phen = 4,7-diphenyl-1,10-phenanthroline; dpp = 2,3-bis(2-pyridyl)pyrazine.

TL variation influences the radiative (k_r) and non-radiative (k_{nr}) decay of the Ru→μ-dpp ^{3}CT excited state, therefore different Ru(II),Ru(II) bimetallics are required for TL = phen and Ph_2phen trimetallics. This results from the TL contribution to the formally Ru(dπ) donor orbitals. Emission is substantially quenched and the lifetime shortened at RT for trimetallic complexes due to rapid and efficient intramolecular electron transfer (k_{et}) from the emissive ^{3}MLCT excited state to populate the energetically close, non-emissive Ru(dπ)→Rh(dσ*) ^{3}MMCT state. Population of a MMCT excited state is supported by electrochemical analyses as the HOMO is Ru-based and the LUMO is Rh-based. Due to the similar energy and nature of the trimetallic and bimetallic complexes′ emissive state and similar τ at 77 K when electron transfer is inhibited, values for k_r and k_{nr} of the bimetallic model are used to calculate rate constants for intramolecular electron transfer, **Equations 3.1-3.3**

$$\tau_{tri} = \frac{1}{(k_r + k_{nr} + k_{et})} \qquad \text{eq. 3.1}$$

$$\tau_{model} = \frac{1}{(k_r + k_{nr})} \qquad \text{eq. 3.2}$$

$$k_{et} = \frac{1}{\tau_{tri}} - \frac{1}{\tau_{model}} \qquad \text{eq. 3.3}$$

where τ_{tri} and τ_{model} are excited state lifetimes of the ^{3}MLCT state for the Ru(II),Rh(III),Ru(II) trimetallic and Ru(II),Ru(II) bimetallic complexes, respectively. The values for k_{et} range from 1.4-2.8 x 10^7 s^{-1} for the series of $[\{(TL)_2Ru(dpp)\}_2RhX_2]^{5+}$ complexes (TL = phen or Ph_2phen; X = Cl^- or Br^-), indicating rapid intramolecular electron transfer to populate the ^{3}MMCT excited state.

Terminal ligand and halide variation within Ru(II),Rh(III),Ru(II) trimetallic complexes influence the observed ^{3}MLCT ES energy (λ) , quantum yield of emission (Φ^{em}), and lifetime (τ) at room temperature, **Figure 3.12**. Electronic effects from TL identity contribute to the formally Ru(dπ) orbital set, thereby fine tuning the energetics of the ^{3}MLCT ES, while halide variation between Cl^- and Br^- does not affect the ^{3}MLCT energy. Modification of the TL set displays a small blue shift from 780 nm for $[\{(phen)_2Ru(dpp)\}_2RhX_2]^{5+}$ (X = Cl^- or Br^-) to 770 nm for $[\{(Ph_2phen)_2Ru(dpp)\}_2RhX_2]^{5+}$ (X = Cl^- or Br^-). While halide variation does not affect the ^{3}MLCT excited state energetics, the Φ^{em} and τ values are decreased in going from Cl^- to Br^- attached to the Rh metal center. The decreased σ-donating ability of Br^- vs. Cl^- further stabilizes the ^{3}MMCT state and increases the driving force for intramolecular electron transfer, as observed with the lower Φ^{em} and τ values, that results in an increased k_{et} for X = Br^- trimetallic complexes. The decreased Φ^{em} from the ^{3}MLCT ES for X = Br^- trimetallics also suggests enhanced population of the ^{3}MMCT state.

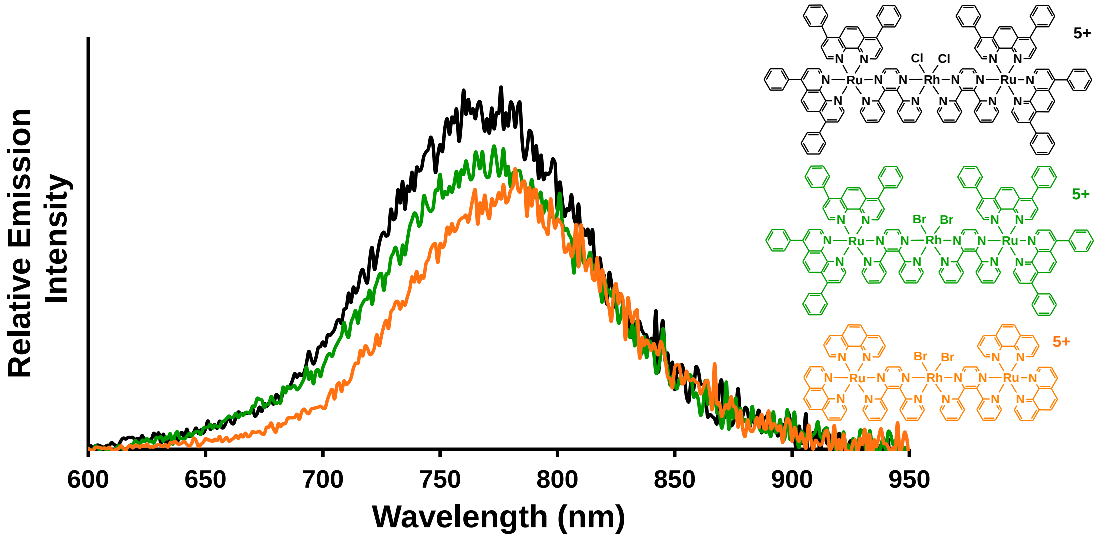

Figure 3.12: Emission spectra of $[\{(Ph_2phen)_2Ru(dpp)\}_2RhCl_2]^{5+}$ (——), $[\{(Ph_2phen)_2Ru(dpp)\}_2RhBr_2]^{5+}$ (——) and $[\{(phen)_2Ru(dpp)\}_2RhBr_2]^{5+}$ (——) excited at 540 nm (absorbance = 0.30), measured in deoxygenated CH_3CN at RT using a 1 cm quartz cuvette, and emission profile corrected for PMT response. Excitation and emission monochromator compartment entrance and exit slit widths set to 1.5 mm (corresponds to ± 6 nm). phen = 1,10-phenanthroline; Ph_2phen = 4,7-diphenyl-1,10-phenanthroline; dpp = 2,3-bis(2-pyridyl)pyrazine.

Low temperature (77 K) measurements in a rigid glass matrix display similar excited state lifetimes (~2.0 μs) of the ^{3}MLCT excited state for Ru(II),Ru(III),Ru(II) trimetallic and model Ru(II),Ru(II) bimetallic complexes. **Figure 3.13** shows a comparison between RT and 77 K emission spectra for $[\{(Ph_2phen)_2Ru(dpp)\}_2RhCl_2](PF_6)_5$. Intramolecular electron transfer from the ^{3}MLCT excited state to the ^{3}MMCT excited state is inhibited in a low temperature, rigid glass matrix as solvent molecules are unable to reorient and repolarize around the outer coordination sphere, resulting in a large reorganization energy that prevents efficient electron transfer between orbitals.[87] These observations coupled with the Rh(dσ*)-based LUMO obtained from electrochemical analyses support the presence of a lower-lying ^{3}MMCT excited state that is populated by intramolecular electron transfer from the ^{3}MLCT excited state at RT in fluid solution. Though expected to be energetically inaccessible[46,65], ^{3}LF states were evaluated as important in these systems. At 77 K, energy transfer between energetically accessible ^{3}LF states and ^{3}MLCT states occurs and ^{3}LF states would display detectable emission. The lack of a ^{3}LF emissive signature further rules out any ^{3}LF population in these supramolecular complexes.

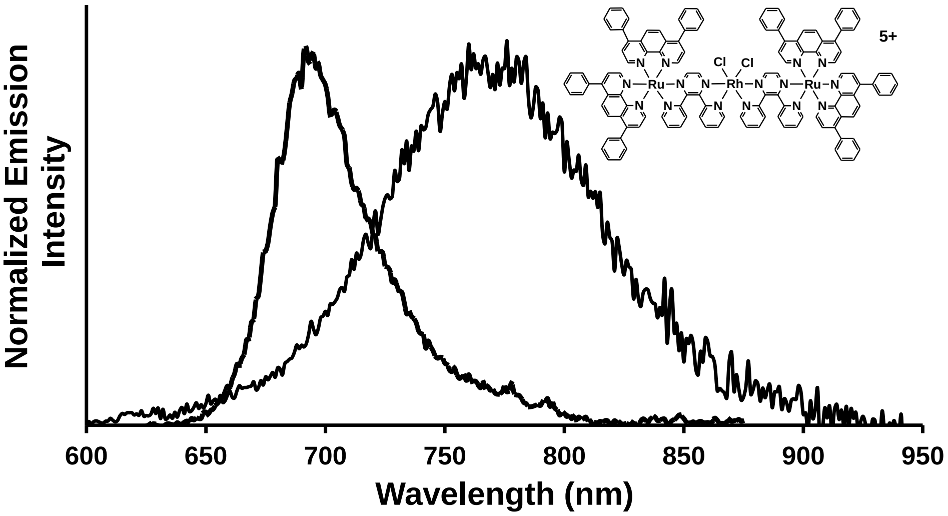

Figure 3.13: Emission spectra of $[\{(Ph_2phen)_2Ru(dpp)\}_2RhCl_2]^{5+}$ measured at RT (——) in deoxygenated CH_3CN using a 1 cm quartz cuvette and at 77 K (- - -) in deoxygenated 4:1 EtOH:MeOH rigid glass matrix using a liquid nitrogen-containing finger dewar. The emission profiles were corrected for PMT response and the excitation and emission monochromator compartment entrance and exit slit widths were set to 1.5 mm (corresponds to ± 6 nm). Ph_2phen = 4,7-diphenyl-1,10-phenanthroline; dpp = 2,3-bis(2-pyridyl)pyrazine.

3.2.4. Photochemical Properties

Photochemical analyses of the Ru(II),Rh(III),Ru(II) trimetallics were performed in the presence of the sacrificial electron donor *N,N*-dimethylaniline (DMA) to observe the ability of the trimetallic complexes to undergo photoinitiated electron collection (PEC) at the Rh(III) metal center. **Equations 3.4-3.11** display possible excited state processes in the absence and presence of DMA upon photoexcitation of the trimetallic species.[98,121,139-141] For simplification, the $[\{(TL)_2Ru(dpp)\}_2RhX_2]^{5+}$ trimetallics (where TL = phen or Ph_2phen; X = Cl^- or Br^-) are represented as $Ru^{II}(dpp)Rh^{III}(dpp)Ru^{II}$ and bold-faced fonts depict electron movement to deviate from initial GS species.

MLCT Photoexcitation

$$\mathrm{Ru^{II}(dpp)Rh^{III}(dpp)Ru^{II}} \xrightarrow{h\nu} {}^{*}\mathbf{Ru^{III}(dpp^{-})}\mathrm{Rh^{III}(dpp)Ru^{II}} \qquad \text{eq. 3.4}$$

Unimolecular Deactivation of ^{3}MLCT State

$${}^{*}\mathbf{Ru^{III}(dpp^{-})}\mathrm{Rh^{III}(dpp)Ru^{II}} \xrightarrow{k_1} \mathrm{Ru^{II}(dpp)Rh^{III}(dpp)Ru^{II}} \qquad \text{eq. 3.5}$$

Bimolecular Deactivation of ^{3}MLCT State

$$\mathrm{DMA} + {}^{*}\mathbf{Ru^{III}(dpp^{-})}\mathrm{Rh^{III}(dpp)Ru^{II}} \xrightarrow{k_2} \mathrm{Ru^{II}(dpp)Rh^{III}(dpp)Ru^{II}} + \mathrm{DMA} \qquad \text{eq. 3.6}$$

Reductive Quenching of ^{3}MLCT State

$$\mathrm{DMA} + {}^{*}\mathbf{Ru^{III}(dpp^{-})}\mathrm{Rh^{III}(dpp)Ru^{II}} \xrightarrow{k_{q1}} \mathrm{Ru^{II}}(\mathbf{dpp^{-}})\mathrm{Rh^{III}(dpp)Ru^{II}} + \mathbf{DMA^{+}} \qquad \text{eq. 3.7}$$

Intramolecular Electron Transfer

$${}^{*}\mathbf{Ru^{III}(dpp^{-})}\mathrm{Rh^{III}(dpp)Ru^{II}} \xrightarrow{k_{et}} {}^{*}\mathbf{Ru^{III}}\mathrm{(dpp)}\mathbf{Rh^{II}}\mathrm{(dpp)Ru^{II}} \qquad \text{eq. 3.8}$$

Unimolecular Deactivation of ^{3}MMCT State

$${}^{*}\mathbf{Ru^{III}}\mathrm{(dpp)}\mathbf{Rh^{II}}\mathrm{(dpp)Ru^{II}} \xrightarrow{k_4} \mathrm{Ru^{II}(dpp)Rh^{III}(dpp)Ru^{II}} \qquad \text{eq. 3.9}$$

Bimolecular Deactivation of ^{3}MMCT State

$$\mathrm{DMA} + {}^{*}\mathbf{Ru^{III}}\mathrm{(dpp)}\mathbf{Rh^{II}}\mathrm{(dpp)Ru^{II}} \xrightarrow{k_3} \mathrm{Ru^{II}(dpp)Rh^{III}(dpp)Ru^{II}} + \mathrm{DMA} \qquad \text{eq. 3.10}$$

Reductive Quenching of ^{3}MMCT State

$$\mathrm{DMA} + {}^{*}\mathbf{Ru^{III}}\mathrm{(dpp)}\mathbf{Rh^{II}}\mathrm{(dpp)Ru^{II}} \xrightarrow{k_{q2}} \mathrm{Ru^{II}(dpp)}\mathbf{Rh^{II}}\mathrm{(dpp)Ru^{II}} + \mathbf{DMA^{+}} \qquad \text{eq. 3.11}$$

Photoexcitation results in population of an ES that contains a formally oxidized Ru(III) metal center and a reduced dpp BL to form the ^{3}MLCT excited state, $\mathbf{Ru^{III}(dpp^{-})}\mathrm{Rh^{III}(dpp)Ru^{II}}$ (**equation 3.4**), which via intramolecular electron transfer leads to a reduced Rh metal center to form the ^{3}MMCT excited state, $\mathbf{Ru^{III}}\mathrm{(dpp)}\mathbf{Rh^{II}}\mathrm{(dpp)Ru^{II}}$ (**equation 3.8**). In the absence of a reductive quencher, the ^{3}MLCT (**equation 3.5**) or ^{3}MMCT (**equation 3.9**) excited state species is expected to unimolecularly relax to the GS and regenerate the initial GS species, $\mathrm{Ru^{II}(dpp)Rh^{III}(dpp)Ru^{II}}$. Photoexcitation in the presence of DMA results in intermolecular electron transfer from DMA to the Ru(III) center, generating a reduced trimetallic species, $\mathrm{Ru^{II}}(\mathbf{dpp^{-}})\mathrm{Rh^{III}(dpp)Ru^{II}}$ and oxidized $\mathbf{DMA^{+}}$ (**equation 3.7**). The MLCT excited state is also able to undergo bimolecular deactivation through non-radiative vibrational coupling with DMA to regenerate the GS trimetallic species or undergo electron transfer followed by rapid back electron transfer (**equation 3.6**). The emissive character of the ^{3}MLCT state provides a probe into the interaction of the photogenerated ES species and the sacrificial electron donor DMA. Emission from the ^{3}MLCT state is quenched upon photoexcitation in the presence of increasing concentration of DMA as displayed using the Stern-Volmer relationship in **Figure 3.14**.

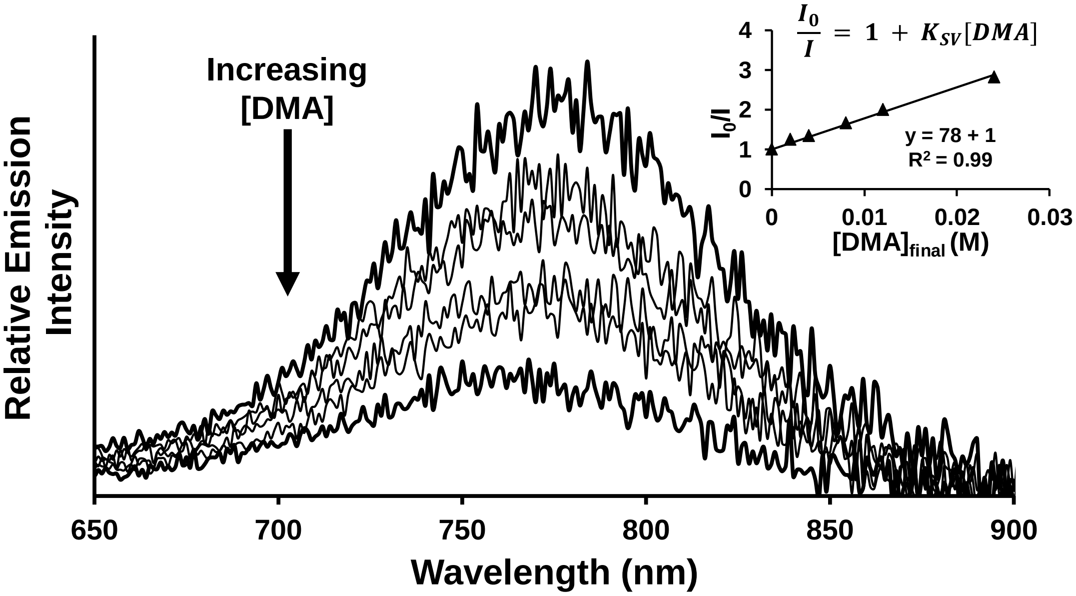

Figure 3.14: Emission quenching of $[\{(Ph_2phen)_2Ru(dpp)\}_2RhCl_2]^{5+}$ ^{3}MLCT excited state in deoxygenated spectral grade CH_3CN at RT in a 1 cm quartz cuvette using increasing concentrations of DMA sacrificial electron donor, where top bold spectrum represents $[DMA]_{final}$ = 0 M and bottom bold spectrum represents $[DMA]_{final}$ = 0.24 M. Inset shows the Stern-Volmer equation and plot depicting a linear relationship between emission quenching and DMA sacrificial electron donor concentration.

The slope of the Stern-Volmer plot provides the Stern-Volmer quenching constant (K_{SV}) which gives insight into the efficiency with which the ES species is able to interact with DMA. From **equation 2.7** (**section 2.2.7**), knowledge of the ^{3}MLCT excited state lifetime provides the rate constant for bimolecular quenching (k_q) which is a summation of the rate constant for bimolecular deactivation (k_2) and reductive quenching (k_{q1}) of the ^{3}MLCT excited state. **Table 3.4** provides this data for $[\{(TL)_2Ru(dpp)\}_2RhX_2]^{5+}$ trimetallics (TL = phen or Ph_2phen; X = Cl^- or Br^-) for which two trends are observed. Halide variation from Cl^- to Br^- and TL variation from Ph_2phen to phen result in a larger value for $k_{q1} + k_2$, indicative of efficient bimolecular quenching of the ^{3}MLCT excited state by DMA. Halide variation between each TL set could be rationalized due to increased competition between intramolecular electron transfer (k_{et}) and reductive quenching (k_{q1}) for X = Br^{-} through enhanced stabilization of the ^{3}MMCT excited state, affording a larger rate constant for the intramolecular electron transfer event which further decreases the observed ^{3}MLCT emission intensity. Observed differences in $k_{q1} + k_2$ for TL variation can be rationalized through structural analysis of the phen and Ph$_2$phen TLs. TL = phen contains a planar ligand backbone that has an extended π-aromatic system capable of π-π stacking with other π-aromatic systems such as DMA. Conversely, TL = Ph$_2$phen possesses phenyl substituents at the 4 and 7 positions of the phenanthroline backbone that are not coplanar with the ligand backbone, therefore disrupting the potential for extended π-aromaticity and efficient π-π stacking with DMA. While all of these values are near the diffusion-control limit ($k_q = 10^{10}$ M^{-1}s^{-1})[121] for bimolecular quenching, the larger values observed for TL = phen may result in more efficient quenching than TL = Ph$_2$phen by placing DMA closer to the Ru center. This same trend was observed for [(TL)$_2$Ru(dpp)]$^{2+}$ monometallic analogues (TL = phen or Ph$_2$phen). Unfortunately, back electron transfer from Ru(II)-polyazine complexes and sacrificial quenchers is very efficient and can occur prior to cage escape resulting in no net electron transfer from DMA to Ru.

Table 3.4: Stern-Volmer Analysis for Bimolecular Quenching of ^{3}MLCT Excited State of Ru(II),Rh(III),Ru(II) Trimetallic Complexes and Ru(II) Monometallic Analogues

Complex [a]	K_{SV} (M^{-1}) [b]	τ_0 (ns)	$k_{q1} + k_2$ (10^9 M^{-1}s^{-1})
$[\{(phen)_2Ru(dpp)\}_2RhCl_2]^{5+}$	135	38	3.9
$[\{(phen)_2Ru(dpp)\}_2RhBr_2]^{5+}$	178	34	5.9
$[\{(Ph_2phen)_2Ru(dpp)\}_2RhCl_2]^{5+}$	78	52	1.5
$[\{(Ph_2phen)_2Ru(dpp)\}_2RhBr_2]^{5+}$	114	40	2.9
$[(phen)_2Ru(dpp)]^{2+}$	523	560	0.93
$[(Ph_2phen)_2Ru(dpp)]^{2+}$	352	820	0.43

[a] Measured in spectral grade deoxygenated CH$_3$CN in the dark at RT. Deoxygenated DMA electron donor was added to cuvette containing complex just prior to measurement. Adapted from ref [133,142].

[b] Stern-Volmer quenching constant (K_{SV}) obtained from slope of Stern-Volmer linear plot.

Given the ability of the trimetallic complexes to undergo reductive quenching of the ^{3}MLCT excited state to afford reduced trimetallic species, the complexes were photochemically reduced in an effort to establish these as photochemical molecular devices for photoinitiated electron collection. Photochemical or electrochemical reduction using a 470 nm LED light source in the presence of DMA or by applying a −0.40 V vs. Ag/AgCl bias, respectively, changes the electronic absorption spectrum over time. As the first reduction within dpp-bridged Ru(II),Rh(III),Ru(II) trimetallics is Rh(dσ*) based and therefore the LUMO, observed spectral shifts associated with electrochemical reduction should mirror spectral shifts through photochemical reduction if photoinitiated electron collection at Rh is occurring. While Rh-based transitions within the electronic absorption spectrum are overpowered by Ru(II) and ligand-based transitions, electronic modification through increased electron density at Rh(III) to form Rh(I) should shift dpp-based transitions to higher energy by destabilizing the dpp π* orbitals. As observed spectroscopically, photochemical (**Figure 3.15A**) or electrochemical (**Figure 3.15B**) reduction results in spectra with similar spectroscopic signals. As time progresses, photolysis in the presence of DMA shifts the Ru(dπ)→dpp(π*) ^{1}CT transition centered at 520 nm to higher energy due to increased electron density at the Rh site by converting the octahedral *cis*-$\mathrm{Rh^{III}X_2}$ environment to a square planar, coordinatively unsaturated $\mathrm{Rh^{I}}$ environment resulting in destabilization of the dpp π* orbital set. Constant-potential electrolysis (CPE) of $[\{(\mathrm{Ph_2phen})_2\mathrm{Ru(dpp)}\}_2\mathrm{RhBr_2}]^{5+}$ at −0.40 V vs. Ag/AgCl reduces the Rh(III) center to Rh(I) and displays transitions within the visible region that are nearly identical to photochemical reduction. This establishes the Ru(II),Rh(III),Ru(II) trimetallics as photochemical molecular devices for photoinitiated electron collection.

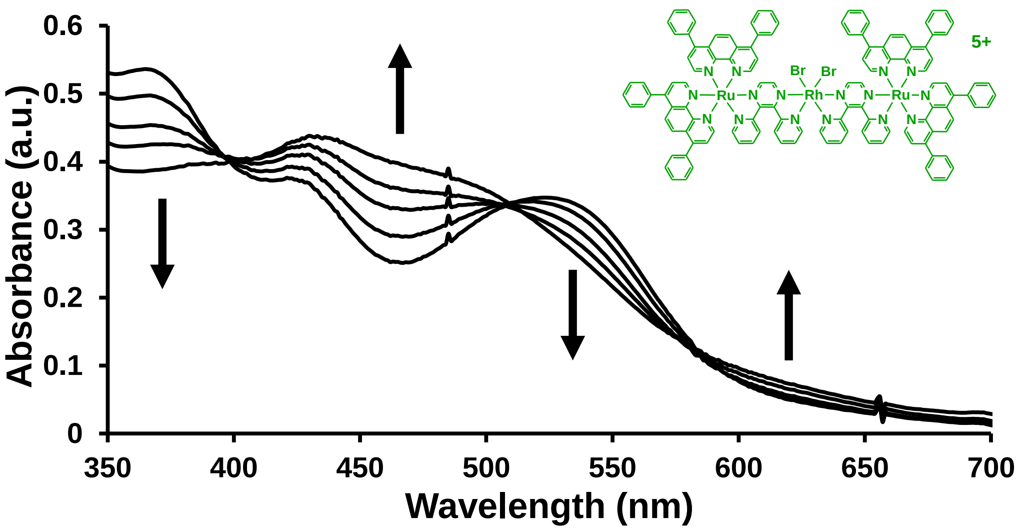

Figure 3.15A: Electronic absorption spectra following photochemical reduction of $[\{(Ph_2phen)_2Ru(dpp)\}_2RhBr_2]^{5+}$ in spectral grade deoxygenated CH_3CN at RT using a 1 cm quartz cuvette in the presence of DMA sacrificial electron donor using a 470 nm LED light source. Initial spectrum corresponds to t = 0 s and final spectrum corresponds to t = 120 s photolysis time. Changes to $\lambda < 350$ nm are obscured by intense absorption from DMA electron donor. Ph_2phen = 4,7-diphenyl-1,10-phenanthroline; dpp = 2,3-bis(2-pyridyl)pyrazine.

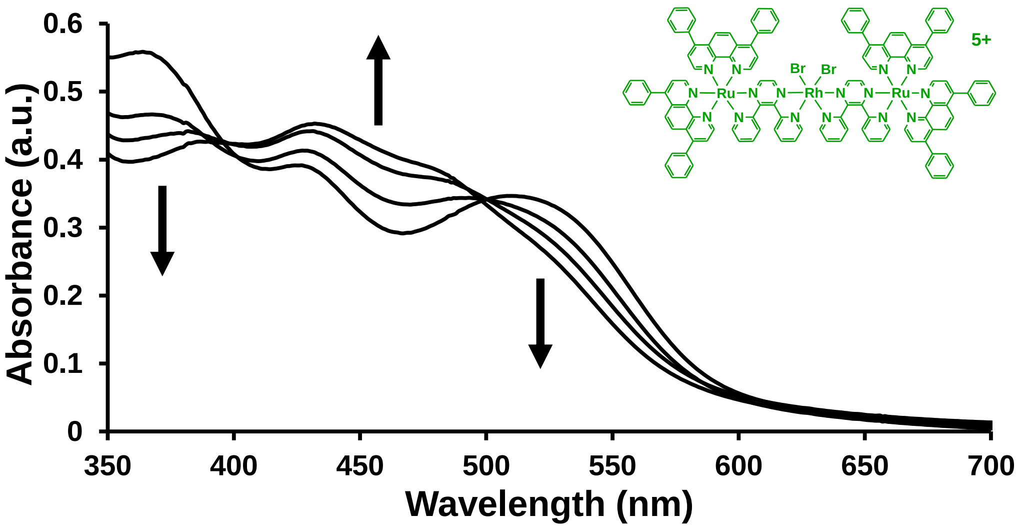

Figure 3.15B: Electronic absorption spectra following electrochemical reduction of $[\{(Ph_2phen)_2Ru(dpp)\}_2RhBr_2]^{5+}$ at an applied potential of −0.40 V vs. Ag/AgCl using a two compartment H-cell with a carbon cloth auxiliary electrode compartment, Pt mesh working electrode and Ag/AgCl (3 M $NaCl_{(aq)}$) reference electrode with 0.1 M Bu_4NPF_6 in deoxygenated CH_3CN at RT. Initial spectrum corresponds to t = 0 min and final spectrum corresponds to t = 30 min electrolysis time. Ph_2phen = 4,7-diphenyl-1,10-phenanthroline; dpp = 2,3-bis(2-pyridyl)pyrazine.

3.2.5. Photocatalytic H_2 Production

With the knowledge that $[\{(TL)_2Ru(dpp)\}_2RhX_2]^{5+}$ trimetallics (TL = phen or Ph_2phen; X = Cl or Br) photochemically collect multiple reducing equivalents to generate Rh(I)-centered trimetallics, photocatalytic studies were performed in the presence of the sacrificial electron donor DMA and H_2O to investigate their ability to function as photocatalysts for the reduction of H_2O to H_2. **Table 3.5** summarizes the data of the photolysis experiments and **Figure 3.16** displays the photocatalytic H_2 production profiles of the $[\{(TL)_2Ru(dpp)\}_2RhX_2]^{5+}$ trimetallic complexes (TL = phen or Ph_2phen; X = Cl or Br) using 65 μM trimetallic, 1.5 M DMA, 0.62 M H_2O, and 0.11 mM $[DMAH^+][CF_3SO_3^-]$ in a CH_3CN solvent system photolyzed at 470 nm for 20 h.

Table 3.5: Photocatalytic H_2 Production from H_2O using Ru(II),Rh(III),Rh(II) Trimetallic Complexes

Complex [a]	Solvent	H_2 (mL)	H_2 (μmol)	TON [b]	Φ_{H_2} x10^2 [c]	Max. Φ_{H_2} x10^2 [d]
$[\{(phen)_2Ru(dpp)\}_2RhCl_2]^{5+}$	CH_3CN	0.10 ± 0.01	4.0 ± 0.2	14 ± 1	0.018 ± 0.001	0.17
$[\{(phen)_2Ru(dpp)\}_2RhBr_2]^{5+}$	CH_3CN	0.14 ± 0.02	5.6 ± 0.7	19 ± 2	0.025 ± 0.003	0.26
$[\{(Ph_2phen)_2Ru(dpp)\}_2RhCl_2]^{5+}$	CH_3CN	1.1 ± 0.1	44 ± 3	150 ± 10	0.20 ± 0.01	1.2
$[\{(Ph_2phen)_2Ru(dpp)\}_2RhBr_2]^{5+}$	CH_3CN	1.4 ± 0.1	58 ± 4	200 ± 10	0.26 ± 0.02	1.9
$[\{(phen)_2Ru(dpp)\}_2RhBr_2]^{5+}$	DMF	0.33 ± 0.03	14 ± 2	47 ± 5	0.061 ± 0.006	0.32
$[\{(Ph_2phen)_2Ru(dpp)\}_2RhBr_2]^{5+}$	DMF	2.0 ± 0.1	82 ± 3	280 ± 10	0.40 ± 0.01	1.8

[a] Results correspond to 20 h photolysis time using 470 nm LED light source and performed in triplicate ([photocatalyst] = 65 μM; [DMA] = 1.5 M; $[H_2O]$ = 0.62 M; $[DMAH^+][CF_3SO_3^-]$ = 0.11 mM; light flux = $2.36 \pm 0.05 \times 10^{19}$ photons/min; reaction solution volume = 4.5 mL; head space volume = 15.5 mL). phen = 1,10-phenanthroline; Ph_2phen = 4,7-diphenyl-1,10-phenanthroline; dpp = 2,3-bis(2-pyridyl)pyrazine. Adapted from ref [133,142].

[b] Values correspond to mol H_2 produced per mol Rh catalytic center.

[c] Φ_{H_2} = overall quantum efficiency of H_2 formation.

[d] Max. Φ_{H_2} = maximum instantaneous quantum efficiency of H_2 formation.

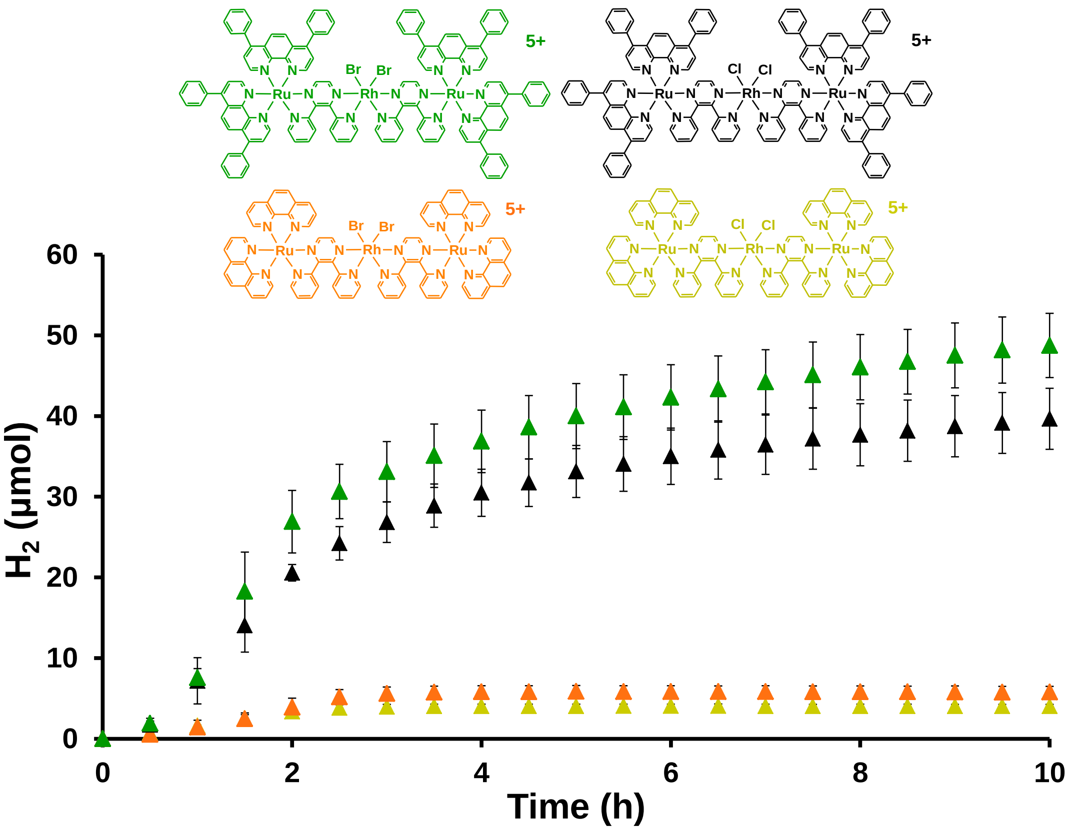

Figure 3.16: Photocatalytic H_2 production profiles of [photocatalyst] = 65 μM, [DMA] = 1.5 M, [H_2O] = 0.62 M, and [$DMAH^+$][$CF_3SO_3^-$] = 0.11 mM in CH_3CN when photolyzed at 470 nm, where photocatalyst is $[\{(phen)_2Ru(dpp)\}_2RhCl_2]^{5+}$ (▲), $[\{(phen)_2Ru(dpp)\}_2RhBr_2]^{5+}$ (▲), $[\{(Ph_2phen)_2Ru(dpp)\}_2RhCl_2]^{5+}$ (▲), and $[\{(Ph_2phen)_2Ru(dpp)\}_2RhBr_2]^{5+}$ (▲). phen = 1,10-phenanthroline; Ph_2phen = 4,7-diphenyl-1,10-phenanthroline; dpp = 2,3-bis(2-pyridyl)pyrazine.

These Ru(II),Rh(III),Ru(II) trimetallics are able to photocatalytically reduce H_2O to H_2 when illuminated with 470 nm light under an inert atmosphere. Previous studies using $[\{(phen)_2Ru(dpp)\}_2RhCl_2]^{5+}$ and $[\{(phen)_2Ru(dpp)\}_2RhBr_2]^{5+}$ were reported after two or four hour photolysis periods and quantified by injecting 100 μL of the photolysis reaction cell's head space into a gas chromatograph, thereby altering the photolysis conditions.[99] The completed series, with $[\{(Ph_2phen)_2Ru(dpp)\}_2RhCl_2]^{5+}$ and $[\{(Ph_2phen)_2Ru(dpp)\}_2RhBr_2]^{5+}$ included, was monitored in real-time using solid-state H_2 sensors to permit immediate analysis of the photolysis reaction without altering the photolysis conditions.[113,128] The H_2 production profiles are typically characterized by H_2 evolution from the photolysis solution within 30 minutes of photoinitiating the reaction. The next two hours display a nearly constant slope, followed by a decrease in the slope with prolonged photolysis displaying a substantially decreased positive slope. However, a positive slope for H_2 production is still observed 20 h after initiating the reaction for $[\{(Ph_2phen)_2Ru(dpp)\}_2RhCl_2]^{5+}$ and $[\{(Ph_2phen)_2Ru(dpp)\}_2RhBr_2]^{5+}$ trimetallic complexes.

Varying the molecular components within the Ru(II),Rh(III),Ru(II) trimetallic architecture displays varied amounts of H_2 produced. After 20 h photolysis in CH_3CN, $[\{(phen)_2Ru(dpp)\}_2RhCl_2]^{5+}$ and $[\{(phen)_2Ru(dpp)\}_2RhBr_2]^{5+}$ produced 4.0 ± 0.2 and 5.6 ± 0.7 μmol H_2, respectively, while $[\{(Ph_2phen)_2Ru(dpp)\}_2RhCl_2]^{5+}$ and $[\{(Ph_2phen)_2Ru(dpp)\}_2RhBr_2]^{5+}$ produced 44 ± 3 μmol H_2 and 58 ± 4 μmol H_2, respectively. Deactivation of the ^{3}MLCT and ^{3}MMCT excited states of TL = phen complexes may result due to efficient π-π interactions between the DMA and phen TL aromatic systems. As observed above, TL = phen trimetallics display larger bimolecular deactivation (k_2) rate constants, which would inhibit efficient reductive product formation of Rh(I) species. Changing the TL to Ph_2phen generates trimetallics with greatly enhanced photocatalytic activity and stability. This result is very surprising given the nature of the photoactive Ru(dπ)→dpp(π*) ^{3}MLCT and Ru(dπ)→Rh(dσ*) ^{3}MMCT excited states are the same throughout the $[\{(TL)_2Ru(dpp)\}_2RhX_2]^{5+}$ series of trimetallics. The enhanced light absorbing properties of Ph_2phen trimetallics throughout the visible region due to a larger extinction coefficient (ε) increases the probability of ES population and therefore ES reactivity. The steric demands imparted by the Ph_2phen TL are important to photocatalyst functioning and may serve to protect the photogenerated Rh(I) center from unwanted side reactions that would deactivate the photocatalyst. This emphasizes the need for a balance between sterics and electronics when designing potential supramolecular photocatalysts.

Halide variation at the *cis*-$Rh^{III}X_2$ ($X = Cl^-$ or Br^-) electron collecting, reactive metal center provides fine tuning of the photocatalytic properties of the Ru(II),Rh(III),Ru(II) trimetallic complexes. Trimetallics where $X = Br^-$, $[\{(phen)_2Ru(dpp)\}_2RhBr_2]^{5+}$ and $[\{(Ph_2phen)_2Ru(dpp)\}_2RhBr_2]^{5+}$, displayed consistently higher amounts of H_2 produced (~1.3x more) in a 20 h period than the respective Cl^- analogues, $[\{(phen)_2Ru(dpp)\}_2RhCl_2]^{5+}$ and $[\{(Ph_2phen)_2Ru(dpp)\}_2RhCl_2]^{5+}$. While the electrochemical and excited state properties suggest a more stabilized ^{3}MMCT excited state for the Br-containing trimetallics, the identity of the photoreduced trimetallics, $[\{(TL)_2Ru(dpp)\}_2Rh^I]^{5+}$, should be the same after halide loss and catalytic activity is expected to be the same. This consistent discrepancy in H_2 production further emphasizes that photoinduced halide loss is a kinetically important step within the photocatalytic cycle with the weaker σ-donating Br^{-} ligand undergoing photodissociation more efficiently. The smaller size and higher affinity of Cl^{-} towards electropositive entities, when compared with Br^{-}, may enable Cl^{-} to serve as a sufficient ligand towards coordinating with Rh throughout the $Rh^{III/II/I}$ redox cycling within the photocatalytic cycle. Coordinating a halide at the Rh catalytically active site would impede photocatalysis as H_2O is unable to interact with Rh. Similarly, the free halide in solution may actually form ion pairs with the positively charged photocatalyst in organic solutions of low relative permittivity, further amplifying the impact of halide identity. The presence of the bulky Ph_2phen TLs protects the photogenerated Rh(I) site from halide coordination with the larger Br^{-} ligand expected to be repelled more efficiently than the smaller Cl^{-} ligand, reiterating the importance of steric and electronic balance within these photocatalytic systems.

The solvent within the photocatalytic system was varied in an effort to better understand the role of solvent during the catalytic cycle. Properties of the solvent such as polarity, dielectric constant, or ligating capabilities may dictate how well the system functions. CH_3CN and DMF were chosen as both solvents are miscible with all components of the photolysis system and display similar dipole moment ($\mu = 3.92$ D (CH_3CN) and 3.82 D (DMF)) and dielectric constant ($\varepsilon_r = 37.5$ (CH_3CN) and 36.7 (DMF)) values, but differing ligating abilities.[143] As Rh(III) undergoes reduction and ligand loss throughout the catalytic cycle to form the coordinatively unsaturated square planar Rh(I) center, the ligating ability of the solvent should impact the efficiency with which H_2O substrate can interact with the Rh(I) catalytically active site. The ligating ability of the two solvents varies as CH_3CN is expected to be a better ligating solvent than DMF.[36] As shown in **Figure 3.17** and **Table 3.5**, varying the solvent from CH_3CN to DMF enhances the catalytic stability of both $[\{(phen)_2Ru(dpp)\}_2RhBr_2]^{5+}$ and $[\{(Ph_2phen)_2Ru(dpp)\}_2RhBr_2]^{5+}$ trimetallic photocatalysts, supporting the hypothesis that a weaker ligating solvent would enhance photocatalysis.

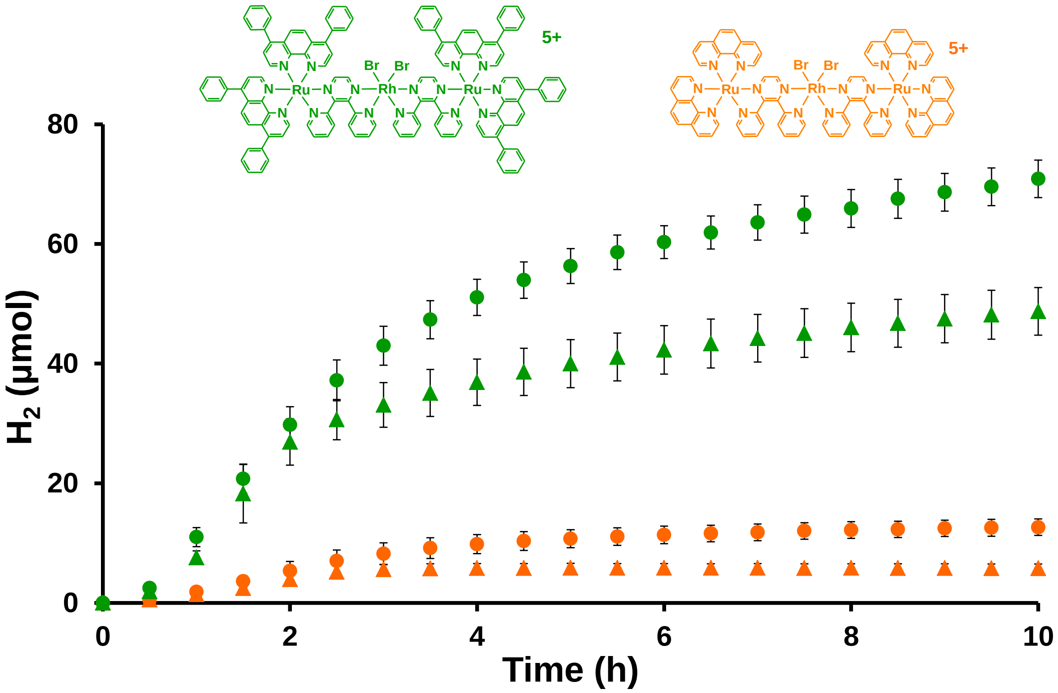

Figure 3.17: Photocatalytic H_2 production profiles of [photocatalyst] = 65 μM, [DMA] = 1.5 M, $[H_2O]$ = 0.62 M, and $[DMAH^+][CF_3SO_3^-]$ = 0.11 mM when photolyzed at 470 nm, where photocatalyst is $[\{(phen)_2Ru(dpp)\}_2RhBr_2]^{5+}$ in CH_3CN (▲), $[\{(phen)_2Ru(dpp)\}_2RhBr_2]^{5+}$ in DMF (●), $[\{(Ph_2phen)_2Ru(dpp)\}_2RhBr_2]^{5+}$ in CH_3CN (▲), and $[\{(Ph_2phen)_2Ru(dpp)\}_2RhBr_2]^{5+}$ in DMF (●). phen = 1,10-phenanthroline; Ph_2phen = 4,7-diphenyl-1,10-phenanthroline; dpp = 2,3-bis(2-pyridyl)pyrazine.

The scale of the photocatalytic H_2 production experiments provides insight into the catalytic cycle and possible catalyst deactivation pathways. Initial photocatalytic studies involved conditions where the solution volume was 4.5 mL, the head space volume was 16 mL, and the light flux was 2.36 x 10^{19} photons/min. By increasing the cell size and number of LEDs photolyzing each cell, a large scaled photocatalytic system is produced, providing a cell with a total volume of 50 mL (25 mL reaction solution; 25 mL head space) illuminated by four 470 nm LEDs with a total flux of 6.27 x 10^{19} photons/min.[128]

Photolysis results show that increasing the head space volume, solution volume, and photon flux impact the rate and efficiency of H_2 production. After 20 h, the most active trimetallic photocatalyst, $[\{(Ph_2phen)_2Ru(dpp)\}_2RhBr_2]^{5+}$, was able to produce 44 ± 6 mL H_2, 1820 ± 260 μmol H_2, 610 ± 90 TON, and 7.3% maximum instantaneous Φ_{H_2} where 120 μM photocatalyst, 3.1 M DMA, 0.62 M H_2O, and 0.11 mM $[CF_3SO_3^-][DMAH^+]$ were photolyzed in a DMF solvent system. This result shows superior photocatalysis by a single component system and is remarkable given this supramolecule must absorb light, separate charge at the molecular level, repeat these processes to collect multiple electrons, bind a substrate, break and form multiple bonds, and release the desired H_2 product. Prolonged photolysis displayed long term stability of the photocatalytic system with a positive slope after 40 h (61 ± 9 mL H_2; 840 ± 130 TON; 2.0% overall Φ_{H_2}). An analogous photolysis experiment using the small scale setup (120 μM photocatalyst; 3.1 M DMA; 0.62 M H_2O; 0.11 mM $[CF_3SO_3^-][DMAH^+]$; DMF solvent; 16 mL head space; 4.5 mL solution volume; 2.36×10^{19} photons/min light flux) produced 4.7 ± 0.3 mL H_2, 190 ± 10 μmol H_2, 360 ± 20 TON, and 2.6% maximum instantaneous Φ_{H_2} after 20 h photolysis, **Figure 3.18**. Increasing the reaction solution and head space volumes may minimize a potential deactivating pathway by which oxidative addition of H_2 to Rh(I) impedes catalytic functioning due to increased partial pressure of H_2 present in the small scale reaction. This stresses the importance of experimental design and how factors such as pressure within the cell, temperature of the reaction solution, amount of photocatalyst, and amount of light affect photocatalysis.

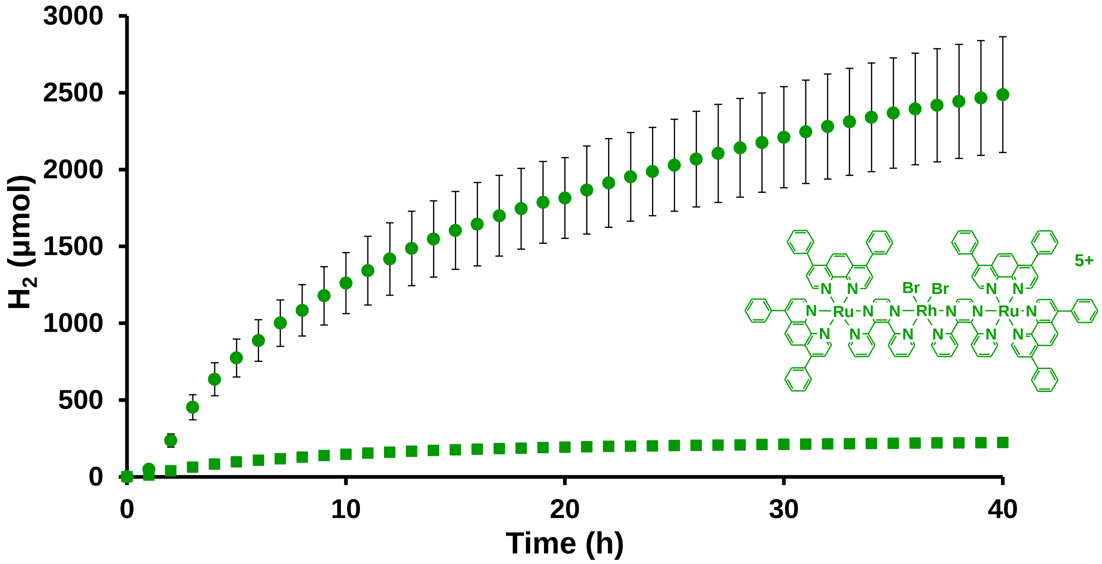

Figure 3.18: Photocatalytic H_2 production profiles of [photocatalyst] = 120 μM, [DMA] = 1.5 M, $[H_2O]$ = 0.62 M, and $[DMAH^+][CF_3SO_3^-]$ = 0.11 mM in DMF when photolyzed at 470 nm, where photocatalyst is $[\{(Ph_2phen)_2Ru(dpp)\}_2RhBr_2]^{5+}$. Green circles (●) represent large scale photolysis (25 mL reaction solution; 25 mL head space; 6.27×10^{19} photons/min light flux) and green squares (■) represent regular scale photolysis (4.5 mL reaction solution; 16 mL head space; 2.36×10^{19} photons/min light flux).

3.3. Ru(II),Rh(III) Bimetallic Complexes

The design of the Ru(II),Rh(III) bimetallic supramolecular architecture maintains the Ru(II) LA bridged to the Rh(III) metal center through a dpp BL, but utilizes only one Ru(II) LA instead of two. Synthesis of Ru(II),Rh(III) bimetallic complexes proved to be more difficult than synthesis of trimetallic complexes as the bimetallics required an additional synthetic step to achieve one TL′ coordinated instead of two BLs. A bidentate TL′ coordinated to Rh(III) in place of the second Ru(II) LA modulates the energetics at the Rh-based orbital set, while providing a saturated coordination sphere for the d^6 pseudo-octahedral Rh(III) metal center. The $[(TL)_2LA(BL)EC\text{-}X_2(TL')]^{3+}$ bimetallic architecture permits systematic component modification throughout, allowing for an in depth understanding of the properties each component presents to the overall supramolecule. With respect to this dissertation, variation of the Ru(II)-TL (bpy or Ph_2phen) and Rh(III)-TL′ ($^tBu_2$bpy or Ph_2phen) were analyzed and therefore the general formula $[(\mathbf{TL})_2Ru(dpp)RhCl_2(\mathbf{TL'})]^{3+}$ is used.

3.3.1. Electrochemical Properties

Electrochemistry provides insight into the complex orbital energetics of Ru(II),Rh(III) bimetallic complexes which display rich anodic and cathodic electrochemistry. Similar to the Ru(II),Rh(III),Ru(II) trimetallic complexes, the electrochemical properties of the $[(TL)_2Ru(dpp)RhCl_2(TL')]^{3+}$ complexes retain the properties of the individual molecular components while also producing properties unique to the newly formed molecular architecture. The electrochemical properties of $[(TL)_2Ru(dpp)RhCl_2(TL')]^{3+}$ bimetallic complexes are tabulated in **Table 3.6** and displayed in **Figure 3.19** and vary with respect to reductive electrochemistry compared to analogous Ru(II),Rh(III),Ru(II) trimetallic systems. The Ru(II),Ru(II) bimetallic complex $[\{(Ph_2phen)_2Ru\}_2(dpp)]^{4+}$, Ru(II),Rh(III),Ru(II) trimetallic complex $[\{(Ph_2phen)_2Ru(dpp)\}_2RhCl_2]^{5+}$ and Ru(II),Rh(III) bimetallic complex $[(Ph_2phen)_2Ru(dpp)RhCl_2(Ph_2phen)]^{3+}$ are compared in **Figure 3.20** to better understand the complex electrochemical characteristics of multimetallic molecular architectures.

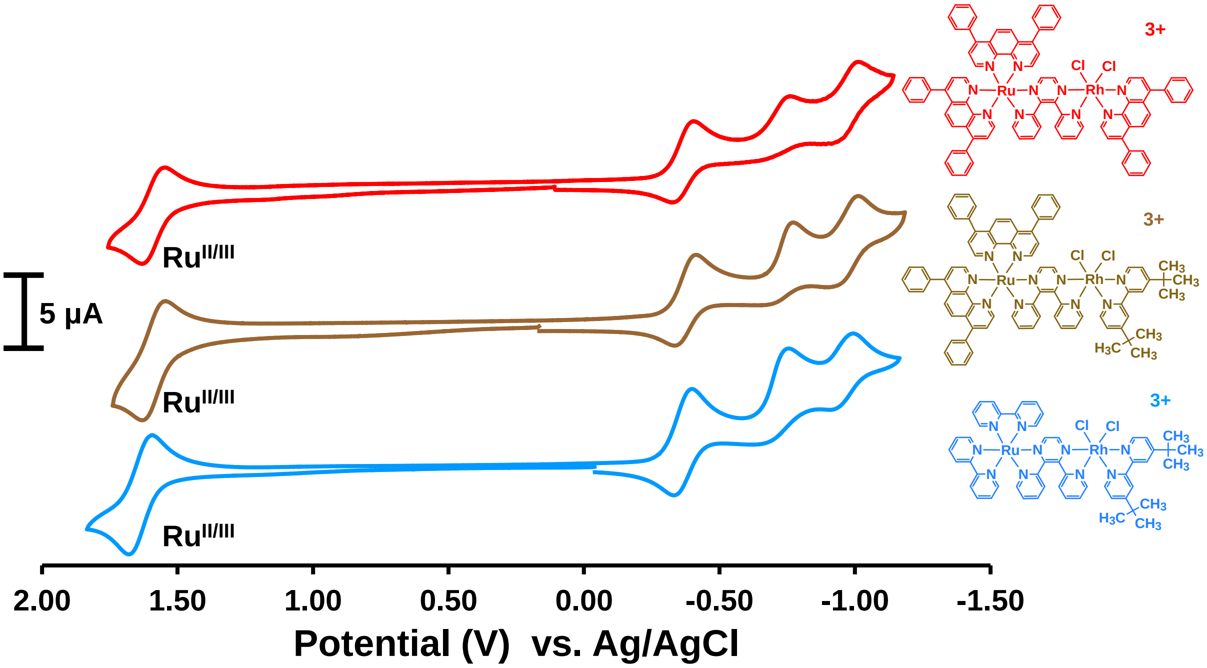

Figure 3.19: Cyclic voltammograms of $[(Ph_2phen)_2Ru(dpp)RhCl_2(Ph_2phen)]^{3+}$ (— top), $[(Ph_2phen)_2Ru(dpp)RhCl_2(^{t}Bu_2bpy)]^{3+}$ (— middle), and $[(bpy)_2Ru(dpp)RhCl_2(^{t}Bu_2bpy)]^{3+}$ (— bottom) measured using a Pt disk working electrode, Pt wire auxiliary electrode, and Ag wire pseudo-reference electrode (converted to Ag/AgCl using ferrocene as an internal standard; $Fe(C_5H_5)_2^{0/+}$ = 0.46 V vs. Ag/AgCl). Measurements were made at RT in CH_3CN using 0.1 M Bu_4NPF_6 supporting electrolyte at a scan rate of 100 mV/s under an inert Ar atmosphere. bpy = 2,2′-bipyridine; $^{t}Bu_2bpy$ = 4,4′-Di-*tert*-butyl-2,2′-bipyridine; Ph_2phen = 4,7-diphenyl-1,10-phenanthroline; dpp = 2,3-bis(2-pyridyl)pyrazine.

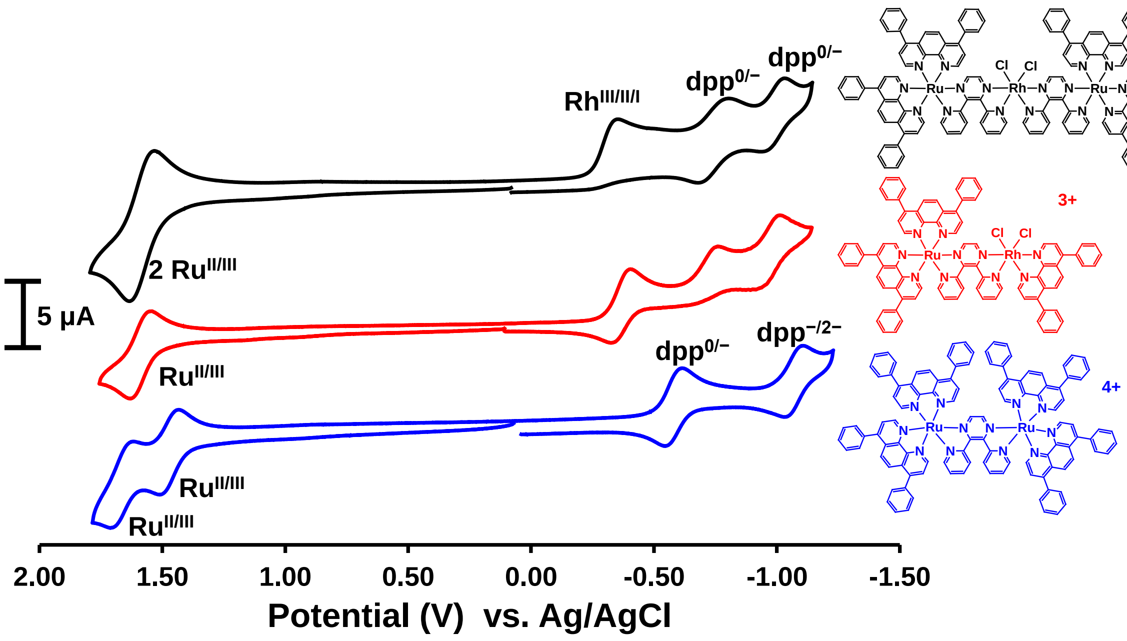

Figure 3.20: Cyclic voltammograms of $[\{(Ph_2phen)_2Ru(dpp)\}_2RhCl_2]^{5+}$ (— top), $[(Ph_2phen)_2Ru(dpp)RhCl_2(Ph_2phen)]^{3+}$ (— middle), and $[\{(Ph_2phen)_2Ru\}_2(dpp)]^{4+}$ (— bottom) measured using a Pt disk working electrode, Pt wire auxiliary electrode, and Ag wire pseudo-reference electrode (converted to Ag/AgCl using ferrocene as an internal standard; $Fe(C_5H_5)_2^{0/+}$ = 0.46 V vs. Ag/AgCl). Measurements were made at RT in CH_3CN using 0.1 M Bu_4NPF_6 supporting electrolyte at a scan rate of 100 mV/s under an inert Ar atmosphere. Ph_2phen = 4,7-diphenyl-1,10-phenanthroline; dpp = 2,3-bis(2-pyridyl)pyrazine.

Table 3.6. Electrochemical Properties of Ru(II),Rh(III) Bimetallic, Ru(II),Ru(II) Homobimetallic, and Ru(II),Rh(III),Ru(II) Trimetallic Complexes

Complex [a]	$E_{1/2}$ (V)	ΔE_p (mV)	i_p^a/i_p^c	Assignment
$[(Ph_2phen)_2Ru(dpp)RhCl_2(^tBu_2bpy)]^{3+}$	+1.59	85	0.8	$Ru^{II/III}$
	−0.37	75	0.8	$dpp^{0/–}$,$Rh^{III/II}$
	−0.76 [b]	--	--	$Rh^{II/I}$
	−0.96	110	0.8	$dpp^{0/–}$
$[(Ph_2phen)_2Ru(dpp)RhCl_2(Ph_2phen)]^{3+}$	+1.59	85	0.8	$Ru^{II/III}$
	−0.37	70	0.4	$Rh^{III/II}$
	−0.77 [b]	--	--	$Rh^{II/I}$
	−0.96	100	0.8	$dpp^{0/–}$
$[(bpy)_2Ru(dpp)RhCl_2(^tBu_2bpy)]^{3+}$	+1.63	90	0.8	$Ru^{II/III}$
	−0.37	70	0.8	$dpp^{0/–}$,$Rh^{III/II}$
	−0.75 [b]	--	--	$Rh^{II/I}$
	−0.95	80	0.8	$dpp^{0/–}$

$[\{(Ph_2phen)_2Ru\}_2(dpp)]^{4+}$	+1.64	80	1.0	$Ru^{II/III}$
	+1.45	75	1.0	$Ru^{II/III}$
	−0.61	70	0.9	$dpp^{0/-}$
	−1.11	70	0.9	$dpp^{-/2-}$
$[\{(Ph_2phen)_2Ru(dpp)\}_2RhCl_2]^{5+}$	+1.58 [c]	130	0.9	2 $Ru^{II/III}$
	−0.35 [d]	--	--	$Rh^{III/II/I}$
	−0.74	120	0.9	$dpp^{0/-}$
	−0.98	110	0.9	$dpp^{0/-}$

[a] All complexes were measured using Pt disk working electrode, Pt wire auxiliary electrode, and Ag wire pseudo-reference electrode (converted to Ag/AgCl using ferrocene as an internal standard; $Fe(C_5H_5)_2^{0/+}$ = 0.46 V vs. Ag/AgCl). Measurements were made at a scan rate of 100 mV/s using deoxygenated 0.1 M Bu_4NPF_6 in distilled CH_3CN at RT. Ph_2phen = 4,7-diphenyl-1,10-phenanthroline; $^tBu_2bpy$ = 4,4′-Di-*tert*-butyl-2,2′-bipyridine; bpy = 2,2′-bipyridine; dpp = 2,3-bis(2-pyridyl)pyrazine. Adapted from ref [133,144].

[b] Reported E_p^c of irreversible one-electron process.

[c] Two overlapping, one-electron reversible processes.

[d] Reported E_p^c of two overlapping, one-electron irreversible process.

With regards to $[(TL)_2Ru(dpp)RhCl_2(TL')]^{3+}$ bimetallics, anodic scans reveal a reversible, one-electron $Ru^{II/III}$ oxidation whose potential is affected by the nature of the coordinated bidentate TL set. This allows for fine tuning of the Ru-based HOMO within this architecture. Coordination of TL = bpy to Ru(II) displays the $Ru^{II/III}$ redox couple at +1.63 V vs. Ag/AgCl for $[(bpy)_2Ru(dpp)RhCl_2(^tBu_2bpy)]^{3+}$, while TL = Ph_2phen coordination shifts the $Ru^{II/III}$ redox couple to a less positive potential of +1.59 V vs. Ag/AgCl for $[(Ph_2phen)_2Ru(dpp)RhCl_2(^tBu_2bpy)]^{3+}$ and $[(Ph_2phen)_2Ru(dpp)RhCl_2(Ph_2phen)]^{3+}$. This small shift to less positive potential for TL = Ph_2phen indicates the electron-withdrawing character of the phenyl substituent on the phen ligand with respect to the Ru center. `

Cathodic scans of $[(TL)_2Ru(dpp)RhCl_2(TL')]^{3+}$ bimetallics present somewhat interesting and complex electrochemistry. Analysis of the first reduction within Ru(II),Rh(III) bimetallic complexes $[(Ph_2phen)_2Ru(dpp)RhCl_2(^tBu_2bpy)]^{3+}$, $[(Ph_2phen)_2Ru(dpp)RhCl_2(Ph_2phen)]^{3+}$, and $[(bpy)_2Ru(dpp)RhCl_2(^tBu_2bpy)]^{3+}$ in CH_3CN shows that varying Rh(III)-TL′ (TL′ = $^tBu_2bpy$ or Ph_2phen) does not substantially impact the potential ($E_{1/2} = -0.37$ V vs. Ag/AgCl; $\Delta E_p \approx 85$ mV) of this first reduction, **Figure 3.19**. However, reversing scan following the first reduction reveals the disparity in reversibility of this first couple between complexes. TL′ = $^tBu_2bpy$ displays more reversible character than TL′ = Ph_2phen, indicating the chemical stability of the one-electron reduced TL′ = $^{t}Bu_2bpy$ bimetallic complexes. **Figure 3.21A** shows an overlay of the first reductive couple and the corresponding ratio of peak currents (i_p^a/i_p^c) observed for $[(Ph_2phen)_2Ru(dpp)RhCl_2(^tBu_2bpy)]^{3+}$ and $[(Ph_2phen)_2Ru(dpp)RhCl_2(Ph_2phen)]^{3+}$ bimetallics using a glassy carbon working electrode to afford enhanced sensitivity at the electrode surface compared to a Pt disk working electrode. The i_p^a/i_p^c ratio of 0.8 vs. 0.4 for $[(Ph_2phen)_2Ru(dpp)RhCl_2(^tBu_2bpy)]^{3+}$ and $[(Ph_2phen)_2Ru(dpp)RhCl_2(Ph_2phen)]^{3+}$, respectively, at 100 mV/s indicates the enhanced stability of the TL′ = $^{t}Bu_2bpy$ complex following electrochemical reduction. Scanning more negatively presents an irreversible second reduction regardless of Rh(III)-TL′ component used with a cathodic peak potential $E_p^c = -0.76$ V vs. Ag/AgCl. The intensity of the second reductive wave is sensitive to TL′ identity as the $^{t}Bu_2bpy$ bimetallics display a larger current value than the TL′ = Ph_2phen bimetallic, **Figure 3.21B**. The intensity for the TL′ = Ph_2phen second reductive wave is less than one electron, indicating the presence of multiple electrochemical mechanisms Further scanning negative shows a quasi-reversible reduction ($E_{1/2} = -0.96$ V vs. Ag/AgCl; $\Delta E \approx 100$ mV) regardless of Rh(III)-TL′ component used. At this point, three equivalents of electrons have passed from the electrode to the Ru(II),Rh(III) bimetallic complexes with the systems proposed as having a $[(TL)_2Ru(dpp^-)Rh^I(TL')]^{2+}$ structure.

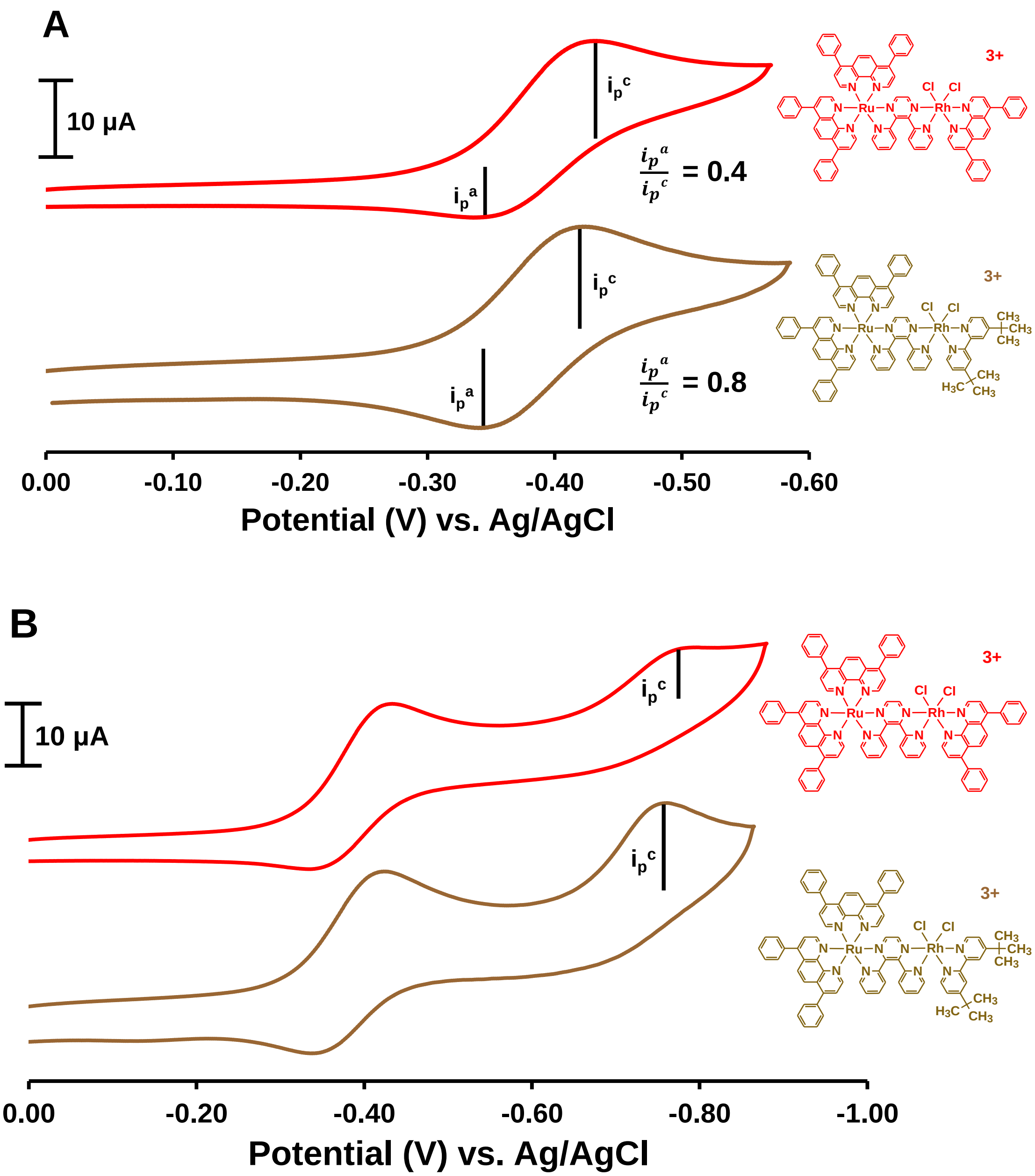

Figure 3.21: Cyclic voltammograms depicting the electrochemical reversibility upon switching scanning potential following the first (A) and second (B) redox couples for $[(Ph_2phen)_2Ru(dpp)RhCl_2(Ph_2phen)]^{3+}$ (—) and $[(Ph_2phen)_2Ru(dpp)RhCl_2(^tBu_2bpy)]^{3+}$ (—) using a glassy carbon working electrode, Pt wire auxiliary electrode, and Ag wire pseudo-reference electrode (converted to Ag/AgCl using ferrocene as an internal standard; $Fe(C_5H_5)_2^{0/+}$ = 0.46 V vs. Ag/AgCl). Measurements were made at RT in CH_3CN using 0.1 M Bu_4NPF_6 supporting electrolyte at a scan rate of 100 mV/s under an inert Ar atmosphere. $^tBu_2bpy$ = 4,4′-Di-*tert*-butyl-2,2′-bipyridine; Ph_2phen = 4,7-diphenyl-1,10-phenanthroline; dpp = 2,3-bis(2-pyridyl)pyrazine.

The electrochemical reductions of Ru(II),Rh(III) bimetallics appear to be a hybrid of the reduction processes for Ru(II),Rh(III),Ru(II) trimetallic and Ru(II),Ru(II) homobimetallic complexes with some variance. Previous analyses have established that dpp-bridged trimetallics of the architecture $[\{(TL)_2Ru(dpp)\}_2RhCl_2]^{5+}$ (TL = bpy, phen, or Ph_2phen)[98,99] undergo two, one-electron reductions of Rh ($Rh^{III/II}$ and $Rh^{II/I}$) with halide loss occurring at each step, followed by two successive, reversible one-electron μ-$dpp^{0/-}$ reductions to form $[\{(TL)_2Ru(dpp^{-})\}_2Rh^{I}]^{3+}$. Conversely, dpp-bridged homobimetallics of the architecture $[\{(TL)_2Ru\}_2(dpp)]^{4+}$ (TL = bpy, phen, and Ph_2phen)[59,61,145] possess a reversible one-electron μ-$dpp^{0/-}$ first reduction followed by a reversible one-electron μ-$dpp^{-/2-}$ second reduction. Electrochemical mechanisms depicting the heterogeneous electron transfer and chemical reaction steps for the trimetallic and homobimetallic architectures are shown in **Figure 3.22**.

$$\begin{array}{cc}
\mathbf{[(TL)_2Ru^{II}(dpp)Rh^{III}X_2(dpp)Ru^{II}(TL)_2]^{5+}} & \\
-e^{-}\ \uparrow\downarrow\ +e^{-} & \mathrm{E} \\
[(TL)_2Ru^{II}(dpp)Rh^{II}X_2(dpp)Ru^{II}(TL)_2]^{4+} & \\
\downarrow\ -X^{-} & \mathrm{C} \\
[(TL)_2Ru^{II}(dpp)Rh^{II}X(dpp)Ru^{II}(TL)_2]^{5+} + X^{-} & \\
-e^{-}\ \uparrow\downarrow\ +e^{-} & \mathrm{E} \\
[(TL)_2Ru^{II}(dpp)Rh^{I}X(dpp)Ru^{II}(TL)_2]^{4+} & \\
\downarrow\ -X^{-} & \mathrm{C} \\
[(TL)_2Ru^{II}(dpp)Rh^{I}(dpp)Ru^{II}(TL)_2]^{5+} + X^{-} & \\
-e^{-}\ \uparrow\downarrow\ +e^{-} & \mathrm{E} \\
[(TL)_2Ru^{II}(dpp^{-})Rh^{I}(dpp)Ru^{II}(TL)_2]^{4+} & \\
-e^{-}\ \uparrow\downarrow\ +e^{-} & \mathrm{E} \\
[(TL)_2Ru^{II}(dpp^{-})Rh^{I}(dpp^{-})Ru^{II}(TL)_2]^{3+} &
\end{array}
\qquad
\begin{array}{cc}
\mathbf{[(TL)_2Ru^{II}(dpp)Ru^{II}(TL)_2]^{4+}} & \\
-e^{-}\ \uparrow\downarrow\ +e^{-} & \mathrm{E} \\
[(TL)_2Ru^{II}(dpp^{-})Ru^{II}(TL)_2]^{3+} & \\
-e^{-}\ \uparrow\downarrow\ +e^{-} & \mathrm{E} \\
[(TL)_2Ru^{II}(dpp^{2-})Ru^{II}(TL)_2]^{2+} &
\end{array}$$

Figure 3.22: Electrochemical mechanisms for cathodic scans of Ru(II),Rh(III),Ru(II) trimetallics (left) and Ru(II),Ru(II) homobimetallics (right). Chemical formulas written in bold represent the synthesized state. E = electron transfer, C = chemical step, TL = terminal ligand, X = halide, dpp = 2,3-bis(2-pyridyl)pyrazine.

Scan rate (25 mV/s to 1000 mV/s) analyses of the Ru(II),Rh(III) bimetallics were performed to provide insight into the electrochemical processes following each reduction. **Figure 3.23** shows the proposed electrochemical mechanisms with multiple pathways for TL′ = Ph_2phen and $^{t}Bu_2bpy$ bimetallic complexes. Switching the potential after the first reduction (−0.60 V) at multiple scan rates displayed varied i_p^a/i_p^c ratios for TL′ = Ph_2phen and $^tBu_2$bpy, indicating different electrochemical pathways for the bimetallic complexes. For TL′ = Ph_2phen, i_p^a/i_p^c values at scan rates of 25 mV/s and 1000 mV/s were 0.4 and 0.7, respectively, whereas TL′ = $^tBu_2$bpy i_p^a/i_p^c values at scan rates of 25 mV/s and 1000 mV/s were 0.8 and 0.8, respectively. Decreasing the scan rate for TL′ = Ph_2phen displayed minimal i_p^a for the first couple, indicating a chemical step had occurred following reduction. Following pathway IV, the first redox event is labeled as the reduction of (dpp)$\mathbf{Rh^{III}}$$Cl_2$($Ph_2$phen) to form (dpp)$\mathbf{Rh^{II}}$$Cl_2$($Ph_2$phen) with a fast chemical reaction resulting in halide loss to form (dpp)Rh^{II}**Cl**(Ph_2phen), followed by a subsequent electron transfer and chemical reaction to form (dpp)$\mathbf{Rh^{I}}$Cl(Ph_2phen) and (dpp)Rh^{I}(Ph_2phen), respectively. The weaker σ-donating nature of the Ph_2phen TL′ ($pK_{a(1)}$ = 4.84 for protonated Ph_2phen)[17] stabilizes the Rh(dσ*) molecular orbitals by decreasing electron density on the (dpp)$Rh^{III}Cl_2$ subunit and maintains a Rh-based LUMO, as observed with Ru(II),Rh(III),Ru(II) trimetallic complexes. The presence of a less than one electron redox couple (2nd reduction) indicates another electrochemical pathway (pathway III) is present whereby initial reduction to form (dpp)$\mathbf{Rh^{II}}$$Cl_2$($Ph_2$phen) is somewhat stable and reduction at −0.76 V vs. Ag/AgCl forms (dpp)$\mathbf{Rh^{I}}$$Cl_2$($Ph_2$phen) followed by two fast halide loss chemical steps to produce (dpp)$\mathbf{Rh^{I}}$(Ph_2phen).

The TL′ = $^tBu_2$bpy complexes behave electrochemically different than TL′ = Ph_2phen and display at least two electrochemical mechanisms. The first reduction displays similar i_p^a/i_p^c ratios from slow to fast scan rates, indicating no chemical step or a very slow chemical step following reduction. The strong σ-donating character of $^tBu_2$bpy TL′ (pK_a = 5.99 for protonated 4-*tert*-butylpyridine) destabilizes the Rh(dσ*) orbitals, resulting in orbital inversion and provides for a μ-dpp-based LUMO, similar to that observed for Ru(II),Ru(II) homobimetallics. This supports the large return wave of the first reduction (i_p^a) for TL′ = $^tBu_2$bpy bimetallics. For pathway II, the increased electron density of the reduced μ-dpp BL, (**dpp**$^-$)$Rh^{III}Cl_2$($^tBu_2$bpy), is able to weaken the Rh-Cl bond and result in slow halide loss to form (dpp$^-$)Rh^{III}**Cl**($^tBu_2$bpy) followed by very fast electron transfer from μ-dpp$^-$ to Rh^{III}, generating (dpp)$\mathbf{Rh^{II}}$Cl($^tBu_2$bpy). Polypyridyl ligand reduction inducing halide loss to allow for fast electron transfer to a metal-based molecular orbital has been observed for Re(I)-polypyridyl complexes.[146,147] Initial reduction of [Re^{I}($^tBu_2$bpy)$(CO)_3$Cl] is primarily localized on the polypyridyl ligand set and induces halide loss, followed by very fast electron transfer to Re.[146] The current for the second reduction at

−0.76 V increases at faster scan rate is labeled as reduction of (dpp)**Rh^{II}**Cl(^{t}Bu$_2$bpy) to (dpp)**Rh^{I}**Cl(^{t}Bu$_2$bpy) followed by fast halide loss to form (dpp)**Rh^{I}**(^{t}Bu$_2$bpy). Pathway I diverges from pathway II following the first redox wave suggesting formation of (**dpp^{-}**)Rh^{III}Cl$_2$(^{t}Bu$_2$bpy) is stable on the electrochemical time scale and the second redox wave is formation of (dpp^{-})**Rh^{II}**Cl$_2$(^{t}Bu$_2$bpy) followed by fast halide loss, (dpp^{-})Rh^{II}**Cl**(^{t}Bu$_2$bpy). The reduced μ-dpp BL weakens the Rh-Cl bond to induce Cl^{-} loss, followed by very fast intramolecular electron transfer to form (dpp)**Rh^{I}**(^{t}Bu$_2$bpy). The third redox wave in both TL′ = ^{t}Bu$_2$bpy and Ph$_2$phen is labeled as reduction of dpp$^{0/-}$ to form [(TL)$_2$Ru(**dpp^{-}**)**Rh^{I}**(TL′)]$^{2+}$. **Figure 3.24** displays the cathodic scans for [(Ph$_2$phen)$_2$Ru(dpp)RhCl$_2$(Ph$_2$phen)]$^{3+}$ and [(Ph$_2$phen)$_2$Ru(dpp)RhCl$_2$(^{t}bu$_2$bpy)]$^{3+}$ with the electrochemical processes labeled for each redox couple.

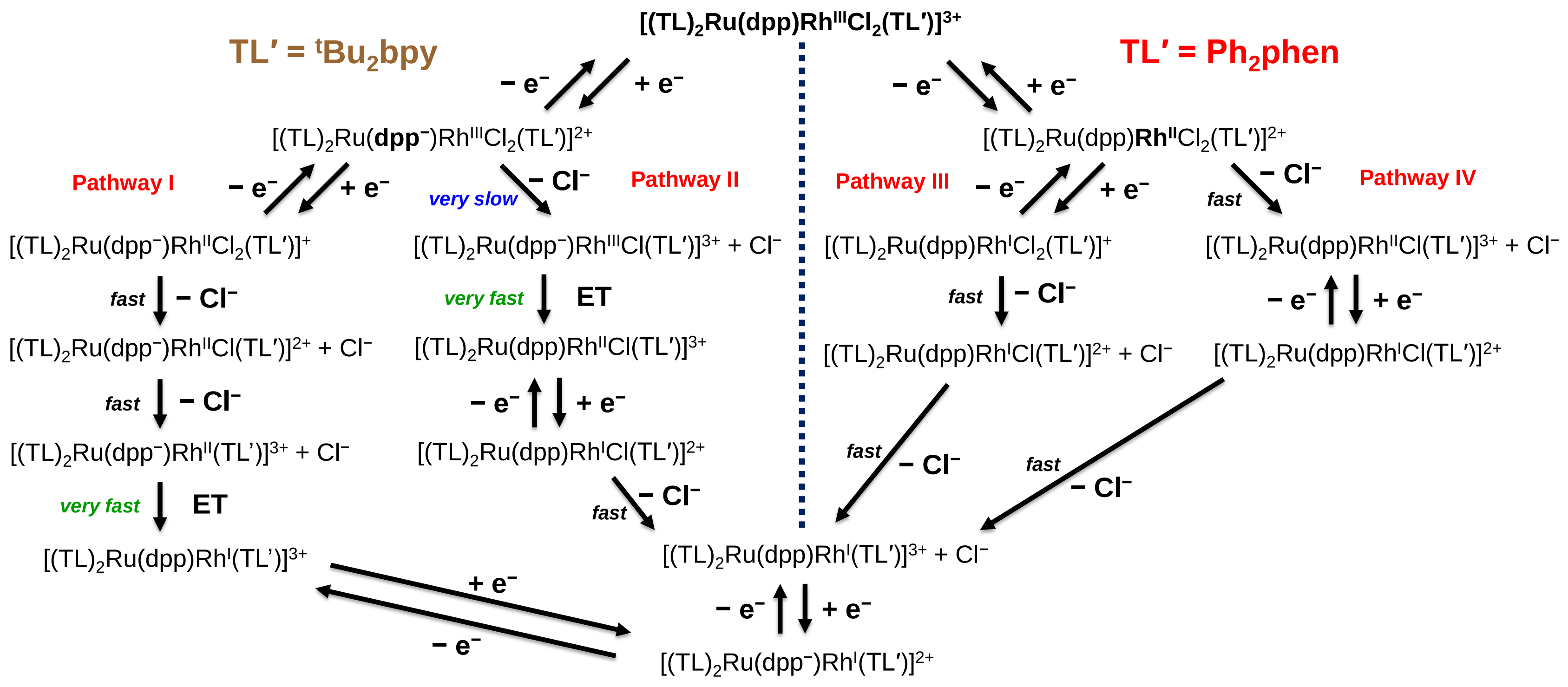

Figure 3.23: Proposed electrochemical mechanisms depicting the various pathways possible upon reduction of Ru(II),Rh(III) bimetallic complexes. Bold chemical formula represents the synthesized state. ET = intramolecular electron transfer, TL = terminal ligand, Ph_2phen = 4,7-diphenyl-1,10-phenanthroline, ${}^tBu_2bpy$ = 4,4′-Di-*tert*-butyl-2,2′-bipyridine, dpp = 2,3-bis(2-pyridyl)pyrazine.

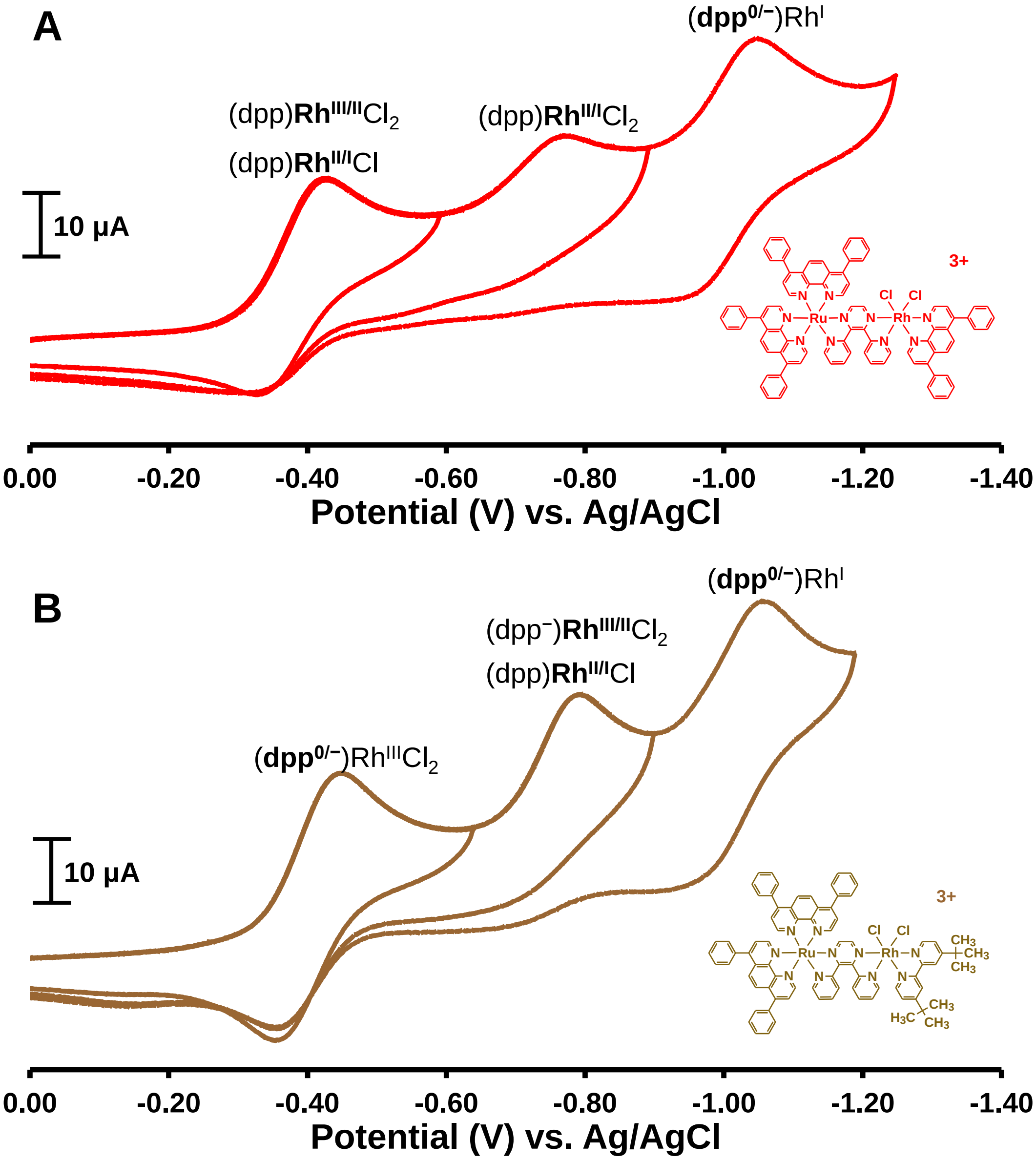

Figure 3.24: Cyclic voltammograms depicting the electrochemical processes of each redox couple for (A) $[(Ph_2phen)_2Ru(dpp)RhCl_2(Ph_2phen)]^{3+}$ (—) and (B) $[(Ph_2phen)_2Ru(dpp)RhCl_2(^tBu_2bpy)]^{3+}$ (—) using a glassy carbon working electrode, Pt wire auxiliary electrode, and Ag wire pseudo-reference electrode (converted to Ag/AgCl using ferrocene as an internal standard; $Fe(C_5H_5)_2^{0/+}$ = 0.46 V vs. Ag/AgCl). Measurements were made at RT in CH_3CN using 0.1 M Bu_4NPF_6 supporting electrolyte at a scan rate of 100 mV/s under an inert Ar atmosphere. $^tBu_2bpy$ = 4,4′-Di-*tert*-butyl-2,2′-bipyridine; Ph_2phen = 4,7-diphenyl-1,10-phenanthroline; dpp = 2,3-bis(2-pyridyl)pyrazine.

The observed electrochemical processes of Ru(II),Rh(III) bimetallic complexes indicate a somewhat complex and interesting electrochemical mechanism with multiple pathways possible. The nature of the TL′ dictates which pathways are involved and require two subsets of mechanisms to account for the non-integer electron couples observed. $[(Ph_2phen)_2Ru(dpp)Rh^{III}Cl_2(Ph_2phen)]^{3+}$ primarily undergoes an irreversible one-electron $Rh^{III/II}$ reduction, followed by halide loss, followed by a second one-electron irreversible reduction ($Rh^{II/I}$) and halide loss to yield $[(Ph_2phen)_2Ru(dpp)Rh^{I}(Ph_2phen)]^{3+}$ (pathway IV in **Figure 3.23**). At fast scan rates, the one-electron reduced species, $[(Ph_2phen)_2Ru(dpp)Rh^{II}Cl_2(Ph_2phen)]^{2+}$, does not lose Cl^- prior to a second one-electron reduction of Rh to form $[(Ph_2phen)_2Ru(dpp)Rh^{I}Cl_2(Ph_2phen)]^{+}$, followed by sequential fast halide loss (pathway III in **Figure 3.23**). The final observed reduction within the potential window is a reversible one-electron $dpp^{0/-}$ reduction. The proposed electrochemical mechanism for TL′ = Ph_2phen is an ECECE mechanism for pathway IV and an EECCE mechanism for pathway III. Conversely, $[(Ph_2phen)_2Ru(dpp)RhCl_2(^tBu_2bpy)]^{3+}$ and $[(bpy)_2Ru(dpp)RhCl_2(^tBu_2bpy)]^{3+}$ undergo a quasi-reversible one-electron $dpp^{0/-}$ first reduction with competing mechanisms thereafter. Slow halide loss followed by very fast intramolecular electron transfer from dpp to Rh yields $[(TL)_2Ru(dpp)Rh^{II}Cl(^tBu_2bpy)]^{3+}$ (pathway II in **Figure 3.23**). Halide loss on reduced diimine complexes has been proposed for $[Re^{I}(^tBu_2bpy)(CO)_3Cl]$.[146] The competing mechanism indicates the reduced μ-dpp species, $[(TL)_2Ru(dpp^-)Rh^{III}Cl_2(^tBu_2bpy)]^{2+}$, is stable on the electrochemical time scale for the first reduction (pathway I in **Figure 3.23**). The second reduction in pathway II is an irreversible one-electron $Rh^{II/I}$ reduction followed by fast halide loss to yield $[(TL)_2Ru(dpp)Rh^{I}(^tBu_2bpy)]^{3+}$ which undergoes a reversible one-electron $dpp^{0/-}$ reduction to yield $[(TL)_2Ru(dpp^-)Rh^{I}(^tBu_2bpy)]^{2+}$. Alternatively, pathway I displays the second reduction as $Rh^{III/II}$ followed by two fast halide losses and intramolecular electron transfer from dpp to Rh to form $[(TL)_2Ru(dpp)Rh^{I}(^tBu_2bpy)]^{2+}$ and the final reduction being $dpp^{0/-}$. The proposed electrochemical mechanism for TL′ = $^tBu_2$bpy is an ECECE mechanism with an intramolecular electron transfer from dpp to Rh following the first chemical step for pathway II and an EECCE mechanism with intramolecular electron transfer from dpp to Rh following the second chemical step for pathway I.

The nearly isoenergetic nature of the electron-deficient dpp(π*) and Rh(dσ*) molecular orbitals within this $[(TL)_2Ru(dpp)RhCl_2(TL')]^{3+}$ molecular architecture are tuned by TL′ identity and afford orbital inversion where μ-dpp is the LUMO in TL = $^tBu_2$bpy complexes and Rh is the

LUMO in TL′ = Ph_2phen complexes. One final comment on the electrochemistry of Ru(II),Rh(III) bimetallics is the observation of separate Rh redox couples for $Rh^{III/II}$ and $Rh^{II/I}$ compared to the overlapping Rh redox couples for Ru(II),Rh(III),Ru(II) trimetallics. The large bulk of the second $(dpp)Ru^{II}(TL)_2$ subunit surrounding Rh within the trimetallics presents conditions favorable for fast halide loss providing an irreversible couple at slow and fast scan rates, **Figures 3.25 and 3.26**. The steric bulk at Rh should weaken the Rh-halide bond upon addition of charge density into a primarily metal-based anti-bonding orbital. Also contributing to the observed electrochemistry is the weak σ-donating character of the second bridged dpp unit that should allow for a second Rh reduction at more positive potential. The title Ru(II),Rh(III) bimetallic complexes lack the excess steric bulk at Rh and the very weak σ-donating μ-dpp BL so that more stable $Rh^{II}Cl_2$ containing species are observed on the electrochemical time scale.

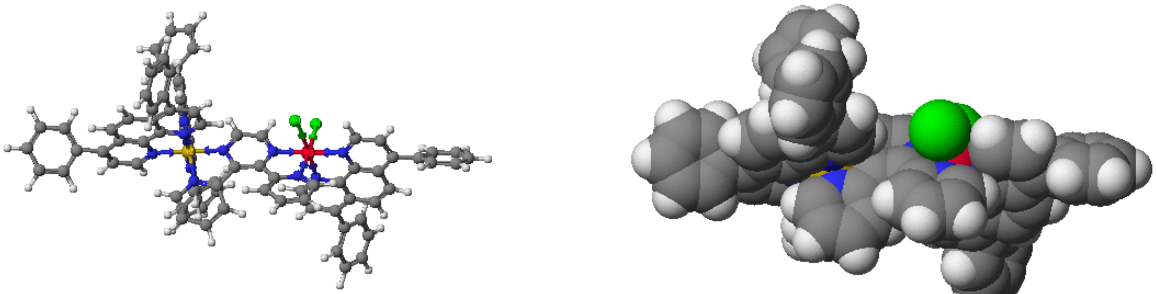

$[(Ph_2phen)_2Ru(dpp)RhCl_2(Ph_2phen)]^{3+}$

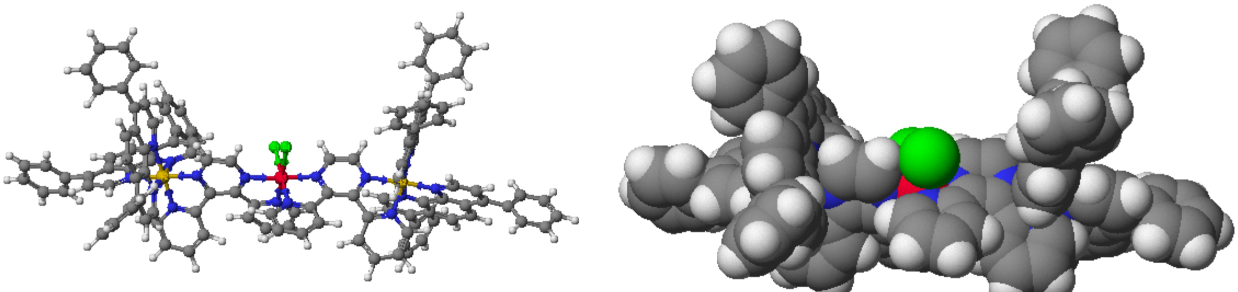

$[\{(Ph_2phen)_2Ru(dpp)\}_2RhCl_2]^{5+}$

Figure 3.25: Three-dimensional structures showing the size disparity for $[(Ph_2phen)_2Ru(dpp)RhCl_2(Ph_2phen)]^{3+}$ bimetallic and $[\{(Ph_2phen)_2Ru(dpp)\}_2RhCl_2]^{5+}$ trimetallic complexes. Left: ball and stick model; Right: space filling model. Structures generated using Scigress 7.7.1 molecular modeling software; red (Rh); gold (Ru); green (Cl); blue (N); gray (C); white (H). Ph_2phen = 4,7-diphenyl-1,10-phenanthroline; dpp = 2,3-bis(2-pyridyl)pyrazine.

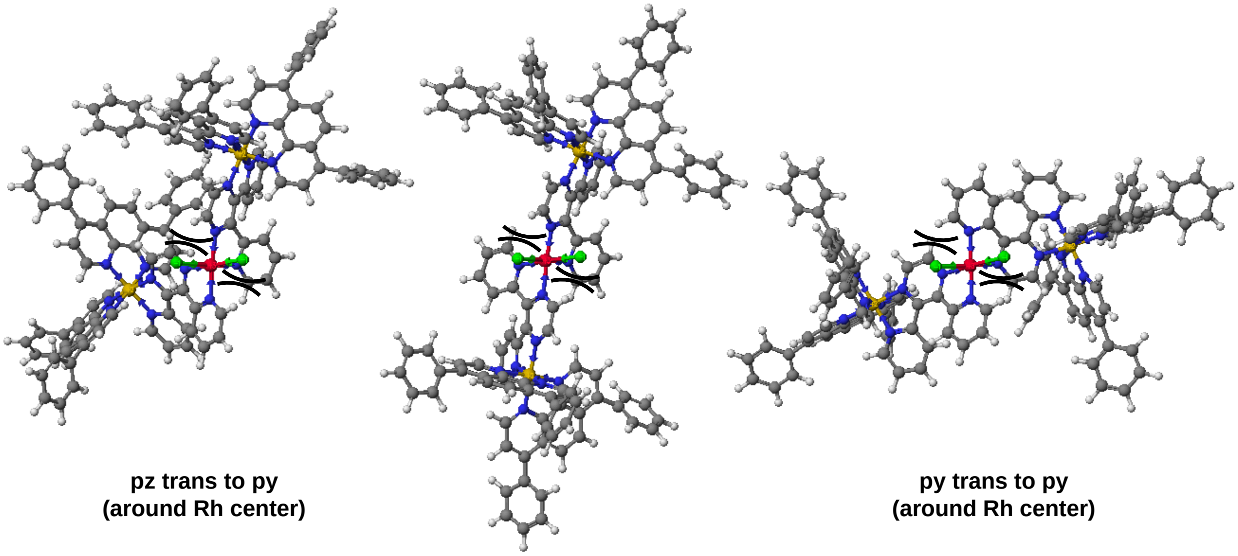

pz trans to py
(around Rh center)

pz trans to pz
(around Rh center)

py trans to py
(around Rh center)

Figure 3.26: Three-dimensional structures showing three possible stereoisomers and the Cl/H steric interactions at the Rh metal center within the $[\{(Ph_2phen)_2Ru(dpp)\}_2RhCl_2]^{5+}$ trimetallic complex. Structures generated using Scigress 7.7.1 molecular modeling software; red (Rh); gold (Ru); green (Cl); blue (N); gray (C); white (H). Ph_2phen = 4,7-diphenyl-1,10-phenanthroline; dpp = 2,3-bis(2-pyridyl)pyrazine; pz = pyrazine; py = pyridine.

3.3.2. Light Absorbing Properties

The $[(TL)_2Ru(dpp)RhCl_2(TL')]^{3+}$ bimetallic complexes are efficient light absorbers throughout the UV and visible regions with TL/TL′ modification tuning the light absorption capabilities, **Figure 3.27**. **Table 3.7** summarizes the dominant transitions for Ru(II),Rh(III) bimetallics, as well as the $[(Ph_2phen)_2Ru(dpp)]^{2+}$ monometallic and $[\{(Ph_2phen)_2Ru(dpp)\}_2RhCl_2]^{5+}$ trimetallic complexes for comparison.

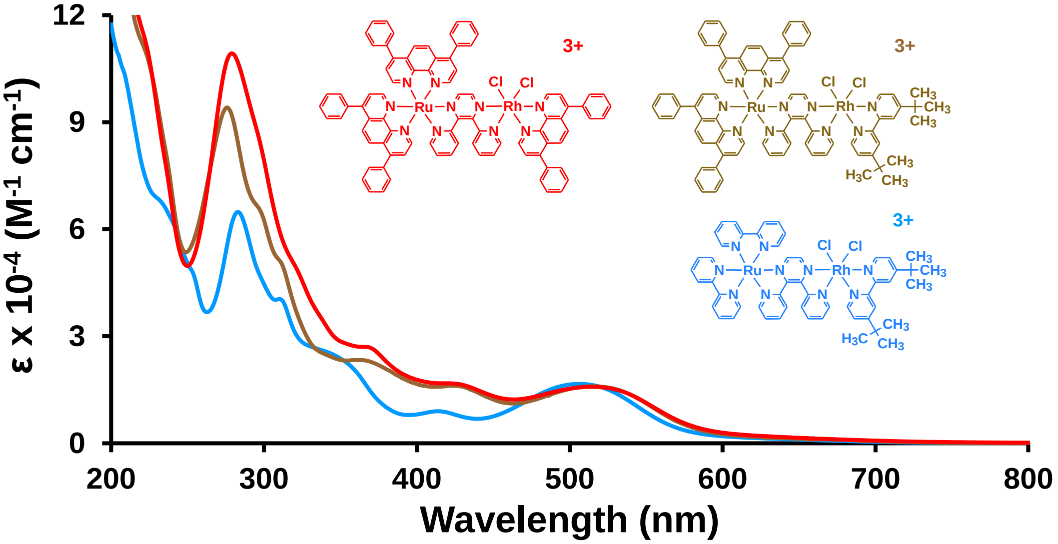

Figure 3.27: Electronic absorption spectra of [(Ph$_2$phen)$_2$Ru(dpp)RhCl$_2$(Ph$_2$phen)](PF$_6$)$_3$ (—), [(Ph$_2$phen)$_2$Ru(dpp)RhCl$_2$(^{t}Bu$_2$bpy)](PF$_6$)$_3$ (—), and [(bpy)$_2$Ru(dpp)RhCl$_2$(^{t}Bu$_2$bpy)](PF$_6$)$_3$ (—) measured at RT in CH$_3$CN using a 1 cm quartz cuvette. Ph$_2$phen = 4,7-diphenyl-1,10-phenanthroline; ^{t}Bu$_2$bpy = 4,4′-Di-*tert*-butyl-2,2′-bipyridine; bpy = 2,2′-bipyridine; dpp = 2,3-bis(2-pyridyl)pyrazine.

Table 3.7: Light Absorbing Properties of Ru(II),Rh(III) Bimetallic Complexes and TL = Ph$_2$phen Monometallic and Trimetallic Complexes

Complex ^{a}	λ^{abs} (nm)	ε x 10^{-4} (M^{-1}cm^{-1})	Assignment
[(bpy)$_2$Ru(dpp)RhCl$_2$(^{t}Bu$_2$bpy)]$^{3+}$	284	6.5	bpy π→π*
	340	2.6	dpp π→π*
	414	0.9	Ru(dπ) → bpy(π*) CT
	506	1.7	Ru(dπ) → dpp(π*) CT
[(Ph$_2$phen)$_2$Ru(dpp)RhCl$_2$(^{t}Bu$_2$bpy)]$^{3+}$	278	9.4	Ph$_2$phen π→π*
	362	2.3	dpp π→π*
	422	1.6	Ru(dπ) → Ph$_2$phen(π*) CT
	514	1.6	Ru(dπ) → dpp(π*) CT
[(Ph$_2$phen)$_2$Ru(dpp)RhCl$_2$(Ph$_2$phen)]$^{3+}$	278	10.9	Ph$_2$phen π→π*
	362	2.7	dpp π→π*
	422	1.7	Ru(dπ) → Ph$_2$phen(π*) CT
	514	1.6	Ru(dπ) → dpp(π*) CT

$[(Ph_2phen)_2Ru(dpp)]^{2+}$ [b]	278	10.2	Ph_2phen $\pi \rightarrow \pi^*$
	314	3.7	dpp $\pi \rightarrow \pi^*$
	438	2.1	Ru(dπ) → Ph_2phen(π^*) CT
	470	1.9	Ru(dπ) → dpp(π^*) CT
$[\{(Ph_2phen)_2Ru(dpp)\}_2RhCl_2]^{5+}$	278	18.5	Ph_2phen $\pi \rightarrow \pi^*$
	366	4.8	dpp $\pi \rightarrow \pi^*$
	426	3.5	Ru(dπ) → Ph_2phen(π^*) CT
	516	3.2	Ru(dπ) → dpp(π^*) CT

[a] Measured in CH_3CN at RT using a 1 cm quartz cuvette. Ph_2phen = 4,7-diphenyl-1,10-phenanthroline; $^tBu_2$bpy = 4,4′-Di-*tert*-butyl-2,2′-bipyridine; bpy = 2,2′-bipyridine; dpp = 2,3-bis(2-pyridyl)pyrazine. Adapted from ref [133,144].
[b] Values consistent with those in reference [55].

As observed with the other dpp-bridged, Ru(II)-polypyridyl molecular architectures, the UV region is dominated by TL and BL $\pi \rightarrow \pi^*$ ^{1}IL transitions while the visible is dominated by Ru(dπ)→TL(π^*) and Ru(dπ)→BL(π^*) ^{1}MLCT transitions. The number and identity of the TL and TL′ dictate the intensity of the observed transitions within the UV region with TL or TL′ = Ph_2phen displaying enhanced molar absorptivity. For $[(Ph_2phen)_2Ru(dpp)RhCl_2(Ph_2phen)]^{3+}$ and $[(Ph_2phen)_2Ru(dpp)RhCl_2(^tBu_2bpy)]^{3+}$, the intense absorption at λ = 278 nm (ε = 109,000 $M^{-1}cm^{-1}$ and ε = 94,000 $M^{-1}cm^{-1}$, respectively) is attributed to the Ph_2phen $\pi \rightarrow \pi^*$ transitions. Substitution of TL = Ph_2phen for bpy shifts the TL $\pi \rightarrow \pi^*$ maximum to 284 nm with a simultaneous decrease in ε value (65,000 $M^{-1}cm^{-1}$). As shown in **Figure 3.28** using $[(Ph_2phen)_2Ru(dpp)RhCl_2(Ph_2phen)]^{3+}$ as an example, covalent coupling of the dpp BL to two electropositive metal centers stabilizes the dpp-based π^* molecular orbitals resulting in a red-shift of the observed dpp $\pi \rightarrow \pi^*$ transitions (λ = 362 nm) when compared with the $[(Ph_2phen)_2Ru(dpp)]^{2+}$ monometallic analogue (λ = 310 nm). This trend is also observed for $[(Ph_2phen)_2Ru(dpp)RhCl_2(^tBu_2bpy)]^{3+}$ (λ = 362 nm) and $[(bpy)_2Ru(dpp)RhCl_2(^tBu_2bpy)]^{3+}$ (λ = 340 nm) complexes. Coordinating the $Rh^{III}Cl_2(Ph_2phen)$ subunit to $[(Ph_2phen)_2Ru(dpp)]^{2+}$ also redistributes the Ph_2phen $\pi \rightarrow \pi^*$ transitions and enhances underlying dpp $\pi \rightarrow \pi^*$ transitions, providing for a wider breadth of intense absorptivity.

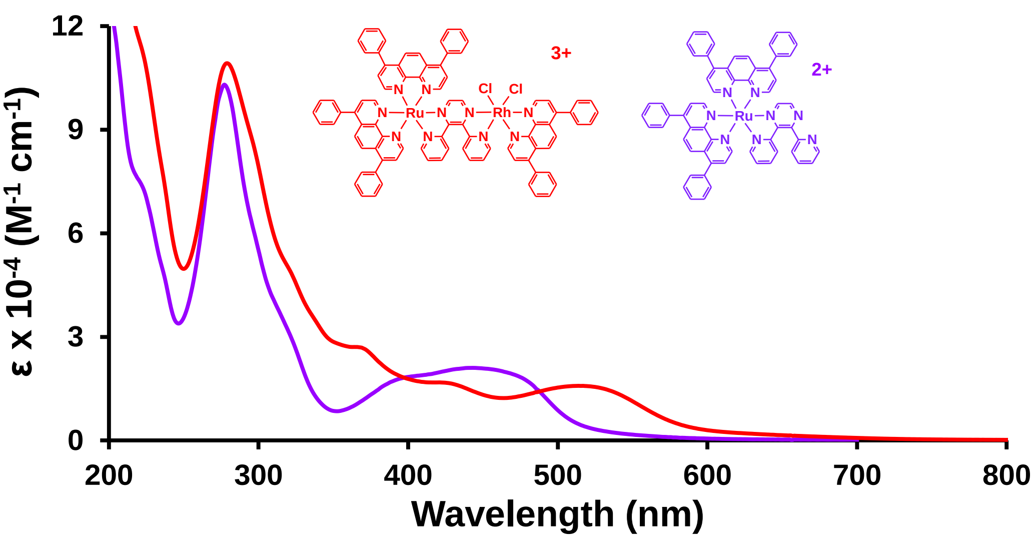

Figure 3.28: Electronic absorption spectra of $[(Ph_2phen)_2Ru(dpp)RhCl_2(Ph_2phen)](PF_6)_3$ (—) and $[(Ph_2phen)_2Ru(dpp)](PF_6)_2$ (—) measured at RT in CH_3CN using a 1 cm quartz cuvette. Ph_2phen = 4,7-diphenyl-1,10-phenanthroline; dpp = 2,3-bis(2-pyridyl)pyrazine.

The Ru(II),Rh(III) bimetallic complexes possess Ru(dπ)→ligand(π*) MLCT transitions in the visible region for each acceptor ligand with the lowest energy transition assigned as Ru(dπ)→dpp(π*) ^{1}MLCT. Comparing $[(Ph_2phen)_2Ru(dpp)RhCl_2(^tBu_2bpy)]^{3+}$ and $[(Ph_2phen)_2Ru(dpp)RhCl_2(Ph_2phen)]^{3+}$ shows the Ru(dπ)→Ph_2phen(π*) ^{1}MLCT transition centered at 422 nm (ε = 17,000 $M^{-1}cm^{-1}$) and the Ru(dπ)→dpp(π*) ^{1}MLCT transition centered at 514 nm (ε = 16,000 $M^{-1}cm^{-1}$) for both complexes. This observation suggests the identity of the TL′ attached to Rh does not strongly influence or perturb the light absorbing properties of the Ru(II),Rh(III) bimetallics in the visible region. Changing the TL attached to Ru influences the visible region in a significant manner. Typically bpy systems have rather low intensity which results in spectral gaps in the electronic absorption spectrum in the ca. 450 nm region with the Ru(dπ)→bpy(π*) CT transition centered at 414 nm (ε = 9,000 $M^{-1}cm^{-1}$) in the $[(bpy)_2Ru(dpp)RhCl_2(^tBu_2bpy)]^{3+}$ bimetallic complex. The Ru(dπ)→dpp(π*) CT transition shifts to higher energy (506 nm, ε = 17,000 $M^{-1}cm^{-1}$) which is paralleled to the stabilization of the Ru(dπ)-based molecular orbitals with TL = bpy as observed in the electrochemistry.

The molar absorptivity for the Ru(II),Rh(III) bimetallics is roughly one half of the analogous Ru(II),Rh(III),Ru(II) trimetallics, indicating the nearly additive character of the light absorbing components. **Figure 3.29** displays this relationship between $[(Ph_2phen)_2Ru(dpp)RhCl_2(Ph_2phen)]^{3+}$ and $[\{(Ph_2phen)_2Ru(dpp)\}_2RhCl_2]^{5+}$ which have ε = 16,000 and 32,000 $M^{-1}cm^{-1}$, respectively, for the Ru(dπ)→dpp(π*) ^{1}MLCT transition. Substituting one of the Ru(II) LA moieties within the trimetallic architecture for a TL′ to generate a Ru(II),Rh(III) bimetallic does not substantially perturb the energy of the transitions. As with the Ru(II),Rh(III),Ru(II) trimetallic complexes, the lowest energy transition is Ru(dπ)→dpp(π*) ^{1}MLCT in character and should populate a Ru(dπ)→dpp(π*) ^{3}MLCT ES upon photoexcitation, allowing for electron density to shift towards the Rh(III) electron accepting site.

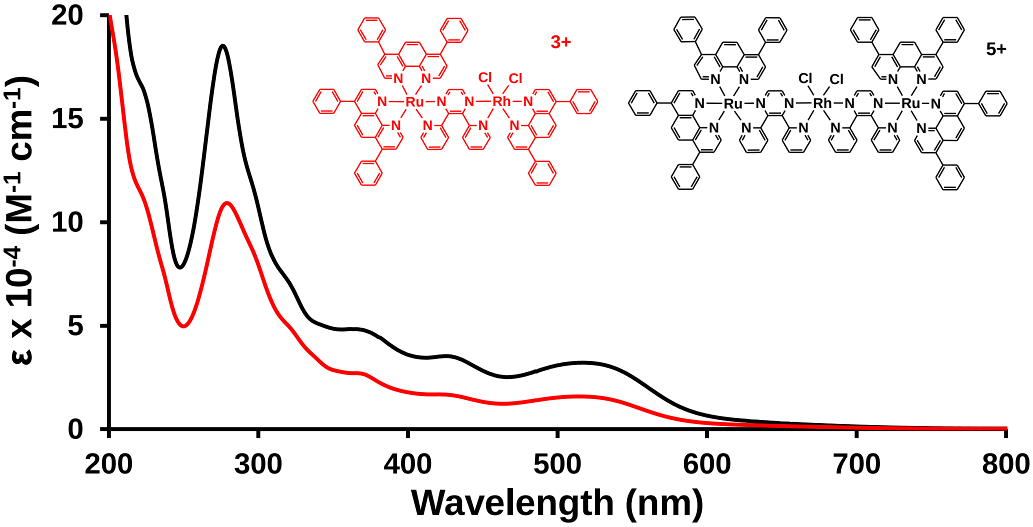

Figure 3.29: Electronic absorption spectra of $[(Ph_2phen)_2Ru(dpp)RhCl_2(Ph_2phen)](PF_6)_3$ (—) and $[\{(Ph_2phen)_2Ru(dpp)\}_2RhCl_2](PF_6)_5$ (—) measured at RT in CH_3CN using a 1 cm quartz cuvette. Ph_2phen = 4,7-diphenyl-1,10-phenanthroline; dpp = 2,3-bis(2-pyridyl)pyrazine.

3.3.3. Excited State Properties

Steady-state and time-resolved luminescence spectroscopy were utilized to gain insight into the complex excited state dynamics of the Ru(II),Rh(III) bimetallic complexes and these properties are summarized in **Table 3.8**. As with the Ru(II),Rh(III),Ru(II) trimetallic complexes, the Ru(II),Ru(II) bimetallic complexes were used as a model for the Ru(II),Rh(III) bimetallics in order to calculate rate constants for intramolecular electron transfer as shown in **Equation 3.3** above. Photoexcitation throughout the UV and visible populate multiple excited states that relax to populate weakly emissive ^{3}MLCT excited states that are Ru(dπ)→μ-dpp(π*) in nature. **Figure 3.30** shows a simplified Jablonski state diagram and the various deactivation pathways possible.

Table 3.8. Photophysical Properties of Ru(II),Rh(III) Bimetallic and Ru(II),Ru(II) Homobimetallic Complexes

	RT [a]						77 K [b]	
Complex	λ^{em} (nm)[c]	Φ^{em} (10^{-4})[d]	τ (ns)[e]	k_r (10^3 s^{-1})	k_{nr} (10^6 s^{-1})	k_{et} (10^7 s^{-1})	λ^{em} (nm)[c]	τ (μs)[e]
$[(Ph_2phen)_2Ru(dpp)RhCl_2(^tBu_2bpy)]^{3+}$	774	2.7	45	9.0	5.3	1.7	706	2.1
$[(Ph_2phen)_2Ru(dpp)RhCl_2(Ph_2phen)]^{3+}$	774	2.9	43	9.0	5.3	1.7	706	2.1
$[(bpy)_2Ru(dpp)RhCl_2(^tBu_2bpy)]^{3+}$	782	1.9	39	7.9	7.9	1.8	720	1.8
$[\{(Ph_2phen)_2Ru\}_2(dpp)]^{4+}$	754	17.3	192	9.0	5.3	--	698	2.0
$[\{(bpy)_2Ru\}_2(dpp)]^{4+}$	758	9.8	126	7.9	7.9	--	715	2.0

[a] Measured in deoxygenated CH_3CN at RT in a 1 cm quartz cuvette. Ph_2phen = 4,7-diphenyl-1,10-phenanthroline; $^tBu_2bpy$ = 4,4′-Di-*tert*-butyl-2,2′-bipyridine; bpy = 2,2′-bipyridine; dpp = 2,3-bis(2-pyridyl)pyrazine. Adapted from ref [133,137].

[b] Measured in 4:1 EtOH:MeOH at 77 K in a quartz finger dewar.

[c] Emission corrected for PMT response using manufacturer-provided correction file.

[d] Error associated with quantum yield measurements ± 5%.

[e] Error associated with lifetime measurements ± 5%.

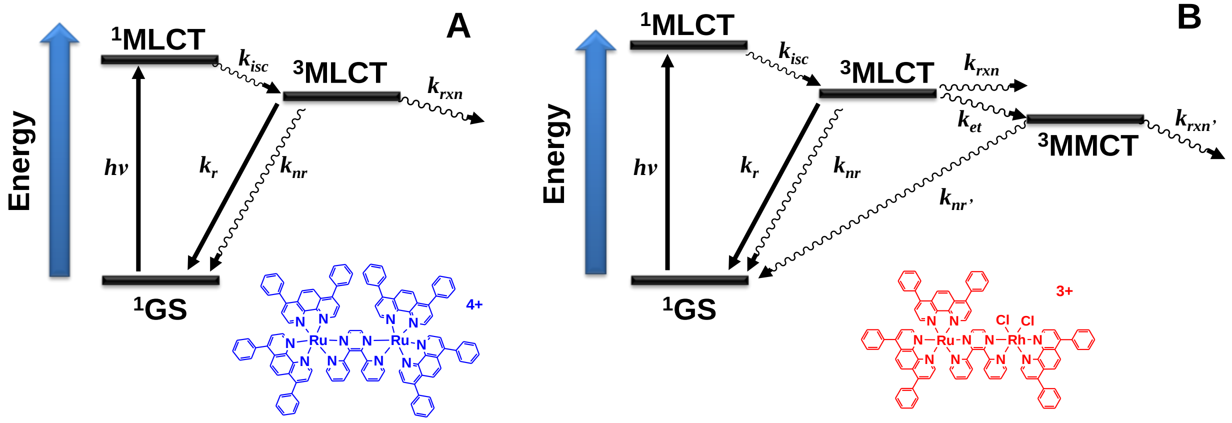

Figure 3.30: Simplified Jablonski state diagrams for the Ru(II),Ru(II) bimetallic model complex $[\{(Ph_2phen)_2Ru\}_2(dpp)](PF_6)_4$ (A) and the Ru(II),Rh(III),Ru(II) trimetallic complex $[(Ph_2phen)_2Ru(dpp)RhCl_2(Ph_2phen)](PF_6)_3$ (B). hν = photoexcitation, k_{isc} = intersystem crossing rate constant, k_r = radiative deactivation rate constant, k_{nr} or $k_{nr'}$ = non-radiative deactivation rate constant, k_{et} = intramolecular electron transfer rate constant, k_{rxn} or $k_{rxn'}$ = photochemical reaction rate constant.

Room temperature luminescence measurements (**Figure 3.31**) display the low-energy (λ) and low quantum yield of emission (Φ^{em}) of the ^{3}MLCT excited states, as well as the short excited state lifetime (τ) of the Ru(II),Rh(III) bimetallic complexes in CH_3CN when compared to the Ru(II),Ru(II) homobimetallic models. $[(Ph_2phen)_2Ru(dpp)RhCl_2(Ph_2phen)]^{3+}$ (λ = 774 nm; Φ^{em} = 2.9 x 10^{-4}; τ = 43 ns), $[(Ph_2phen)_2Ru(dpp)RhCl_2(^tBu_2bpy)]^{3+}$ (λ = 774 nm; Φ^{em} = 2.7 x 10^{-4}; τ = 45 ns), and $[(bpy)_2Ru(dpp)RhCl_2(^tBu_2bpy)]^{3+}$ (λ = 782 nm; Φ^{em} = 1.9 x 10^{-4}; τ = 39 ns) display similar properties that are modulated by Ru(II)-TL modification as observed for analogous Ru(II),Rh(III),Ru(II) trimetallic and Ru(II),Ru(II) bimetallic complexes. Modifying $[(Ph_2phen)_2Ru(dpp)RhCl_2(TL')]^{3+}$ from TL′ = Ph_2phen to $^tBu_2bpy$ at the Rh(III) site does not significantly affect the ES dynamics for Ru(II),Rh(III) bimetallics, further emphasizing the influence from the Ru(II) LA subunit.

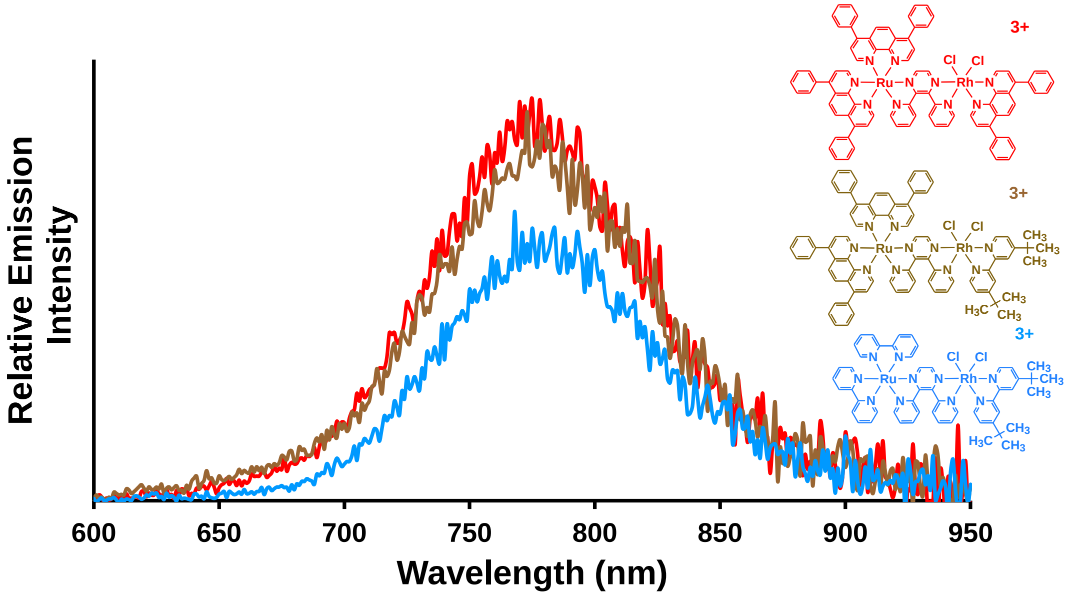

Figure 3.31: Emission spectra of $[(Ph_2phen)_2Ru(dpp)RhCl_2(Ph_2phen)](PF_6)_3$ (—), $[(Ph_2phen)_2Ru(dpp)RhCl_2(^tBu_2bpy)](PF_6)_3$ (—), and $[(bpy)_2Ru(dpp)RhCl_2(^tBu_2bpy)](PF_6)_3$ (—) excited at 540 nm (absorbance = 0.30), measured in deoxygenated CH_3CN at RT using a 1 cm quartz cuvette, and emission profile corrected for PMT response. Excitation and emission monochromator compartment entrance and exit slit widths set to 1.5 mm (corresponds to ± 6 nm). Ph_2phen = 4,7-diphenyl-1,10-phenanthroline; $^tBu_2bpy$ = 4,4′-Di-*tert*-butyl-2,2′-bipyridine; dpp = 2,3-bis(2-pyridyl)pyrazine.

Emission from the Ru(dπ)→μ-dpp(π*) ^{3}MLCT ES is quenched ~85-90% of the analogous TL Ru(II),Ru(II) bimetallic model (**Figure 3.32**), suggesting the presence of a lower-lying ES. The ^{3}MLCT excited state is efficiently deactivated due to intramolecular electron transfer (k_{et}) to populate the Ru(dπ)→Rh(dσ*) ^{3}MMCT ES at room temperature. Using $[\{(Ph_2phen)_2Ru\}_2(dpp)]^{4+}$ (λ = 754 nm; $\Phi^{em} = 1.7 \times 10^{-3}$; τ = 192 ns) and $[\{(bpy)_2Ru\}_2(dpp)]^{4+}$ (λ = 758 nm; $\Phi^{em} = 9.8 \times 10^{-4}$; τ = 126 ns) bimetallic complexes as model systems for Ru(II),Rh(III) bimetallics, the rate constant for k_{et} was calculated to be between 1.7-1.8 x 10^7 s^{-1} given the assumption that radiative (k_r) and non-radiative (k_{nr}) rate constants are the same for the two systems. This assumption is made as the energy and nature of the emitting Ru(dπ)→μ-dpp(π*) CT state are similar between Ru(II),Ru(II) and Ru(II),Rh(III) bimetallic complexes and display similar excited state lifetimes at 77 K. Deactivation of the formally Ru(dπ)→dpp(π*) ^{3}MLCT excited state in the form of intramolecular electron transfer to populate the Ru(dπ)→Rh(dσ*) ^{3}MMCT excited state is supported by low temperature lifetime measurements (77 K) in an alcoholic rigid glass matrix. Inhibition of intramolecular electron transfer is observed at 77 K for the Ru(II),Rh(III) bimetallic complexes as the excited state lifetime of the emissive ^{3}MLCT state is similar to that of the Ru(II),Ru(II) bimetallic models which do not undergo intramolecular electron transfer. These results indicate the extremely close energetic proximity of the dpp(π*) and Rh(dσ*) orbitals and Ru(dπ)→μ-dpp(π*) ^{3}MLCT vs. Ru(dπ)→Rh(dσ*) ^{3}MMCT states in this motif. While proposing lowest-lying Ru(dπ)→Rh(dσ*) ^{3}MMCT states is in conflict with the observed electrochemistry for TL′ = ^{t}Bu$_2$bpy complexes, the nearly isoenergetic dpp(π*) and Rh(dσ*) orbitals should allow for thermal population of ^{3}MMCT states at ambient temperatures. The room temperature and 77 K analyses of TL′ = ^{t}Bu$_2$bpy and Ph$_2$phen complexes are similar indicating that population of ^{3}MLCT and ^{3}MMCT states occurs for both sets of complexes. Population of photoactive Ru(dπ)→μ-dpp(π*) ^{3}MLCT and Ru(dπ)→Rh(dσ*) ^{3}MMCT states allows for generation of a photoreduced Rh species in the presence of a sacrificial electron donor and affords electron collection on the Rh metal center to deliver to a substrate.

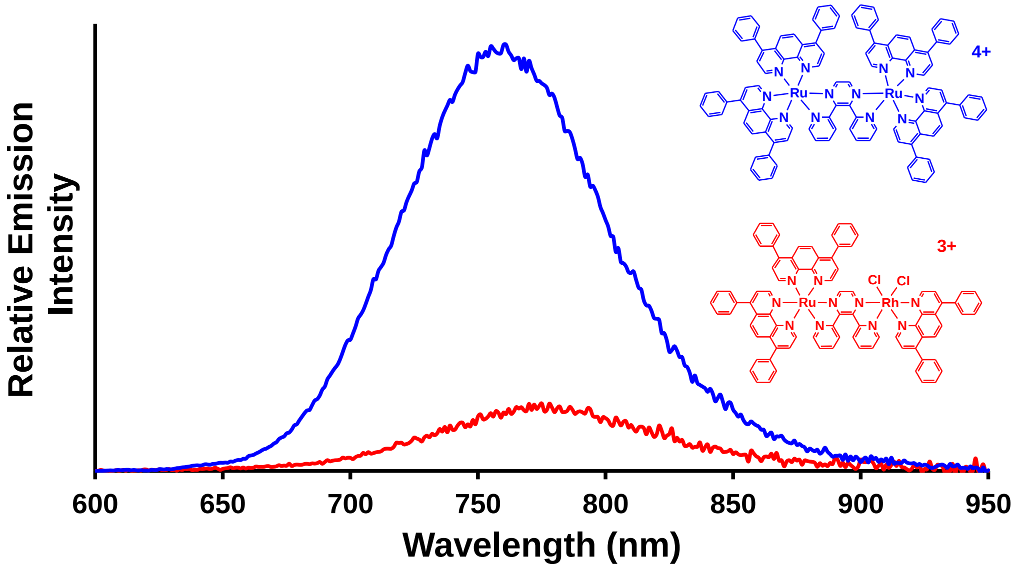

Figure 3.32: Emission spectra of $[(Ph_2phen)_2Ru(dpp)RhCl_2(Ph_2phen)]^{3+}$ (—) and $[\{(Ph_2phen)_2Ru\}_2(dpp)]^{4+}$ (—) excited at 540 nm (absorbance = 0.30), measured in deoxygenated CH_3CN at RT using a 1 cm quartz cuvette, and emission profile corrected for PMT response. Excitation and emission monochromator compartment entrance and exit slit widths set to 1.5 mm (corresponds to ± 6 nm). Ph_2phen = 4,7-diphenyl-1,10-phenanthroline; dpp = 2,3-bis(2-pyridyl)pyrazine.

3.3.4. Photocatalytic H_2 Production

Given the electrochemical, light absorbing, and excited state properties of Ru(II),Rh(III) bimetallic complexes are similar to Ru(II),Rh(III),Ru(II) trimetallic complexes that function as photocatalysts for the reduction of H_2O to H_2, photolysis studies were performed using the Ru(II),Rh(III) bimetallics in an effort to assess their photocatalytic functioning for H_2O reduction. The bimetallic complex $[(phen)_2Ru(dpp)Rh^{III}Cl_2(bpy)]^{3+}$, synthesized and characterized by Jing Wang, was initially assayed for photocatalytic functioning as it displayed photoinitiated electron collection at the Rh metal center to form $[(phen)_2Ru(dpp)Rh^{I}(bpy)]^{+}$.[148] Photoexcitation at 470 nm using 110 μM bimetallic, 1.5 M DMA, 0.62 M H_2O, and 110 μM $[DMAH^+][CF_3SO_3^-]$ in a CH_3CN solvent system produced no observable H_2 after two hours photolysis. Exhaustive electrochemical analyses of $[(phen)_2Ru(dpp)RhCl_2(bpy)]^{3+}$ performed by Jing Wang, coupled with product analysis using ESI-MS, displayed evidence of Ru(II),Rh(I)-Rh(I),Ru(II) dimerization within the bimetallic species upon bulk electrolysis past the Rh reduction (−0.45 V vs. Ag/AgCl). The same bulk electrolysis analysis performed using the analogous trimetallic $[\{(phen)_2Ru(dpp)\}_2RhCl_2]^{5+}$, a known H_2O reduction photocatalyst, did not show evidence of Rh(I)-Rh(I) dimerization. The presence of dimerization in the reduced bimetallic but not reduced trimetallic species, **Figure 3.33**, suggests the steric hindrance enforced by the second $(dpp)Ru^{II}(TL)_2$ subunit inhibits dimerization. Low-valent Rh polypyridyl complexes such as $[Rh^{III}(bpy)_3]^{3+}$ and $[Rh^{III}(bpy)_2Cl_2]^+$ are known to undergo two one-electron reductions with subsequent ligand loss to form $[Rh^I(bpy)_2]^+$. Production of Rh(I) is followed by dimerization to produce $[Rh^I(bpy)_2]_2^{2+}$ and $[Rh^I(bpy)_2]_2H^{3+}$.[24,149] The Rh(I) dimers are expected to inhibit efficient photocatalysis throughout the H_2O reduction catalytic cycle due to the competing Rh-Rh dimerization as a deactivating pathway. The catalytic inertness of Rh(I)-Rh(I) dimers was observed with the bimetallic complex $[(phen)_2Ru(dpp)RhCl_2(bpy)]^{3+}$, emphasizing the need for steric bulk surrounding the reduced Rh(I) reactive metal center.

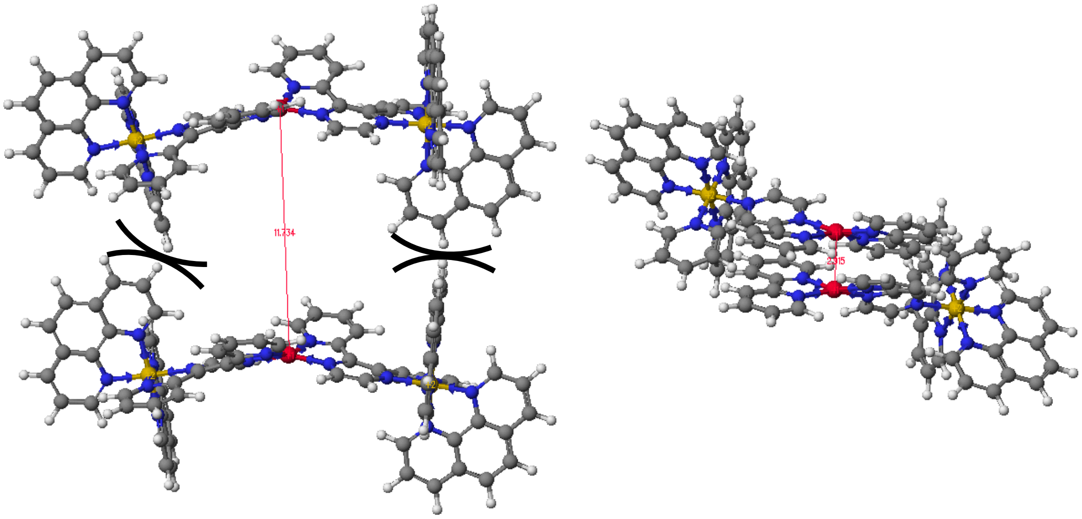

$[\{(phen)_2Ru(dpp)\}_2Rh^I]^{5+}$ dimer inhibition (Rh(I)-Rh(I) distance >10 Å)

$[(phen)_2Ru(dpp)Rh^I(bpy)]^{3+}$ dimerization (Rh(I)-Rh(I) distance ~2.9-3.0 Å)

Figure 3.33: Three-dimensional structures representing dimer inhibition of $[\{(phen)_2Ru(dpp)\}_2Rh^I]^{5+}$ (left) and Rh(I)-Rh(I) dimerization of $[(phen)_2Ru(dpp)Rh^I(bpy)]^{3+}$ (right). Structures generated using Scigress 7.7.1 molecular modeling software; red (Rh); gold (Ru); blue (N); gray (C); white (H). phen = 1,10-phenanthroline; bpy = 2,2′-bipyridine; dpp = 2,3-bis(2-pyridyl)pyrazine.

In an effort to avoid the Rh(I)-Rh(I) dimerization deactivating pathway, the TL′ coordinated to Rh was modified to incorporate a sterically bulky bidentate polypyridyl terminal ligand, while the light absorbing properties were attenuated through Ru(II)-TL modification. Inclusion of *tert*-butyl substituents at the 4 and 4′ positions of 2,2′-bipyridine is hypothesized to provide the necessary steric bulk to inhibit dimerization, **Figure 3.34**. However, electrochemical analysis and initial photolysis results using $[(bpy)_2Ru(dpp)RhCl_2({}^tBu_2bpy)]^{3+}$ indicate that the electronic modification to the Rh environment due to increased electron-density from the *tert*-butyl substituents affords orbital inversion and inefficient photocatalysis. To alleviate this issue, the use of the weaker electron-donating Ph_2phen TL′ provides minimal electronic modification at Rh while maintaining steric bulk. Photolysis studies were performed using $[(Ph_2phen)_2Ru(dpp)RhCl_2(Ph_2phen)]^{3+}$, $[(Ph_2phen)_2Ru(dpp)RhCl_2({}^tBu_2bpy)]^{3+}$, and $[(bpy)_2Ru(dpp)RhCl_2({}^tBu_2bpy)]^{3+}$ to better understand the impact TL and/or TL′ variation has on photocatalytic functioning of Ru(II),Rh(III) bimetallic supramolecules and these results are tabulated in **Table 3.9**. Photoexcitation using a 470 nm LED light source in the presence of 130 μM bimetallic, 1.5 M DMA electron donor, 0.62 M H_2O substrate, and 0.11 mM $[DMAH^+][CF_3SO_3^-]$ in a CH_3CN solvent system yields photoactive $[(Ph_2phen)_2Ru(dpp)RhCl_2(Ph_2phen)]^{3+}$ and $[(Ph_2phen)_2Ru(dpp)RhCl_2({}^tBu_2bpy)]^{3+}$ H_2-producing photocatalysts and the relatively inert $[(bpy)_2Ru(dpp)RhCl_2({}^tBu_2bpy)]^{3+}$ photocatalyst, **Figure 3.35**.

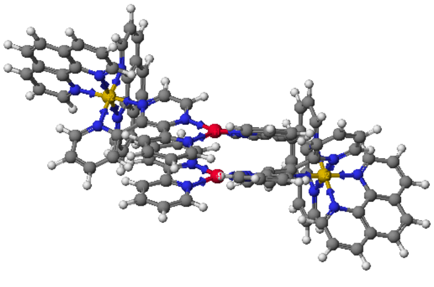

$[(phen)_2Ru(dpp)Rh^I(bpy)]^{3+}$
dimerization

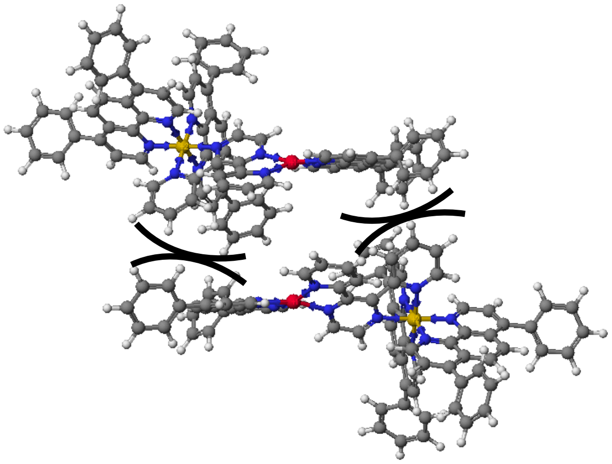

$[(Ph_2phen)_2Ru(dpp)Rh^I(Ph_2phen)]^{3+}$
dimer inhibition

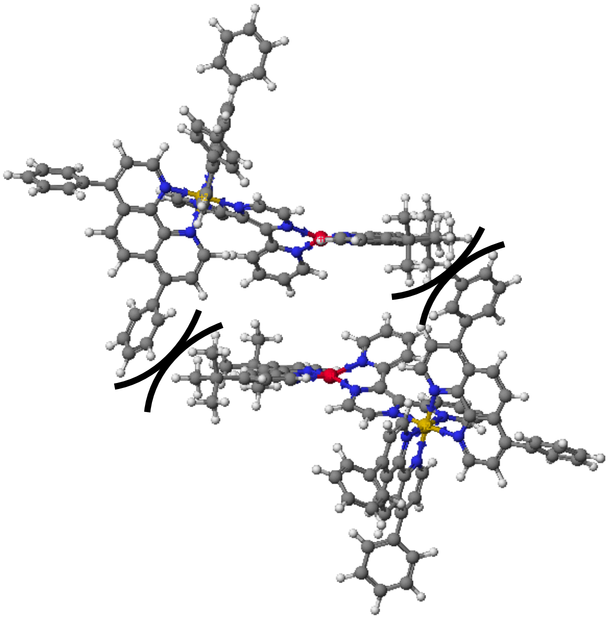

$[(Ph_2phen)_2Ru(dpp)Rh^I(^tBu_2bpy)]^{3+}$
dimer inhibition

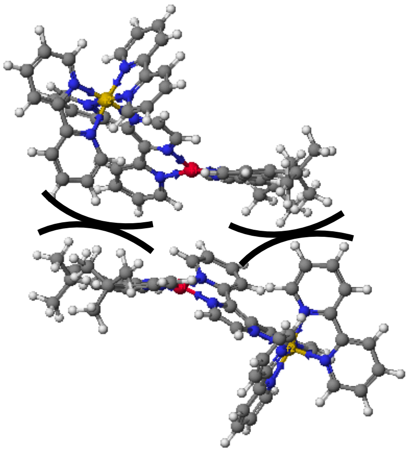

$[(bpy)_2Ru(dpp)Rh^I(^tBu_2bpy)]^{3+}$
dimer inhibition

Figure 3.34: Three-dimensional structures representing reduced Ru(II),Rh(I) bimetallic complexes and the ability to form or not to form Rh(I)-Rh(I) dimers due to structural design. Structures generated using Scigress 7.7.1 molecular modeling software; red (Rh); gold (Ru); blue (N); gray (C); white (H). Ph_2phen = 4,7-diphenyl-1,10-phenanthroline; $^tBu_2bpy$ = 4,4′-Di-*tert*-butyl-2,2′-bipyridine; bpy = 2,2′-bipyridine; dpp = 2,3-bis(2-pyridyl)pyrazine.

Table 3.9. Photocatalytic H_2 Production from H_2O using Ru(II),Rh(III) Bimetallic Complexes

Complex [a]	Solvent	H_2 (mL)	H_2 (μmol)	TON[b]	Max. Φ_{H_2} [c] (%)
$[(Ph_2phen)_2Ru(dpp)RhCl_2(^tBu_2bpy)]^{3+}$	CH_3CN	0.30 ± 0.02	12 ± 1	21 ± 2	0.56 ± 0.02
$[(Ph_2phen)_2Ru(dpp)RhCl_2(Ph_2phen)]^{3+}$	CH_3CN	0.69 ± 0.05	28 ± 2	49 ± 4	0.89 ± 0.03
$[(bpy)_2Ru(dpp)RhCl_2(^tBu_2bpy)]^{3+}$	CH_3CN	0.09 ± 0.02	4 ± 1	6 ± 1	0.11 ± 0.01
$[(Ph_2phen)_2Ru(dpp)RhCl_2(^tBu_2bpy)]^{3+}$	DMF	0.51 ± 0.03	21 ± 2	36 ± 2	0.74 ± 0.03
$[(Ph_2phen)_2Ru(dpp)RhCl_2(Ph_2phen)]^{3+}$	DMF	1.1 ± 0.1	47 ± 3	81 ± 5	0.88 ± 0.03
$[(bpy)_2Ru(dpp)RhCl_2(^tBu_2bpy)]^{3+}$	DMF	0.09 ± 0.01	4 ± 1	6 ± 1	0.11 ± 0.01

[a] Results correspond to 20 h photolysis time ([photocatalyst] = 130 μM; [DMA] = 1.5 M; $[H_2O]$ = 0.62 M; $[CF_3SO_3^-][DMAH^+]$ = 0.11 mM; λ_{irr} = 470 nm; light flux = 2.36 ± 0.05 x 10^{19} photons/min; reaction solution volume = 4.5 mL; head space volume = 15.5 mL). Ph_2phen = 4,7-diphenyl-1,10-phenanthroline; $^tBu_2bpy$ = 4,4′-Di-*tert*-butyl-2,2′-bipyridine; bpy = 2,2′-bipyridine; dpp = 2,3-bis(2-pyridyl)pyrazine. Adapted from ref [144].

[b] TON = mol H_2 produced per mol Rh catalytic center.

[c] Max. Φ_{H_2} = Maximum instantaneous quantum efficiency of H_2 produced.

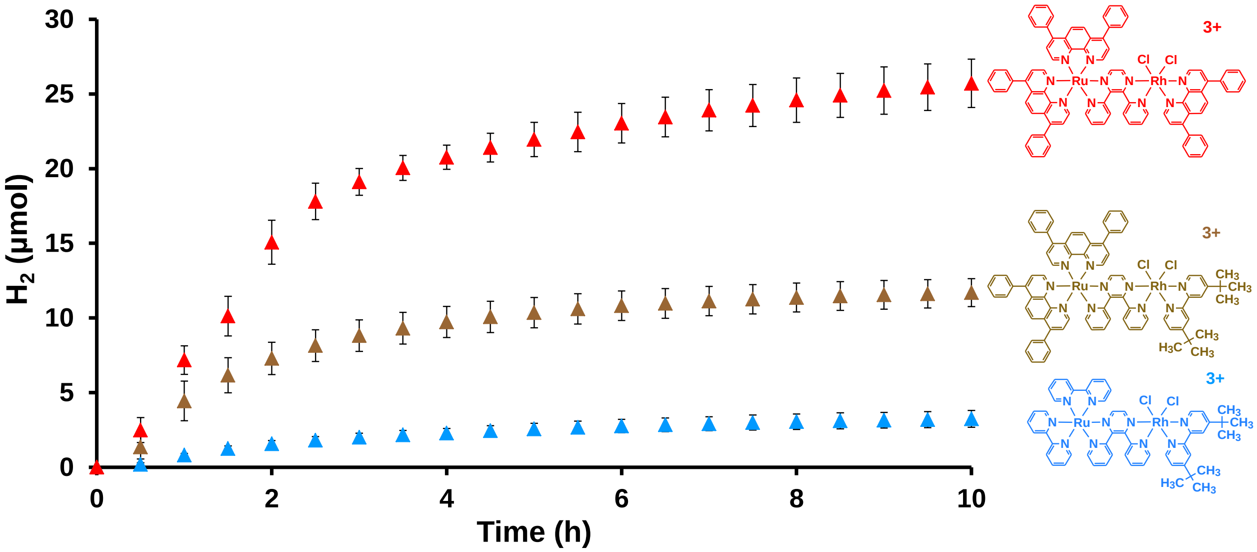

Figure 3.35: Photocatalytic H_2 production profiles of [photocatalyst] = 130 μM, [DMA] = 1.5 M, $[H_2O]$ = 0.62 M, and $[DMAH^+][CF_3SO_3^-]$ = 0.11 mM in CH_3CN photolyzed at 470 nm. Photocatalyst is $[(bpy)_2Ru(dpp)RhCl_2(^tBu_2bpy)]^{3+}$ (▲), $[(Ph_2phen)_2Ru(dpp)RhCl_2(^tBu_2bpy)]^{3+}$ (▲), and $[(Ph_2phen)_2Ru(dpp)RhCl_2(Ph_2phen)]^{3+}$ (▲). Ph_2phen = 4,7-diphenyl-1,10-phenanthroline; $^tBu_2bpy$ = 4,4′-Di-*tert*-butyl-2,2′-bipyridine; bpy = 2,2′-bipyridine; dpp = 2,3-bis(2-pyridyl)pyrazine.

Formation of the catalytically active Ru(II),Rh(I) species requires several processes that must occur efficiently, followed by subsequent oxidative addition of H_2O or protonation by H^+ of the Rh^{I} species, **Equations 3.12-3.21**. The nature of the TL coordinated to Ru is expected to impact light absorption and excited state processes, while TL′ coordinated to Rh should modulate the Rh(dσ*) energetics and ultimately electron collection at Rh. For simplification, the $[(TL)_2Ru(dpp)RhCl_2(TL')]^{3+}$ bimetallics (TL = Ph_2phen or bpy; TL′ = Ph_2phen or ${}^{t}Bu_2$bpy) are represented as $[Ru^{II}(dpp)Rh^{III}Cl_2]^{n+}$.

1st MLCT Photoexcitation

$$[Ru^{II}(dpp)Rh^{III}Cl_2]^{3+} \xrightarrow{h\nu} {}^{*}[Ru^{III}(dpp^{-})Rh^{III}Cl_2]^{3+} \qquad \text{eq. 3.12}$$

Reductive Quenching of ^{3}MLCT State

$$\text{DMA} + {}^{*}[Ru^{III}(dpp^{-})Rh^{III}Cl_2]^{3+} \rightarrow [Ru^{II}(dpp^{-})Rh^{III}Cl_2]^{2+} + \text{DMA}^{+} \qquad \text{eq. 3.13}$$

Intramolecular Electron Transfer

$$[Ru^{II}(dpp^{-})Rh^{III}Cl_2]^{2+} \rightarrow [Ru^{II}(dpp)Rh^{II}Cl_2]^{2+} \qquad \text{eq. 3.14}$$

Halide Ligand Loss

$$[Ru^{II}(dpp)Rh^{II}Cl_2]^{2+} \rightarrow [Ru^{II}(dpp)Rh^{II}Cl]^{3+} + Cl^{-} \qquad \text{eq. 3.15}$$

2nd MLCT Photoexcitation

$$[Ru^{II}(dpp)Rh^{II}Cl]^{3+} \rightarrow {}^{*}[Ru^{III}(dpp^{-})Rh^{II}Cl]^{3+} \qquad \text{eq. 3.16}$$

Reductive Quenching of ^{3}MLCT State

$$\text{DMA} + {}^{*}[Ru^{III}(dpp^{-})Rh^{II}Cl]^{3+} \rightarrow [Ru^{II}(dpp^{-})Rh^{II}Cl]^{2+} + \text{DMA}^{+} \qquad \text{eq. 3.17}$$

Intramolecular Electron Transfer

$$[Ru^{II}(dpp^{-})Rh^{II}Cl]^{2+} \rightarrow [Ru^{II}(dpp)Rh^{I}Cl]^{2+} \qquad \text{eq. 3.18}$$

Halide Ligand Loss

$$[Ru^{II}(dpp)Rh^{I}Cl]^{2+} \rightarrow [Ru^{II}(dpp)Rh^{I}]^{3+} + Cl^{-} \qquad \text{eq. 3.19}$$

Oxidative Addition of H_2O

$$H_2O + [Ru^{II}(dpp)Rh^{I}]^{3+} \rightarrow [Ru^{II}(dpp)Rh^{III}H(OH)]^{3+} \qquad \text{eq. 3.20}$$

Protonation

$$H^{+} + [Ru^{II}(dpp)Rh^{I}]^{3+} \rightarrow [Ru^{II}(dpp)Rh^{III}H(\text{solvent})]^{4+} \qquad \text{eq. 3.21}$$

The $[(Ph_2phen)_2Ru(dpp)RhCl_2(Ph_2phen)]^{3+}$ bimetallic displays enhanced photocatalytic activity (22 ± 1 μmol H_2; 0.54 ± 0.03 mL H_2; 38 ± 2 TON; 0.004 overall Φ_{H_2} after 5 h) in CH_3CN compared to the $[(Ph_2phen)_2Ru(dpp)RhCl_2(^tBu_2bpy)]^{3+}$ bimetallic system (10 ± 1 μmol H_2; 0.25 ± 0.02 mL H_2; 18 ± 2 TON; 0.002 overall Φ_{H_2} after 5 h) where Rh-TL′ has been varied to the electron-donating $^tBu_2bpy$ ligand. As shown through electrochemical analysis, the initially reduced species, $[(Ph_2phen)_2Ru(dpp^-)Rh^{III}Cl_2(^tBu_2bpy)]^{2+}$, requires either halide loss to form the reduced Rh^{II} species, $[(Ph_2phen)_2Ru(dpp)Rh^{II}Cl(^tBu_2bpy)]^{2+}$, or more negative potential, $[(Ph_2phen)_2Ru(dpp^-)Rh^{II}Cl(^tBu_2bpy)]^{2+}$. The electron-donating character of $^tBu_2bpy$ destabilizes the Rh(dσ*) orbitals and affords orbital inversion by which dpp reduction occurs first, hindering fast electron collection. The slow Cl^- loss prior to dpp^- electron transfer to Rh prevents fast photoinitiated electron collection at Rh, inhibiting efficient photocatalysis. The presence of the electron-rich $^tBu_2bpy$ TL′ may also destabilize the Ru(dπ)→Rh(dσ*) ^{3}MMCT excited state, requiring thermal activation from the ^{3}MLCT state to populate the ^{3}MMCT state and hinder efficient electron collection. This discrepancy in photocatalysis between TL′ = Ph_2phen and $^tBu_2bpy$ is observed as at early photolysis times ($t < 2$ h) the slope for H_2 production using the $[(Ph_2phen)_2Ru(dpp)Rh^I(Ph_2phen)]^{3+}$ is twice that of $[(Ph_2phen)_2Ru(dpp)Rh^I(^tBu_2bpy)]^{3+}$, further supporting the instability of the initially formed $[(Ph_2phen)_2Ru(dpp)Rh^{II}Cl_2(Ph_2phen)]^{2+}$ and fast halide loss to produce $[(Ph_2phen)_2Ru(dpp)Rh^{II}Cl(Ph_2phen)]^{3+}$ when compared to the relative stability of the initially formed $[(Ph_2phen)_2Ru(dpp^-)Rh^{III}Cl_2(^tBu_2bpy)]^{2+}$ species.

Modifying the Ru(II)-TL from Ph_2phen to bpy, $[(bpy)_2Ru(dpp)RhCl_2(^tBu_2bpy)]^{3+}$ (2.6 ± 0.4 μmol H_2; 0.06 ± 0.01 mL H_2; 4± 1 TON; 0.0004 overall Φ_{H_2} after 5 h), diminishes the photocatalytic activity similarly to that observed for Ru(II),Rh(III),Ru(II) trimetallics where Ru-TL = bpy systems have been shown to perform less efficiently to Ru-TL = Ph_2phen systems under multiple conditions.[133] The chromophoric $(bpy)_2Ru^{II}(dpp)$ subunit decreases the light absorbing capabilities of the bimetallic complex, while the catalytic *cis*-$Rh^{III}Cl_2(^tBu_2bpy)$ center provides conditions unfavorable for efficient photoinitiated electron collection. The relatively inert $[(bpy)_2Ru(dpp)RhCl_2(^tBu_2bpy)]^{3+}$ bimetallic is important as this discovery emphasizes the importance of designing molecular photocatalysts with appropriate light absorbing capabilities that excite and populate photoactive excited states, steric demands to prevent the catalytically inert dimerization deactivating pathway, and suitable electronics at the Rh^{III} metal center to afford efficient photoinitiated electron collection. The photocatalytic properties coupled with the quenched RT emission, decreased RT excited state lifetime, and elongation of 77 K excited lifetime comparable to Ru(II),Rh(III),Ru(II) trimetallics suggests population of photoactive Ru(dπ)→Rh(dσ*) ^{3}MMCT state regardless of Rh(III)-TL′ identity. Complexes where TL′ = ^{t}Bu$_2$bpy may require thermal population of Ru(dπ)→Rh(dσ*) ^{3}MMCT excited states, while TL′ = Ph$_2$phen ^{3}MMCT excited states are stabilized in energy. The choice of TL′ needs to be sterically bulky, minimize electron donation to Rh, and maximize electron acceptance from Rh, while TL coordinated to Ru needs to provide strong light absorption and longer-lived Ru(dπ)→BL(π*) ^{3}MLCT excited states.

The ligating ability of the solvent within the photolysis system is expected to impact the efficiency of photocatalytic functioning. Changing the solvent from CH_3CN to DMF enhances photocatalytic activity for the $[\{(TL)_2Ru(dpp)\}_2RhBr_2]^{5+}$ (TL = phen or Ph$_2$phen) trimetallic complexes and this trend was tested using the Ru(II),Rh(III) bimetallics. As expected due to the decreased ligating ability of DMF vs. CH_3CN , changing photocatalysis solvent from CH_3CN to DMF enhances photocatalytic H_2 production for $[(Ph_2phen)_2Ru(dpp)RhCl_2(Ph_2phen)]^{3+}$ from 28 ± 2 μmol (CH_3CN) to 47 ± 3 μmol (DMF) of H_2 and for $[(Ph_2phen)_2Ru(dpp)RhCl_2(^tBu_2bpy)]^{3+}$ from 12 ± 1 μmol (CH_3CN) to 21 ± 2 μmol (DMF) of H_2, **Figure 3.36**. Redox cycling between Rh(III), Rh(II), and Rh(I) involves a coordinatively unsaturated Rh center, necessitating ligand coordination at the Rh^{II} and Rh^{III} sites. Required subsequent release at the Rh^{I} site impedes catalytic functioning in the presence of strongly ligating solvents such as CH_3CN is observed. This same trend was not observed for $[(bpy)_2Ru(dpp)RhCl_2(^tBu_2bpy)]^{3+}$ as both CH_3CN and DMF solvent systems displayed relatively poor photocatalytic activity (4 ± 1 μmol H_2) , further emphasizing the multi-dimensional nature (light absorption, sterics, and electronics) of designing photocatalytically active, H_2O reduction photocatalysts within the Ru(II),Rh(III) bimetallic architecture.

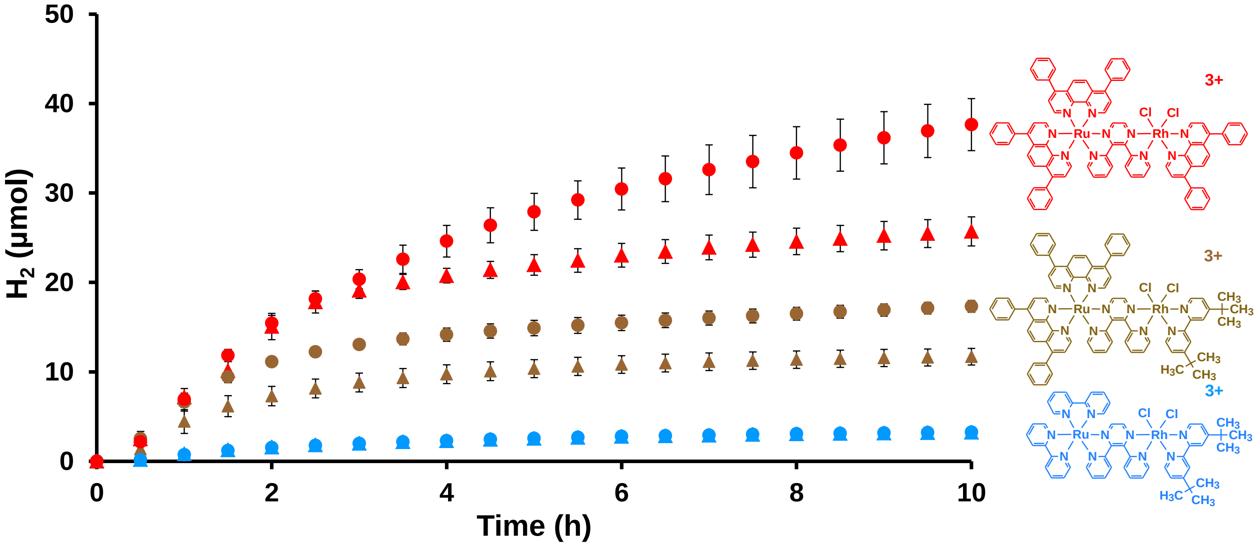

Figure 3.36: Photocatalytic H_2 production profiles of [photocatalyst] = 130 μM, [DMA] = 1.5 M, [H_2O] = 0.62 M, and [$DMAH^+$][$CF_3SO_3^-$] = 0.11 mM when photolyzed at 470 nm, where photocatalyst is $[(bpy)_2Ru(dpp)RhCl_2(^tBu_2bpy)]^{3+}$ in CH_3CN (▲), $[(bpy)_2Ru(dpp)RhCl_2(^tBu_2bpy)]^{3+}$ in DMF (●), $[(Ph_2phen)_2Ru(dpp)RhCl_2(^tBu_2bpy)]^{3+}$ in CH_3CN (▲), $[(Ph_2phen)_2Ru(dpp)RhCl_2(^tBu_2bpy)]^{3+}$ in DMF (●), $[(Ph_2phen)_2Ru(dpp)RhCl_2(Ph_2phen)]^{3+}$ in CH_3CN (▲), and $[(Ph_2phen)_2Ru(dpp)RhCl_2(Ph_2phen)]^{3+}$ in DMF (●). Ph_2phen = 4,7-diphenyl-1,10-phenanthroline; $^tBu_2bpy$ = 4,4′-Di-*tert*-butyl-2,2′-bipyridine; bpy = 2,2′-bipyridine; dpp = 2,3-bis(2-pyridyl)pyrazine.

The $[(TL)_2Ru(dpp)RhCl_2(TL')]^{3+}$ bimetallic molecular architecture couples only one Ru(II) LA moiety to the Rh(III) RM center instead of two Ru(II) LAs as seen with the $[\{(TL)_2Ru(dpp)\}_2RhX_2]^{5+}$ molecular architecture, therefore any comparisons are mitigated by the varied structure and must consider concentration and/or absorbance of the two architectures. The $[(Ph_2phen)_2Ru(dpp)RhCl_2(Ph_2phen)]^{3+}$ bimetallic and $[\{(Ph_2phen)_2Ru(dpp)\}_2RhCl_2]^{5+}$ trimetallic were compared by concentration matching (65 μM) and by absorbance matching (absorbance at 470 nm = 0.46 a.u.), **Figure 3.37**. Concentration matching to 65 μM in CH_3CN solvent system produced roughly one half the amount of H_2 for the $[(Ph_2phen)_2Ru(dpp)RhCl_2(Ph_2phen)]^{3+}$ bimetallic when compared to the analogous $[\{(Ph_2phen)_2Ru(dpp)\}_2RhCl_2]^{5+}$ trimetallic (20 ± 3 μmol H_2 vs. 44 ± 3 μmol H_2, respectively, after 20 h photolysis). This is expected due to the ~50% absorptivity of the bimetallics versus the trimetallics. Absorbance matching the trimetallic and bimetallic complexes results in a 2x increase in $[(Ph_2phen)_2Ru(dpp)RhCl_2(Ph_2phen)]^{3+}$ concentration (130 μM); however the amount of H_2 produced did not double (28 ± 2 μmol H_2

after 20 h photolysis), nor is it the same as the amount of H_2 produced for the trimetallic. At early times, the ratio of the rate for H_2 production between the concentration matched trimetallic and bimetallic samples is 1:1 after 1 h of photolysis. After 2 h of photolysis, the ratio between the two rates of H_2 production changes with the bimetallic displaying a lower rate (9.4 vs. 7.2 μmol H_2/h for the trimetallic and bimetallic, respectively), indicating catalyst deactivation at an earlier time compared to the trimetallic analogue. Continued photolysis further displays the disparity in the rate of H_2 production for the two complexes, suggesting the mode of catalyst deactivation is different within the two architectures. While TL′ = Ph_2phen bimetallics are not expected to form Rh(I)-Rh(I) dimers due to the steric bulk of Ph_2phen, the size of the second (dpp)Ru^{II}(Ph_2phen)$_2$ LA subunit should further protect the photogenerated Rh(I) species from other catalyst deactivating pathways, such as ligand binding or unwanted DMA oxidation products, better than a single TL at Rh.

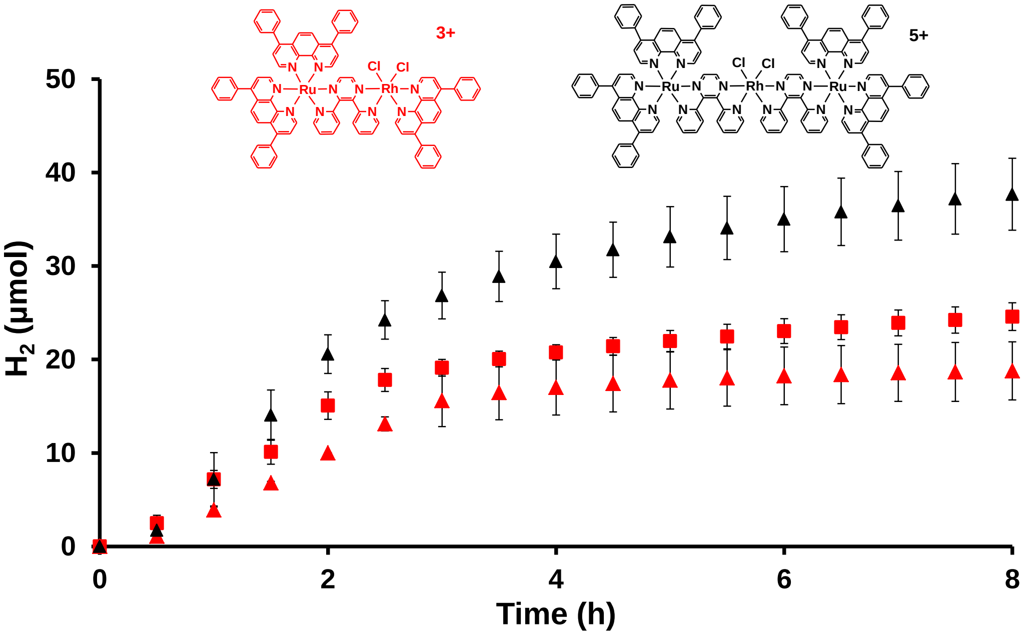

Figure 3.37: Photocatalytic H_2 production profiles of [photocatalyst] = varied, [DMA] = 1.5 M, [H_2O] = 0.62 M, and [$DMAH^+$][$CF_3SO_3^-$] = 0.11 mM in CH_3CN when photolyzed at 470 nm, where photocatalyst is 65 μM [(Ph_2phen)$_2$Ru(dpp)RhCl_2(Ph_2phen)]$^{3+}$ (▲),130 μM [(Ph_2phen)$_2$Ru(dpp)RhCl_2(Ph_2phen)]$^{3+}$ (■), and 65 μM [{(Ph_2phen)$_2$Ru(dpp)}$_2$RhCl_2]$^{5+}$ (▲). Ph_2phen = 4,7-diphenyl-1,10-phenanthroline; dpp = 2,3-bis(2-pyridyl)pyrazine.

4. Conclusions and Future Work

4.1. Conclusions

Polyazine-bridged Ru(II),Rh(III),Ru(II) trimetallic and Ru(II),Rh(III) bimetallic supramolecular complexes were synthesized, characterized, and analyzed to probe fundamental properties, perturbation of subunit properties upon coupling, and as potential H_2O reduction photocatalysts. Trimetallics of the design $[\{(TL)_2Ru(dpp)\}_2RhX_2]^{5+}$ (TL = phen or Ph_2phen; X = Cl^- or Br^-) were synthesized using a building block approach whereby the $[(TL)_2Ru(dpp)]^{2+}$ monometallic was reacted with the $RhX_3{\cdot}3H_2O$ starting material in a 2:1 molar ratio. Similarly, bimetallics of the design $[(TL)_2Ru(dpp)RhCl_2(TL')]^{3+}$ (TL = bpy or Ph_2phen; TL′ = Ph_2phen or ${}^tBu_2$bpy) were synthesized by reacting the $[(TL)_2Ru(dpp)]^{2+}$ monometallic with the $[RhCl_3(TL')(CH_3OH)]$ monometallic in a 1:1 molar ratio. Synthesis using the building block approach allowed for analysis and purification of each component in an effort to better understand the properties and characteristics of the newly generated supramolecular species as well as to study the very weakly emissive systems ($\Phi^{em} \approx 10^{-4}$). This work presents the first detailed study of the Ru(II),Rh(III) bimetallic architecture, as well as the first study of Ph_2phen-containing Ru(II),Rh(III),Ru(II) trimetallic or Ru(II),Rh(III) bimetallic motifs.

Both supramolecular architectures display rich anodic and cathodic electrochemistry with anodic scans yielding Ru-based oxidations and cathodic scans yielding Rh- and dpp-based reductions prior to TL-based reductions. Within the Ru(II),Rh(III),Ru(II) trimetallic architecture, varying the TL from phen to Ph_2phen shifts the reversible two overlapping, one-electron $Ru^{II/III}$ oxidations from +1.62 V to +1.58 V vs. Ag/AgCl. Varying the halide from Cl^- to Br^- shifts the irreversible, two overlapping one-electron $Rh^{III/II}$ and $Rh^{II/I}$ reductions from −0.35 V to −0.32 V vs. Ag/AgCl. This establishes the HOMO and LUMO as being Ru(dπ) and Rh(dσ*) in character, respectively. The Ru(II),Rh(III) bimetallic architecture shows a reversible one-electron $Ru^{II/III}$ oxidation at +1.59 V vs. Ag/AgCl for Ru(II)-TL = Ph_2phen complexes that shifts to more positive potential (+1.63 V vs. Ag/AgCl) when Ru(II)-TL is replaced with bpy. Cathodic scans present very complex electrochemistry with couples of inequivalent current characteristic of a chemical reaction occurring on a similar time scale to the electrochemical study. The complex electrochemistry for these Ru(II),Rh(III) supramolecules is unprecedented in the literature. This work suggests an initial reduction of the Rh(dσ*)-based orbital and subsequent halide loss for

Rh(III)-TL′ = Ph_2phen bimetallics and initial reduction of the dpp(π)-based orbital, slow halide loss, and fast electron transfer from dpp to Rh for Rh(III)-TL′ = $^{t}Bu_2$bpy bimetallics. These observations indicate the nearly isoenergetic nature of the Rh(dσ*) and dpp(π*) orbital sets in this motif and establishes the HOMO as Ru(dπ)-based with the LUMO being hard to establish but hypothesized as dpp(π*) in TL′ = $^{t}Bu_2$bpy bimetallics and Rh(dσ*) in TL′ = Ph_2phen bimetallics. The stronger electron-donation of the $^{t}Bu_2$bpy vs. Ph_2phen TL′ destabilizes the Rh(dσ*) orbitals, affording orbital inversion with the dpp(π*) orbitals.

The trimetallic and bimetallic complexes are efficient light absorbers throughout the UV and visible, with ligand-centered transitions primarily in the UV and MLCT transitions located in the visible. The Ru(II),Rh(III),Ru(II) trimetallic and Ru(II),Rh(III) bimetallic motifs provide significantly enhanced absorptivity in the red relative to typical $[Ru(LL)_3]^{2+}$ systems allowing for better solar spectrum coverage in these supramolecular motifs. Trimetallics where TL = Ph_2phen, $[\{(Ph_2phen)_2Ru(dpp)\}_2RhCl_2]^{5+}$ and $[\{(Ph_2phen)_2Ru(dpp)\}_2RhBr_2]^{5+}$, possess enhanced spectral coverage due to the increased molar absorptivity of the Ru(dπ)→Ph_2phen(π*) ^{1}MLCT transitions (λ^{abs} = 426 nm; ε = 3.6 x 10^4 $M^{-1}cm^{-1}$) compared to the Ru(dπ)→phen(π*) ^{1}MLCT transitions for $[\{(phen)_2Ru(dpp)\}_2RhBr_2]^{5+}$ (λ^{abs} = 412 nm; ε = 1.7 x 10^4 $M^{-1}cm^{-1}$). The lowest energy transition for trimetallic complexes is Ru(dπ)→dpp(π*) ^{1}MLCT in nature, indicative of absorption resulting in charge density localized on dpp BL and spatially near the unoccupied Rh-based orbitals. The Ru(II),Rh(III) bimetallic complexes display the same light absorbing properties as the trimetallic species with about one half the molar absorptivity indicative of the additive spectroscopy in these motifs and the single light absorbing Ru center in the Ru(II),Rh(III) bimetallics. Once again, Ru(II)-TL = Ph_2phen complexes, $[(Ph_2phen)_2Ru(dpp)RhCl_2(Ph_2phen)]^{3+}$ and $[(Ph_2phen)_2Ru(dpp)RhCl_2(^{t}Bu_2bpy)]^{3+}$, contain enhanced spectral coverage throughout with the Ru(dπ)→Ph_2phen(π*) ^{1}MLCT transitions (λ^{abs} = 422 nm; ε = 1.7 x 10^4 $M^{-1}cm^{-1}$) when compared with Ru(dπ)→bpy(π*) ^{1}MLCT transitions for $[(bpy)_2Ru(dpp)RhCl_2(^{t}Bu_2bpy)]^{3+}$ (λ^{abs} = 414 nm; ε = 0.9 x 10^4 $M^{-1}cm^{-1}$). The lowest energy transition is Ru(dπ)→dpp(π*) ^{1}MLCT in nature for all Ru(II),Rh(III) bimetallics as well, suggesting similar excited state dynamics are expected.

The excited state dynamics of both trimetallic and bimetallic supramolecular architectures are interesting with many excited states in close energetic proximity and display weak, low energy emission from the short-lived Ru(dπ)→μ-dpp(π*) ^{3}MLCT excited state. Using the analogous TL Ru(II),Ru(II) homobimetallics as models, emission quenching of

$[\{(phen)_2Ru(dpp)\}_2RhBr_2]^{5+}$, $[\{(Ph_2phen)_2Ru(dpp)\}_2RhCl_2]^{5+}$, and $[\{(Ph_2phen)_2Ru(dpp)\}_2RhBr_2]^{5+}$ occurs with ~85-90% due to rapid intramolecular electron transfer to populate the low-lying Ru(dπ)→Rh(dσ*) ^{3}MMCT excited state with $k_{et} \approx 10^7$ s^{-1}. The same degree of quenching is observed for the Ru(II),Rh(III) bimetallic complexes $[(Ph_2phen)_2Ru(dpp)RhCl_2(Ph_2phen)]^{3+}$, $[(Ph_2phen)_2Ru(dpp)RhCl_2(^tBu_2bpy)]^{3+}$, and $[(bpy)_2Ru(dpp)RhCl_2(^tBu_2bpy)]^{3+}$, suggesting population of a low-lying ^{3}MMCT state at room temperature. The excited state lifetimes of these Rh-containing trimetallics and bimetallics are between ~30-50 ns, a substantial decrease when compared with the Ru(II),Ru(II) homobimetallic models (~140-190 ns) which lack low energy, unoccupied Rh-based orbitals capable of accepting an electron from the optically populated dpp π* orbitals. Excited state lifetime measurements at 77 K for Rh-containing trimetallics and bimetallics display similar lifetimes for the analogous Ru(II),Ru(II) homobimetallic models indicating electron transfer is occurring at RT as well as ruling out energy transfer at RT in the Rh-containing species. Electron transfer is inhibited in rigid media at 77 K whereas energy transfer is not, further supporting low-lying Ru→Rh ^{3}MMCT excited states in all herein reported Ru(II),Rh(III),Ru(II) and Ru(II),Rh(III) motifs. Using a sacrificial electron donor to reductively quench the photogenerated formally Ru(III) in the ^{3}MLCT or ^{3}MMCT excited state species affords electron collection at the Rh metal center. Under the proper conditions collected electrons can be delivered to an appropriate substrate.

Photocatalytic studies performed using Ru(II),Rh(III),Ru(II) trimetallic and Ru(II),Rh(III) bimetallic complexes establish that both molecular architectures are capable of functioning as H_2 photocatalysts in the reduction of H_2O when the appropriate molecular components are utilized to provide the needed electronic, excited state, and steric properties. The trimetallic architecture has shown that varying the halide from Cl^- to Br^- enhances photocatalytic H_2 production over time with ~30% increase in yield. The increase in photocatalytic activity is somewhat unexpected as halide loss is observed upon the initial reduction of the Rh center and these systems undergo many turnovers. The impact of halide could be ascribed to the ability of the free halide in solution from the photoreduced supramolecule to serve as a ligand and bind to the coordinatively unsaturated Rh(I) metal center and thereby impede catalysis. The observed differences in activity at low concentrations (μM) of photocatalysts may suggest ion pairing between the positively charged catalyst and the negatively charged halide. The smaller size and greater electron affinity of Cl^- results in more efficient interaction with the photogenerated Rh(I) center than the Br^-

analogues. Modifying the TL from phen to Ph_2phen within the trimetallics greatly enhances H_2 production (10-fold) in an unexpected manner. The larger size of TL = Ph_2phen trimetallics serves to protect the photogenerated Rh(I) center from unwanted reactions and superior absorptivity increases the probability of photoexcitation to yield photoactive states when compared with the smaller, less light absorbing TL = phen trimetallics. The exposed planarity of the TL = phen π system may also serve to enhance π-π stacking with the DMA π-system close to the Ru donor inhibiting efficient photocatalysis via enhanced back electron transfer. The $[\{(Ph_2phen)_2Ru(dpp)\}_2RhBr_2]^{5+}$ system provided a Φ_{H_2} of 0.07, the highest reported single component system.[133] This Φ_{H_2} of 0.07 is the product of the efficiency for photoexcitation to populate the reactive excited state, reductive quenching by DMA, halide loss, subsequent photoexcitation of the Rh^{II}-containing species, reductive quenching by DMA, halide loss, and reactions to bind substrate, reduce the substrate, and release H_2.

The Ru(II),Rh(III) bimetallic architecture has shown that the identity of the TL coordinated to Ru as well as Rh greatly impacts photocatalysis. The bimetallics where Ru(II)-TL = Ph_2phen, $[(Ph_2phen)_2Ru(dpp)RhCl_2(Ph_2phen)]^{3+}$ and $[(Ph_2phen)_2Ru(dpp)RhCl_2(^tBu_2bpy)]^{3+}$, are more active than the Ru(II)-TL = bpy complex, $[(bpy)_2Ru(dpp)RhCl_2(^tBu_2bpy)]^{3+}$. Similar to the trimetallic series, the enhanced absorptivity and larger size of TL = Ph_2phen bimetallics provide for more excited bimetallic molecules to yield the photoactive Rh(I) species and to provide greater protection of the photogenerated Rh(I) species. The TL attached to Rh not only provides steric protection, but also modulates the electronics of the Rh center. When comparing the two bimetallics $[(Ph_2phen)_2Ru(dpp)RhCl_2(Ph_2phen)]^{3+}$ and $[(Ph_2phen)_2Ru(dpp)RhCl_2(^tBu_2bpy)]^{3+}$, the Rh-TL′ = Ph_2phen complex is much more active than the Rh-TL′ = $^tBu_2$bpy complex even though the $^tBu_2$bpy provides greater steric protection of the Rh center. The $[(bpy)_2Ru(dpp)RhCl_2(^tBu_2bpy)]^{3+}$ bimetallic is relatively inactive as the Rh is more electron rich and ineffective at collecting multiple reducing equivalents. Orbital inversion is observed for TL′ = $^tBu_2$bpy bimetallics where dpp(π*) is the LUMO as opposed to Rh(dσ*), thereby inhibiting efficient electron collection at the Rh metal center and impeding photocatalysis compared to TL′ = Ph_2phen which possesses a Rh-based LUMO and electron collection at the Rh metal center. The bimetallics reported herein are the only active Ru,Rh bimetallic catalysts for H_2O reduction and provide for more simplistic systems to allow additional methods such as NMR spectroscopy to be used to probe catalytic intermediates and independent fine tuning of the Rh(dσ*) orbital energetics by TL′ variation.

The studies performed within this dissertation provide insight into tuning properties of supramolecules and emphasize the importance of structural design and component modification to afford photocatalytically active H_2O reduction photocatalysts. The results provide evidence to begin establishing a mechanism of catalysis. The choice of redox-active and light absorbing moieties provides for efficient population of photoactive states to generate electron collection at the Rh metal center. Enhanced photocatalysis was achieved through minor structural modifications stressing the impact of each molecular component within the supramolecular architecture. System parameters such as solvent, concentration, as well as many others make optimization a complex multi-dimensional problem. This work has also shown that modifying the molecular architecture from two Ru(II) LAs to one Ru(II) LA still provides active H_2O reduction photocatalysts and that sterics and electronics play a large role in their ability to function efficiently. Single-component, homogeneous photocatalysts provide an important backdrop to better understanding the factors influencing H_2O reduction to H_2 using solar energy as well as the fundamental arena of multielectron photochemistry.

4.2. Future Work

4.2.1. Intermediates of Photocatalytic Cycle

Throughout the photocatalytic cycle for H_2O reduction to H_2, multiple intermediate structures are formed. **Figure 4.1** displays a proposed photocatalytic cycle for H_2O reduction using the trimetallic architecture, where $[Ru^{II}(dpp)Rh^{III}X_2(dpp)Ru^{II}]^{5+}$ is used for simplification. The synthesized $[Ru^{II}(dpp)Rh^{III}X_2(dpp)Ru^{II}]^{5+}$ trimetallic complexes are pre-catalysts that require photoexcitation, reductive quenching, intramolecular electron transfer, and halide ligand loss to occur twice to generate the proposed catalytically active $[Ru^{II}(dpp)Rh^{I}(dpp)Ru^{II}]^{5+}$ species. The photoreduced Rh(I) species enters the catalytic cycle whereby interaction with H_2O occurs through oxidative addition, $[Ru^{II}(dpp)Rh^{III}H(OH)(dpp)Ru^{II}]^{5+}$ (**Figure 4.1**), or interaction with H^+ occurs through Rh(I) protonation, $[Ru^{II}(dpp)Rh^{III}H(solvent)(dpp)Ru^{II}]^{6+}$ or $[Ru^{II}(dpp)Rh^{III}H(OH_2)(dpp)Ru^{II}]^{6+}$. Protonolysis can occur by protonation of the Rh(III)-hydride species, producing H_2 and a five-coordinate Rh(III) environment that can be filled by solvent binding to generate a six-coordinate Rh(III) pseudo-octahedral environment, $(dpp)Rh^{III}(OH)(solvent)(dpp)$, $(dpp)Rh^{III}(solvent)_2(dpp)$, or $(dpp)Rh^{III}(OH_2)(solvent)(dpp)$. Regeneration of the $[Ru^{II}(dpp)Rh^{I}(dpp)Ru^{II}]^{5+}$ catalyst is achieved by photoexcitation, reductive quenching, intramolecular electron transfer, and ligand loss (processes occur twice). Direct synthesis of a Rh(I) species would provide evidence that the photocatalytically active moiety is a polyazine-bridged Ru(II),Rh(I) containing species. If oxidative addition of H_2O is the primary mechanistic pathway to H_2 formation, addition of H_2O to this Rh(I) species would be beneficial and allow for product analysis. Synthesis of a $Rh^{III}(OH_2)$ species could provide insight into the mode of interaction between Rh and H_2O to produce H_2, whether it is by oxidation addition, protonation, ligand coordination, or protonolysis.[150,151] Synthesis of a $Rh^{III}(OH)$ containing complex would allow for analysis of a potential deactivating pathway as the concentration of OH^- in solution may increase over time. DMA oxidation to form the $DMA^{+\bullet}$ radical cation is known to produce multiple products such as *N*-methylaniline, *N*,*N*,*N′*,*N′*-tetramethylbenzidine, and 4,4′-methylenebis(*N*,*N*-dimethylaniline) which may serve to deactivate the photocatalyst. Analysis of these byproducts within the catalytic cycle would be beneficial to designing a better photocatalytic system.

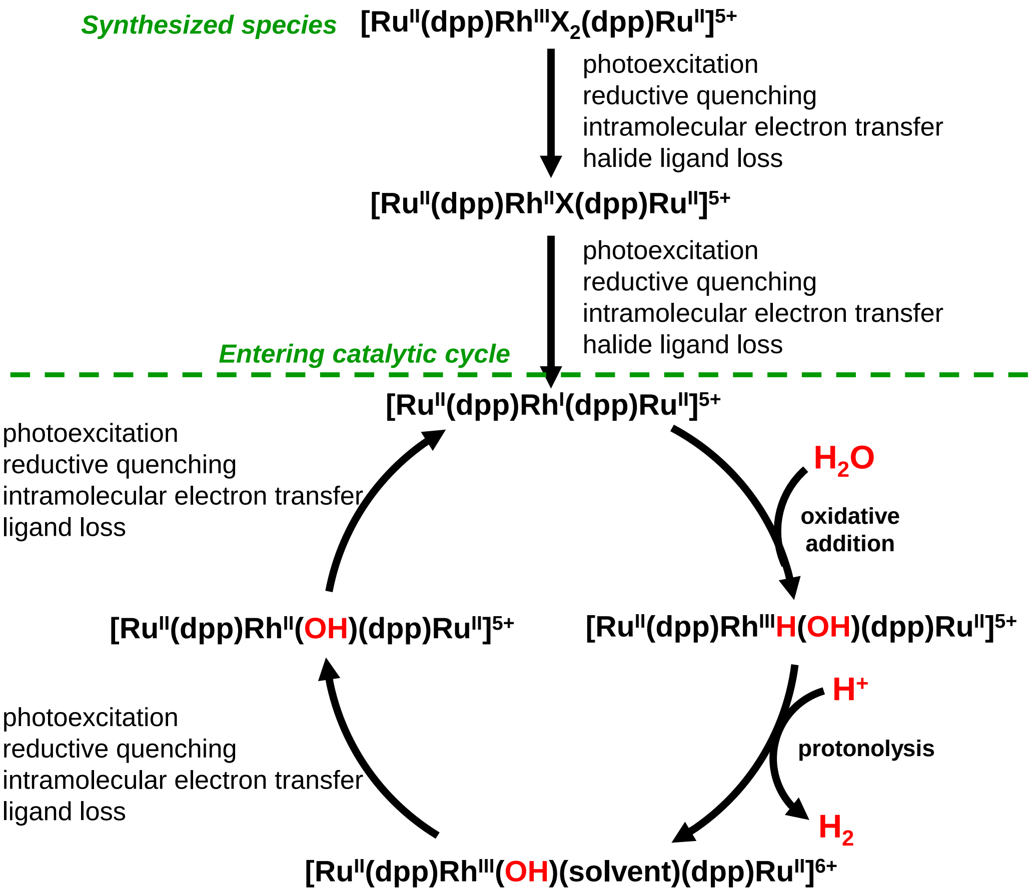

Figure 4.1: Proposed photocatalytic cycle for the reduction of H_2O to H_2 by oxidative addition of H_2O to the photoreduced $[Ru^{II}(dpp)Rh^{I}(dpp)Ru^{II}]^{5+}$ trimetallic complex is followed by protonolysis. dpp = 2,3-bis(2-pyridyl)pyrazine; X = halide ligand.

4.2.2. Transient Absorption Spectroscopy

Excited state absorption measurements and the subsequent decay to the ground state provide insight into excited state dynamics of polyazine-bridged Ru(II),Rh(III) supramolecular complexes.[46,82,84-87,145,152,153] Changes in observed optical density (ΔOD) by monitoring the electronic absorption spectrum following photoexcitation indicate the identity of excited state formation. Preliminary work was performed with the assistance of Dr. M. Kyle Brennaman and Prof. Thomas J. Meyer at the University of North Carolina at Chapel Hill on a nanosecond timescale. Photoexcitation at λ^{irr} = 532 nm in CH_3CN solvent using $[\{(TL)_2Ru(dpp)\}_2RhX_2]^{5+}$ trimetallic and $[(TL)_2Ru(dpp)RhCl_2(TL')]^{3+}$ bimetallic complexes displayed spectroscopic signals indicative of Ru(dπ)→dpp(π*) ^{3}MLCT formation, **Figure 4.2**. Monitoring the change in absorption as a function of time at a specific wavelength provides a decay profile similar to that of time-resolved luminescence studies. Interestingly, biexponential decay was observed, suggesting deactivation from the ^{3}MLCT excited state involves multiple pathways. In order to provide further proof that ^{3}MLCT deactivation involves intramolecular electron transfer to populate a Ru(dπ)→Rh(dσ*) ^{3}MMCT excited state, transient absorption and luminescence studies at varied temperatures should be performed. Given that at low temperature intramolecular electron transfer is impeded, varying the temperature and monitoring the absorption and luminescence spectra would provide information regarding activation energy for such an electron transfer event to occur. Further studies involving the inclusion of a sacrificial electron donor within the transient absorption analysis could provide information regarding rates of electron transfer, excited state formation, and excited state deactivation. Ultra-fast, sub-picosecond transient absorption analysis may also provide information regarding formation of the ^{3}MLCT and ^{3}MMCT excited states. Synthetically varying the trimetallic and bimetallic structure to include spectroscopically defined Rh-based transitions would provide a spectroscopic signal to monitor upon photoexcitation as well.

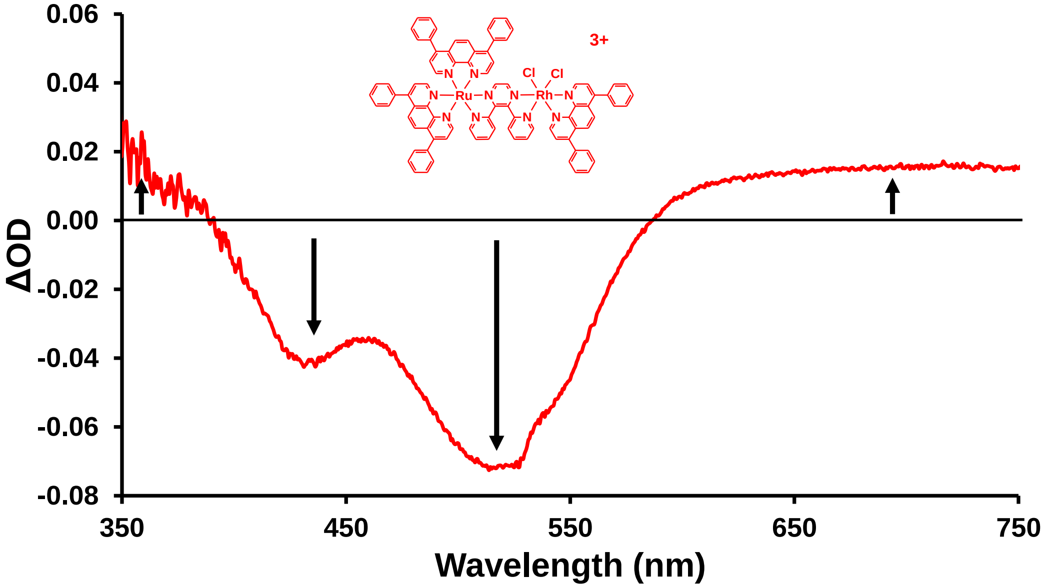

Figure 4.2: Differential absorption spectrum of $[(Ph_2phen)_2Ru(dpp)RhCl_2(Ph_2phen)]^{3+}$ measured in CH_3CN at t = 10 ns after the laser pulse. The black arrows correspond to changes in the ground state and excited state absorption spectra. Ph_2phen = 4,7-diphenyl-1,10-phenanthroline; dpp = 2,3-bis(2-pyridyl)pyrazine.

4.2.3. Single-Component Homogeneous Water Splitting Photocatalyst

This dissertation has focused on the fundamental properties related to designing an efficient H_2O reduction photocatalyst. Understanding the factors that afford single molecule light absorption, charge separation, and collection of multiple reducing equivalents at a localized site allows for future systems to be designed that perform at an even higher efficiency. An ambitious task would be the design of a single-component homogeneous water splitting photocatalyst to reduce and oxidize H_2O to generate H_2 and O_2, respectively. Heterogeneous systems have been designed to perform overall water splitting, but a homogeneous system would allow for systematic component variation to better understand what properties are needed for efficient photocatalysis. Recent advances in H_2O oxidation photocatalysis have generated only a handful of complexes.[154-156] **Figure 4.3** shows proposed homogeneous water splitting photocatalysts that couple one and two Ru(II),Rh(III) light absorbing-H_2O reducing components to a Ru-based H_2O oxidation catalytic site. Oxidation of H_2O in these systems requires a high-valent Ru metal center with efficient charge separation to generate O_2. The presence of the electron collecting Rh(III) reactive metal center should afford efficient electron collection, as well as the ability to reduce H_2O to H_2, thereby providing large positive charge on the Ru catalytic site. The protons removed from H_2O to generate O_2 would then be reduced by the Rh metal center. This study would serve as a back drop to understanding how these reactive metal centers work in conjunction with light absorbing moieties so that implementing these systems in solid state or heterogeneous systems would be an easy transition.

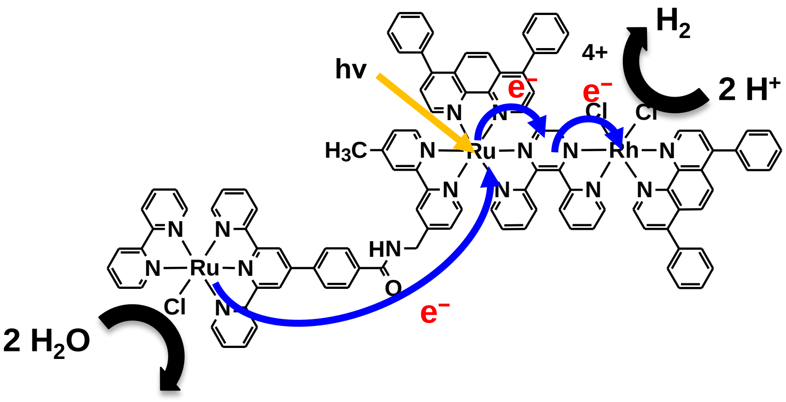

Ru_{CAT}-Ru_{LA}-Rh

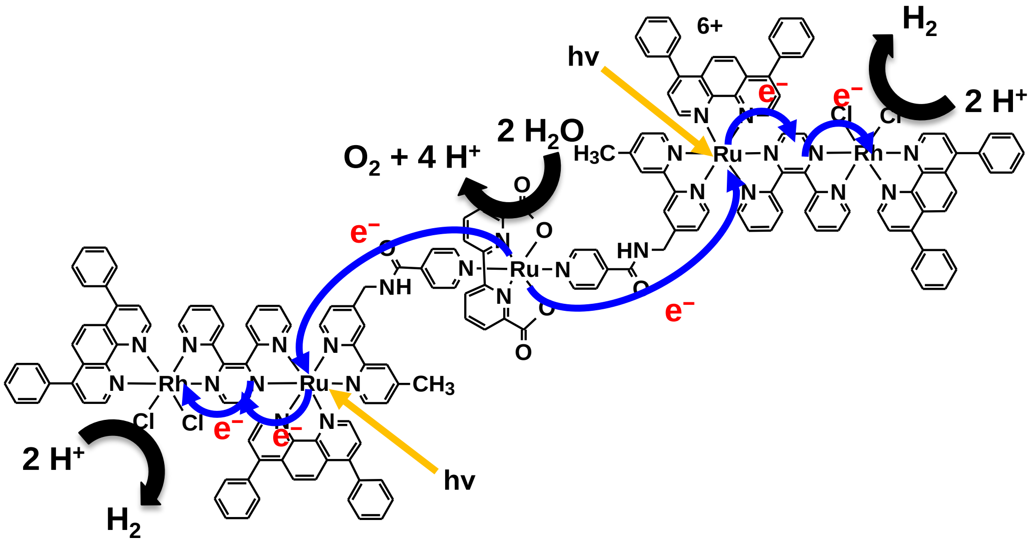

Rh-Ru_{LA}-Ru_{CAT}-Ru_{LA}-Rh

Figure 4.3: Proposed single-component homogeneous water splitting photocatalysts coupling one or two Ru(II),Rh(III) light absorbing-H_2O reduction sites to a Ru(II) H_2O oxidation site. LA = light absorber; CAT = H_2O oxidation catalytic site.

References

(1) Armaroli, N.; Balzani, V., "The future of energy supply: Challenges and opportunities." *Angewandte Chemie-International Edition,* **2007**, *46*, 52-66.

(2) Balzani, V.; Credi, A.; Venturi, M., "Photochemical conversion of solar energy." *ChemSusChem,* **2008**, *1*, 26-58.

(3) Lewis, N. S.; Nocera, D. G., "Powering the planet: Chemical challenges in solar energy utilization." *Proceedings of the National Academy of Sciences of the United States of America,* **2006**, *103*, 15729-15735.

(4) "DOE Report of the Basic Energy Sciences Workshop on Solar Utilization," 2005.

(5) Emery, K.: Reference solar spectral irradiance: air mass 1.5. 2000.

(6) Walter, M. G.; Warren, E. L.; McKone, J. R.; Boettcher, S. W.; Mi, Q. X.; Santori, E. A.; Lewis, N. S., "Solar water splitting cells." *Chemical Reviews,* **2010**, *110*, 6446-6473.

(7) Kudo, A.; Miseki, Y., "Heterogeneous photocatalyst materials for water splitting." *Chemical Society Reviews,* **2009**, *38*, 253-278.

(8) Bard, A. J.; Fox, M. A., "Artificial photosynthesis: Solar splitting of water to hydrogen and oxygen." *Accounts of Chemical Research,* **1995**, *28*, 141-145.

(9) Harris, D., *Quantitative Chemical Analysis*; 6th ed.; W. H. Freeman and Company: New York, 2003.

(10) McDaniel, N. D.; Bernhard, S., "Solar fuels: thermodynamics, candidates, tactics, and figures of merit." *Dalton Transactions,* **2010**, *39*, 10021-10030.

(11) Armaroli, N.; Balzani, V., "The hydrogen issue." *ChemSusChem,* **2011**, *4*, 21-36.

(12) Pellegrin, Y.; Odobel, F., "Molecular devices featuring sequential photoinduced charge separations for the storage of multiple redox equivalents." *Coordination Chemistry Reviews,* **2011**, *255*, 2578-2593.

(13) Meyer, T. J., "Chemical approaches to artificial photosynthesis." *Accounts of Chemical Research,* **1989**, *22*, 163-170.

(14) Gust, D.; Moore, T. A.; Moore, A. L., "Mimicking photosynthetic solar energy transduction." *Accounts of Chemical Research,* **2001**, *34*, 40-48.

(15) Alstrum-Acevedo, J. H.; Brennaman, M. K.; Meyer, T. J., "Chemical approaches to artificial photosynthesis. 2." *Inorganic Chemistry,* **2005**, *44*, 6802-6827.

(16) Roundhill, D. M., *Photochemistry and Photophysics of Metal Complexes*; Plenum Press: New York City, 1994.

(17) Kalyanasundaram, K., *Photochemistry of Polypyridine and Porphyrin Complexes*; Academic Press: London, 1992.

(18) Watts, R. J., "Ruthenium polypyridyls - A case study." *Journal of Chemical Education,* **1983**, *60*, 834-842.

(19) Kawanishi, Y.; Kitamura, N.; Tazuke, S., "Dependence of spectroscopic, electrochemical, and excited-state properties of tris chelate ruthenium(II) complexes on ligand structure " *Inorganic Chemistry,* **1989**, *28*, 2968-2975.

(20) Kalyanasundaram, K., "Photophysics, photochemistry, and solar-energy conversion with tris(bipyridyl)ruthenium(II) and its analogs " *Coordination Chemistry Reviews,* **1982**, *46*, 159-244.

(21) Durham, B.; Caspar, J. V.; Nagle, J. K.; Meyer, T. J., "Photochemistry of $Ru(bpy)_3^{2+}$." *Journal of the American Chemical Society,* **1982**, *104*, 4803-4810.

(22) Fujishima, A.; Honda, K., "Electrochemical photolysis of water at a semiconductor electrode." *Nature,* **1972**, *238,* 37-38.

(23) Amouyal, E., "Photochemical production of hydrogen and oxygen from water: A review and state of the art." *Solar Energy Materials and Solar Cells,* **1995**, *38*, 249-276.

(24) Chou, M.; Creutz, C.; Mahajan, D.; Sutin, N.; Zipp, A. P., "Nature of bis(2,2'-bipyridine)rhodium(I) in aqueous soluions." *Inorganic Chemistry,* **1982**, *21*, 3989-3997.

(25) Chan, S. F.; Chou, M.; Creutz, C.; Matsubara, T.; Sutin, N., "Mechanism of the formation of dihydrogen from the photoinduced reactions of poly(pyridine)ruthenium(II) and poly(pyridine)rhodium(III) complexes " *Journal of the American Chemical Society,* **1981**, *103*, 369-379.

(26) Kirch, M.; Lehn, J. M.; Sauvage, J. P., "Hydrogen generation by visible-light irradiation of aqueous-solutions of metal-complexes - approach to the photo-chemical conversion and storage of solar-energy " *Helvetica Chimica Acta,* **1979**, *62*, 1345-1384.

(27) Lehn, J. M.; Sauvage, J. P., "Chemical storage of light energy - catalytic generation of hydrogen by visible light or sunlight - irradiation of neutral aqueous-solutions " *Nouveau Journal De Chimie-New Journal of Chemistry,* **1977**, *1*, 449-451.

(28) Brown, G. M.; Chan, S. F.; Creutz, C.; Schwarz, H. A.; Sutin, N., "Mechanism of the formation of dihydrogen from the photoinduced reactions of tris(bipyridine)ruthenium(II) and tris(bipyridine)rhodium(III)." *Journal of the American Chemical Society,* **1979**, *101*, 7638-7640.

(29) Zhang, P.; Jacques, P. A.; Chavarot-Keridou, M.; Wang, M.; Sun, L. C.; Fontecave, M.; Artero, V., "Phosphine coordination to a cobalt diimine-dioxime catalyst increases stability during light-driven H_2 production." *Inorganic Chemistry,* **2012**, *51*, 2115-2120.

(30) Hansen, S.; Klahn, M.; Beweries, T.; Rosenthal, U., "An intermolecular heterobimetallic system for photocatalytic water reduction." *ChemSusChem,* **2012**, *5*, 656-660.

(31) Guttentag, M.; Rodenberg, A.; Kopelent, R.; Probst, B.; Buchwalder, C.; Brandstatter, M.; Hamm, P.; Alberto, R., "Photocatalytic H_2 production with a rhenium/cobalt system in water under acidic conditions." *European Journal of Inorganic Chemistry,* **2012**, 59-64.

(32) Probst, B.; Guttentag, M.; Rodenberg, A.; Hamm, P.; Alberto, R., "Photocatalytic H_2 production from water with rhenium and cobalt complexes." *Inorganic Chemistry,* **2011**, *50*, 3404-3412.

(33) McLaughlin, M. P.; McCormick, T. M.; Eisenberg, R.; Holland, P. L., "A stable molecular nickel catalyst for the homogeneous photogeneration of hydrogen in aqueous solution." *Chemical Communications,* **2011**, *47*, 7989-7991.

(34) Fukuzumi, S.; Kobayashi, T.; Suenobu, T., "Photocatalytic production of hydrogen by disproportionation of one-electron-reduced rhodium and iridium-ruthenium complexes in water." *Angewandte Chemie-International Edition,* **2011**, *50*, 728-731.

(35) Du, P. W.; Knowles, K.; Eisenberg, R., "A homogeneous system for the photogeneration of hydrogen from water based on a platinum(II) terpyridyl acetylide chromophore and a molecular cobalt catalyst." *Journal of the American Chemical Society,* **2008**, *130*, 12576-12577.

(36) Cline, E. D.; Adamson, S. E.; Bernhard, S., "Homogeneous catalytic system for photoinduced hydrogen production utilizing iridium and rhodium complexes." *Inorganic Chemistry,* **2008**, *47*, 10378-10388.

(37) Holliday, B. J.; Mirkin, C. A., "Strategies for the construction of supramolecular compounds through coordination chemistry." *Angewandte Chemie-International Edition,* **2001**, *40*, 2022-2043.
(38) Zeng, F. W.; Zimmerman, S. C., "Dendrimers in supramolecular chemistry: From molecular recognition to self-assembly." *Chemical Reviews,* **1997**, *97*, 1681-1712.
(39) James, S. L., "Metal-organic frameworks." *Chemical Society Reviews,* **2003**, *32*, 276-288.
(40) Balzani, V.; Gomez-Lopez, M.; Stoddart, J. F., "Molecular machines." *Accounts of Chemical Research,* **1998**, *31*, 405-414.
(41) Balzani, V.; Juris, A.; Venturi, M.; Campagna, S.; Serroni, S., "Luminescent and redox-active polynuclear transition metal complexes." *Chemical Reviews*, **1996**, *96*, 759-833.
(42) Balzani, V.; Moggi, L.; Scandola, F., Towards a Supramolecular Photochemistry: Assembly of Molecular Components to Obtain Photochemical Molecular Devices. In *Supramolecular Photochemistry*; Balzani, V., Ed.; NATO ASI Series 214, Reidel, Dordrecht: The Netherlands, 1987; pp 1-28.
(43) Denti, G.; Campagna, S.; Sabatino, L.; Serrni, S.; Ciano, M.; Balzani, V., "Luminescent and redox-reactive building blocks for the design of photochemical molecular devices: Mono-, di-, tri-, and tetranuclear ruthenium(II) polypyridine complexes." *Inorganic Chemistry,* **1990**, *29*, 4750-4758.
(44) Balzani, V., "Photochemical molecular devices." *Photochemical & Photobiological Sciences,* **2003**, *2*, 459-476.
(45) Brewer, K. J.; Swavey, S.; Williams, R. L.; Fang, Z.; Bullock, E. R., "Designing Mixed-Metal Supramolecular Complexes." *Proceedings of SPIE,* **2001**, *4512*, 53-64.
(46) Indelli, M. T.; Chiorboli, C.; Scandola, F., Photochemistry and photophysics of coordination compounds: Rhodium. In *Photochemistry and Photophysics of Coordination Compounds I*; Springer-Verlag Berlin: Berlin, 2007; Vol. 280; pp 215-255.
(47) Chiorboli, C.; Indelli, M. T.; Scandola, F., Photoinduced electron/energy transfer across molecular bridges in binuclear metal complexes. In *Molecular Wires: From Design to Properties*; Springer-Verlag Berlin: Berlin, 2005; Vol. 257; pp 63-102.
(48) Sauvage, J. P.; Collin, J. P.; Chambron, J. C.; Guillerez, S.; Coudret, C.; Balzani, V.; Barigelletti, F.; Decola, L.; Flamigni, L., "Ruthenium(II) and osmium(II) bis(terpyridine) complexes in covalently-linked multicomponent systems - synthesis, electrochemical-behavior, absorption-spectra, and photochemical and photophysical properties " *Chemical Reviews,* **1994**, *94,* 993-1019.
(49) Juris, A.; Balzani, V.; Barigelletti, F.; Campagna, S.; Belser, P.; Von Zelewsky, A., "Ru(II) polypyridine complexes - photophysics, photochemistry, electrochemistry, and chemi-luminescence " *Coordination Chemistry Reviews,* **1988**, *84*, 85-277.
(50) Campagna, S.; Puntoriero, F.; Nastasi, F.; Bergamini, G.; Balzani, V., Photochemistry and photophysics of coordination compounds: Ruthenium. In *Photochemistry and Photophysics of Coordination Compounds I*; Springer-Verlag Berlin: Berlin, 2007; Vol. 280; pp 117-214.
(51) Barigelletti, F.; Juris, A.; Balzani, V.; Belser, P.; Vonzelewsky, A., "Influence of the ligand structure on the electrochemical and spectroscopic properties of ruthenium(II) polypyridine complexes." *Inorganic Chemistry,* **1987**, *26*, 4115-4119.
(52) Cotton, F. A., *Chemical Applications of Group Theory*; 3rd ed.; John Wiley & Sons, Inc.: New York, 1990.

(53) Elvington, M.; Brewer, K. J., Electrochemistry. In *Applications of Physical Methods to Inorganic and Bioiniorganic Chemistry*; Scott, R. A., Lukehart, C. M., Eds.; John Wiley & Sons, 2007; pp 17-38.

(54) Bard, A. J.; Faulkner, L. R., *Electrochemical Methods: Fundamentals and Applications*; 2nd ed.; John Wiley and Sons: New York, 2001.

(55) Mongelli, M. T.; Brewer, K. J., "Synthesis and study of the light absorbing, redox and photophysical properties of Ru(II) and Os(11) complexes of 4,7-diphenyl-1,10-phenanthroline containing the polyazine bridging ligand 2,3-bis(2-pyridyl)pyrazine." *Inorganic Chemistry Communications,* **2006**, *9*, 877-881.

(56) Murphy, W. R.; Brewer, K. J.; Gettliffe, G.; Petersen, J. D., "Luminescent tetrametallic complexes of ruthenium." *Inorganic Chemistry,* **1989**, *28*, 81-84.

(57) Brewer, K. J.; Murphy, W. R.; Spurlin, S. R.; Petersen, J. D., "The next generation of (polyazine)ruthenium(II) complexes." *Inorganic Chemistry,* **1986**, *25*, 882-884.

(58) Tokel-Takvoryan, N. E.; Hemingway, R. E.; Bard, A. J., "Electrogenerated chemiluminescence. XIII. Electrochemical and electrogenerated chemiluminescence studies of ruthenium chelates." *Journal of the American Chemical Society,* **1973**, *95*, 6582-6589.

(59) Braunstein, C. H.; Baker, A. D.; Strekas, T. C.; Gafney, H. D., "Spectroscopic and electrochemical properties of the dimer tetrakis(2,2'-bipyridine)(mu-2,3-bis(2-pyridyl)pyrazine)diruthenium(II) and its monomeric analog." *Inorganic Chemistry,* **1984**, *23*, 857-864.

(60) Molnar, S. M.; Neville, K. R.; Jensen, G. E.; Brewer, K. J., "Utilization of substituted polyazine bridging ligands to tune the spectroscopic and electrochemical properties of bimetallic ruthenium complexes." *Inorganica Chimica Acta,* **1993**, *206*, 69-76.

(61) Wallace, A. W.; Murphy, W. R.; Petersen, J. D., "Electrochemical and photophysical properties of monometallic and bimetallic ruthenium(II) complexes " *Inorganica Chimica Acta,* **1989**, *166*, 47-54.

(62) Fuchs, Y.; Lofters, S.; Dieter, T.; Shi, W.; Morgan, R.; Strekas, T. C.; Gafney, H. D.; Baker, A. D., "Spectroscopic and electrochemical properties of dimeric ruthenium(II) diimine complexes and determination of their excited state redox properties." *Journal of the American Chemical Society,* **1987**, *109*, 2691-2697.

(63) Ferraudi, G. J., *Elements of Inorganic Photochemistry*; John Wiley & Sons, Inc.: New York, 1988.

(64) Turro, N. J., *Modern Molecular Photochemistry*; University Science Books: Sausalito, 1991.

(65) Crosby, G. A., "Spectroscopic investigations of excited-states of transition-metal complexes." *Accounts of Chemical Research,* **1975**, *8*, 231-238.

(66) Lin, C. T.; Bottcher, W.; Chou, M.; Creutz, C.; Sutin, N., "Mechanism of quenching of emission of substituted polypyridineruthenium(II) complexes by iron(III), chromium(III), and europium(III) ions." *Journal of the American Chemical Society,* **1976**, *98*, 6536-6544.

(67) Kalyanasundaram, K.; Nazeeruddin, M. K., "Photophysics and photoredox reactions of ligand-bridged binuclear polypyridyl complexes of ruthenium(II) and of their monomeric analogs " *Inorganic Chemistry,* **1990**, *29*, 1888-1897.

(68) Higgins, S. L. H.; White, T. A.; Winkel, B. S. J.; Brewer, K. J., "Redox, spectroscopic, and photophysical properties of Ru-Pt mixed-metal complexes incorporating 4,7-diphenyl-

1,10-phenanthroline as efficient DNA binding and photocleaving agents." *Inorganic Chemistry,* **2011**, *50*, 463-470.

(69) Wang, X. Y.; Del Guerzo, A.; Schmehl, R. H., "Photophysical behavior of transition metal complexes having interacting ligand localized and metal-to-ligand charge transfer states." *Journal of Photochemistry and Photobiology C-Photochemistry Reviews,* **2004**, *5*, 55-77.

(70) Watts, R. J.; Crosby, G. A., "Spectroscopic characterization of complexes of ruthenium(II) and iridium(II) with 4,4'-diphenyl-2,2'-bipyridine and 4,7-diphenyl-1,10-phenanthroline." *Journal of the American Chemical Society,* **1971**, *93*, 3184-3188.

(71) Kober, E. M.; Meyer, T. J., "Critical Deactivating Modes for the Metal-2,2'-bipyridine or 1,10-phenanthroline MLCT Excited States." *Inorganic Chemistry,* **1985**, *24*, 106-108.

(72) Treadway, J. A.; Loeb, B.; Lopez, R.; Anderson, P. A.; Keene, F. R.; Meyer, T. J., "Effect of delocalization and rigidity in the acceptor ligand on MLCT excited-state decay." *Inorganic Chemistry,* **1996**, *35*, 2242-2246.

(73) Arias, M.; Concepcion, J.; Crivelli, I.; Delgadillo, A.; Diaz, R.; Francois, A.; Gajardo, F.; Lopez, R.; Leiva, A. M.; Loeb, B., "Influence of ligand structure and molecular geometry on the properties of d(6) polypyridinic transition metal complexes." *Chemical Physics,* **2006**, *326*, 54-70.

(74) Caspar, J. V.; Meyer, T. J., "Application of the energy gap law to nonradiative, excited state decay." *Journal of Physical Chemistry,* **1983**, *87*, 952-957.

(75) Caspar, J. V.; Kober, E. M.; Sullivan, B. P.; Meyer, T. J., "Application of the energy gap law to the decay of charge transfer excited states." *Journal of the American Chemical Society,* **1982**, *104*, 630-632.

(76) Englman, R.; Jortner, J., "The energy gap law for radiationless transitions in large molecules." *Molecular Physics: An International Journal at the Interface Between Chemistry and Physics*, **1970**, *18*, 145 - 164.

(77) Alford, P. C.; Cook, M. J.; Lewis, A. P.; McAuliffe, G. S. G.; Skarda, V.; Thomson, A. J.; Glasper, J. L.; Robbins, D. J., "Luminescent metal complexes. Part 5. Luminescent properties of ring-substituted 1,10-phenanthroline tris-complexes of ruthenium(II)." *Journal of the Chemical Society-Perkin Transactions 2,* **1985**, 705-709.

(78) Kew, G.; DeArmond, K.; Hanck, K., "Electrochemistry of rhodium-dipyridyl complexes." *Journal of Physical Chemistry,* **1974**, *78*, 727-734.

(79) Bolinger, C. M.; Story, N.; Sullivan, B. P.; Meyer, T. J., "Electrocatalytic reduction of carbon dioxide by 2,2'-bipyridine complexes of rhodium and iridium." *Inorganic Chemistry,* **1988**, *27*, 4582-4587.

(80) Rasmussen, S. C.; Richter, M. M.; Yi, E.; Place, H.; Brewer, K. J., "Synthesis and characterization of a series of novel rhodium and iridium complexes containing polypyridyl bridging ligands: potential uses in the development of multimetal catalysts for carbon dioxide reduction." *Inorganic Chemistry,* **1990**, *29*, 3926-3932.

(81) DeArmond, M. K.; Hillis, J. E., "Luminescence of transition metal d^6 chelates." *The Journal of Chemical Physics,* **1971**, *54*, 2247-2253.

(82) Kalyanasundaram, K.; Graetzel, M.; Nazeeruddin, M. K., "Excited-state interactions in ligand-bridged chromophore-quencher complexes containing rhodium(III) and ruthenium(II) polypyridyl units." *The Journal of Physical Chemistry,* **1992**, *96*, 5865-5872.

(83) Zigler, D. F.; Wang, J.; Brewer, K. J., "Ruthenium(II)-polyazine light absorbers bridged to reactive *cis*-dichlororhodium(III) centers in a bimetallic molecular architecture." *Inorganic Chemistry*, **2008**, *47*, 11342-11350.

(84) Indelli, M. T.; Chiorboli, C.; Flamigni, L.; De Cola, L.; Scandola, F., "Photoinduced electron transfer across oligo-p-phenylene bridges. Distance and conformational effects in Ru(II)-Rh(III) dyads." *Inorganic Chemistry*, **2007**, *46*, 5630-5641.

(85) Indelli, M. T.; Scandola, F.; Flamigni, L.; Collin, J. P.; Sauvage, J. P.; Sour, A., "Photoinduced electron transfer in ruthenium(II)-rhodium(III) terpyridine dyads." *Inorganic Chemistry*, **1997**, *36*, 4247-4250.

(86) Indelli, M. T.; Scandola, F.; Collin, J.-P.; Sauvage, J.-P.; Sour, A., "Photoinduced electron and energy transfer in rigidly bridged Ru(II)/Rh(III) binuclear complexes." *Inorganic Chemistry*, **1996**, *35*, 303-312.

(87) Indelli, M. T.; Bignozzi, C. A.; Harriman, A.; Schoonover, J. R.; Scandola, F., "Four intercomponent processes in a Ru(II)-Rh(III) polypyridine dyad: electron transfer from excited donor, electron transfer to excited acceptor, charge recombination, and electronic energy transfer." *Journal of the American Chemical Society*, **1994**, *116*, 3768-3779.

(88) Nozaki, K.; Ohno, T.; Haga, M., "Intramolecular electron transfer in photoexcited Ru(II)-Rh(III) binuclear compounds." *Journal of Physical Chemistry*, **1992**, *96*, 10880-10888.

(89) Furue, M.; Hirata, M.; Kinoshita, S.; Kushida, T.; Kamachi, M., "Intramolecular electron-transfer of covalently-linked polypyridine ruthenium(II)/rhodium(III) binuclear complexes in the excited state. Observation of the marcus inverted region." *Chemistry Letters*, **1990**, *19*, 2065-2068.

(90) Wasielewski, M. R., "Photoinduced electron transfer in supramolecular systems for artificial photosynthesis." *Chemical Reviews*, **1992**, *92*, 435-461.

(91) Rillema, D. P.; Mack, K. B., "The low-lying excited state in ligand pi-acceptor complexes of ruthenium(II) - mononuclear and binuclear species " *Inorganic Chemistry*, **1982**, *21*, 3849-3854.

(92) Molnar, S. M.; Nallas, G.; Bridgewater, J. S.; Brewer, K. J., "Photoinitiated electron collection in a mixed-metal trimetallic complex of the form $[\{(bpy)_2Ru(dpb)\}_2IrCl_2\}(PF_6)_5$ (bpy = 2,2'-bipyridine and dpb = 2,3-bis(2-pyridyl)benzoquinoxaline)." *Journal of the American Chemical Society*, **1994**, *116*, 5206-5210.

(93) Molnar, S. M.; Jensen, G. E.; Vogler, L. M.; Jones, S. W.; Laverman, L.; Bridgewater, J. S.; Richter, M. M.; Brewer, K. J., "Photochemical properties of mixed-metal supramolecular complexes." *Journal of Photochemistry and Photobiology A: Chemistry*, **1994**, *80*, 315-322.

(94) Konduri, R.; Ye, H. W.; MacDonnell, F. M.; Serroni, S.; Campagna, S.; Rajeshwar, K., "Ruthenium photocatalysts capable of reversibly storing up to four electrons in a single acceptor ligand: A step closer to artificial photosynthesis." *Angewandte Chemie-International Edition*, **2002**, *41*, 3185-3187.

(95) Kim, M. J.; Konduri, R.; Ye, H. W.; MacDonnell, F. M.; Puntoriero, F.; Serroni, S.; Campagna, S.; Holder, T.; Kinsel, G.; Rajeshwar, K., "Dinuclear ruthenium(II) polypyridyl complexes containing large, redox-active, aromatic bridging ligands: Synthesis, characterization, and intramolecular quenching of MLCT excited states." *Inorganic Chemistry*, **2002**, *41*, 2471-2476.

(96) Polyansky, D. E.; Cabelli, D.; Muckerman, J. T.; Fukushima, T.; Tanaka, K.; Fujita, E., "Mechanism of hydride donor generation using a Ru(II) complex containing an NAD(+)

model ligand: Pulse and steady-state radiolysis studies." *Inorganic Chemistry,* **2008**, *47*, 3958-3968.

(97) Polyansky, D.; Cabelli, D.; Muckerman, J. T.; Fujita, E.; Koizumi, T.; Fukushima, T.; Wada, T.; Tanaka, K., "Photochemical and radiolytic production of an organic hydride donor with a Ru-II complex containing an NAD(+) model ligand." *Angewandte Chemie-International Edition,* **2007**, *46*, 4169-4172.

(98) Elvington, M.; Brewer, K. J., "Photoinitiated electron collection at a metal in a rhodium-centered mixed-metal supramolecular complex." *Inorganic Chemistry,* **2006**, *45*, 5242-5244.

(99) Arachchige, S. M.; Brown, J. R.; Chang, E.; Jain, A.; Zigler, D. F.; Rangan, K.; Brewer, K. J., "Design considerations for a system for photocatalytic hydrogen production from water employing mixed-metal photochemical molecular devices for photoinitiated electron collection." *Inorganic Chemistry,* **2009**, *48*, 1989-2000.

(100) Arachchige, S. M.; Brown, J.; Brewer, K. J., "Photochemical hydrogen production from water using the new photocatalyst $[\{(bpy)_2Ru(dpp)\}_2RhBr_2](PF_6)_5$." *Journal of Photochemistry and Photobiology A: Chemistry,* **2008**, *197*, 13-17.

(101) Teets, T. S.; Nocera, D. G., "Photocatalytic hydrogen production." *Chemical Communications*, **2011**, *47*, 9268-9274.

(102) Inagaki, A.; Akita, M., "Visible-light promoted bimetallic catalysis." *Coordination Chemistry Reviews,* **2010**, *254*, 1220-1239.

(103) Wang, M.; Na, Y.; Gorlov, M.; Sun, L. C., "Light-driven hydrogen production catalysed by transition metal complexes in homogeneous systems." *Dalton Transactions,* **2009**, 6458-6467.

(104) Tinker, L. L.; McDaniel, N. D.; Bernhard, S., "Progress towards solar-powered homogeneous water photolysis." *Journal of Materials Chemistry,* **2009**, *19*, 3328-3337.

(105) Ozawa, H.; Sakai, K., "Photo-hydrogen-evolving molecular devices driving visible-light-induced water reduction into molecular hydrogen: structure-activity relationship and reaction mechanism." *Chemical Communications,* **2011**, *47*, 2227-2242.

(106) Ozawa, H.; Haga, M. A.; Sakai, K., "A photo-hydrogen-evolving molecular device driving visible-light-induced EDTA-reduction of water into molecular hydrogen." *Journal of the American Chemical Society*, **2006**, *128*, 4926-4927.

(107) Rau, S.; Schafer, B.; Gleich, D.; Anders, E.; Rudolph, M.; Friedrich, M.; Gorls, H.; Henry, W.; Vos, J. G., "A supramolecular photocatalyst for the production of hydrogen and the selective hydrogenation of tolane." *Angewandte Chemie-International Edition,* **2006**, *45*, 6215-6218.

(108) Lei, P.; Hedlund, M.; Lomoth, R.; Rensmo, H.; Johansson, O.; Hammarstrom, L., "The role of colloid formation in the photoinduced H-2 production with a Ru-II-Pd-II supramolecular complex: A study by GC, XPS, and TEM." *Journal of the American Chemical Society,* **2008**, *130*, 26-+.

(109) Du, P.; Schneider, J.; Fan, L.; Zhao, W.; Patel, U.; Castellano, F. N.; Eisenberg, R., "Bi- and terpyridyl platinum(II) chloro complexes: Molecular catalysts for the photogeneration of hydrogen from water or simply precursors for colloidal platinum?" *Journal of the American Chemical Society,* **2008**, *130*, 5056-5058.

(110) Fihri, A.; Artero, V.; Razavet, M.; Baffert, C.; Leibl, W.; Fontecave, M., "Cobaloxime-based photocatalytic devices for hydrogen production." *Angewandte Chemie-International Edition*, **2008**, *47*, 564-567.

(111) Fihri, A.; Artero, V.; Pereira, A.; Fontecave, M., "Efficient H-2-producing photocatalytic systems based on cyclometalated iridium- and tricarbonylrhenium-diimine photosensitizers and cobaloxime catalysts." *Dalton Transactions,* **2008**, 5567-5569.

(112) Elvington, M.; Brown, J.; Arachchige, S. M.; Brewer, K. J., "Photocatalytic hydrogen production from water employing a Ru, Rh, Ru molecular device for photoinitiated electron collection." *Journal of the American Chemical Society,* **2007**, *129*, 10644-10645.

(113) Knoll, J. D.; Arachchige, S. M.; Brewer, K. J., "A structurally diverse Ru(II),Pt(II) tetrametallic motif for photoinitiated electron collection and photocatalytic hydrogen production." *ChemSusChem,* **2011**, *4*, 252-261.

(114) Knoll, J. D.; Higgins, S. L. H.; White, T. A.; Brewer, K. J., " Terminal and bridging ligand variation in structurally diverse polyazine-bridged Ru(II),Pt(II) supramolecules providing insight into the functioning as water reduction photocatalysts to produce H_2." *Submitted to Inorganic Chemistry*.

(115) Sullivan, B. P.; Salmon, D. J.; Meyer, T. J., "Mixed phosphine 2,2'-bipyridine complexes of ruthenium." *Inorganic Chemistry,* **1978**, *17*, 3334-3341.

(116) Basile, L. A.; Barton, J. K., "Design of a double-stranded DNA cleaving agent with two polyamine metal-binding arms: $Ru(DIP)_2Macro^{n+}$." *Journal of the American Chemical Society*, **1987**, *109*, 7548-7550.

(117) McKenzie, E. D.; Plowman, R. A., "Rhodium(III) compounds with 1,10-phenanthroline and 2,2′-bipyridyl." *Journal of Inorganic and Nuclear Chemistry,* **1970**, *32*, 199-212.

(118) Bieda, R.; Ott, I.; Gust, R.; Sheldrick, W. S., "Cytotoxic rhodium(III) polypyridyl complexes containing the tris(pyrazolyl)methane coligand: Synthesis, DNA binding properties and structure-activity relationships." *European Journal of Inorganic Chemistry,* **2009**, 3821-3831.

(119) Sau, Y.-K.; Chan, K.-W.; Zhang, Q.-F.; Williams, I. D.; Leung, W.-H., "Alkyl and aryl compounds of rhodium(III) and iridium(III) supported by 4,4‘-Di-tert-butyl-2,2‘-bipyridyl." *Organometallics,* **2007**, *26*, 6338-6345.

(120) Osteryoung, J. G.; Osteryoung, R. A., "Square wave voltammetry." *Analytical Chemistry,* **1985**, *57*, 101A-110A.

(121) Lakowicz, J. R., *Principles of fluorescence spectroscopy*; 3rd ed.; Springer: New York, 2006.

(122) Hofstadler, S. A.; Bakhtiar, R.; Smith, R. D., "Electrospray ionization mass spectroscopy: Part I. Instrumentation and spectral interpretation." *Journal of Chemical Education,* **1996**, *73*, A82.

(123) Winter, M.: Sheffield ChemPuter. 1993-2001.

(124) Gennett, T.; Milner, D. F.; Weaver, M. J., "Role of solvent reorganization dynamics in electron-transfer processes. Theory-experiment comparisons for electrochemical and homogeneous electron exchange involving metallocene redox couples." *Journal of Physical Chemistry,* **1985**, *89*, 2787-2794.

(125) Skoog, D. A.; Holler, F. J.; Crouch, S. R., *Principles of instrumental analysis*; 6th ed.; Thomas Brooks/Cole: Belmont, 2007.

(126) Brewer, K. J.; Calvin, M.; Lumpkin, R. S.; Otvos, J. W.; Spreer, L. O., "Synthesis, structure, and characterization of mixed-valence manganese(III)-manganese(IV) bis(μ-oxo) complex with a macrocyclic tetraaza ligand." *Inorganic Chemistry,* **1989**, *28*, 4446-4451.

(127) Brown, J. R.; Elvington, M.; Mongelli, M. T.; Zigler, D. F.; Brewer, K. J., "Analytical methods development for supramolecular design in solar hydrogen production." *Proc. SPIE-Opt. Photo. Sol. Hydrogen Nanotechnology,* **2006**, *6340*, 634007W634001-634013.

(128) Arachchige, S. M.; Shaw, R.; White, T. A.; Shenoy, V.; Tsui, H.-M.; Brewer, K. J., "High turnover in a photocatalytic system for water reduction to produce hydrogen using a Ru,Rh,Ru photoinitiated electron collector." *ChemSusChem,* **2011**, *4*, 514518.

(129) Kuhn, H. J.; Braslavsky, S. E.; Schmidt, R., "Chemical actinometry." *Pure and Applied Chemistry,* **2004**, *76*, 2105-2146.

(130) Nallas, G. N. A.; Jones, S. W.; Brewer, K. J., "Bipyrimidine-bridged mixed-metal trimetallic complexes of ruthenium(II) with rhodium(III) or iridium(III), $\{[(bpy)_2Ru(bpm)]_2MCl_2\}^{5+}$." *Inorganic Chemistry,* **1996**, *35*, 6974-6980.

(131) Swavey, S.; Brewer, K. J., "Synthesis and study of Ru,Rh,Ru triads: Modulation of orbital energies in a supramolecular architecture." *Inorganic Chemistry,* **2002**, *41*, 4044-4050.

(132) Bieda, R.; Ott, I.; Dobroschke, M.; Prokop, A.; Gust, R.; Sheldrick, W. S., "Structure-activity relationships and DNA binding properties of apoptosis inducing cytotoxic rhodium(III) polypyridyl complexes containing the cyclic thioether 9 aneS(3)." *Journal of Inorganic Biochemistry,* **2009**, *103*, 698-708.

(133) White, T. A.; Higgins, S. L. H.; Arachchige, S. M.; Brewer, K. J., "Efficient photocatalytic hydrogen production in a single-component system using Ru,Rh,Ru supramolecules containing 4,7-diphenyl-1,10-phenanthroline." *Angew. Chem.-Int. Ed.,* **2011**, *50*, 12209-12213.

(134) White, T. A.; Rangan, K.; Brewer, K. J., "Synthesis, characterization, and study of the photophysics and photocatalytic properties of the photoinitiated electron collector $[\{(phen)_2Ru(dpp)\}_2RhBr_2](PF_6)_5$." *Journal of Photochemistry and Photobiology A: Chemistry,* **2010**, *209*, 203-209.

(135) Amarante, D.; Cherian, C.; Ernmel, C.; Chen, H. Y.; Dayal, S.; Koshy, M.; Megehee, E. G., "Improved synthetic routes to rhodium bipyridine complexes: Comparison of microwave vs. conventional synthesis." *Inorganica Chimica Acta,* **2005**, *358*, 2231-2238.

(136) Kew, G.; Hanck, K.; Dearmond, K., "Voltammetry of rhodium-1,10-phenanthroline complexes." *Journal of Physical Chemistry,* **1975**, *79*, 1828-1835.

(137) White, T.; Arachchige, S.; Sedai, B.; Brewer, K., "Emission spectroscopy as a probe into photoinduced intramolecular electron transfer in polyazine bridged Ru(II),Rh(III) supramolecular complexes." *Materials,* **2010**, *3*, 4328-4354.

(138) Demas, J. N.; Taylor, D. G., "Intersystem crossing yields in ruthenium(II) and osmium(II) photosensitizers " *Inorganic Chemistry,* **1979**, *18*, 3177-3179.

(139) Haga, M.; Dodsworth, E. S.; Eryavec, G.; Seymour, P.; Lever, A. B. P., "Luminescence quenching of the tris(2,2'-bipyrazine)ruthenium(II) cation and its monoprotonated complex." *Inorganic Chemistry,* **1985**, *24*, 1901-1906.

(140) Bock, C. R.; Connor, J. A.; Gutierrez, A. R.; Meyer, T. J.; Whitten, D. G.; Sullivan, B. P.; Nagle, J. K., "Estimation of excited-state redox potentials by electron-transfer quenching. Application of electron-transfer theory to excited-state redox processes." *Journal of the American Chemical Society,* **1979**, *101*, 4815-4824.

(141) Anderson, C. P.; Salmon, D. J.; Meyer, T. J.; Young, R. C., "Photochemical generation of $Ru(bpy)_3^+$ and O_2^-." *Journal of the American Chemical Society,* **1977**, *99*, 1980-1982.

(142) White, T. A.; Knoll, J. D.; Arachchige, S. M.; Brewer, K. J., "A series of supramolecular complexes for solar energy conversion via water reduction to produce hydrogen: An

excited state kinetic analysis of Ru(II), Rh(III), Ru(II) photoinitiated electron collectors." *Materials,* **2012**, *5*, 27-46.

(143) *CRC Handbook of Chemistry and Physics*; 78th ed.; CRC Press: New York, 1997.

(144) White, T. A.; Whitaker, B. N.; Brewer, K. J., "Discovering the balance of steric and electronic factors needed to provide a new structural motif for photocatalytic hydrogen production from water." *Journal of the American Chemical Society,* **2011**, *133*, 15332-15334.

(145) Berger, R. M., "Excited-state absorption spectroscopy and spectroelectrochemistry of tetrakis(2,2'-bipyridine)(μ-2,3-bis(2-pyridyl)pyrazine)diruthenium(II) and its mononuclear counterpart: A comparative study." *Inorganic Chemistry,* **1990**, *29*, 1920-1924.

(146) Smieja, J. M.; Kubiak, C. P., "Re(bipy-tBu)$(CO)_3$Cl-improved Catalytic Activity for Reduction of Carbon Dioxide: IR-Spectroelectrochemical and Mechanistic Studies." *Inorganic Chemistry,* **2010**, *49*, 9283-9289.

(147) Stor, G. J.; Hartl, F.; van Outersterp, J. W. M.; Stufkens, D. J., "Spectroelectrochemical (IR, UV/Vis) determination of the reduction pathways for a series of $[Re(CO)_3(\alpha\text{-diimine})L']^{0/+}$ (L' = Halide, Otf^-, THF, MeCN, *n*-PrCN, PPh_3, $P(OMe)_3$) Complexes." *Organometallics,* **1995**, *14*, 1115-1131.

(148) Wang, J.; White, T. A.; Arachchige, S. M.; Brewer, K. J., "A new structural motif for photoinitiated electron collection: Ru,Rh bimetallics providing insight into H_2 production via photocatalysis of water reduction by Ru,Rh,Ru supramolecules." *Chemical Communications,* **2011**, *47*, 4451-4453.

(149) Schwarz, H. A.; Creutz, C., "Reactions of tris(2,2-bipyridine)rhodium(II) and bis(2,2'-bipyridine)rhodium(II) complexes in aqueous solution." *Inorganic Chemistry,* **1983**, *22*, 707-713.

(150) Ozerov, O. V., "Oxidative addition of water to transition metal complexes." *Chemical Society Reviews,* **2009**, *38*, 83-88.

(151) Piers, W. E., "Future trends in organometallic chemistry: Organometallic approaches to water splitting." *Organometallics,* **2011**, *30*, 13-16.

(152) Kleverlaan, C. J.; Indelli, M. T.; Bignozzi, C. A.; Pavanin, L.; Scandola, F.; Hasselman, G. M.; Meyer, G. J., "Stepwise charge separation in heterotriads. Binuclear Ru(II)-Rh(III) complexes on nanocrystalline titanium dioxide." *Journal of the American Chemical Society,* **2000**, *122*, 2840-2849.

(153) McCusker, J. K., "Femtosecond absorption spectroscopy of transition metal charge-transfer complexes." *Accounts of Chemical Research,* **2003**, *36*, 876-887.

(154) Li, F.; Jiang, Y.; Zhang, B. B.; Huang, F.; Gao, Y.; Sun, L. C., "Towards A Solar Fuel Device: Light-Driven Water Oxidation Catalyzed by a Supramolecular Assembly." *Angewandte Chemie-International Edition,* **2012**, *51*, 2417-2420.

(155) Kaveevivitchai, N.; Chitta, R.; Zong, R. F.; El Ojaimi, M.; Thummel, R. P., "A Molecular Light-Driven Water Oxidation Catalyst." *Journal of the American Chemical Society,* **2012**, *134*, 10721-10724.

(156) Ashford, D. L.; Stewart, D. J.; Glasson, C. R.; Binstead, R. A.; Harrison, D. P.; Norris, M. R.; Concepcion, J. J.; Fang, Z.; Templeton, J. L.; Meyer, T. J., "An Amide-Linked Chromophore-Catalyst Assembly for Water Oxidation." *Inorganic Chemistry,* **2012**, *51*, 6428-6430.

Appendix

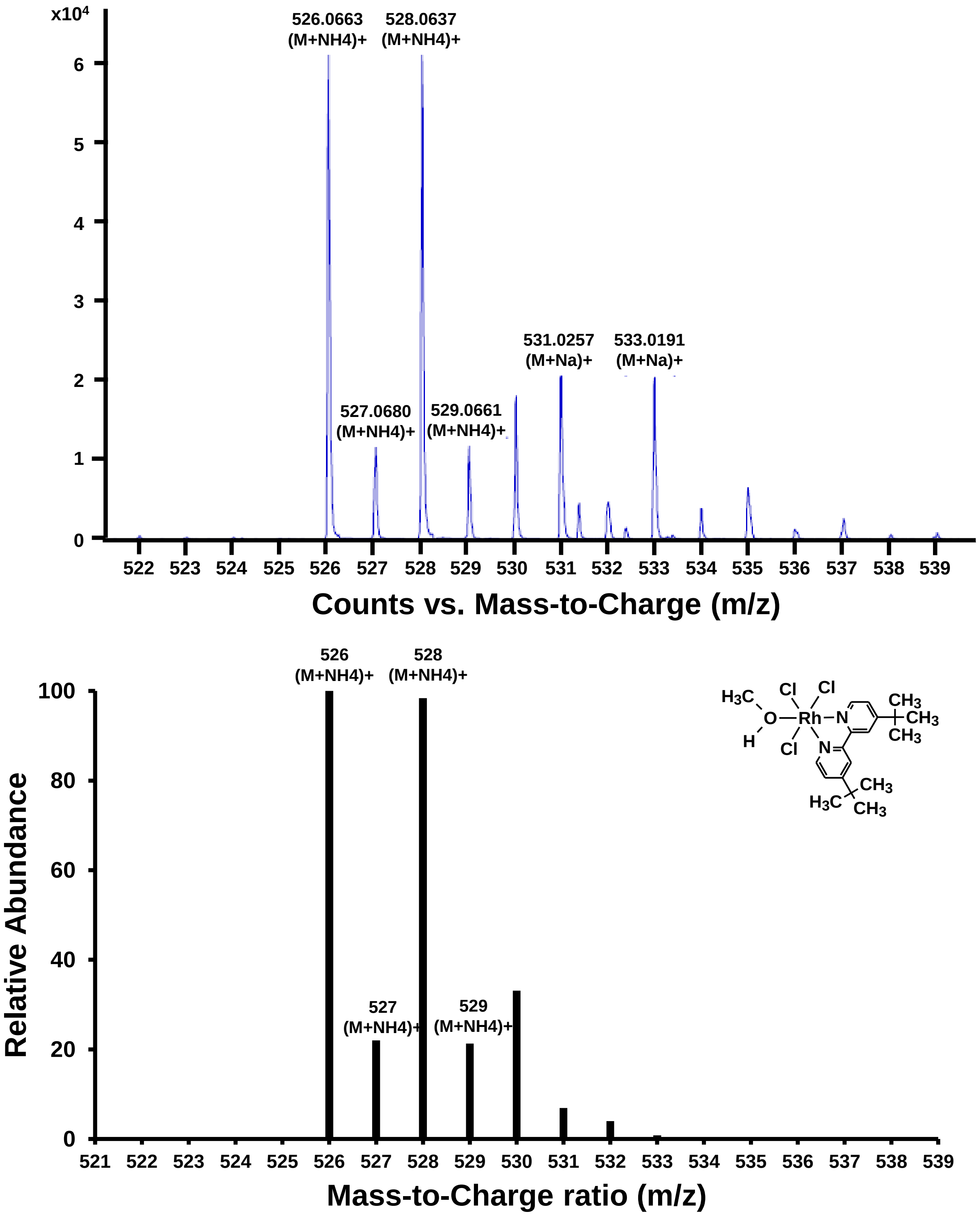

Figure A-1. Experimental (top) and calculated (bottom) mass spectra of $[RhCl_3(^tBu_2bpy)(CH_3OH)]$. The molecular ion peak corresponds to $[M+NH_4]^+$.

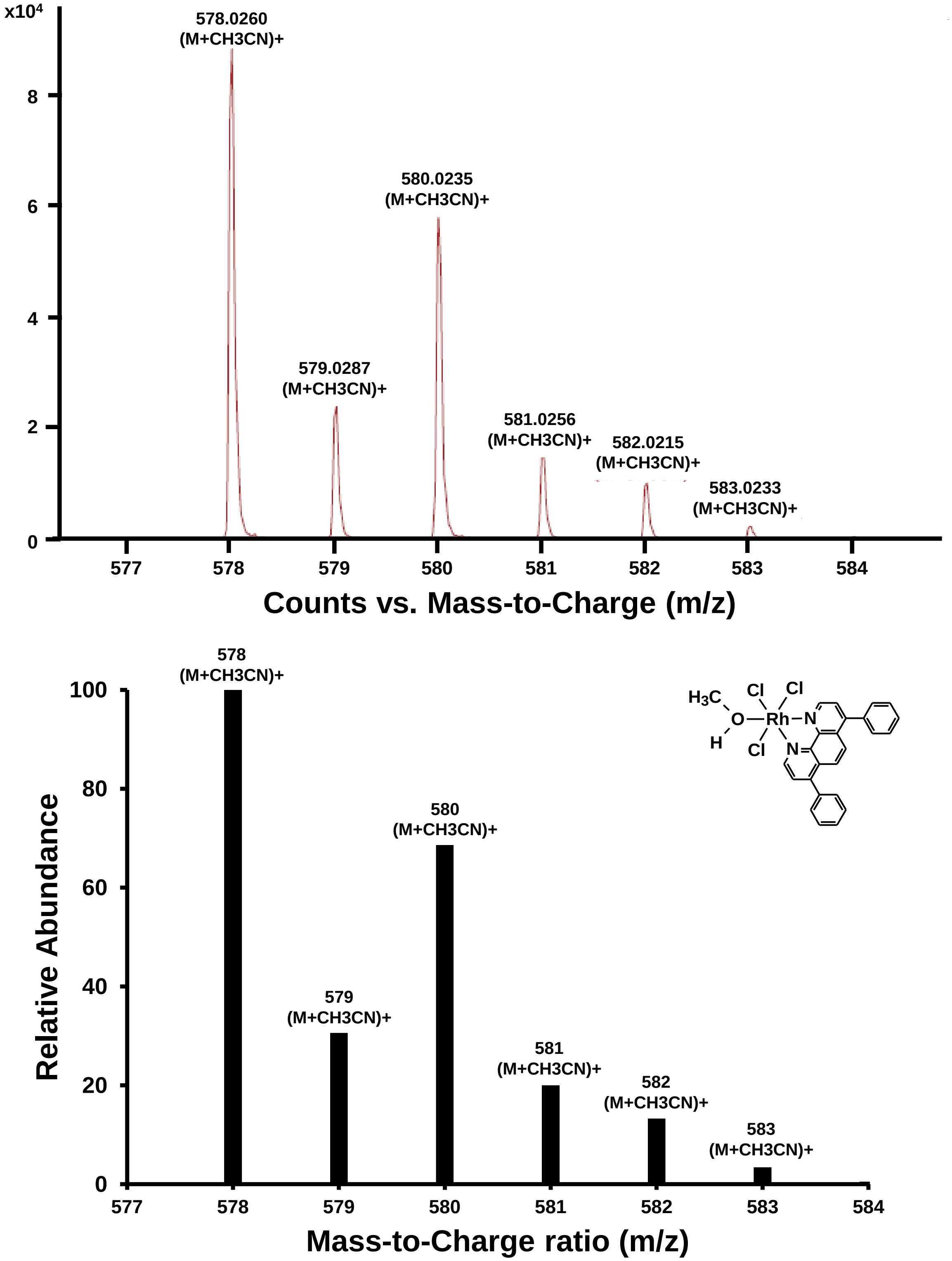

Figure A-2. Experimental (top) and calculated (bottom) mass spectra of [$RhCl_3(Ph_2phen)(CH_3OH)$]. The molecular ion peak corresponds to [$M+CH_3CN$]$^+$.

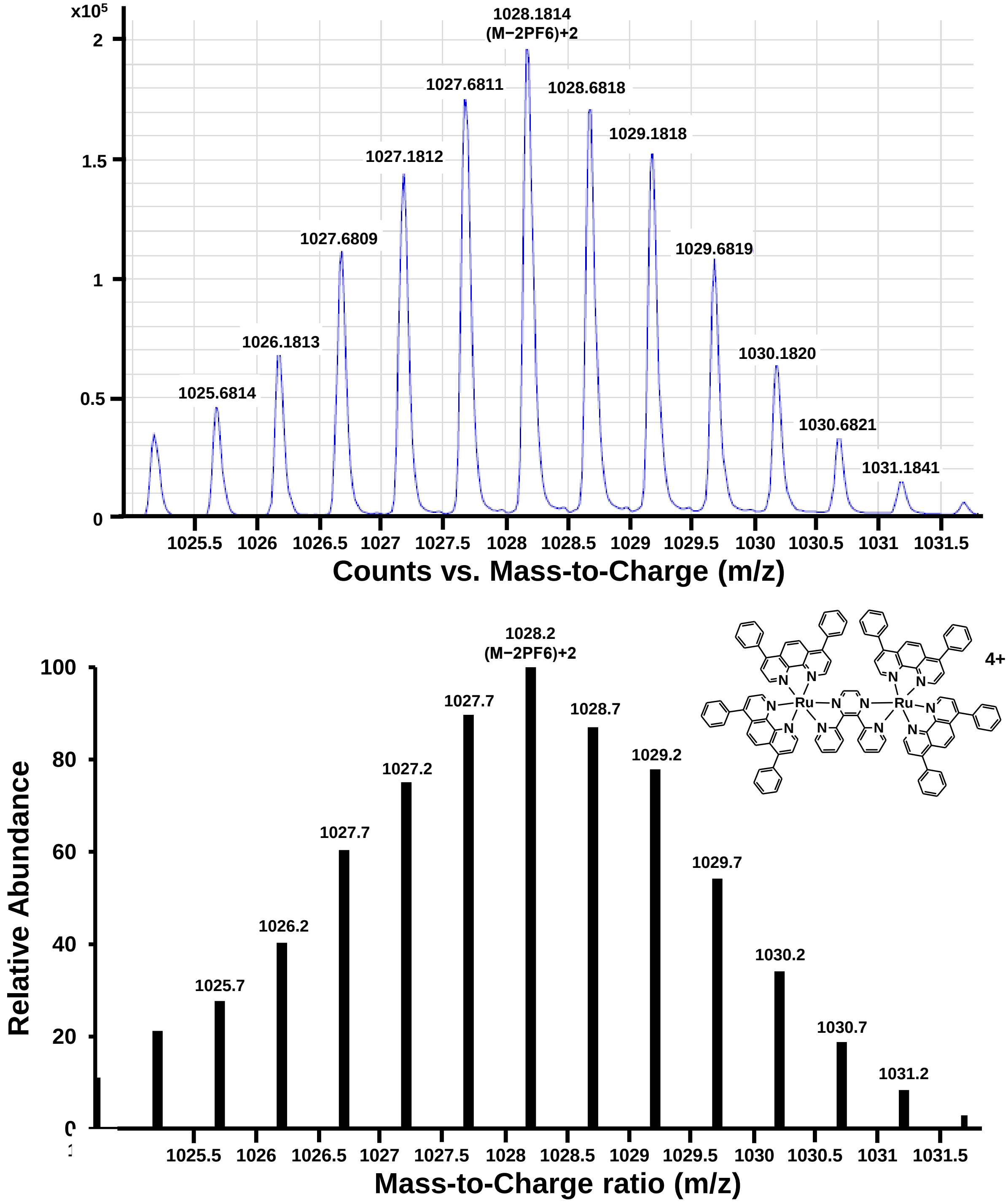

Figure A-3. Experimental (top) and calculated (bottom) mass spectra of $[\{(Ph_2phen)_2Ru\}_2(dpp)](PF_6)_4$. The molecular ion peak corresponds to $[M{-}2PF_6]^{2+}$.

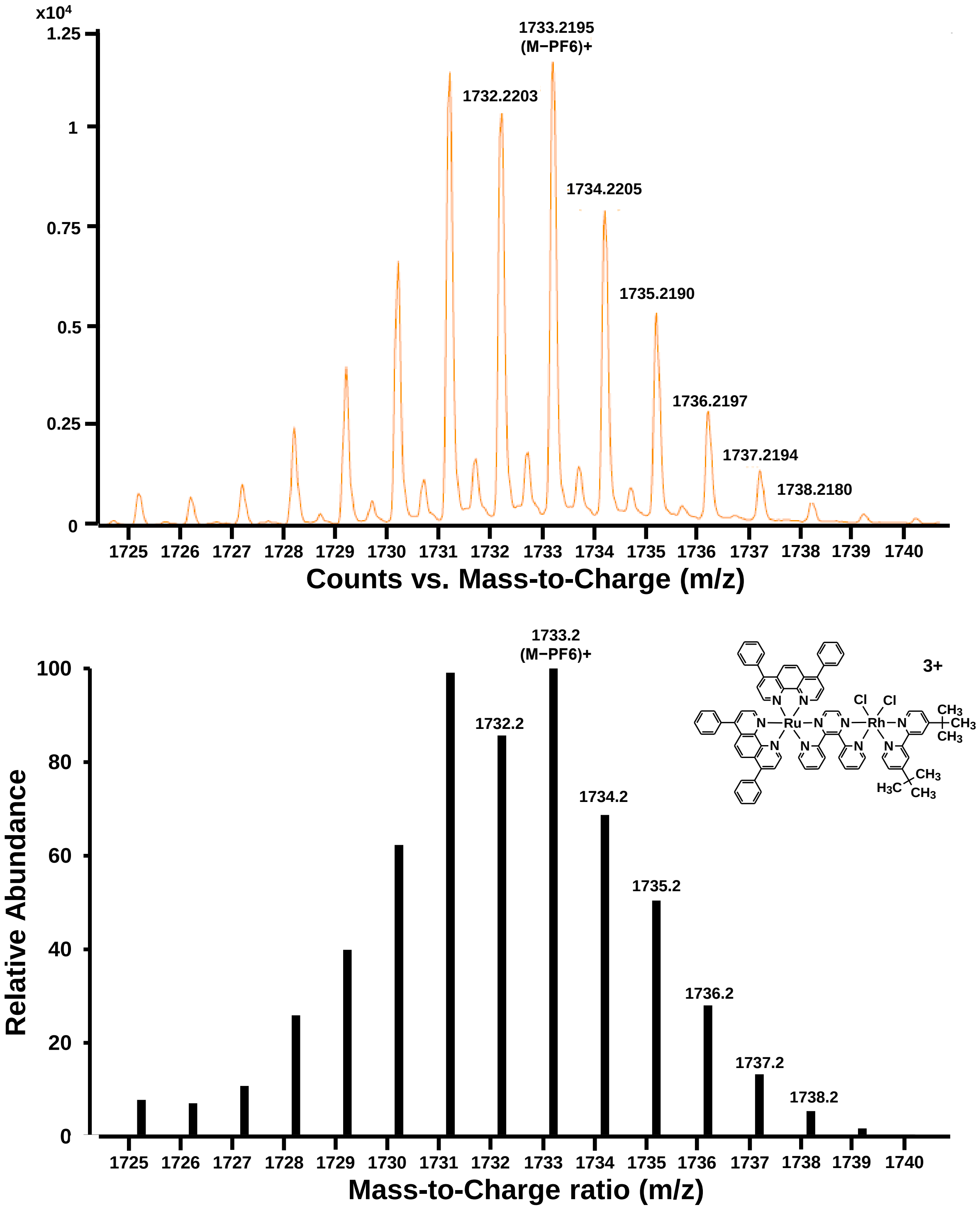

Figure A-4. Experimental (top) and calculated (bottom) mass spectra of $[(Ph_2phen)_2Ru(dpp)RhCl_2(^tBu_2bpy)](PF_6)_3$. The molecular ion peak corresponds to $[M{-}PF_6]^+$.

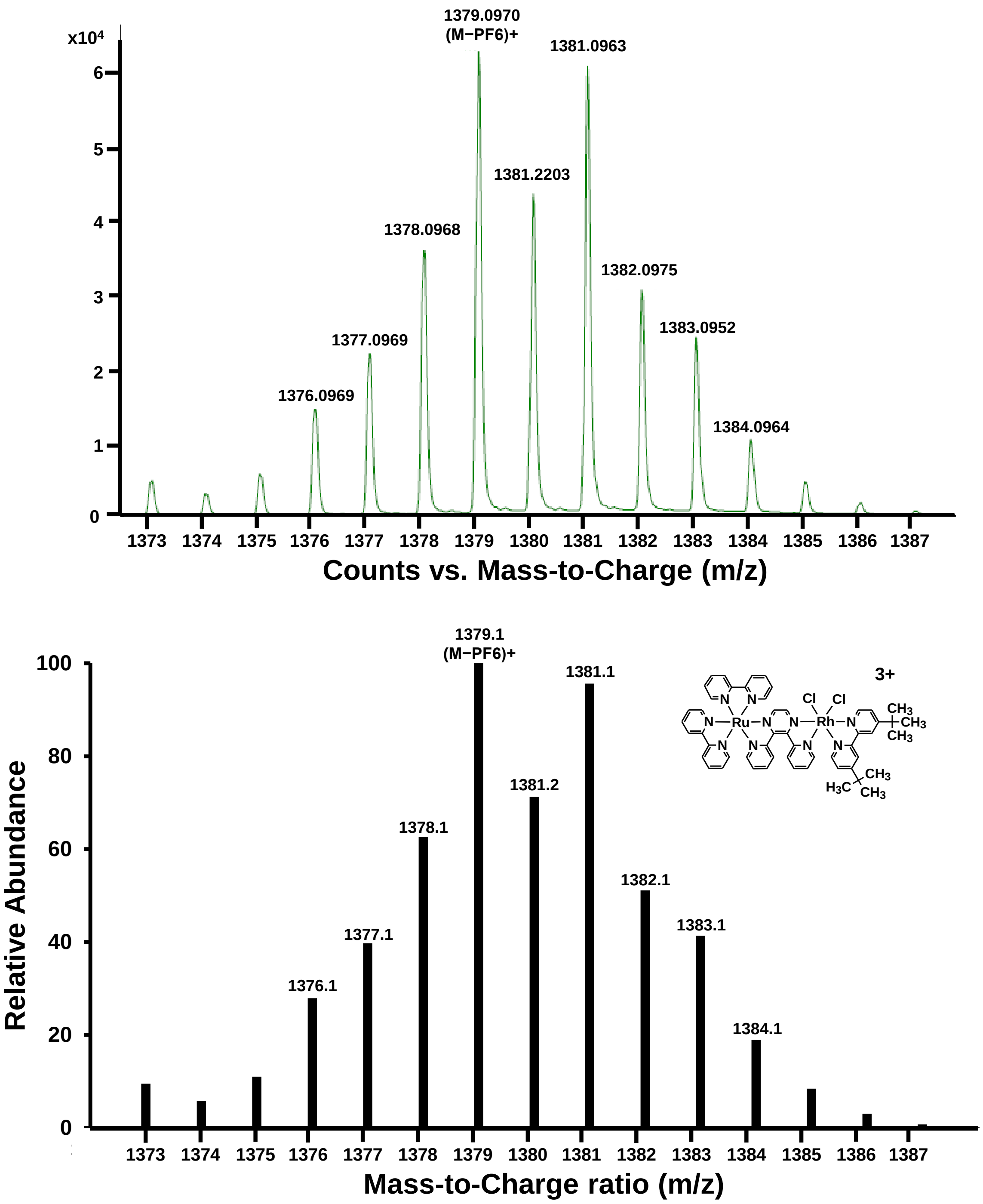

Figure A-5. Experimental (top) and calculated (bottom) mass spectra of $[(bpy)_2Ru(dpp)RhCl_2(^tBu_2bpy)](PF_6)_3$. The molecular ion peak corresponds to $[M-PF_6]^+$.

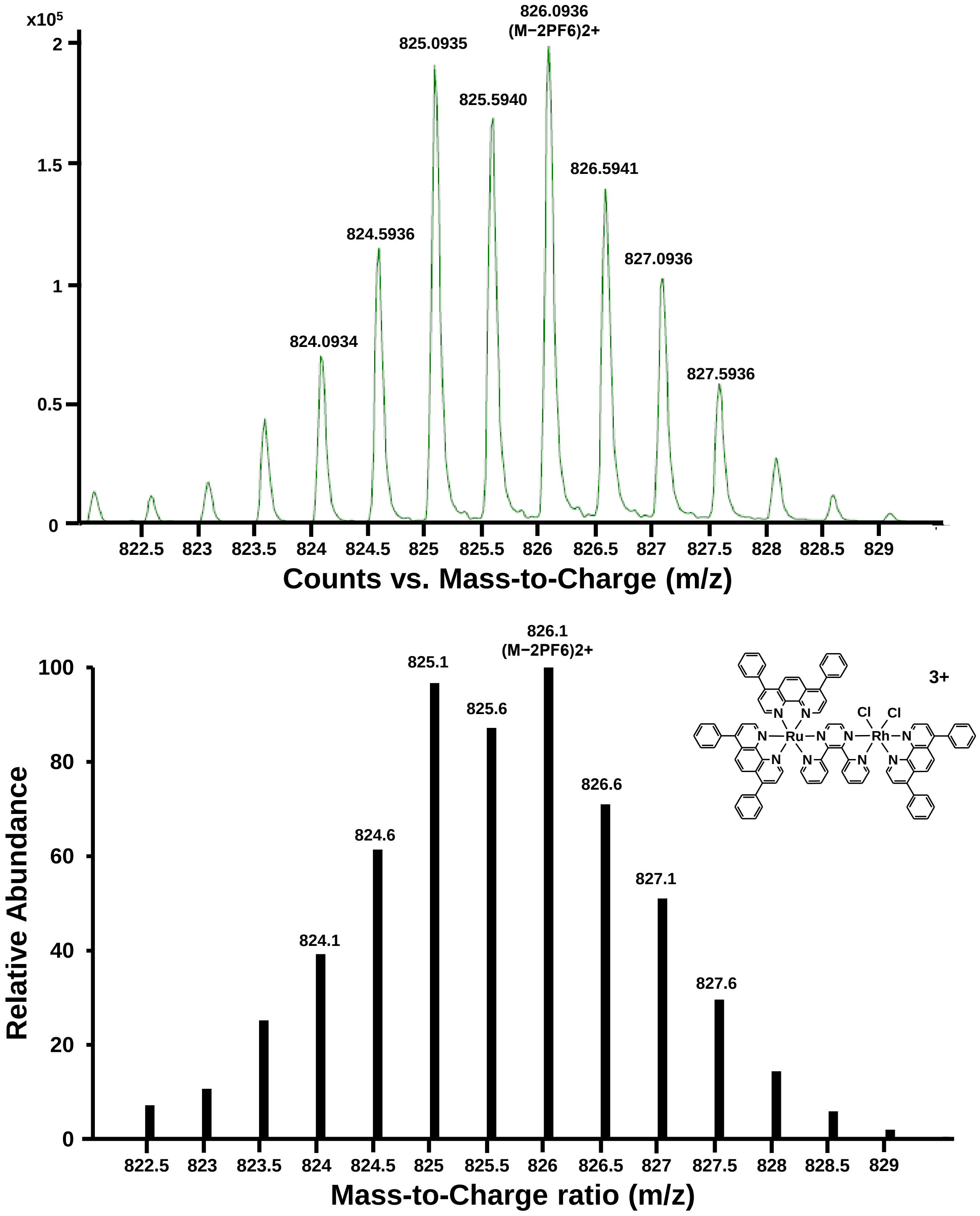

Figure A-6. Experimental (top) and calculated (bottom) mass spectra of $[(Ph_2phen)_2Ru(dpp)RhCl_2(Ph_2phen)](PF_6)_3$. The molecular ion peak corresponds to $[M{-}2PF_6]^{2+}$.

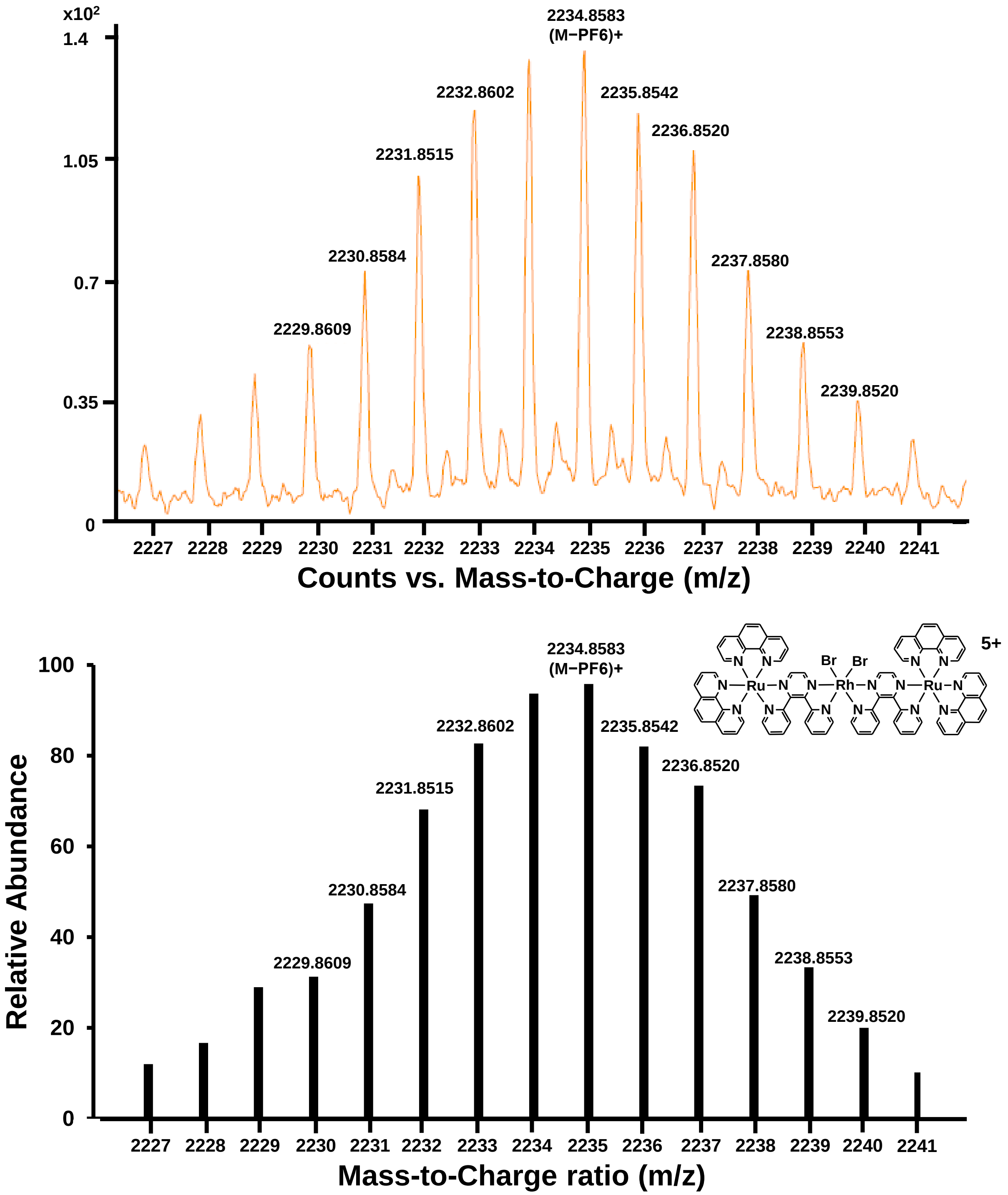

Figure A-7. Experimental (top) and calculated (bottom) mass spectra of $[\{(phen)_2Ru(dpp)\}_2RhBr_2](PF_6)_5$. The molecular ion peak corresponds to $[M{-}PF_6]^+$.

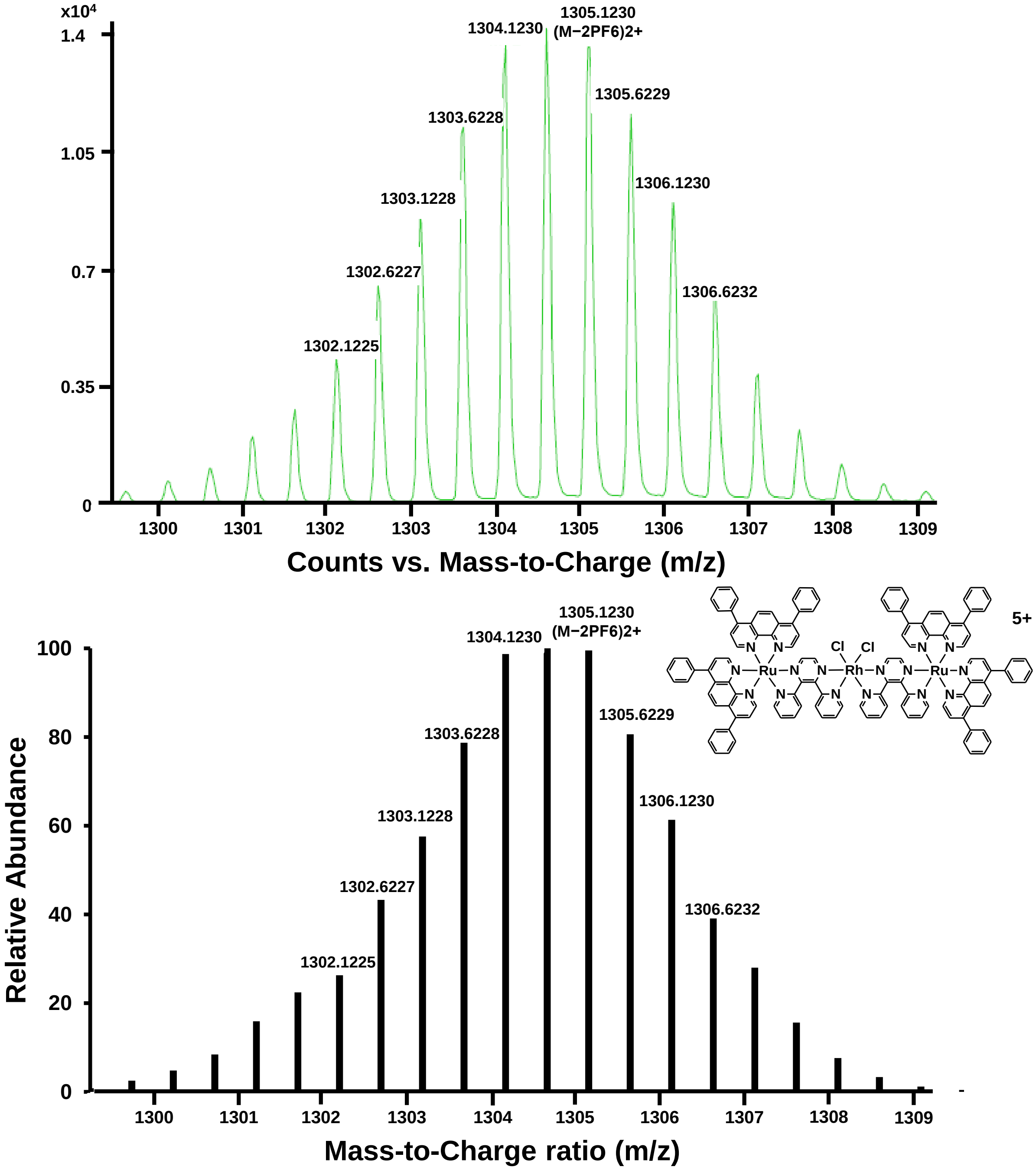

Figure A-8. Experimental (top) and calculated (bottom) mass spectra of $[\{(Ph_2phen)_2Ru(dpp)\}_2RhCl_2](PF_6)_5$. The molecular ion peak corresponds to $[M{-}2PF_6]^{2+}$.

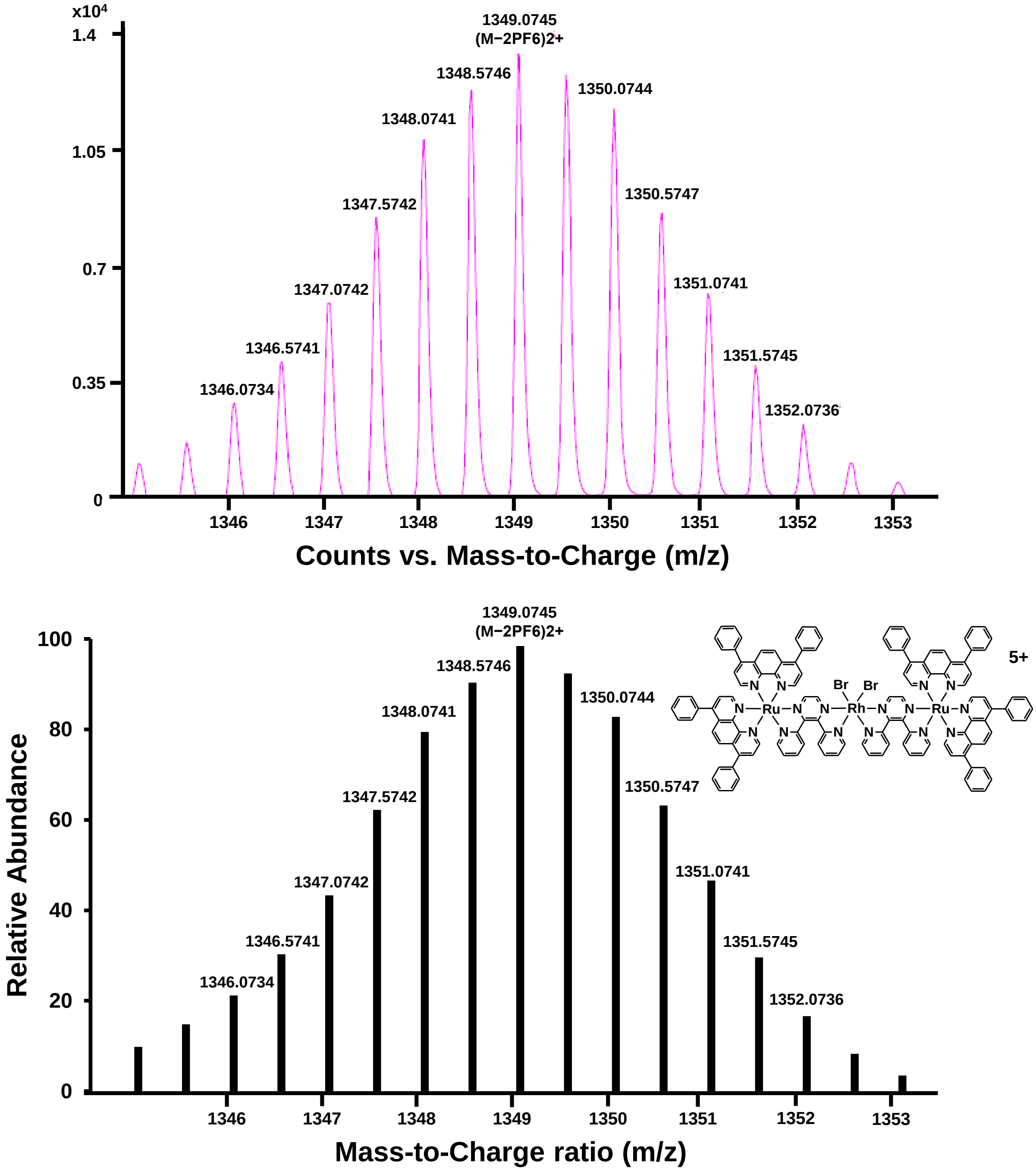

Figure A-9. Experimental (top) and calculated (bottom) mass spectra of $[\{(Ph_2phen)_2Ru(dpp)\}_2RhBr_2](PF_6)_5$. The molecular ion peak corresponds to $[M{-}2PF_6]^{2+}$.

Table A-1. Electrochemical and Photophysical Properties of Complexes

Complex	E_{ox} (V) [a]	E_{red} (V) [a]	λ_{max}^{abs} (nm) [b]	λ_{max}^{em} (nm) [b]	Φ^{em} [b]	τ (ns) [b]
$[Ru(bpy)_3]^{2+}$ [c]	+1.31	−1.30	449	603	0.070	850
$[Ru(phen)_3]^{2+}$ [c]	+1.31	−1.31	443	585	0.020	400
$[Ru(Ph_2phen)_3]^{2+}$ [d,e,f]	+1.29	−1.27	460 [p]	618 [q]	0.366 [q]	6400 [q]
$[Ru(dpp)_3]^{2+}$ [g,h,i]	+1.72	−0.91	457	623		183
$[(bpy)_2Ru(dpp)]^{2+}$ [i,j,k]	+1.38	−1.01	464	691	0.023	240
$[(phen)_2Ru(dpp)]^{2+}$ [i,l]	+1.45	−1.02	465	652		252
$[(Ph_2phen)_2Ru(dpp)]^{2+}$ [l,m]	+1.41	−0.98	474	664	0.035	820
$[\{(bpy)_2Ru\}_2(dpp)]^{4+}$ [i,j]	+1.43	−0.61	523	758	0.00098	126
$[\{(phen)_2Ru\}_2(dpp)]^{4+}$ [l]	+1.50	−0.62	525	750	0.0016	170
$[\{(Ph_2phen)_2Ru\}_2(dpp)]^{4+}$ [l]	+1.45	−0.61	540	754	0.0017	192
$[Rh(bpy)_2Cl_2]^{+}$ [n,o]		−0.89 [r]	310			
$[Rh(bpy)_2Br_2]^{+}$ [o]		−0.79	311			
$[\{(phen)_2Ru(dpp)\}_2RhCl_2]^{5+}$ [l]	+1.61	−0.35	516	780	0.00022	38
$[\{(phen)_2Ru(dpp)\}_2RhBr_2]^{5+}$ [l]	+1.62	−0.32	516	780	0.00017	34
$[\{(Ph_2phen)_2Ru(dpp)\}_2RhCl_2]^{5+}$ [l]	+1.59	−0.35	516	770	0.00024	52
$[\{(Ph_2phen)_2Ru(dpp)\}_2RhBr_2]^{5+}$ [l]	+1.58	−0.32	516	770	0.00020	40
$[(Ph_2phen)_2Ru(dpp)RhCl_2(^tBu_2bpy)]^{3+}$ [l]	+1.59	−0.37	514	774	0.00027	45
$[(Ph_2phen)_2Ru(dpp)RhCl_2(Ph_2phen)]^{3+}$ [l]	+1.59	−0.37	514	774	0.00029	43
$[(bpy)_2Ru(dpp)RhCl_2(^tBu_2bpy)]^{3+}$ [l]	+1.63	−0.37	506	782	0.00019	39

[a] Values reported vs. Ag/AgCl in CH_3CN using 0.1 M Bu_4NPF_6 unless otherwise stated.
[b] Measured at RT in CH_3CN unless otherwise stated. [c] From reference 18. [d] From reference 54. [e] From reference 65. [f] From reference 76. [g] From reference 55. [h] From reference 66. [i] From reference 60. [j] From reference 59. [k] From reference 42. [l] This work. [m] From reference 67. [n] From reference 78. [o] From reference 79. [p] Measured in H_2O. [q] Measured in 4:1 EtOH/MeOH at 20 °C. [r] Measured using 0.1 M tetraethylammonium perchlorate (TEAP) in CH_3CN.